UNIVERSITY OF BIRMINGHAM

SYNCHRONIZATION OF NETWORKED STARING RADAR WITH LOW PHASE NOISE PHOTONIC OSCILLATORS

by

DARREN GRIFFITHS

A thesis submitted to the University of Birmingham for the degree of

DOCTOR OF PHILOSOPHY

Alkaline Group

School of Physics and Astronomy

College of Engineering and Physical Sciences

University of Birmingham

September 2024

Abstract

Networked radar systems provide benefits in terms of extended coverage, resiliency and improvements to target tracking and classification. The remote sensor nodes provide additional challenges of distributing the local oscillator signal simultaneously to both the transmitter and receiver. This leads to increased requirements for timing synchronization as well as a reliance on stable and accurate oscillators due to the lack of inherent phase noise suppression. The focus of this work is to apply methods to synchronize two static L-band staring radar systems, and is achieved via signal processing methods as well as the use of disciplined oscillator configurations.

The use of digital signal processing techniques for synchronization provides adaptability and simplicity to the radar hardware. Novel methods have been developed with the subject of radar networks operating in an urban environment in mind. The range profile correlation method provides time offset correction for the radar and the multiple reference phase correction (MRPC) method corrects residual phase errors, both improving synchronization accuracy and suppressing phase noise. Both this techniques make use of alternative reference sources in the urban environment.

Alternatively, the use of atomic clocks provides a solution which is not reliant of external reference sources. This work is part of the development towards the quantum enabled network radar and reports on the use of a new Fabry-Perot cavity based, microwave photonic common-mode configuration for supplying disciplined oscillators to each node. This method has been applied to the network, achieving synchronization accuracy of 14 ps over the period of 600 s. Use of this photonics technology can have impacts on synchronization of various networked sensor systems.

Acknowledgements

Firstly I would like to give a huge thanks to my supervisors. Prof. Yeshpal Singh has always been very supportive and I am glad to have him as my supervisor. He consistently provides equipment for the group, and I feel fortunate to have his support in attending and presenting at various international conferences over the past few years. Also, it has been a pleasure to have Prof. Chris Baker as my supervisor. As one of the leading experts in the radar field, he has been indispensable and provided many insights into distributed radar and coherency. He has always been available to provide support with research publications, etc, despite being in retirement for which I am very grateful.

I would like to thank the radar sub group of the Alkaline team Dr. Jithin Kannanthara and Gwynfor Donlan, who I have worked closely with over the course of my PhD and have been useful members of the team. Also, I would like to thank Dr. Mohammed Jahangir, who has been very useful throughout the course of my PhD and has aided with organisation of the installation of the radars and radar measurements. Huge thanks also to Prof. Michail Antoniou, for the countless discussions we had on the radar oscillator measurements and radar synchronization. In addition, thank you to the Defence Science and Technology laboratory (DSTL) who have provided funding for my PhD.

To the many other people who have supported me throughout the course of the PhD. Former post doc of the Alkaline and radar team Dr. Jonathan Jones how has taught me alot about time and frequency measurement in my initial years. Former Alkaline team post doc Dr. Qiushuo Sun for always been available to advise with various aspects of my PhD, even after her departure. Abhilash Jha, who has had many conversations of optical clocks, usually over a bottle

of whiskey. Jordan Wayland, who has had various useful discussion with me on optical cavities. Dr. Yogeshwar Kale, who has always been there to help with any issues I came across with optics experiments. Also, to the rest of the Alkaline team current and former such as, Sandhya Ganesh, Yuheng Huyan, Balsant Tiwari, Dr. Manan Jain, Dr. Alok Singh, Dr. Shengnan Zhang and countless others. To the radar team on the MISL side current and former, Dr. Daniel White, Xiaofei Ren, Nuoshi Chen, Dr George Atkinson and many more. Duleep Wickramasinghe and Chris Swinerd for the continued support and Dr. David Morris for providing the second Rakon OCXO on loan for radar measurements. To the UCL radar sensing team consisting of Dr. Matthew Ritchie and Dr. Piers Beasley for collaborations on the GPSDO work.

Finally, a special mention to all of my girlfriend, Erica who has given me a lot of support over throughout the last 4 years, all of my friends and family and everyone who I may have missed, all of your support has been greatly appreciated.

Contents

List of Figures

List of Tables

Chapter 1

Introduction

1.1 Motivation

Since the inception of radar systems in the 1920s, their use has been mainly in the use for defence applications [1]. However, they have proven to be vital instruments for various civilian applications such as in airports [2], airlines [3], automotives [4], weather monitoring [5] and space exploration [6]. Although radars alone can be a powerful sensor, challenges such as detection of low reflectivity "stealth" targets [7], shadowing effects [8], clutter and multipath interference [9] have inspired the research effort into distributed networked radar systems [10].

This work addresses some of the barriers to networked radar such as synchronization [11] and the lack of inherent phase noise cancellation [12]. The use case, for the radar systems used as a part of this work, is for small unmanned aerial vehicle (S-UAV) detection in urban environments where the difficulty of detection is amplified due to low radar cross section (RCS), slow velocity, low altitude and strong stationary clutter [9].

Large man-made structures situated within urban settings produce backscatter, with a power several orders of magnitude greater than the intended target [9]. If the clutter power is sufficiently strong, the effect of phase noise is higher than the thermal noise floor of the radar receiver, at the Doppler frequencies of interest. The degradation of SNR is proportional to the power of the strongest signal, which is usually the stationary clutter in the resolution cell, appearing at

zero Doppler frequency. This can also occur when a large structure is present in adjacent range gates and within the angular sidelobes. Therefore, a single clutter contribution can cause a reduction in sensitivity in multiple regions. In a monostatic system, there is a level of phase noise compensation [12], but in the case of a distributed system, more reliance is placed upon the frequency stability and accuracy of the local oscillator.

In the case of a non co-located transmitter and receiver, incoherency between the local oscillators can impact the performance. Phase errors result in coherent integration loss [13] and timing offsets cause a range uncertainty [11], while frequency offsets induce a shift in the observed object velocity and also produce an equivalent timing error drift [11].

Within this work, various methods of synchronization are explored, ranging from the use of digital signal processing, disciplining oscillators using the current global navigation satellite systems (GNSS) infrastructure, and novel photonics based oscillator schemes resulting in 10 picosecond level synchronization accuracy.

1.2 Publications

Journal Articles

• **[J5] Griffiths, D**., Kannanthara, J., Donlan, G., Jahangir, M., Baker, C.J., Antoniou, M., Singh, Y. (2024). 'Precision Synchronization of Networked Radar using an Optical Clock Laser.' [Manuscript in preparation]

• **[J4] Griffiths, D**., Donlan, G., Kannanthara, J., Jahangir, M., Baker, C.J., Antoniou, M., Singh, Y. (2024). 'Phase Synchronization of Bistatic Radar by Exploiting the Urban Scene.' [Submitted, under review]

• **[J3] Griffiths, D**., Jahangir, M., Kannanthara, J., Donlan, G., Baker, C. J., Antoniou, M., & Singh, Y. (2024). Fully digital, urban networked staring radar: Simulation and experimentation. IET Radar, Sonar and Navigation, 18(5), 657–673.

https://doi.org/10.1049/rsn2.12499

• **[J2]** Jahangir, M., **Griffiths, D**., White, D., Donlan, G., Ren, X., Kannanthara, J., Singh, Y., Wayman, J. P., Baker, C. J., Sadler, J. P., Reynolds, S. J., & Antoniou, M. (2024). 'Development of a networked photonic-enabled staring radar testbed for urban surveillance.' IET Radar, Sonar and Navigation, 18(1), 41–55.
https://doi.org/10.1049/rsn2.12524

• **[J1]** Kannanthara, J., **Griffiths, D**., Jahangir, M., Jones, J. M., Baker, C. J., Antoniou, M., Bell, C. J., White, H., Bongs, K., & Singh, Y. (2023). 'Whole system radar modelling: Simulation and validation.' IET Radar, Sonar and Navigation, 17(6), 1050–1060.
https://doi.org/10.1049/rsn2.12399

Peer-reviewed Conference Publications

• **[C8] Griffiths, D**., Jahangir, M., Beasley, P., Ritchie, M., Kannanthara, J., Donlan, G., Baker, C.J., Antoniou, M., Singh, Y. (2024). 'Synchronization Performance of L-Band Staring Radar with Different GPSDOs.' [Manuscript in preparation]

• **[C7]** Donlan, G., **Griffiths, D**., Jahangir, M., Kannanthara, J., Baker, C.J., Antoniou, M., Singh, Y. (2024). 'L-Band Staring Radar Performance in Response to Differing LOs.' [Manuscript in preparation]

• **[C6] Griffiths, D**., Jahangir, M., Donlan, G., Kannanthara, J., Antoniou, M., Baker, C., & Singh, Y. (2023). 'Microwave Photonics in Networked Staring Radar.' 2023 International Topical Meeting on Microwave Photonics (MWP), 1–4.
https://doi.org/10.1109/MWP58203.2023.10416574

• **[C5] Griffiths, D**., Jahangir, M., White, D., Kannanthara, J., Donlan, G., Baker, C. J., Singh,

Y., & Antoniou, M. (2023). 'Urban Clutter Analysis for Drone Detection using L-band Staring Radar.' 2023 IEEE International Radar Conference (RADAR), 1–6.
https://doi.org/10.1109/RADAR54928.2023.10371017

• **[C4]** Jahangir, M., **Griffiths, D**., Singh, Y., Antoniou, M. (2023). 'Building a Quantum-Enabled, Networked Radar Testbed for Urban Surveillance of Low Observable Aerial Targets – Current Status.' 10th NATO Military Sensing Symposium.
https://doi.org/10.14339/STO-MP-SET-311-MSS-028-PDF

• **[C3]** Jahangir, M., Atkinson, G., White, D., **Griffiths, D**., Ren, X., Wayman, J., Baker, C.J., Sadler, J., Reynolds, J., Antoniou, M. (2022). 'Networked Staring Radar Testbed for Urban Surveillance: Status and Preliminary Results.' IEEE International Radar Conference (RADAR).
https://doi.org/10.1049/icp.2022.2363

• **[C2] Griffiths, D**., Jahangir, M., Kannanthara, J., Baker, C. J., Antoniou, M., & Singh, Y. (2022). 'Direct Signal Synchronization for Staring Passive Bistatic Radar.' International Conference on Radar Systems (RADAR 2022), 220–225.
https://doi.org/10.1049/ICP.2022.231910.1049/ICP.2022.2319

• **[C1]** Jones, J.M, **Griffiths, D**., Kannanthara, J., Jahangir, M., Antoniou, M., Baker C.J., Bongs, K., Singh, Y. (2022). 'Quantum Enabled Radar Sensing.' 2022 IEEE International Topical Meeting on Microwave Photonics, MWP 2022.
https://doi.org/10.1109/MWP54208.2022.9997763

1.3 Original Contributions

• Development of synchronization processing for the bistatic L-band staring radar system. **[C2]**

• Developed the bistatic data corrections for compensation of timing error in the L-band staring radar network using a range correlation method. **[J3]**

• Developed the bistatic detection capability using the L-band staring radar systems. **[C2] [J3] [J4] [J5]**

• Involved in performing the frequency stability characterization of the various oscillators and the oscillator-radar interface up to the transmitted signal and developed tools for characterising synchronization performance of the L-Band radar network. **[J5] [C4] [C6] [C7]**

• Developed a novel phase synchronization scheme for bistatic radar, based on use of multiple reference sources for phase estimation. **[J4]**

• Developed a simulation toolbox for the staring radar network, simulating multiple targets, clutter and radar nodes, including their respective local oscillators with frequency instabilities. **[J3]**

• Contributed to the development of the quantum-enabled networked radar at UoB of UK as part of the Quantum Technology Hub in Sensors and Timing. **[J5] [C1] [C4] [C6] [C7]**

• Developed a active stabilized fibre link setup for optical frequency transfer between Quantum Technology (QT) Hub labs, which became a prototype for developing the HARPO systems. **[J5]**

• Development of the microwave photonic common mode configuration, utilizing a master optical cavity, optical frequency combs and microwave photonic generation. This method enables coherent comb operation in distributed radar, achieving a high level of synchronization and ultra-low phase noise local oscillators. **[J5] [C6]**

1.4 Thesis Outline

Excluding the current introductory chapter, the content of the remaining chapters of this thesis are described:

Chapter 2 - Radar Systems : This chapter provides a brief introduction to radar system with respect to the radar equation. Also, the topic of networked radar is introduced, along with the effects of noise in the radar.

Chapter 3 - Quantum Enabled Networked Radar Overview : This chapter provides an overview of the Quantum enabled radar project, explain how optical atomic clocks can be beneficial to distributed radar. Then each of the different subsystems are introduced with the focus on the components of modern photonics based technologies ranging from optical atomic clocks to photonic radar.

Chapter 4 - Staring Radar Network Modelling : This chapter describes the work on the network radar simulation. The simulation architecture is described, with the ability to simulate multiple L-band staring radar systems together and including each of their oscillator dynamics for emulation of synchronization errors.

Chapter 5 - Radar Hardware and Measurement Procedure : This chapter describes the hardware processing chain of the L-band staring radar from the local oscillator, to the transmitted signal, to the digital signal processing. Also, the procedures for radar measurements are introduced.

Chapter 6 - Networked Radar: Digital Signal Processing Synchronization Techniques : This chapter dives into the work using the L-band staring radars in a bistatic configuration. Analysis of various effects of a non-coherent network are presented before introducing methods to synchronize the radars using software. Two novel synchronization schemes are applied for use in an urban environment, one using range profile correlation to correct timing error and another using multiple reference phase correction (MRPC) to correct residual phase errors between the two nodes.

Chapter 7 - Networked Radar: Synchronization Using Ultra Stable Oscillators : This chapter focused on the effect of disciplined and stable oscillators to synchronize network radar

and reduce the effects of phase noise. The first half is focused on GPS disciplined oscillators, their ability to synchronize the L-band system and which characteristics are most important for optimal performance. The second half is focused on the use of optical clock technology and provides a novel method to synchronize radar systems using a microwave photonics (MWP) common-mode configuration to synchronize to the 10 picosecond level along with a comparison of target detection performance for a wide range of oscillator configurations. Finally the future outlook on the development of radars and photonic oscillator technology is discussed.

Chapter 8 - Conclusion : This chapter concludes the thesis.

Chapter 2

Radar Systems

Radars currently have applications in many areas including target detection of aircraft [3], area mapping [14], and weather surveillance [5], although this report will be mainly focused on target detection [15]. There are various types of radars, including pulse Doppler radars that produce periodic pulses [16], holographic staring radar [17] that illuminates the entire field of view (FOV) simultaneously, and synthetic aperture radar (SAR), that utilises moving radar platforms for a fine special resolution [18], among many others. Radars can have "move to scan" / mechanical antennas or can be electronically scanned array antennas that change the phase of the received signals to digitally form beams towards different directions [19] [20]. One key radar design which will be focused on is network radars, where multiple individual radars work together as a single sensor to provide enhanced performance [10].

This chapter will start with the radar basics, where the basic operation of a monostatic radar is described. This is followed by an introduction to different noise types that affect radar systems, and finally, a section on network radar along with the differences this brings and their requirements for synchronization.

2.1 Introduction to Radar Systems

One of the key tasks in most radar applications is for the system to be able to make detections, and it is able to do this by transmitting a signal using a transmitting antenna, and then listening to

target echoes using a receiver antenna. The target's received signal must be detected amidst the inherent thermal noise present in all radar receivers. For the object to be successfully detected, the target signal must exceed a specified threshold, which is decided by the background noise level. The location of the target in 3 dimensions can be determined by measuring the range and the angles for azimuth and elevation. The range can be deduced by measuring the time difference between when the signal was transmitted and the instant that the target echo is received. By using the assumption that the distance between the transmitter and target is the same as the distance between the receiver and target, and also using the known constant for the speed of light in the atmosphere, equation 2.1 can be used to calculate the targets range (R).

$$R = \frac{c\delta}{2} \tag{2.1}$$

Where c is the speed of light and δ is the time difference between transmission and reception of the pulse (time delay).

Generally, two angles are needed to measure in 3 dimensions and these are the azimuth angle (left/right angle) and the elevation (up/down angle) so that the target can be determined at a certain point in the spherical coordinate system. The method used to scan through each angle is dependent on the radar design, especially the antenna design and whether it is mechanically scanned or a phased array antenna. Depending on the beam width and directivity pattern, more beams will be needed to cover the entire field of view (FOV) [19]. The FOV is defined as the entire volume of space that the radar can detect targets. Then a combination of finding the beam with the maximum target return and interpolation can be used to find both azimuth and elevation angles. In a mechanical antenna, the antenna would be steered at various angles for small numbers of pulses, and the antenna position at the moment of detection will be taken as the target angle. While in a phased array antenna, the phase at each transmitter is changed to steer the beam in various directions. Each group of pulses will be stored into a frame for processing, each angle will be stored into a different frame and therefore, multiple frames are needed for each scan. This is true for a multibeam system but a staring radar such as the one used in this report, each transmitted pulse covers the entire FOV so only a single scan angle

is needed and digital beamforming on receive is used to point the beam at different angles to record the target angle measurement [17]. For a staring radar, only a single frame is needed for each scan providing the advantage of simultaneous detection of multiple targets in the FOV, independent of their position.

A detection is made based on the power of the signal return, a threshold is set based on the background noise level and if the recording is sufficiently high (for example a typical radar could require 20 dB above the noise floor) then a detection can be made [19]. However, one of the problems encountered when making detections is clutter. Thus, for example in the case of ground-based radar, returns would not only be received from targets but also from various sources of clutter such as buildings, trees and the ground. As these would typically have much larger surface areas, they can produce the majority of the signal returns and potentially drown out signal echoes from targets [9]. This problem is conventionally addressed by Doppler processing, and the approach is effective provided radar clutter and targets move at substantially different velocities. Doppler radars measure the phase of the returned signal as well as the amplitude, allowing for the range rate of the target (velocity of the target relative to the radar) to be measured by determining the Doppler frequency. Moving targets can then be separated from the unwanted stationary clutter as they will produce a Doppler shift (f_D). The amount of Doppler shift a moving target will produce will be dependent on the range rate of the target ($\frac{dR}{dt}$) and the frequency of the transmitter signal (f) as shown in Equation 2.2 [15].

$$f_D = \frac{-2f}{c}\frac{dR}{dt} \tag{2.2}$$

2.2 Radar Equation

The ability for a radar to make a detection is defined by the signal to noise ratio (SNR) and this can be derived based on the various radar and target characteristics for any radar but for this case, it will be based on the radar range equation for an L-band staring radar shown in equation 2.3 [15]. In this radar, pulses are emitted at the pulse repetition frequency (PRF) and sampled at various

ranges equivalent to their respective time delays. A number of channels are used dependant on the number of receiving elements (N_{Ch}) and these are combined during the processing to form beams. Also a number of pulses (N_{FFT}) are grouped into a frame and integrated together to increase the SNR. More details about the radar data frame will be explained in Chapter 4

$$SNR = \frac{P_T G_T G_R \sigma \lambda^2 N_{FFT} N_{Ch}}{(4\pi)^3 R^4 k T_0 B F L} \tag{2.3}$$

Where P_T is the power of the transmitted signal, G_T and G_R are the antenna gains of the transmitter and receivers respectively, σ is the radar cross section (RCS), λ is the wavelength of the transmitted signal, k is the Boltzmann constant, T_0 is the standard operating temperature (290 K), B is the receiver bandwidth, F is the noise figure (defined as the ratio between the SNR at the receiver input and output) and L indicates any additional losses from ideal conditions.

The following sub-section explains the individual contributions in equation 2.3 and effectively derive this equation in reverse.

2.2.1 Transmitter and Antenna

In order to send out a radar signal, there needs to be a transmitter to generate the signal. The signal generator stage of the transmitter comprises the power supply to generate the high voltage DC signal, a modulator to generate pulses in a pulsed radar and the oscillator to ensure the signal phase is coherent and the general timing sequence is synchronized with other subsystems of the radar. The power supply and the modulator will determine the transmitted power and the pulse repetition frequency of the radar and will determine the operating ranges of the radar as can be seen by the P_T term in equation 2.3.

In order for the signal to be radiated into the environment, a transmitting antenna is required. The design choices of the antenna determine the directivity of the beam so that the radiation can be focused into specific directions and with a higher gain with respect to the isotropic gain [19]. Equation 2.4 determines the maximum directivity gain of the transmitting antenna and G_T is included as the total gain contribution of the transmitting antenna in the radar range equation

(equation 2.3).

$$G_T = \frac{\eta_a 4\pi A}{\lambda^2} \tag{2.4}$$

Where A is the aperture area and η_a is aperture efficiency. Also, as seen by equation 2.4 the choice of wavelength determines the maximum directivity gain. Radars that transmit at lower frequencies generally will require larger antennas due to this. Another important parameter is beamwidth, defined as the angular region between the points where the transmitted power decreases by 3 dB from the peak of the main beam. [15]

2.2.2 Propagation to and from the Target

Once the radiation has been radiated into the environment, the next stage is for the signal to travel from the transmitting antenna to the target. The propagation of the signal through free space induces loss. This is due to various factors such as the divergence of the beam as it spreads out in a spherical type pattern and the attenuation caused by various effects in the atmosphere [15]. The divergence of the beam is the biggest contributing factor for losses in lower frequency radar systems (less than 10 GHz) where the effect of atmospheric attenuation is less than 0.01 dB/km [21] and can be described with equation 2.5.

$$P_f = \frac{P_i}{4\pi R^2} \tag{2.5}$$

P_i is the initial power of the signal, P_f is the power density after signal propagation and R is the distance the signal is required to travel between the transmitter and the target. The signal would also need to travel again upon reflection back to the receiving antenna and this will incur the same type of loss. Therefore, combining both sets of propagation losses will produce the $\frac{1}{(4\pi)^2 R^4}$ contribution within the radar range equation (equation 2.3).

2.2.3 Target Reflections

When the signal reaches the target there will be losses due to the absorption and re-radiation from the surface of the target. This is not a factor that can be controlled in most applications but may be useful to consider when designing other parts of the radar. Targets in the real world are complex and will cause the signal to scatter and reflect in different ways. The size of the target is one of the factors of determining the RCS, large aircraft will reflect more of the radar signal than a bird for example. The shape of the object is a factor, a flat plate will produce a large RCS and for more complex targets a change in aspect angle can result in dramatic changes in RCS [22]. Also, the material should be considered, stealth aircraft commonly use absorbing materials as they are efficient in converting more of the electromagnetic energy into heat energy and reducing reflection [22]. Due to the complexity of the scattering mechanisms from complex targets, reflection is simply compressed into a single term called the RCS (σ measured in square meters) and can be defined as the ratio between the power density after reflection and prior to reflection. The RCS term is contained in the radar range equation to represent the contribution of the losses due to reflection from the target.

2.2.4 Receiver

Receivers can be viewed as the section of the radar that converts the incoming radiation into digital signals for processing. The first stage, is the receiving antenna which can be the same as the transmitting antenna or they could be separate. There is an additional loss component at the receiving antenna as only a small fraction of the reflected signal at range R is intercepted by the antenna. The power density of the signal of this stage can be multiplied by the effective area (A_e) which is shown in equation 2.6.

$$A_e = \frac{G_R \lambda^2}{4\pi} \tag{2.6}$$

Where G_R is the gain of the receiving antenna and can be calculated equivalently to equation 2.4. Once the signal is received, the signal will be processed internally. Receivers also contain

amplifiers, various filters, mixers and an analogue to digital converter (ADC) so that the signal can be processed digitally. Low noise amplifiers (LNA) are used to boost the signal power with minimal degradation to the SNR, therefore maintaining a lower noise figure. The terms on the right-hand side of equation 2.6 are contained in the radar range equation to show the contribution of the receiver.

2.2.5 Processing Gains

More detail about the individual processing steps used within this work will be presented in Appendix A but the general contribution to the radar range equation is the number of channels and number of pulses for integration.

N_{CH} represents the number of receiver channels used and each will be combined together to form beams. N_{FFT} represents the number of pulses integrated together and consequentially also determines the integration time of the radar. As the number of pulses integrated and number of channels increases, the SNR again increases proportionally. N_{CH} is constrained by the hardware available and the size of the radar but theoretically more channels are better. N_{FFT} is also preferred to be longer but there are also trade-offs to consider such as how long the target is expected to stay in the resolution cell and processing time. These two properties N_{FFT} and N_{CH} are contained within the radar range equation (equation 2.3) to show the main contributions of the processing on the SNR.

2.3 Noise in Radar Systems

In the real world, there is noise due to various mechanisms that can distort or even mask signals. This section will separate noise into two types, thermal noise and phase noise. Phase noise is not accounted for within the radar equation but it is useful to consider, since it is a crucial subject of this thesis.

2.3.1 Thermal Noise

Although thermal noise is unavoidable, its properties can be exploited in order to reduce its negative effect as much as possible. The main source of thermal energy in radar systems is usually from the random motion of electrons within electrical circuits in the receiver. The thermal noise is known to be white and Gaussian, meaning that the frequency spectrum of the noise fluctuates but is flat on average and that the probability density function, of the voltage of the thermal noise returns, follows a Gaussian pattern [23]. The Gaussian pattern means that it has an average value and is symmetric about the mean. Inherently, the mean power of the noise sets the limit for target detection. However, even if the target echo is weak, integrating multiple pulses can enhance the signal power more significantly than the noise power, thereby effectively increasing the Signal-to-Noise Ratio (SNR).

In radar systems, the thermal noise power (P_n) is set by the receiver system and can be defined by equation 2.7 [15].

$$P_n = kT_0FB \tag{2.7}$$

k is simply the Boltzmann constant (1.38 x 10^{-23} W S K^{-1}), T_0 is the operating temperature, B is the bandwidth of the receiver and F is the noise figure.

The key properties that can be changed are the bandwidth and the noise figure. The bandwidth can be reduced, to proportionally reduce the total noise power in the radar as seen by equation 2.7 but there is a trade off with radar resolution. Shorter pulses require larger bandwidths and the minimum requirement for bandwidth can be shown to be $\frac{1}{\tau}$ where τ is the pulse width. This ensures that the spectral components of the pulse are preserved. Otherwise, the pulse shape may become distorted, resulting in degraded SNR [19]. The noise figure is determined by the various filters and amplifiers within the receiver, the design of the receiver should carefully optimise the noise figure in order to reduce the thermal noise. The main contribution to the noise figure is the LNA that occurs at the start of the chain and its purpose is to produce high gain while having as little extra noise generated by the amplifier itself [24].

2.3.2 Phase Noise

In addition to thermal noise, there is also another type of noise prevalent in radar systems and this is phase noise. Unlike thermal noise, phase noise power is dependent on frequency and is very different in behaviour. This type of noise typically occurs near a carrier signal and falls off as the frequency offset increases [25].

The phase noise is the one-sided spectral density of the phase fluctuations measured in dBc/Hz [26], and is dependant on the local oscillator stability and additive noise throughout the radar RF chain. Oscillators are designed to give a pure periodic signal in order to function as a timing device. However, real oscillators are not perfectly pure tones and this introduces jitter in the time domain which can be seen as slight variations in the time instant that each zero crossing occurs. Also, the phase noise can be described as having slight frequency fluctuations over time.

More information about how it is measured in an oscillator is described in Appendix B, with the phase noise profiles for various oscillators presented in Chapter 7. Also, different types of phase noise (such as white noise, flicker noise, etc...) are simulated onto a radar signal within the modelling work in Chapter 4.

2.3.3 Combined effect of noise on Radar Systems

At a basic level, it is the thermal noise that limits the detection sensitivity and this cannot be improved beyond that as set by the receiver noise figure. However, in some circumstances, an issue is presented when needing to distinguish between target echoes on one hand, and background disturbances (e.g. land, sea, rain, etc), or "clutter", on the other. However, this ability is fundamentally limited by phase noise, introduced by various subsystems of the radar.

The complexity of the radar returns, including their amplitude, distribution, velocity, and variations, combined with the numerous sources of clutter, presents a significant challenge for radar systems for two interrelated reasons.

Firstly, that clutter returns usually exceed those of targets by several orders of magnitude [9]. This problem is conventionally addressed by Doppler processing, which is effective when radar

clutter and targets move at different velocities, as discussed earlier in section 2.1. However, in practice, phase noise can spread into adjacent frequencies, causing even static clutter to appear with moving components in the Doppler domain. This results in masking of weaker target echoes and lower Doppler frequency returns, as illustrated in figure 2.1 of clutter and target spectra in the radar, in one range and angle cell, i.e. the basis for Doppler radar detection. By improving the quality of the local oscillator, the overall radar noise floor is reduced, assuming other components in the radar are not limiting or contributing additive noise.

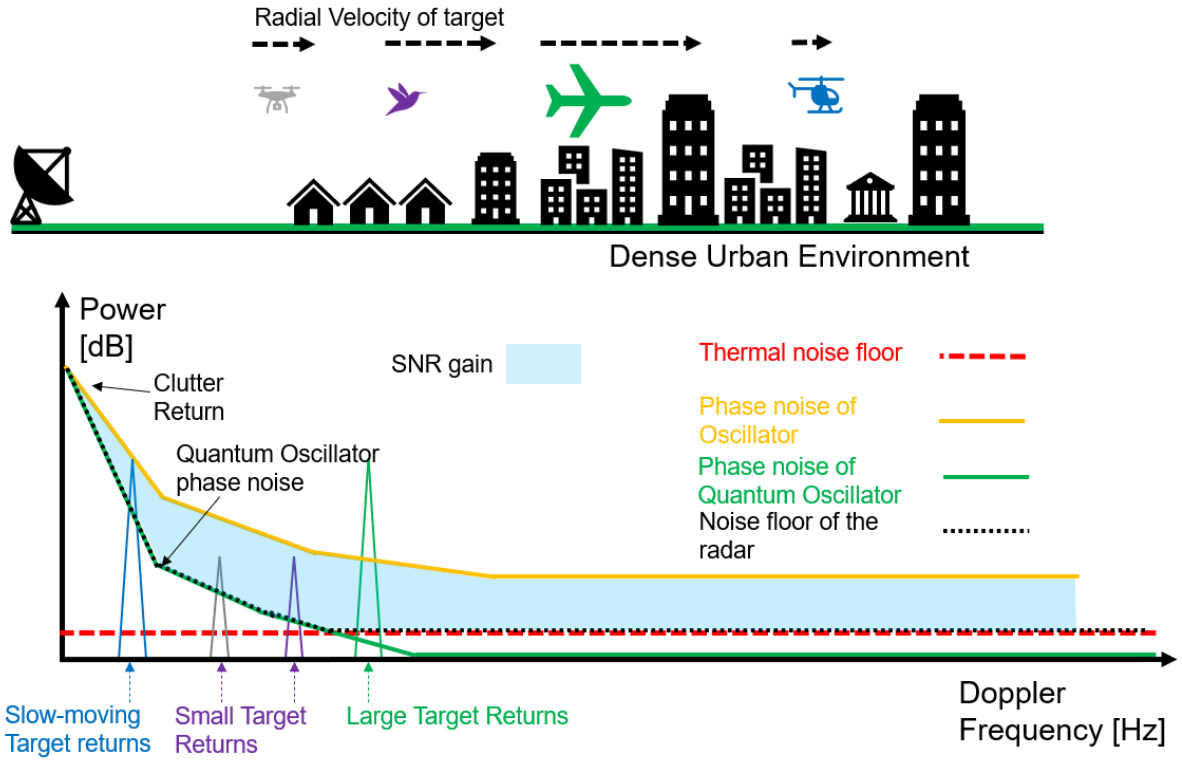

Figure 2.1: Graphic demonstrating the effect of phase noise on reducing the detectability of small or slow-moving targets.

Phase noise thus poses a fundamental limit to radar sensitivity and that is agnostic of the radar function (detect, track, or identify) and the specific application of the radar system. A reduction in phase noise will translate into greater sensitivity and hence better target detection, tracking etc.

Phase noise is dependent on the stability of the oscillator and the power of the received signal since phase noise is measured in dBc/Hz as a function of frequency offset from the carrier [25].

Since Birmingham is a built-up urban area, the field of view covers many high clutter regions due to large structures. Although, there are still several smaller residential or grassy regions that have comparatively lower clutter. Whether the clutter power is high or low, the fall-off rate of the phase noise will remain the same. Therefore, in high clutter regions, the phase noise lies above where the noise floor would be at higher frequencies. In this case, we can consider the radar to be phase noise limited and it is due to the instabilities in the oscillator signal that cause diminishing performance.

Sampling rates (slow time) in radar systems are constrained by the PRF, and the Nyquist frequency sets the limit for the maximum frequency that can be measured without ambiguity. The Nyquist frequency is defined as half of the sample rate and any frequencies present that are higher than this will appear to be mirrored above this as they are under sampled. For example, if the PRF of the radar is 10 kHz, the Nyquist frequency would become 5 kHz and if there was originally a frequency component at 6 kHz, it would fold across the Fourier spectrum and appear at -4 kHz instead. Therefore, phase noise contributions outside of this Nyquist band will fold back into the Nyquist band and add constructively. Potentially raising the phase noise levels at all frequency offsets.

An ideal radar LO will have low phase noise at the low frequency offsets for detection of slow moving targets, close to the stationary clutter. Also, it should have low phase noise at high frequency offsets, since the Nyquist frequency causes additional increase in the band limited noise, as mentioned previously.

2.4 Bistatic and Networked Radar

Previously in this section, the focus was on a monostatic radar setup which is the most simple and common approach. However, during this project, the effect of having 2 radars in a network configuration will have to be considered. There are various advantages to this including, detection of stealthy targets, immunity to electronic attack, detection of targets travelling in tangential trajectories and more [10]. The key difference is that the transmitters and receivers

can be spatially separated from each other. This can lead to many different configurations depending on the locations, how many radar nodes are in use and which are transmitters, receivers or both. In situations where the transmitter and receiver are separated this is called a bistatic setup [10].

One of the differences that can be examined with a networked radar is the difference it makes to the radar range equation. Thus, for the case of the bistatic set-up due to the new geometry, this leads to an altered bistatic radar range equation that is given as follows [15].

$$SNR = \frac{P_T G_T G_R \sigma_B \lambda N_{FFT} N_{Ch}}{(4\pi)^3 R^4 k T_0 B F} \tag{2.8}$$

Where R_R and R_T are the range between the target and receiver and the range between the target and transmitter respectively. σ_B is the bistatic RCS which would vary from the monostatic RCS especially at larger bistatic angles (the angle at the vertex consisting of the transmitter, target and receiver) [27]. Equation 2.8 also implies that, unlike in a monostatic system where the contours of constant SNR and constant range are collinear and circular, in a bistatic system, these contours become ellipses, and the contours of constant SNR become ovals of Cassini [10], this can be seen in Figure 2.2. Another effect of the new geometry is that the area of each resolution cell is no longer equal which means that the range and angular resolution is dependant on target position.

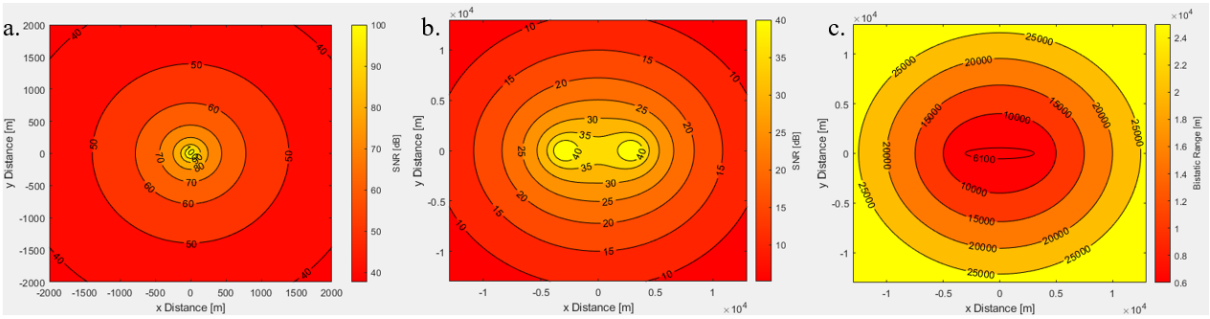

Figure 2.2: Constant SNR and range contours for monostatic and bistatic radar. (a) Both constant SNR and Range contours are circular for a monostatic radar. (b) Constant SNR contours are ovals of Cassini for a bistatic setup. (c) Constant range contours are ellipses for a bistatic setup.

The consequence of the new geometry is that it makes operation fairly more complex. In a monostatic radar, the calculation of the target position is fairly simple when the angle of arrival

(AOA) and the range is known.

Usually, to gather information about a detection, range, angle, position in 3 dimensions and its range rate are calculated in a monostatic radar as described in chapter 2.1. In the bistatic geometry, the range is calculated in a similar way by measuring the time delay between transmission and reception of the radar signal but unlike in the monostatic case, this doesn't directly contain information about target to receiver range (R_R) They cannot be separated without additional information and solving the bistatic triangle, which is illustrated in Figure 2.3. Assuming the locations or the transmitting and receiving nodes are fixed and are known, the baseline (L) can also be known. The AOA is found in the same way as in a monostatic radar and can be used to calculate the solid angle between the baseline and the transmitter (θ_{LR}). The target position can then be seen as where the AOA trajectory and the ellipse for the specific bistatic range meet or equivalently, the bistatic triangle in the plane made of the transmitter, receiver and the target. The cosine rule can be used on the bistatic triangle as in Equation 2.9 and used with the bistatic range (R_B) (Equation 2.10) to determine the receiver to target range (R_R) (Equation 2.11).

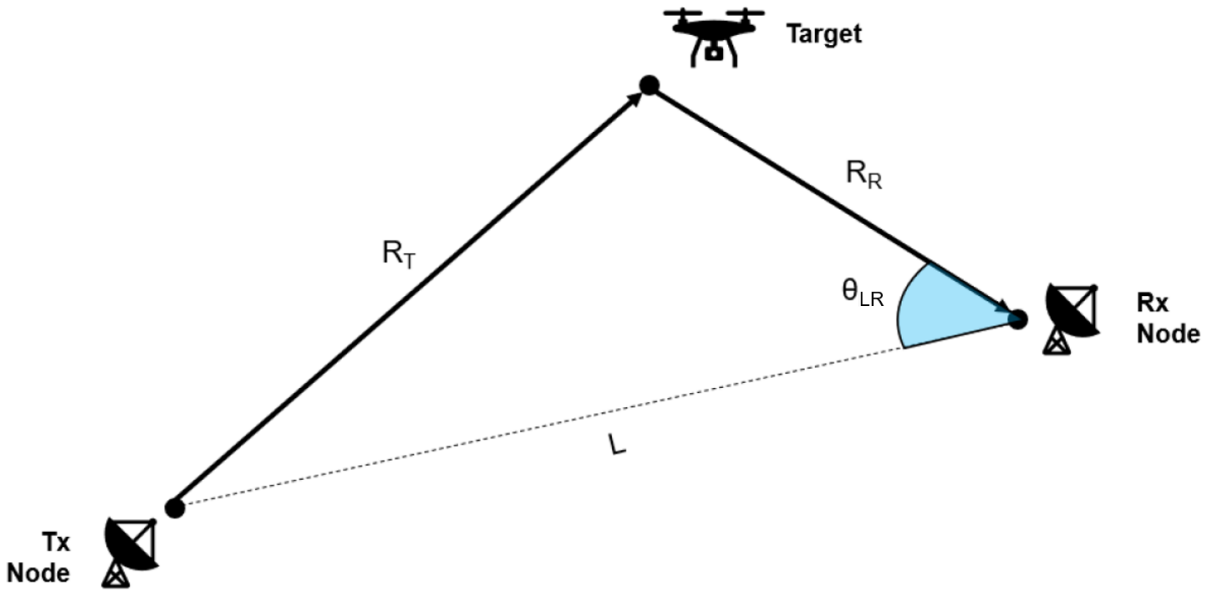

Figure 2.3: Bistatic triangle for target localisation in a bistatic configuration.

$$R_T = \sqrt{L^2 + R_R^2 - 2LR_R cos(\theta_{LR})} \tag{2.9}$$

$$R_B = R_T + R_R \tag{2.10}$$

$$R_R = \frac{R_B^2 - L^2}{2(R_B - Lcos(\theta_{LR}))} \tag{2.11}$$

Finally, the range rate is calculated in the same way by measuring the Doppler frequency shift of the target. However, the Doppler frequency shift is a result of the rate of change of the bistatic range as shown in Equation 2.12 [10].

$$f_D = \frac{-1}{\lambda}\frac{d(R_T + R_R)}{dt} \tag{2.12}$$

2.5 Synchronization requirements

In addition to these extra challenges, in order to achieve coherency between several different spatially separated radar nodes, time, frequency and phase synchronisation must be achieved. This is typically achieved either by using the same clock and sending to each radar individually [28], disciplining each oscillator to a frequency reference [29] [30] or multiple highly stable and accurate clocks can be used within each radar [28]. In a monostatic radar, the transmitter and receiver both utilise the same clock and therefore, phase fluctuations are correlated, rather than random, allowing for some level of cancellation. This does not tend to be the case for a bistatic radar for the case when separate oscillators are used at each node, signifying the need for high spectral purity radar signals to be used.

The key goal of this project is to achieve synchronisation between the staring radar network at the University of Birmingham and this section will be dedicated to this topic. There are many potential benefits to having separated radar receivers and transmitters but this comes at a cost of greater timing requirements. At the heart of each radar, an internal clock runs and is the key to keeping the timing of the radar. In a monostatic radar, each hardware component that has a timing requirement will share the same internal clock, although instabilities are a problem, they will be correlated between the different components. However, when the receiver and transmitter are separated it is more difficult to share the same signal. One solution is to have a

single clock and to distribute the signal between the two radars however this would introduce propagation attenuation and delay, and additive noise due to the path. Another solution is to use two separate identical oscillators at the two radar nodes, but, for non co-located radar nodes, the oscillators need to also be accurate, as well as being stable or it would result in a systematic frequency offset.

The following subsections will discuss the various requirements for synchronisation, where a certain level of synchronisation can be considered sufficient for a certain application. The means of quantifying synchronisation and measuring this will be discussed.

Oscillators are not perfect and possess inherent instabilities that introduce phase noise. Ideally, the frequencies of the signals at both radar nodes in a network would be identical, and their phases would match at any given moment. However, these instabilities can cause the two signals to drift over time. An oscillator can be likened to a clock, with its phase changing continuously over time. If two oscillators start simultaneously with the same phase, their accumulated phases will likely differ after a period of time. This discrepancy in accumulated phase corresponds to a time error between the two oscillators, which needs to be minimized.

Time synchronisation of the radar is critical, as a deviation in the timing can result in range errors. Frequency and phase synchronisation are required as they will allow maximum gain over longer coherent interval times [32]. If the clock is to drift significantly over the integration period, the targets will start to blur or drift in both range and Doppler and result in a reduced probability of detection or errors in positional measurement [26]. The required oscillator stability can be estimated by equation 2.13 [31].

$$f_{Stability} = \frac{\Delta\phi}{2\pi f T_{int}} \tag{2.13}$$

Where $\Delta\phi$ is the allowed phase drift, T_{int} is the integration time and f is the radars operating frequency for the L-band staring radar used, the parameters are:

- Operating frequency [f] = 1.255 GHz
- Integration time [T_{int}] = 0.557 s (assuming 4096 pulses used)
- Allowed phase deviation [$\Delta\phi$] = 0.01 radians

These parameters would require fractional frequency stability of 2.3 x 10^{-12} at 0.557 s averaging time, according to equation 2.13. Additional information about frequency stability measures such as the unitless measure of fractional frequency stability are described in Appendix B.

2.6 Summary

This chapter has provided a summary of the working principle of radar systems, both monostatic and bistatic. Also, the effects of thermal noise and phase noise on degradation of performance of a radar have been discussed. In addition, the requirements for synchronization in a distributed radar network, along with what is expected from the L-band staring radar used within this work is described.

From the values provided, the time synchronization requirements for the L-band staring radar are not unreachable from what is expected from GPSDOs. Frequency stability requirements can also be achieved if a high quality oven controlled crystal oscillator OCXO is used as the oscillator to be disciplined. For reference, work on the use of different GPSDOs within the radar network are presented in Chapter 7. However, radar systems with shorter pulse widths and higher operating frequencies would have much higher requirements for oscillator stability. In this work this radar is used as a testbed to determine what levels of synchronization accuracy are achievable in a distributed radar network.

The following chapter will introduce the Quantum enabled network radar project and give a literature review on each of the different subsystems involved.

Chapter 3

Quantum Enabled Networked Radar Overview

This chapter details the Quantum enabled networked radar (QER) project within the UK Quantum Technology (QT) Hub [33] and acts as the motivation for much of the work in this thesis (not to be confused with 'Quantum radar'). Firstly, the project is introduced and the overall concept and architecture is shown in accordance with the existing radar and optical clock setups at the University of Birmingham. Then, each section focuses on the individual steps starting from the optical atomic clocks, cavity stabilized lasers, active phase stabilized fibre networks, frequency combs and microwave photonic generation. For each step, the technology is introduced along with a brief literature review and then an explanation of how it will be implemented within this project.

3.1 Architecture

The requirements for low phase noise oscillators and network synchronization in radar systems has been explained in the previous section. This project looks to use the current state of the art oscillators (strontium optical lattice clocks) within radars for the first time and measure the performance enhancements that are achievable. Modern radar networks with a synchronization requirement typically use GPSDOs due to the low cost and the wide availability of GNSS signals

[29]. However, the worlds best in terms of frequency stability (at the time of writing) is only achievable using optical atomic clocks [34]. Fractional frequency instability of GPSDOs are generally at the 10^{-13} level, whereas the state of-the-art optical clocks are able to reach levels of 10^{-18}. There are also atomic clocks with intermediate performance such as active hydrogen masers [35] and caesium fountain clocks [36] with typical noise floors in the order of 10^{-15} and 10^{-16} respectively.

Superior levels of stability from optical clocks can provide various benefits. Improved levels of synchronization is achievable, improving from the nano second level of timing error from GPSDOs to potentially sub picosecond timing errors using optical atomic clocks. This can contribute to range measurement accuracy of targets to the millimetre level and below. Also, the reliance on GNSS is a drawback for critical infrastructure, as it can be easily spoofed. Another benefit, is the improvement of the sensitivity of radar systems due to the reduced phase noise possible from microwave photonics and optical cavity technology, which can be utilized alongside the optical clocks and will be discussed in the following sections.

Three key obstacles are the conversion from optical to RF, additive noise from each of the downconversion stages and additive noise from frequency transfer. Radar systems using microwave domain oscillators and frequency standards have already been realised, but there are now additional challenges when using an optical frequency standard. The atomic transitions used as the clock reference are in the 100s of THz regime, whereas radar systems require a local oscillator in the RF regime, typically in the 10s of MHz regime. Therefore, a method of downconverting the signal seven orders of magnitude is required. In addition, there is the challenge of accomplishing this without degrading the stability of the optical clock. It is known that upconversion processes will add noise to electrical signals (both fundamentally and additive, as demonstrated in Chapter 7.1) [38] and also active components used for downconversion of frequency are also prone to adding additive phase noise [39]. It is therefore imperative that the additive noise is minimised at each stage. As will be seen, optical clocks are currently at a low technological readiness level and many of the most high performing systems are based in a lab, covering entire optical tables. They are not suitable for transportation into the radar cabin at this

stage and therefore an additional challenge of transporting the signal to the radar cabin, again without degrading the stability.

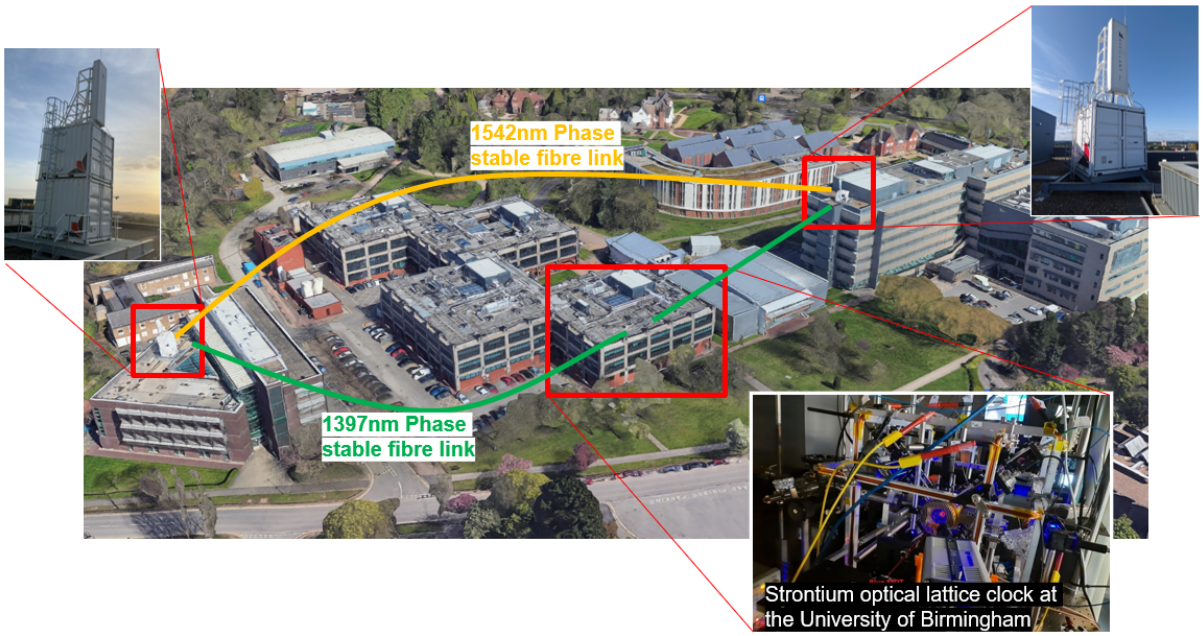

Figure 3.1: Staring radar and timing facility overview. Top down image showing 2 L-band staring radar nodes, fibre links and the clock labs (Google maps).

An overview of the radar-clock infrastructure is shown in Figure 3.1. Two radar systems are installed, each on the European Research Institute (ERI) building and the Gisbert-Kapp (GK) building. In the centre, the Alkaline research group and QT hub labs are based and this is the home of the UoB optical clock. For this work the lab based strontium optical lattice clock is being used and is under development by the clock team [40] [41]. The lattice clock is based in a lab and the clock laser light is transferred to the radar cabins via single mode optical fibre links covering the university campus. There is also the consideration to ensure the three fibre links connecting the two radars and the clock lab are phase stable.

The block diagram describing the process for the clock signal to reach the radar cabin in its required format are shown in a simplified form in Figure 3.2. The strontium optical clock consists of the physics package which enables the atoms to be prepared and trapped within the vacuum chamber, ready to be probed by the clock laser. The atoms act as the reference for the clock. The clock laser is stabilized via an optical cavity, providing short term stability, and is disciplined to the atoms to provide long term stability. The stability of the optical clock is imparted to a

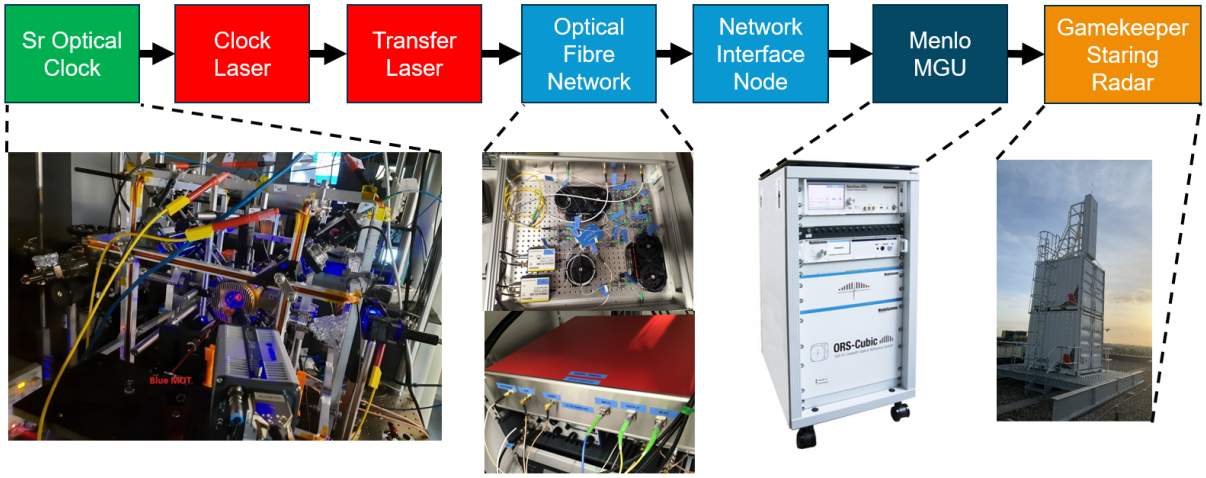

Figure 3.2: Block diagram of the optical clock to radar interface for the quantum enabled radar.

transfer laser, making it suitable for transmission using traditional telecom single-mode fibre. The optical fibre network consisting of an active phase noise stabilization system to transfer the low noise clock signal to the radar cabin. Within the cabin an interface node consisting of a beat detection to measure the frequency difference between the incoming clock signal and an input frequency comb. The next stage is the microwave generation unit which is a MENLO ultra-stable microwave unit (UMS) [42], which contains an optical frequency comb which locks to the incoming clock signal and the microwave photonics generation unit to produce the ultra stable microwave signal. Finally, the microwave signal is down-converted and conditioned to meet the requirements to be used for the radars LO before being sent up to the radar cabin via coaxial cable. Each of these sections will be described in more detail in the following sections.

For the second radar node, the initial plan is to demonstrate operation using the same optical clock signal. Therefore, all steps from the optical fibre network to the radar are repeated for the second node. Future realizations can involve a second strontium optical clock to take advantage of their superior accuracy and stability to maintain timing throughout the network while using independent LOs.

3.2 Atomic Optical Clocks

At the time of writing, the most stable oscillators in the world are those of optical atomic clocks [34]. Before this, this title was held by caesium atomic clocks [36] and therefore, the caesium clock transition frequency became the definition of the SI (International System of Units) second. Microwave clocks typically take 1 day to reach instability levels in the order of 10^{-15} whereas, optical clocks can reach the same level in seconds. [43]. There is a push towards redefinition of the SI second [44], since current optical clocks can perform 100 times better than caesium fountains. Figure 3.3 shows that absolute frequency measurements of state of the art optical clocks are limited as they need to be measured relative to the caesium fountain standards [45].

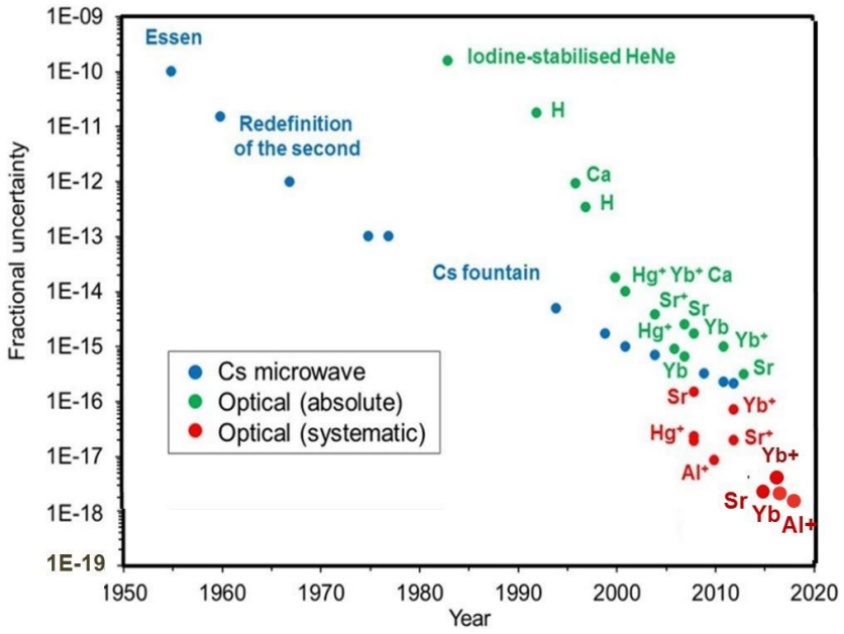

Figure 3.3: Progression of frequency accuracy for state of the art frequency standards. Courtesy of Patrick Gill [45]

Atomic clocks (both microwave or optical) consist of an oscillator which can be made up of a tunable crystal oscillator or a CW laser source and a frequency reference which is provided by an atomic transition $\nu = (E_1 - E_2)/\hbar$. Atomic clocks started with the invention of the Caesium clock in 1955 [46] involving a quartz oscillator disciplined to the 9.19 GHz ground state hyperfine energy level in Caesium-133. Over the following decades, caesium clocks became more accurate, reaching the 10^{-13} level. After this, other species of atomic clocks such

as Hydrogen masers [47] and Rubidium atomic clocks [48] were invented.

Equation 3.1 estimates the theoretically achievable fractional frequency stability achievable in an atomic clock [49]. Where ν and $\Delta\nu$ are the transition frequency and linewidth respectively. T_m is the measurement time, N is the number of atoms and τ is the averaging time. This suggests that improvements in stability of an atomic clock can arise from a decrease in measurement time or and increase in the number of atoms or transition frequency used.

$$\sigma(y) \propto \frac{\Delta\nu}{\nu}\sqrt{\frac{T_m}{N\tau}} \tag{3.1}$$

Further improvements were achieved with the aid of laser cooling. The discovery of laser cooling and trapping in 1975 [50] was crucial for the development of atomic clocks utilizing narrow optical transitions and led to the noble prize in physics in 1997 by Steven Chu, Claude Cohen-Tannoudji, and William D. Phillips [51]. This development then led to the invention of the caesium fountain clock [36] which included a cooling stage to reduce thermal motion of the atoms. This allowed for the atoms to be launched and dropped within the fountain. Although this causes an increase in the measurement time (T_m), due to this and the slower thermal motion of the atoms, the linewidth ($\frac{\Delta\nu}{\nu}$) is reduced and therefore, improving stability towards 10^{-16}.

Atomic clocks built from optical transitions (100s of THz) can provide orders of magnitude improvement over those built from electronic transitions (10s of GHz). However, various technological challenges prevented the development of optical atomic clocks. These involved finding a suitable transition with narrow linewidth and that the lasers were available, to access the cooling transitions as well as the clock laser transition. After the advent of the optical frequency comb and narrow linewidth lasers (see section 3.3 and 3.5) at the suitable transition wavelengths, this paved the way for optical atomic clocks with frequency stability below 10^{-16}.

Shortly thereafter, in 2002, an optical clock utilizing iodine molecules was developed in [52]. Some of the first optical atomic clocks were based from single trapped ions such as the Mercury ion ($^{199}Hg^{+}$) clock [53] and the Aluminium ion ($^{27}Al^{+}$) clock [54] with systematic uncertainty measured up to 2 x 10^{-17}. Soon after this, many other different species of optical atomic clocks were being investigated, such as those utilizing strontium atoms.

Another key development was to use an optical lattice to trap a large amount of atoms. This increases N significantly in Equation 3.1, improving stability of the clock by averaging down the noise of individual atoms. Katori [55] proposed a magic wavelength where the light shift contribution from the ground and excited states cancel out, minimizing differential stark shifts, leading to the development of the neutral atom based, Strontium optical lattice clock [56].

An example of the atomic package for a (^{88}Sr) optical lattice clock is shown in Figure 3.4a and represents the setup developed by Yogeshwar Kale of a compact clock at Birmingham [57]. It is designed with a low form factor but contains the key elements for a functioning clock such as the atom dispenser, science chamber, vacuum ion pumps, etc... A brief description of the steps of achieving the frequency reference in a (^{88}Sr) lattice clock is described.

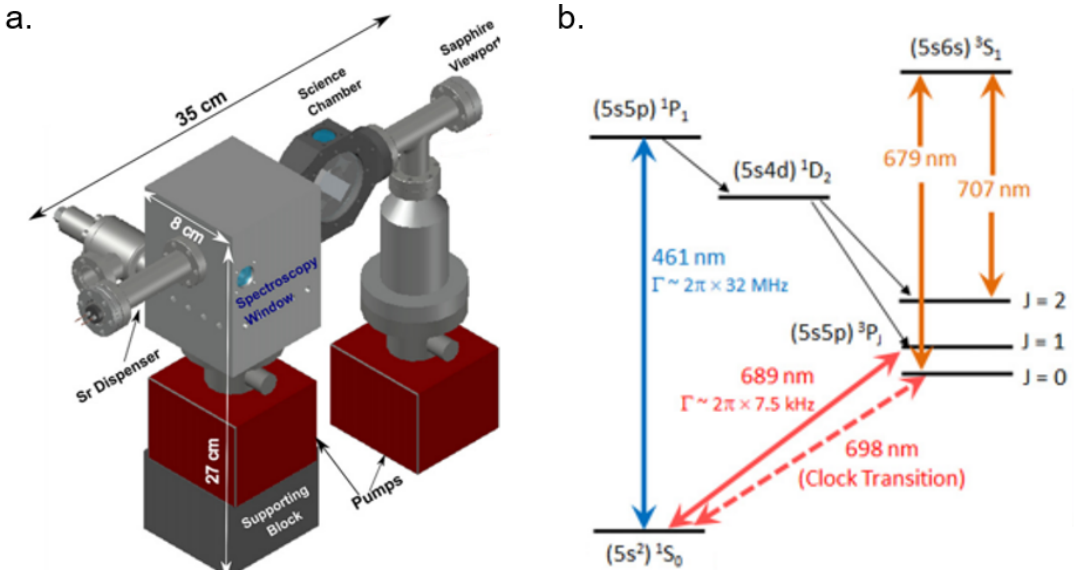

Figure 3.4: (a) Schematic view of Mini clock, Strontium optical lattice clock. (b) Atomic transition diagram for an optical clock using Strontium 88. Courtesy of Yogeshwar Kale. [57]

Various different transitions need to be addressed for preparation of the atoms and probing of the clock transition. These include the clock transition for the reference, cooling transitions for reducing thermal motion of the atoms and repump transitions to close cooling cycles. Each of these require the lasers addressing the required wavelengths and properties.

The clock transition requirements for an optical clock generally need to have a long lifetime (τ) allowing for narrow linewidths ($\Delta\nu$), as described by equation 3.2, facilitating long coherence times provided there is adequate environmental control. For Sr clocks, this is addressed by the

$^1S_0$ to $^3P_0$ transition at 698 nm, with a linewidth on the order of 1 mHz (for ^{87}Sr). The energy level structure, focusing on the transitions addressed in the clock, are shown in Figure 3.4b.

$$\Delta\nu = \frac{1}{2\pi\tau} \tag{3.2}$$

Cooling transitions must be considered to reduce the thermal motion of the atoms, reducing collisions and preparing them for high precision spectroscopy such that that the narrow clock transition can be suitably resolved. Initial cooling is performed with a broad transition with very short lifetime in the excited state for fast cycling. For Sr, this is addressed with the $^1S_0$ to $^1P_1$ transition at 461 nm, where the excited state has a lifetime of only 5 ns. This cools the atoms to temperatures of around 770-2000 μK, but further cooling is then required [58].

Further cooling uses a narrower linewidth transition and in Sr clocks this is addressed using the $^1S_0$ to $^3P_1$ transition at 689 nm with a natural linewidth of 7.5 kHz. Second stage cooling can provide atom temperatures in the region of 180 - 2000 nK [49].

To fully close the cooling cycle, additional repump lasers are required to address energy levels that don't have rapid decay times. Occasionally, from the first cooling cycle, atoms in the $^1P_1$ state will decay to the $^3P_2$ state which has a longer lifetime. Therefore, a 707 nm repump can move the atoms to the $^3S_1$ to then decay to the ground state ($^1S_0$). The second repump is intended for atoms in the $^3P_0$ state as a result of the second stage cooling. Therefore, a 679 nm repump laser is used for the $^3P_0$ to $^3S_1$ transition for faster cycling of the atoms back to the ground state [59].

Finally, a lattice laser is required, this allows the already cooled atoms to be trapped in potential via the interaction of the atomic dipole moment with the varying electric field from the laser [55]. The laser is at 813 nm and is tuned to the magic wavelength to prevent offsets of the transition frequency due to differential stark shift of the ground state ($^1S_0$) and the excited clock state ($^3P_0$). High laser power of 100s of mW are used for deep lattice depth potentials, ensuring atoms can remain trapped in the potential wells and forming a periodic array structure of atom sites [55].

This has addressed the various lasers and their requirements but as for the entire optical

clock, it consists of the physics package (which itself consists of everything required to prepare the atoms, and perform spectroscopy), an oscillator which can be steered and a counter. The oscillator is an ultra stable laser, locked to an optical cavity (see Chapter 3.3) and the counter is provided by an optical frequency comb (see Chapter 3.5) and a frequency counter.

The science chamber itself consists of an atom dispenser to heat up the strontium source and allow for the emission of atoms. Ion pumps provide ultra high vacuum within the interior, reducing collisions with other atoms. A science chamber is included, where the atoms will be trapped and suspended in the optical lattice. The science chamber will have multiple viewports for all the different lasers, allowing for laser trapping and cooling, probing the clock transition and also state detection. Additionally, magnetic coils are incorporated, consisting of tightly wound copper coils designed to generate a strong and controllable magnetic field gradient within the science chamber.

For a generic ^{88}Sr optical lattice clock [57] [59], the process of preparing the atoms is described. The strontium source is heated in the atom dispenser and are sent towards the science chamber. The atoms are captured in a magneto-optical trap (MOT), using a combination of the magnetic coils and the 461 nm lasers to perform the first cooling stage. At this stage the atoms are trapped in the "blue MOT". The repump lasers are activated to move atoms out of the $^3P_2$ energy level. Next, the second cooling stage is performed to further reduce the thermal motion of the atoms and achieve "red MOT". However, this is done in two stages. Firstly, for broadband red MOT, the 689 nm laser is artificially broadened via frequency modulation in order to capture a wider range of atomic velocities. Then, for single frequency red MOT, the bandwidth of the laser is reduced and precisely tuned to the $^1S_0$ to $^3P_1$ transition to cool down the atoms even further. The atoms are loaded into the lattice. The 813 nm laser is tuned to the magic wavelength, and since the velocity range of the atoms is low enough, they are able to be trapped into the 1D lattice. Next stage is the probe and detection. A large number of atoms are trapped in the lattice and are within the ground state ($^1S_0$). All other lasers are switched off, except the lattice, and the 698 nm laser is emitted through the lattice, exciting a fraction of them into the clock state ($^3P_0$). The probe laser (461 nm) and CCD camera are switched on for

a short duration to measure the atoms in the ground state. The probe laser will only interact with atoms remaining in the ground state, exciting the $^1S_0$ to $^1P_1$ transition and the florescence created when decaying back down to the ground state is detectable on the camera and is used to estimate the number of atoms in the ground state (N_g). This destructive method ensures the atoms in the ground state are lost for the next step. The other atoms, that were excited by the clock laser, are next measured. Theoretically, the remaining atoms (N - N_G) are still in the $^3P_0$ state. These are now returned to the ground state for via the 679 nm and 707 nm repumps before again performing a measurement with the probe laser and CCD camera to estimate the number of atoms in the excited state (N_E). The values of N_E and N_G are used to measure the absorption spectrum and therefore determine where the clock laser frequency is relative to the resonance of the clock transition and is steered accordingly.

This describes the simplified operation of a clock using the ^{88}Sr isotope, although ^{87}Sr is also commonly used as a basis for an optical clock. The key difference between the two is that ^{87}Sr is fermionic and has nuclear spin. The energy level structure is mostly the same, but there is now hyperfine splitting of the energy levels to take care of and therefore, is more complex. ^{87}Sr is usually the isotope of choice due to the more precise control available of the atomic states to reduce systematic effects [59].

Various Sr optical lattice clocks have been developed with measured stability in the 10^{-18} region [60] [61] [62], and [34] has reported a systematic uncertainty of 8.1 x 10^{-19}. Other species of clocks are also showing promise such as the Yb lattice clock [63] [64] and the Al^+ clock [65] with reported systematic uncertainty of 1.4 x 10^{-18} and 9.4 x 10^{-19}.

Although these clocks provide orders of magnitude performance improvements over current commercial standards, they need to be made more compact and functional outside of the lab environment. Few groups have built transportable such as a Sr lattice clock in a van form factor [66], a Sr lattice clock [67] contained within 3 separate, short transportable racks and an optical clock for space applications [68]. Still there is much to be done to bring them to the level so that they can be used in civilian applications.

Within this work, the lab based strontium optical lattice clock being developed at the Uni-

versity of Birmingham is intended to be used as the reference for the radar systems to test the capability. The atomic reference use the ^{88}Sr isotope and provide long term stability beyond 10^{-16}.

3.3 Optical Cavity and Ultra Stable Laser Systems

Ultra stable lasers are used for various applications including for atomic physics [69]. They are an integral part of an atomic optical clock but, are also used as a stand-alone oscillator [64]. Stand-alone commercial laser systems can be obtained at relatively low linewidths on the order of 10s of kHz resulting in a frequency stability of around 10^{-11} at 1s averaging time [70]. However, for use as a clock laser in an optical clock, this is not narrow enough to achieve the high stabilities possible and accurately probe the 698 nm transition. The main solution is to use Fabry-Perot resonators as cavities for laser stabilization to reach sub-Hz linewidths and a fractional frequency stability in the 10^{-15} region and below at 1 s.

A simplified diagram of the a Fabry-Perot cavity is shown in Figure 3.5. The input beam is aligned into the cavity such that it is reflected back in the same beam with highly reflective mirrors being used to trap light within the cavity for numerous round trips. The laser frequency is tuned to match the resonant condition ($L = n\lambda$) for a standing wave to form, creating a high gain interference pattern between the mirrors [71]. A spacer material with low thermal expansion ensures the distance between the two reflective surfaces remains constant to a high degree [72].

The amount of time the light is able to remain trapped in the cavity is an indication of the achievable stability. One of the key parameters used to characterise a cavity is the finesse ($\mathcal{F}$) and is dependant on the reflection coefficients of the mirrors (r_1 and r_2) [73].

$$\mathcal{F} = \frac{\pi\sqrt{r_1 r_2}}{1 - r_1 r_2} \tag{3.3}$$

At typical optical frequencies (in the order of 400 THz), a 1Hz change in the frequency is equivalent to a 2 fm change in the length of the cavity [43], highlighting the importance of

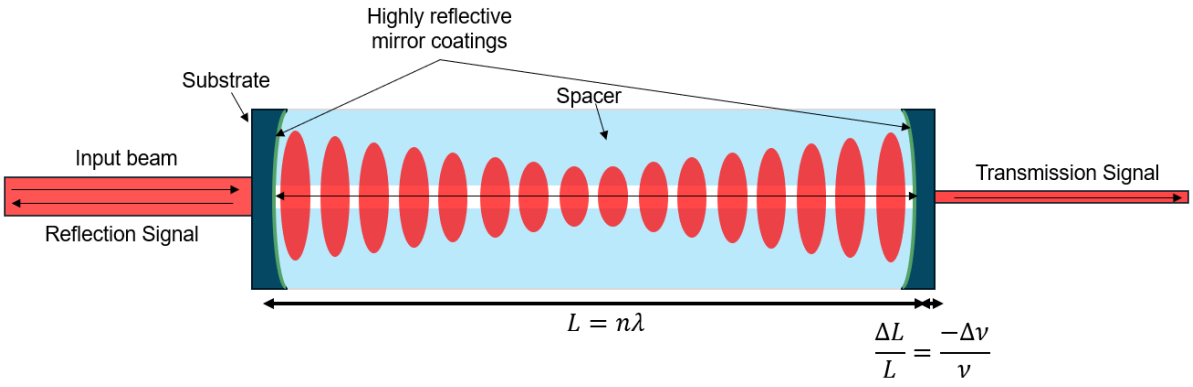

Figure 3.5: Diagram showing the principles of an ultra stable laser stabilized to a Fabry-Perot optical cavity.

maintaining the length. Therefore many technical challenges need to be addressed:

(1) Spacer material properties: The spacer must not only be mechanically stable to deformations but also needs to fulfil its purpose of maintaining a stable cavity length. The main material property of concern is a low thermal expansion coefficient at the operating temperature. Ultra-low expansion glass (ULE) is commonly used due since they possess a zero-crossing thermal expansion coefficient near room temperature [74].

(2) Temperature: The effect of temperature variations on the length are minimised due to the correct choice of spacer material but it is still important to consider since other components such as the mirror coatings would have different thermal expansion properties. Therefore, temperature is generally controlled in high performance cavities using insulating layers around the cavity as well as active temperature stabilization systems on the interior.

(3) Vibrations: Environmental disturbances can result in fluctuation of the cavity length. This remains one of the more difficult challenges for use of longer cavities in pertubative environments such as at sea. However, vibrations on the cavity can be minimised using active vibration stabilization platforms. Also the support positions of the cavity can be optimized such that vibration sensitivity is minimised in all three axial directions such as in [75].

(4) Contamination control: Dust particles can accumulate on the surfaces of the mirrors causing scattering and absorption of light. Residual particles in the cavity are reduced by operating in ultra high vacuum.

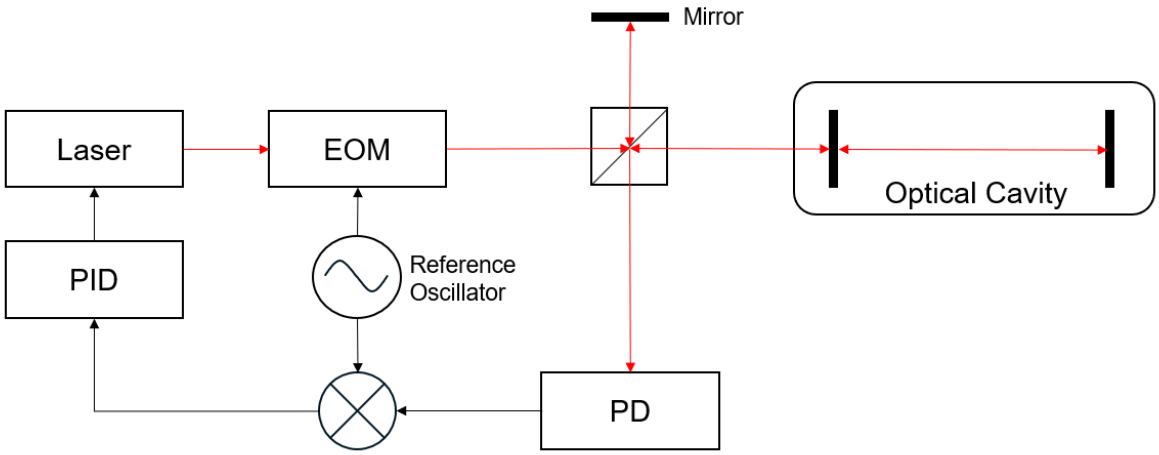

Figure 3.6: Block diagram of a simplified PDH locking system for an ultra-stable laser. PID - Proportional integral derivative loop, EOM - Electro-optic modulator, PD - Photodetector.

With all of these solutions in place, the length of the optical cavity is stable and the next step is to stabilize the laser light to the cavity. The Pound Drever Hall (PDH) locking method [76] [77] is used create the feedback loop to the laser. A simplified schematic of the PDH method is shown in Figure 3.6. The general idea is that the frequency response of the cavity will represent a narrow peak corresponding to the resonance condition of the standing wave. An electro-optic modulator (EOM) is used to form sidebands either side of the laser entering the cavity. However, only the main peak will resonate and will be the only component present in the reflected signal. Then a photodetector (PD) can detect the phase difference between the reflected signal and the modulated signal, providing information on the lasers position relative to the cavity resonance. A potential integral derivative (PID) circuit, can then be used to turn the error signal into feedback to the laser current which will change the instantaneous frequency accordingly. This feedback loop ensures the frequency is stabilized to the optical cavity length.

State of the art optical cavities are designed with their thermal noise limitations in mind. This sets the ultimate limit or the flicker noise floor based on thermal noise contributions due to the the spacer, substrate and coating. The power spectral density (PSD) of thermal noise due to contributions of the spacer are described in [78]. A detailed analysis of thermal noise contributions, also including those from the two mirror substrates and coatings can be found in [73] [71]. As shown in equation 3.4, the achievable fractional frequency stability (σ_y) can be

related to the cavity length (L_{cav}), temperature (T) and Young's modulus of the material (E) [43].

$$\sigma_y \propto \frac{1}{L_{cav}} \sqrt{\frac{K_B T}{E}} \tag{3.4}$$

Efforts to push the thermal noise floor limits by increasing the cavity length (L_{cav}) have been led by National physical laboratory (NPL), who have demonstrated a 48.5 cm ULE cavity with an estimated thermal noise floor of 6 x 10^{-17} [71], and measured 1.1 x 10^{-16} at 10 s averaging time. On the other hand, Physikalisch-Technische Bundesanstalt (PTB) have led efforts on cryogenic based cavities [79] to reduce the thermal noise via reduction of temperature (T). By using silicon mirrors and spacers with a zero crossing thermal expansion coefficient at 124 K and realising instabilities of 4 x 10^{-17} at 1-10 s averaging times [73], corresponding to a laser linewidth below 10mHz [80].

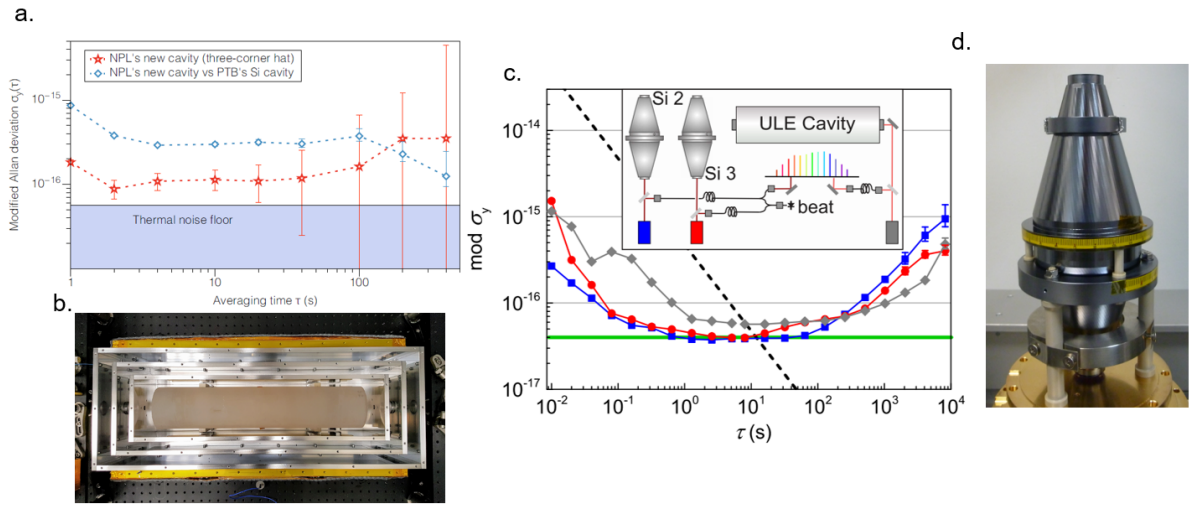

Figure 3.7: NPL 48.5 cm ULE cavity Courtesy of Marco Schioppo [72]. (a) Frequency stability measurement, (b) photograph of the system. PLB cryogenic silicon cavity, Courtesy of Jialiang Yu [73]. (c) Frequency stability measurement, (d) photograph of the system.

The instability curves for these cavities previously mentioned are shown in Figure 3.7. Although they provide better short term stability over other oscillator technologies, the long term stability is limited as can be seen by the upward trends at averaging times greater than 100 s. These are due to drifts in the cavity length (due to material relaxation [73]), and although there is work to characterise and predict these effects to improve the long term stability (by

compensation of the drift via an AOM in the path, i.e. de-drifting) [73], this would limit their application where low timing errors are required. Therefore, in the same way that crystal oscillators are disciplined to GNSS signals, optical cavities can also benefit from a frequency standard and this can be provided by the atomic transition in atomic optical clocks. Typically an optical cavity stabilized laser is used as the clock laser within a high performance optical clock, making use of the cavities short term stability and the long term stability provided by the atomic reference.

Within this project, the ultra stable laser cavity is made up of a MENLO systems optical reference system (ORS) [81]. This consists of an NPL cubic cavity [75] made up of ULE 5 cm spacer and crystalline (XTAL) coated mirrors. The ORS also consists of a 1397 nm laser and PDH locking electronics. This represents the transfer laser in Figure 3.2. The reason for this choice is twofold. Firstly the wavelength of 1397 nm allows for transfer over 1-2 km of single mode optical fibre without critical attenuation. Also, the CW laser is almost exactly half of the frequency needed to excite the $^1S_0$ to $^3P_0$ transition in Strontium and therefore, can act as the clock laser in the optical lattice clock after second harmonic generation, making this an integral piece in the setup. Since at the moment of writing, the transfer laser is not being used in the full system and has only been used for characterization of other laser systems. Another 2 ultra stable cavity lasers that are used within Chapter 7 are ORS cubic cavitys at 1542 nm and they are located within each of the radars for enabling independent locking of the OFC.

3.4 Fibre Networks

Time and frequency transfer is required to connect remote nodes in networks, such as for telecommunications and radar networks [13]. GNSS signals are a cheap and commonly used source for this, where remote clocks are referenced to signals emitted from satellites containing caesium frequency standards. However limitations such as variable troposphere delay [82], multipath [83] and hardware delays [83] set a limit for the accuracy of clock transfer. This section focuses on the development of an improved method of frequency transfer using optical

means. This method, introduced in [84], is active fibre phase noise stabilization of CW laser light.

The use of optical fibres as a means for frequency dissemination is attractive because of their properties such as low attenuation compared to coaxial cables. Single mode telecommunications fibre typically has losses of only 0.2 dB/km at 1550 nm and 0.5 dB/km at 1300 nm [85]. Also, optical fibre allow for transfer of the optical signals directly and therefore, the highest precision cavities and optical clocks can be transferred with no instability added through down-conversions and up-conversions to, and from, the RF domain. The prevalence of single-mode optical fibres in existing infrastructure enables the use of this method over international distances.

The challenges that need to be addressed as a result of sending ultra-stable signals through optical fibre are as follows:

(1) Attenuation - The attenuation is significantly lower than coaxial cable but is still present and accumulates over long distances. A double pass link between Reims and Strasbourg, consisting of 940 km of fibre, produced a total attenuation of 262 dB [86]. Attenuation can be caused by a combination of fibre attenuation and connection points, some of these connections consist of straight connectors causing loss and reflections. This needs to addressed by amplification or regeneration of the signal at intermediate points in the link.

(2) Delay - Light travelling through the fibre will experience a delay. However, the time offset is not the main concern but rather the variable delay. A change in delay results in a change in the phase and frequency, adding phase noise to the original signal. Thermal expansion is one of the contributors, for fused silica, typical thermal expansion coefficient is 5 x 10^{-7} mK^{-1} [87]. A change in temperature also causes thermo-optic effect, changes of refractive index (n) for fused silica is 1 x 10^{-5} [87]. Another contributor to phase noise is strain induced in the fibre due to seismic changes, causing elongation of the fibre. Each of these combine to produce phase noise that would need to be compensated for.

(3) Polarisation rotation - Changes in the birefringence properties in the fibre can also cause changes in the polarization of the light as it propagates through the fibre [88]. This can cause the attenuation to vary with time and may need to be controlled for high performance links.

The simplified schematic for a phase noise stabilization system is shown in Figure 3.8. The main stages are an unbalanced Michaelsen interferometer, AOM and fibre link double pass, signal amplification or regeneration and the feedback loop correction stage.

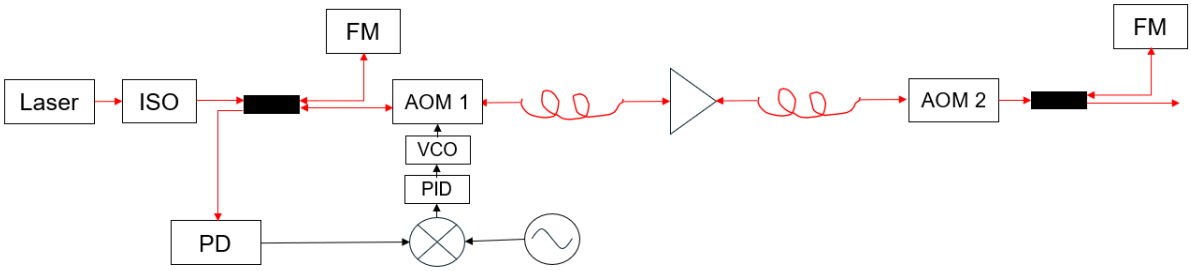

Figure 3.8: Simplified schematic of a generic fibre phase noise stabilization system. ISO - Isolator, FM - Faraday mirror, AOM - Acoustic optical modulator, VCO - Voltage controlled oscillator, PID - Proportional integral derivative loop, PD - Photodetector.

Firstly for the interferometer, one arm is used for the reference and is reflected at the Faraday mirror, while the longer arm is directed towards the AOM and to the fibre input. The light is then passed through the AOMs and the fibre network. Upon reaching the remote output, part of the light is reflected and sent back into the same fibre, being double passed through each of the AOMs on the way. At this stage, the light has accumulated phase and frequency shifts due to the fibre and AOMs according to equation 3.5.

$$f_{beat} = 2f_{AOM1} + 2f_{AOM2} + 2\phi_{fibre} \tag{3.5}$$

Along the link, there may be significant attenuation stages along the way and therefore there are periodic regeneration and amplification stages. These are required to be bi-directional due to the double pass nature of the link. The reflected light then returns to the interferometer and is compared with the reference light on a photodetector producing (f_{beat}). This contains the systematic shifts from AOMs ($2f_{AOM1}$ and $2f_{AOM2}$) as well as the random shifts contributed from the fibre phase noise ($2\phi_{fibre}$). The systematic shifts can be mixed out using a local oscillator, producing an error signal (containing only $2\phi_{fibre}$). A PID controller and voltage controlled oscillator (VCO) can be used to provide feedback to the AOM and compensate for the variable delay on the fibre.

Some of the technical challenges and limitations of phase stabilized fibre transfer are:

Amplification - To maintain the signal strength over long haul fibre links, the uni-directional amplifiers are unsuitable due to the requirement of 2 way propagation. Unfortunately, these are typically used in existing fibre networks and typically they contain an optical isolator so they can operate at high gain without backscatter. The most common amplification method are bi-direction erbium doped fibre amplifiers (EDFAs) [89]. Also, fibre Brillouin amplifiers [90] and Raman amplifiers have been developed for this purpose [91]. An alternative method is to use a repeater laser station (RLS) as in [92], where a separate laser is used to ensure sufficient power and is phase locked to the incoming light.

Limited bandwidth - The correction of the phase can only occur after two way propagation, and due to the finite speed of light in a medium, there is a minimum delay before the correction can be applied. This sets a limitation on the maximum bandwidth of the feedback loop and is dependant on the length of the stabilized path. This is termed, delay-unsuppressed noise in [93] and it is found that the phase noise as a result will degrade proportionally with $L^{3/2}$. A workaround is to split the long stabilized link into multiple shorter stabilized links, increasing the bandwidth of the system but also the cost and complexity. This can be done using a separate feedback loop for each segment [86].

Other residual errors - This scheme assumes the phase noise added onto the fibre is the same on both forward and reverse trips and results in a loss of localized noise information and results in a source of residual error [94]. Uncompensated fibre paths in the system will also add additional noise and much be kept as short as possible and unexposed if they are in free space. For any unavoidable uncompensated paths, they can be temperature stabilized to reduce their effect.

Phase noise stabilized fibre links have been developed between various institutes throughout Europe such as between the Max Plank Institute (MPQ) and PTB [95], also, between NPL and SYRTE [86]. In [72], the 2200 km stabilized fibre link was used for a comparison of the two cavities mentioned in the previous chapter from NPL [71] and PTB [73] up to the 7 x 10^{-17} level.

Within this project the phase noise stabilization scheme is used to disseminate light between

different nodes of the radar network. A prototype phase noise stabilization system is developed within this thesis and detailed in Section 7.3.1 to disseminate 689 nm and 698 nm cavity stabilized lasers from one lab to another over a distance of 100 m in polarization maintaining fibre. Free space optics are used for both the local and remote processing branches and therefore some of the components differ from Figure 3.8. However, the general procedure is comparable. This system was used to aid the development of a fibre based system, named HARPO, by Gwynfor Donlan and Jithin Kannanthara. The HARPO is used to disseminate 1397 nm and 1542 nm cavity stabilised lasers between the three nodes of the radar-clock network. 2 dark fibre links are dedicated to sending 1397 nm light, via the transfer laser, from the clock lab to the two radar nodes. Also, another dark fibre link between the radars is dedicated to sending 1542 nm light from a transportable ORS.

3.5 Frequency Combs

The frequency comb is responsible for conversion between the optical and RF domain for compatibility of the radar system. This section will describe the purpose and operation of optical frequency combs (OFC), discuss recent developments in this technology and finally describe how the OFC is used specifically within the QER.

OFCs are used widely within various different fields such as metrology [72], telecommunications [96] and spectroscopy [97]. Prior to the invention of OFCs, the pathway between RF and optical frequencies could only be bridged using many PLL up conversion stages concatenated together [98] or optical interval division [99]. The complexity and numerous stages of this approach limited its feasibility for wider application and reduced the achievable overall stability. The idea of using stable pulse trains was envisioned as early as 1977, where Hansch's team demonstrated one of the first femtosecond mode locked lasers in [100]. In 1999, [101] performed the first absolute frequency measurement of the 1S - 2S hydrogen transition using a frequency comb, demonstrating the feasibility of frequency combs for optical measurements. A detailed history of the optical frequency comb technology can be found in [102]. The invention

of the optical frequency comb led to the 2005 nobel prize in physics, shared by Roy Glauber, John Hall and Theodor Hänsch [103]. Analogies between OFCs and the concept of a frequency ruler are frequently drawn, as you will see throughout this section. Additionally, OFCs can be likened to a set of rotating mechanical gears, representing both the optical and RF domains, as illustrated in Figure 3.9 [104].

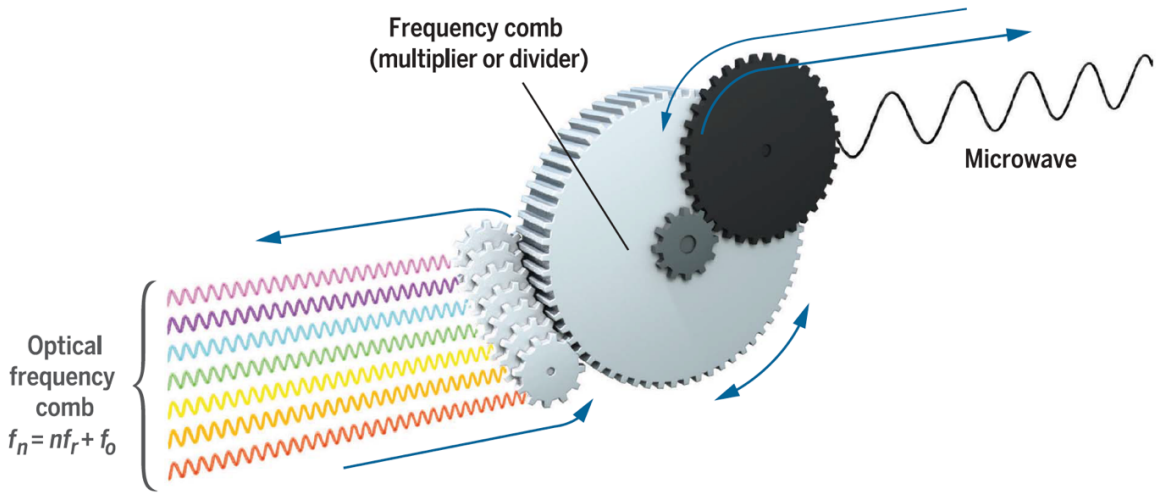

Figure 3.9: Frequency comb gear diagram. Credit: NIST

A block diagram of the general procedure for generating a frequency comb is shown in Figure 3.10 and is suitable for describing OFCs based on optical fibre. Femtosecond fibre lasers are the most commonly used variant due to their robustness to environmental effects and longevity that has been demonstrated [105]. Such an example is, Menlo systems have demonstrated the use of a fibre based frequency comb on a sounding rocket in [106]. Therefore for the generic description of frequency comb generation, it will be limited to fibre based combs.

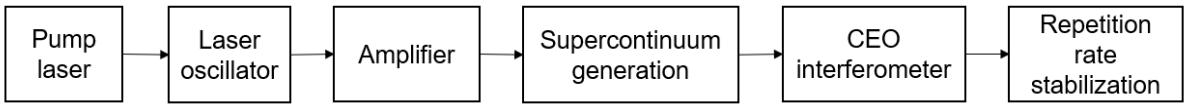

Figure 3.10: Block diagram of the sequence of generating a stabilized octave spanning, fibre based OFC.

Fundamentally, an OFC consists of a cavity in which a laser is locked to. Unlike the cavity described in the previous section, the OFC cavity is designed for pulsed operation rather than

CW operation and this is attained through mode locking of several modes within the cavity. The contribution of all of these modes creates a pulsed profile in the time domain with a spacing T and a 'comb' like structure in the frequency domain consisting of equally spaced spectral lines spaced by f_{RR}, which represents a pulse train in the temporal domain. This is illustrated within Figure 3.11 [104].

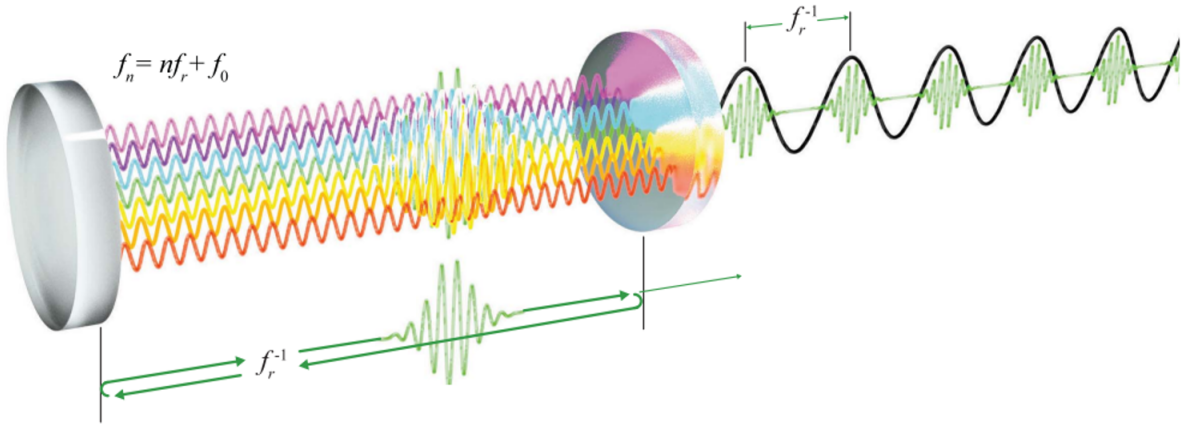

Figure 3.11: Visualization of a mode locked laser, buildup of multiple modes within an optical cavity, producing a pulse train. Credit: Scott Diddams [104]

For a fibre based frequency comb, the cavity can be made up of a nonlinear optical loop mirror (NOML) as shown in a schematic in Figure 3.12 [107]. The loop is made up of non-linear optical fibre and a gain region. For 1550 nm combs, erbium doped fibre amplifiers (EDFA) are used for the gain region, with an input port for the pump lasers. This structure is self oscillating such that the pump laser at 980 nm can generate photons at 1550 nm within the Er doped gain region via stimulated emission [107]. The reflection from the downward leg creates a counter propagating path in the cavity causing interference between itself and the forward propagating light causing different modes to form due to constructive and destructive interference. At higher pump powers, self phase modulation (SPM) and cross phase modulation (XPM) occur due to the Kerr effect due to the non linear fibre used [108]. As a result of broadening, the NOML outputs narrow femtosecond pulses of constant repetition rate.

However, at this stage the typical bandwidths are on the order of 20-50 nm [107] and are not enough to perform self-referencing which requires octave spanning combs. Therefore, there is a

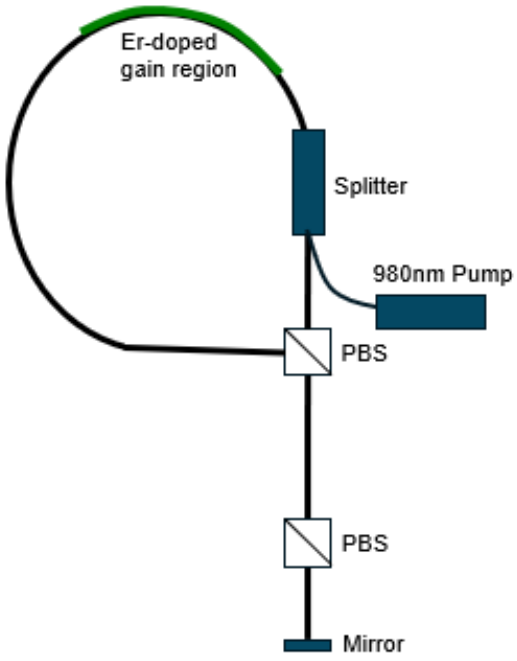

Figure 3.12: Schematic diagram of a generic NOML for frequency comb generation. PBS - Polarization beam splitter

further step for supercontinuum generation consisting of amplification and injection into highly non linear fibre (HNLF) which further broadens the comb spectrum via SPM and XPM. [108].

Once the octave spanning comb is achieved this way, there are still instabilities on the comb and therefore the self referencing via an f-2f interferometer is required [102]. A schematic for the f-2f interferometer is seen in Figure 3.13. The carrier envelope offset (CEO) is the frequency offset between the 0th mode and the DC line, caused by phase shifts of the peak of the electric field between consecutive pulses. The CEO is measured on a photodiode by beating together a particular comb mode which is then doubled using second harmonic generation [102] $f_1 = 2(f_{CEO} + f_n)$ and its 2n counterpart within the comb spectrum $f_{CEO} + f_{2n}$. The result is the difference between these two frequencies f_{CEO} which can then be controlled to enable for flexibility of the comb spectrum. A feedback loop is initiated which mixes down the f_{CEO} output with a reference oscillator at the target frequency and to generate the error signal. A PID controller is then able to feedback to the actuator, in this case can be an AOM in the path of the initial pump laser [109].

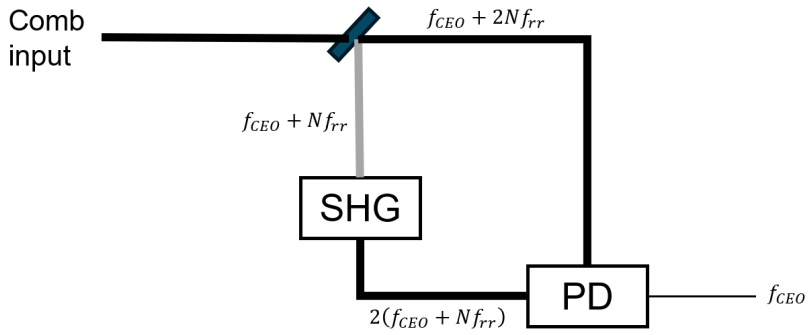

Figure 3.13: Schematic diagram of a f-2f interferometer for CEO stabilization. SHG - Second harmonic generation, PD - Photodetector.

To ensure that the exact spacing between each of the equidistant modes are known, the repetition frequency of the pulse train also needs to be stabilized. The repetition rate can be stabilised in two different ways depending if the comb is locking to an RF source such as a crystal oscillator or a Hydrogen maser, alternatively it can be stabilized to an optical source such as a cavity stabilized laser or an optical atomic clock.

The mechanisms for the repetition rate lock are similar to the CEO stabilization in terms of the feedback loop. However, the method of measurement and therefore generation of the error signal are different. For f_{RR} stabilization to an RF reference, the comb repetition rate is measured directly on a high bandwidth photodetector. The error signal is generated by scaling down the measured repetition rate to align with the reference oscillator frequency, and then mixing it down to baseband. When an optical reference is used [110], instead the beat frequency between the CW optical reference laser and the nearest comb mode are measured on a photodetector which is then mixed down by a synthesiser (which can be referenced to a frequency standard for absolute accuracy) to generate the error signal. The stabilization of CEO and repetition rate are visualised in Figure 3.14. The CEO lock ensures that the spacing between the DC line and the zeroth mode are maintained. The RR lock ensures the spacing between the modes are maintained while alternatively, if a stable CW reference is available, it ensures the comb is locked coherently with that optical source.

One of the most powerful functions of an OFC is the absolute measurement of optical frequencies throughout the entire octave comb spectrum. For a CW laser present within the

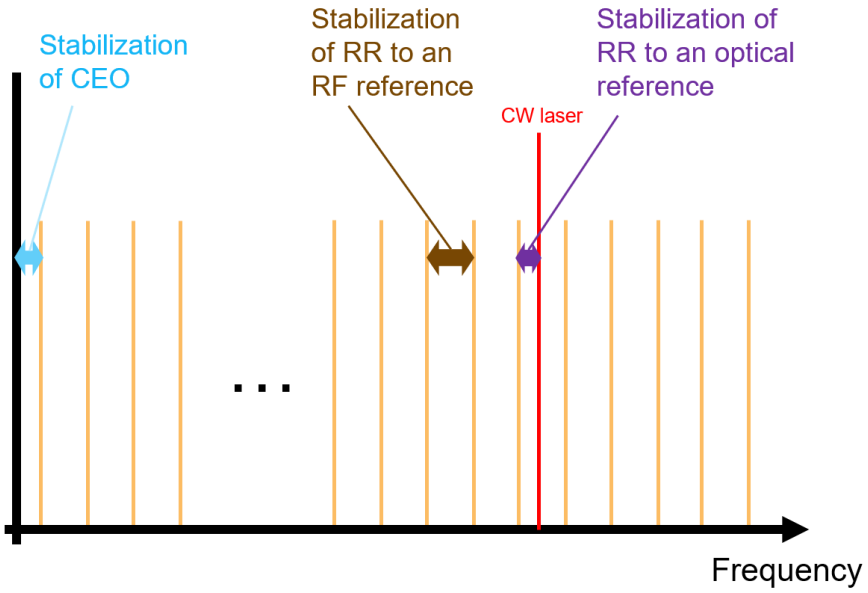

Figure 3.14: Diagram illustrating the locking mechanisms for an OFC.

range of the comb spectrum, the absolute frequency can be defined by equation 3.6 where n is the comb mode number closest to the CW laser frequency and f_{beat} is the difference frequency between the nth mode and the CW laser frequency. Also, the CEO frequency can be locked on either the positive or negative sign and the beat sign can either be positive or negative depending on which side of the comb mode it lies on.

$$f_{CW} = \pm f_{CEO} + n f_{RR} \pm f_{beat} \tag{3.6}$$

Since f_{CEO} is locked to a known frequency, f_{RR}, can be measured by inputting the pulse train to a high bandwidth photodetector and f_{beat} can also be measured on a photodetector, the exact frequency of the CW laser can be determined using equation 3.6, assuming comb number n is known. Various methods can be used to measure n, one of them is shown in [111], by changing the repetition rate in a two step process. This provides a very effective way to track the frequency of lasers at much better resolution. For a stable laser that is fluctuating by 1Hz, the frequency can be measured to a resolution of approximately 1 Hz, compared to a wavemeter where the resolution is typically limited to around 100 kHz.

As mentioned in previous sections on optical clocks and ultra-stable cavity lasers, the state

of the art levels of frequency stability can only be obtained by optical oscillators. The method of locking to an optical reference allows for the transfer of the stability of the laser to the frequency comb. Each of the different comb modes would ideally maintain the same stability as the optical reference. This is powerful as it would allow for a transfer between different parts of the optical spectrum that are otherwise unreachable by high bandwidth photodetectors. This is however, dependant on the amount of additive noise via the stability transfer. This has not been a limitation at this stage as it has been demonstrated in [112], where a multi line comb comparison demonstrated spectral purity transfer with instability of 1.6 x 10^{-18} at 1s and reaching a minimum of 5 x 10^{-20} at 400 s. This was further improved in [110] with frequency agreement of two frequency combs to the 20th decimal place in less than 100 s and averaging down to 1.5 x 10^{-20}. This measurement shown that the spectral purity transfer is at least an order of magnitude better than the best optical clock throughout the measurement.

Performance of OFCs have demonstrated the ability to transfer the stability of optical clocks with precision that exceeds what is achievable with the clocks themselves, within lab conditions. However, there is another challenge when trying to use them in more strenuous applications where low size weight and power (SWAP) is crucial. Commercial fibre based frequency combs have been reduced to the level of a rack mountable system [113], with sufficient requirements for optical clock stability transfer. However, to reach even smaller form factors, developments of micro-combs are underway [114] which allow OFCs to be used within photonic integrated circuits (PIC).

Within the QER project, the frequency combs used are the Menlo Systems, Smartcomb [113]. There are two of these, one in each radar cabin and with identical specifications. They are fibre based frequency combs with a repetition rate of 125 MHz and CEO of ± 10 MHz. The smartcombs are able to be locked to an optical reference which will be the 1397 nm transfer laser via an external beat detection unit (BDU). The BDU enables for filtering of the comb spectrum around the desired wavelengths and coupling of the CW laser into the same fibre to allow for generation of the beatnote between the 1397 nm CW and the nearest comb mode. In addition to this the OFC can also lock to a 1542 nm optical reference and this will be used within networked

radar measurements within Chapter 7.

3.6 Microwave Photonics for Low Phase Noise RF Generation

The next stage involves exploiting the stable repetition of the frequency comb to generate high spectral purity RF signal to be used as the radars local oscillator. This section starts by introducing the field of microwave photonics with focus on generation of microwave signals via optical means. Then the process of generating RF via a frequency comb using the optical frequency division method is described. Finally, the description of how this fits into the QER is mentioned.

Typically for radar applications, high frequency or highly tunable signals with low phase noise are required. The use of electronic oscillators is possible but there are various challenges to overcome. For example a crystal oscillator typically operating at a lower frequency (e.g. 100 MHz) would need to be upconverted if used in an X-band radar system at around 10 GHz. This would add significant phase noise to the signal [115], in this case, at least 40 dB addition of phase noise. Also, crystal oscillators provide limited frequency tunability. For example a typical commercial OCXO at 100 MHz, the electronic frequency control adjustment range is around ±2 ppm [116]. In addition, if oscillator signals need to be transferred to a remote site, high attenuations are involved from RF transfer over coaxial cable.

As mentioned in Chapter 3.3, optical fibres provide huge advantages in terms of dissemination of signals due to the low attenuation [85]. Also, high frequency and flexibility microwave signals are possible using optical sources due to the high stability and bandwidth of laser systems.

An overview of microwave photonics can be found in [117] [118] demonstrating the early work on photonic RF generation as well as optical processing and beamforming applications. However, in this work, the focus is only on photonic RF generation. The general process of producing an RF signal using 2 lasers is shown in Figure 3.15 [117], and is essentially a beatnote between the two optical signals, producing an oscillating electrical output equal to the difference frequency of the two signals. The frequency is dependant on the amount one laser is detuned

compared to the other and the phase noise is dependant on the coherency of the two laser sources. Using this technique, it is possible to generate microwave signals in the mmwave regime where it is difficult to generate electronically without adding significant phase noise [119].

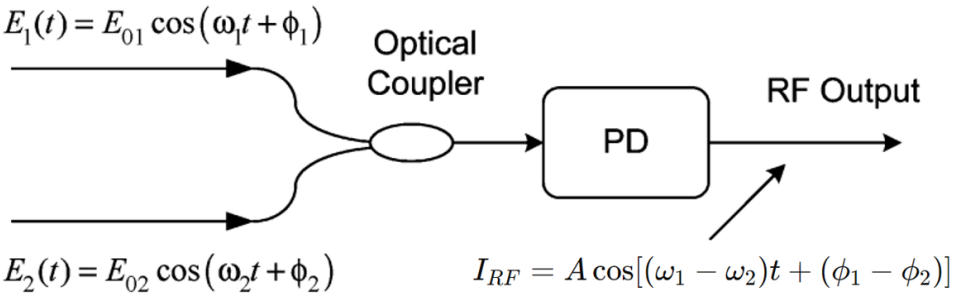

Figure 3.15: Block diagram showing the basic concept of photonic microwave generation. Courtesy of Jianping [117].

For two completely independent lasers, the phase noise of the RF output is expected to be poor. Therefore, initial methods have been developed to improve the coherency such as injection locking [120], optical phase locked loops [121], phase modulation [122] and dual-wavelength laser sources [123]. Methods based on opto-electronic oscillators (OEO) are effective for low phase noise as they can generate low noise, high frequency signals while not requiring a reference oscillator [118]. Also, methods to utilize enhanced tuning bandwidth have been developed such as in [124], where a Fabry-Perot laser diode with external injection locking is used to create an oscillator tunable from 6.41 GHz to 10.85 GHz. Even higher frequencies in the mmWave band have been generated via photonic enabled multiplication schemes in [119].

Arbitrary waveform using photonic oscillators are discussed in [125] for high spacial resolution radar systems. An example of linearly chirped waveforms with up to 2 GHz bandwidth have been generated in [126], using tunable optoelectronic oscillator and a recirculating phase modulation loop.

It was mentioned in the previous section that high finesse optical cavities can stabilize the repetition rate of an OFC, producing a spectrum of phase coherent modes. The concept of low noise microwave generation based on optical frequency division is described in [127] which leverages this effect, and so far has produced the lowest phase noise signals of all methods at frequencies of 10-12 GHz [128]. Applying the pulse train signal from the OFC onto a

photodetector, RF signals at integer multiples of the repetition rate are produced. This is due to the different modes mixing together simultaneously. For example mode m mixing with mode m+1 but also with mode m+2, m+3, m+4, etc... This essentially shifts the comb spectrum down to the RF domain (excluding the CEO). Since each of the comb modes are phase coherent, the result is many low phase noise signals which can be filtered out accordingly. As described in [127], a 1 GHz repetition rate Ti:sapphire comb is employed and the 10th harmonic of the photodetector output produces a 10 GHz output with phase noise of -104 dBc/Hz at 1 Hz offset from carrier. If lower carrier frequencies are required, then the phase noise is potentially reduced further via electronic frequency division [115], which as mentioned earlier, is much more effective at producing low PN signals than electronic up-conversion of conventional oscillators.

One issue with this approach is that combs from Ti:sapphire or fibre lasers typically have a lower repetition rate and to generate the high frequencies, a high number of harmonics are needed and can saturate the photodetector. This reduces the SNR of the desired harmonic, therefore limiting the phase noise achievable. This issue is addressed in [129] with a repetition rate multiplication scheme which is made up of cascaded mach-zehnder interferometers (MZM). Each interferometer is tuned to have a path length difference equal to half of the pulse interval, such that the repetition rate is doubled upon recombining as shown in Figure 3.16 [129]. As a result, high frequency signals require less harmonics to be generated on the photodetector, improving the phase noise floor.

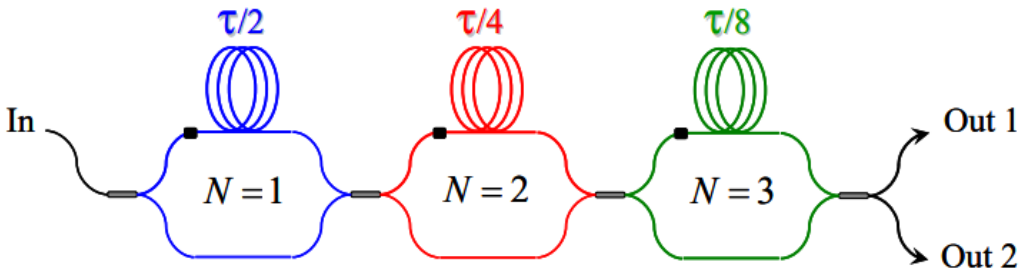

Figure 3.16: OFC repetition rate multiplication using MZMs. courtesy of Haboucha [129].

Another limitation is with the photodetector used, they need to be of sufficient bandwidth and exhibit linear properties in order to produce high SNR signals at high frequencies. In [130]

modified uni-travelling carrier (MUTC) photodiodes are developed. They have achieved 10 GHz signals with strengths up to 14 dBm, allowing for phase noise floor reductions to -177 dBc/Hz.

A combination of using the optical frequency division method, repetition rate multiplication and high bandwidth MUTC photodetectors, microwave generators with low phase noise at all frequency offsets can be achieved, outperforming all other oscillator types to the best of my knowledge. One of the lowest phase noise microwave signals reported are generated in [131] using the techniques previously described and achieve a 12 GHz carrier with -106 dBc/Hz at 1 Hz and below -170 dBc/Hz at 10 kHz offset frequency.

A more compact version of this oscillator (19 inch rack size) was developed in [132], using the techniques mentioned previously allowing this technology to be used outside of laboratory conditions. A cavity stabilized frequency comb with a repetition rate of 250 MHz is set through a four stage cascaded MZM multiplier, resulting in a 4 GHz repetition rate. The third harmonic is filtered to generate a low phase noise 12 GHz signal with a measured residual phase noise of -115 dBc/Hz at 1 Hz and less than -168 dBc/Hz at 10 kHz offset for the photonic microwave generation.

Microwave photonics are proven to be useful in generation of radar signals with appealing properties such as low phase noise, frequency flexibility and arbitrary waveform shaping. Also, photonic microwave generation systems are becoming more compact. However, there is still the vision to make these systems even smaller, to the point where they can all fit within a PIC. This field of integrated microwave photonics has recently gained much interest [133]. Highly tunable integrated microwave sources have been developed in [134], with an impressive tuning range from 1 to 112 GHz, although the phase noise is still high due to the incoherent laser sources. The key challenge is the integration of a high Q factor cavity into the chip [135]. Soliton microcombs have been produced with repetition rates at the X and K bands for direct microwave generation on an integrated photodiode in [136]. However, one of the smallest form factor and lowest phase noise, photonic chip RF generators to date are presented in [137]. This device used 2 semiconductor lasers that are stabilized by self injection locking to separate, high

Q factor, spiral micro resonators. They are then further stabilized with a chip integrated F-P cavity. Another separate microcomb, seeded by another laser is then stabilized using the Two point optical frequency division (2P-OFD) scheme. This technique involves anchoring two spectral endpoints of the comb with the two cavity stabilized lasers. Unlike traditional optical frequency combs that need to be self-referenced and require octave comb spanning OFCs, this microcomb is able to operate with lower pump power. The system produces 20 GHz microwave signals with phase noise of -135 dBc/Hz at 10 kHz offset which is approaching that of larger optical frequency division systems. A table showing the relative performance achievalbe from the different methods of photonic generation is shown in Figure 3.17 [128]. Overall, this is a very promising area and is expected to be used for many applications in the future.

Method	Frequency [GHz]	PN@10kHz [dBc/Hz]	Long-term Stability	SSR [dB]
Optical frequency multiplication	up to 100	depends on ref. signal and degrades with 20lg(N)	depends on ref. signal	depends on ref. signal
Optical phase-lock loop	up to 1000	depends on ref. signal and loop parameter	depends on ref. signal	/
Brillouin oscillator	21.7	-90	5×10^{-12}	about 70
Sideband-injection-locked laser	36	-102	/	about 82
Kerr frequency comb oscillator	9.9	<-121	10^{-10}	> 60
Optical-to-radio frequency division	12	<-173	6.5×10^{-16}	/
Optical-microwave synchronization	10	<-145	depends on MLL	/
Optoelectronic oscillator	10	<-150	$<10^{-12}$	about 140

Figure 3.17: Comparison of different photonic RF generation methods. SSR: spur suppression ratio. Courtesy of Shilong Pan [128].

The microwave photonics used within this work is the spectral purity unit, a subsystem of the ultrastable microwave system, from MENLO systems [42] and is based on the form factor of [132]. The comb light is taken from the smartcomb unit and the 125 MHz repetition rate is multiplied by a factor of 16 via a four stage MZM interleaver, providing 2 GHz repetition rate. The 5th harmonic 10 GHz output is filtered from the photodiode output and is then divided electronically producing outputs at 10 GHz, 5 GHz and 1.25 GHz. Additional details are provided in [138]. The phase noise results of the 10 GHz output are reported to be -89 dBc/Hz at 1 Hz and -135 dBc/Hz at 10 kHz offset frequency.

3.7 Summary

In terms of using these technologies in radar systems, there is little published work in the literature. Optical atomic clocks and Fabry-Perot based oscillators have been almost unreachable to the RF domain before the advent of the optical frequency comb in 1999. Even after the development of the optical frequency division method for low phase noise microwave generation, such high stability oscillators are still a rarity due to the equipment and technological challenges involved. Only select institutions around the world have a fully operational "ticking" strontium optical lattice clock. Therefore, many applications of these technologies remain unexplored, including those in radar systems.

However, the use of photonics in radar is an area developing much interest [128] [139] since the first demonstration of a fully photonic-based radar system [140]. So far, photonic based radars have not been focused on the area of ultra-low phase noise but rather some of the other benefits of using optical signals. One such example within the same system [141], demonstrates a photonics based transceiver operating on both the S and X bands, transmitting pulses sequentially. The radar utilizes a mode locked laser, with modes located at the two bands to ensure both are coherent to each other, allowing for more effective fusion of the data. Also, the extended frequency coverage has been demonstrated in photonic RF scanning receivers [142], making it possible to simultaneously map signals at 20 GHz and 40 GHz. High bandwidth capability is demonstrated in [143], generating a chirped pulse train spanning from 5 GHz to 60 GHz which was able to resolve 2 targets with a separation of only 6.3 cm. Another example in [144], demonstrates a 30 GHz bandwidth photonics enabled radar and lidar system for contactless vital sign detection. The use of phase noise stabilized links has also been explored in [28] for dissemination of a H-maser reference to radar nodes in different cities.

Photonics can provide many advantages in radar systems as mentioned above, but so far the use of ultra-low phase noise microwaves with F-P cavities, and OFD have not been reported in the literature to the best of my knowledge, at the time of writing and will be one of the focuses of this work. Chapter 7 will demonstrate the use of the photonic microwave signals within the L-band staring radar network for low phase noise, better synchronization purposes.

Chapter 4

Staring Radar Network Modelling

This chapter focuses on the modelling of an L-band staring radar network with particular focus on the effect of oscillator offsets and instabilities on network synchronization. Also the simulation is used as a platform to test processing methods developed within this work. This can be important in allowing us to understand the inner workings of the radar and to make predictions that could aid us in the design. The focus is on getting a fairly realistic model which can obtain similar results to the real radar system but also some simplifications are made so that we can focus on the parameters that are believed to be most important.

4.1 Gamekeeper 16U

The radar that is used throughout the thesis is an L-band staring radar, named the Gamekeeper-16U. designed by Thales, Aveillant [145]. The purpose of the radar is for accurate low altitude aircraft detection and for detection of SUAS targets such as drones. The radar consists of a cabin base which contains the radar main computer and servers, (also contains many of the oscillators that will be explained in later sections) and the radome on top which contains most of the radars RF chain, staring beam transmitter and receivers. Two of these systems were installed at the University of Birmingham to be used in a radar network. Figure 4.1 shows a close up photo of both of the radars.

These radars are classed as pulse Doppler radars which transmit a single frequency in the

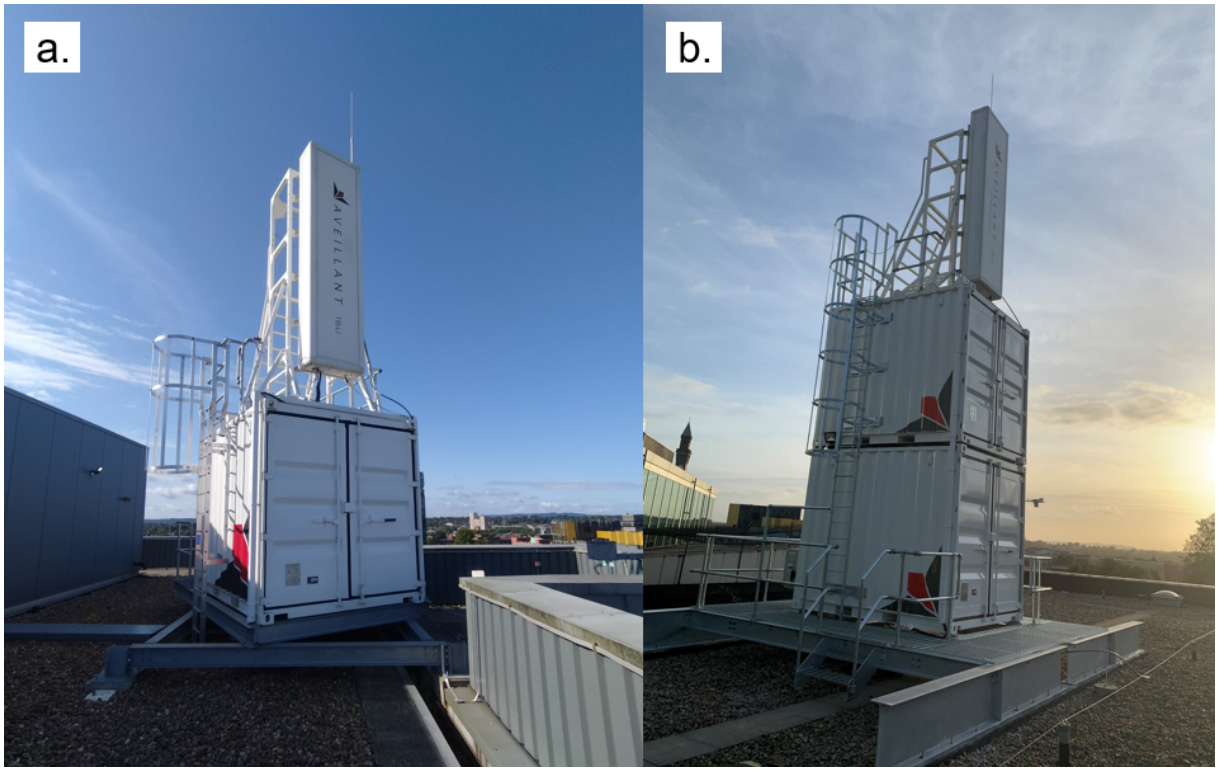

Figure 4.1: Photos of the L-Band staring radars. (a) GK000 installed atop Gisbert Kapp building. (b) GK007 installed atop ERI building.

L-band with a pulsed shaped waveform and a fixed pulse repetition frequency (PRF) of 7.3 kHz. The transmitter produces a spotlight staring beam which illuminates the entire field of view allowing for the capability of simultaneous detection of many targets. The radome itself is fixed in position so the field of view (FOV) is limited to the forward facing direction of the radome but the azimuth and elevation swath are approximately 90 degrees and 60 degrees respectively. The instrumented range is 5-10 km depending on the radar configuration used. To determine a targets angle of arrival (AOA), electronically scanned phased array technology is used. The radome consists of 64 receive elements placed in a 16 by 4 grid arrangement where the 16 elements are placed vertically providing an enhanced resolution in elevation. Each element records the IQ data for each of the 64 elements allowing for digital beamforming on receive, this is implemented into the post-processing chain.

4.2 Networked Radar Simulations

This chapter is consists of work from the published paper "Fully digital, urban networked staring radar: Simulation and experimentation" [146]. Text and figures have been reused from this publication. The work regarding development of this simulation tool, testing and the analysis of the outputs have been performed by myself.

The simulations are designed based on the Gamekeeper 16U network and consist of 5 main phases. The full flow diagram with each of the 5 phases are shown in Figure 4.2.

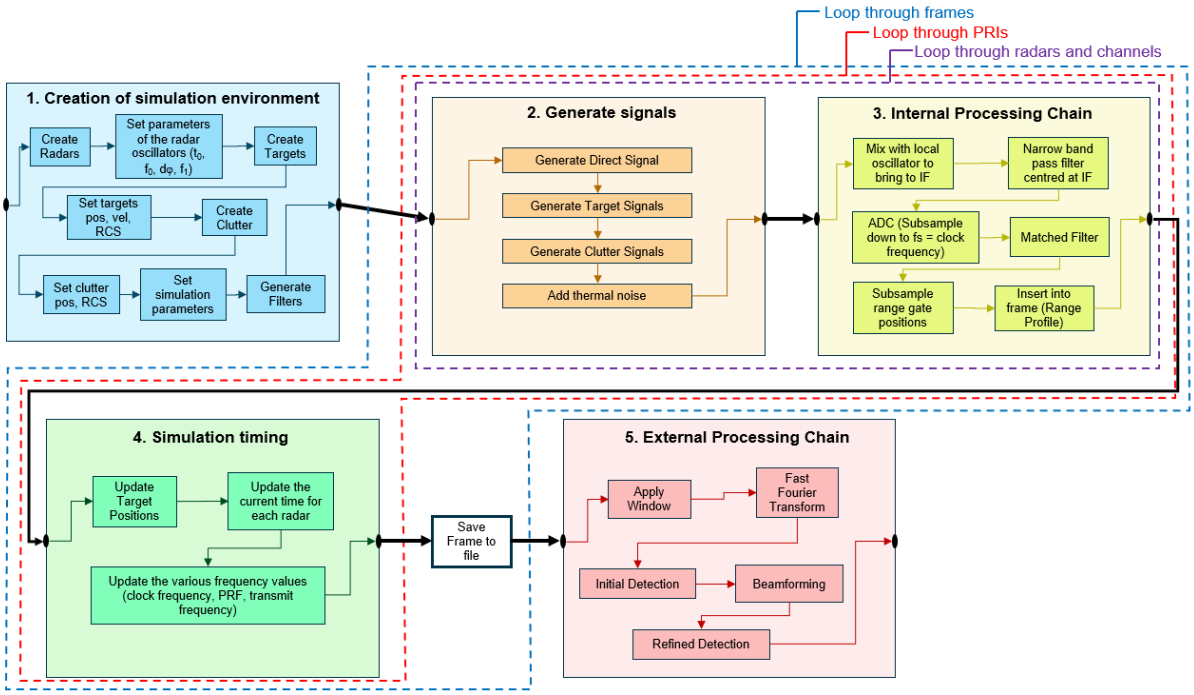

Figure 4.2: Full networked radar simulation block diagram.

Firstly, the user is able to define the radar environment which can consist of how many radars are in the field along with their respective configuration. Each radar will have a defined position and bearing. Similarly to the radar experiments, a radar can be tagged as a passive bistatic receiver and in this case it will not transmit any pulse. Each node will also have a local oscillator regardless of whether it is transmitting or not, which also has frequency instability imprinted onto it in the form of phase noise and frequency drifts. There are various parameters to select for adding the frequency instability, firstly there is the initial frequency offset which typically happens when using oscillators that are not disciplined to a frequency standard, here

it is simulated as an initial shift of the frequency in units of Hz. An initial time offset is also defined since the radars may not be triggered to start their pulse sequences at the same time, and will result in a misaligned recording window. A linear frequency drift is also simulated which is common in many oscillators such as OCXOs and F-P cavity based oscillators. For the simulation of phase noise there are 5 parameters that will together determine the phase noise profile of the oscillator and these are calculated empirically to match the phase noise profile of a known oscillator. The 5 phase noise parameters relate to the different noise types; white phase noise, flicker noise, phase walk PM, flicker walk and phase walk FM and these are equivalent to phase noise roll off of 0 dB/dec, 10 dB/dec ... 40 dB/dec respectively. One of the radars will be marked as the reference radar in which the generated data will be in the perspective of that radar. Also the reference radar will be assumed to have a 'perfect' noiseless oscillator without any phase noise added, this allows for the assumption of no phase noise added by the ADC and allows to implement the ADC as a simple subsampling. Also the number of targets can be defined with each of their respective initial positions, RCS, velocity. And the clutter can also be defined, these are similar to the targets but with no velocity. Other general parameters that can be modified include the base sampling frequency which determine how many samples per cycle are generated for the radars carrier frequency, the receive antenna array configuration (How many elements are used and the element spacing) and length of the recording window.

Next is the signal generation step which is performed for each radar and PRI. After a set amount of PRIs are completed they are grouped into a data frame and if multiple frames are to be generated then this is performed for each frame. The signal is generated directly at the receiver for each of the array elements using equation 4.1 where the outer loop iterates through each radar transmitter and the inner loops iterate through the different targets and clutter within the scene. Each target signal $t_n(t)$ takes the form of equation 4.2, where A is the attenuation parameter determined by a form of the general radar equation. E(t) is the envelope function, τ is the time delay calculated from the combined transmitter to target distance (R_T) and target to receiver distance (R_R). The phase noise and frequency drift is applied through an additional phase parameter $\phi(t)$. The clutter $c_m(t)$ and the direct signal $d_r(t)$ have the same form except τ

will be different.

$$y(t) = \sum_{r=1:R}^{r} \left[d_r(t) + \sum_{n=1:N}^{n} t_n(t) + \sum_{m=1:M}^{m} c_m(t) \right] + w(t) \tag{4.1}$$

$$t_n(t) = E(t) A e^{i(2\pi f_{c,n}(t-\tau)+\phi(t))} \tag{4.2}$$

$$A = \sqrt{\frac{P_{TX}\sigma\lambda^2 G_T G_R}{R_T^2 R_R^2 (4\pi)^3}} \tag{4.3}$$

$$\phi(t) = p_0\phi_0(t) + p_1\phi_1(t) + p_2\phi_2(t) + p_3\phi_3(t) + p_4\phi_4(t) + t^2 f_1 \tag{4.4}$$

P_{TX} represents the power of the transmitter in units of W, σ is the RCS, λ the wavelength of the transmitted signal, G_T and G_R are the antenna gains of the transmitter and receiver respectively. Equation 4.4 shows how the phase noise is added to the returning signal. ϕ_0(t) to ϕ_4(t) represent each of the different noise types mentioned previously from white noise to random walk FM. f_1 is the frequency drift parameter and this term represents the sub PRI phase progression contribution due to the linear frequency drift. These are all generated individually with their respective parameters set by the user and then summed together finally to provide the combined phase progression throughout the PRI.

The first noise type ϕ_0(t) represents the white noise, and represents a zero mean Gaussian noise process. This has a flat power spectral density and sometimes referred to as the thermal noise floor. Figure 4.3a and b shows the phase of a signal containing only white noise and its equivalent phase noise spectrum. A parameter relating to white noise p_0 is selectable and corresponds to the standard deviation of the Gaussian distribution.

Flicker noise (ϕ_1(t)) is generated by a method used in [147] for N samples and are then scaled using the flicker noise parameter p_1, by changing p_1, the flicker noise corner can be adjusted accordingly. Figure 4.3c shows the behaviour of the signal phase when only applying flicker noise and Figure 4.3d shows the spectrum with the correct gradient of -10 dB/dec.

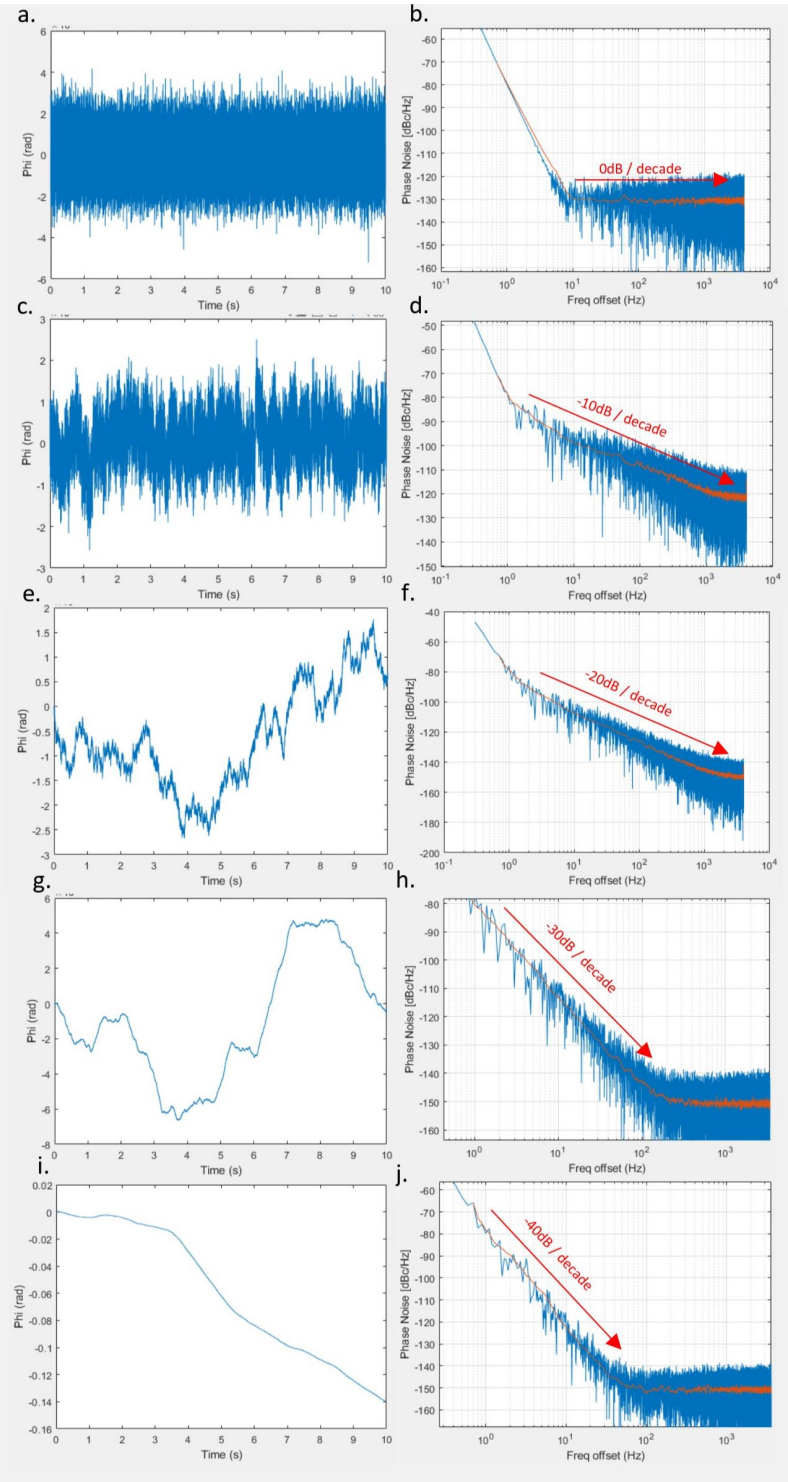

Figure 4.3: Simulated radar carrier signal with different phase noise types. White noise (a) time domain, (b) phase noise profile. Flicker noise (c) time domain, (d) phase noise profile. Random walk PM (e) time domain, (f) phase noise profile. Flicker walk (g) time domain, (h) phase noise profile. Random walk FM (i) time domain, (j) phase noise profile.

For the other noise types, it is shown in [148] that differentiated random walk noise (f^{-2}) provides white noise (f^{0}) and vice versa. Therefore, performing numerical integration on a set of white noise data converts it into random walk noise data. Also, it can be shown that by performing the numerical integration onto phase with a power law of (f^{α}) the result will have a power law of ($f^{\alpha-2}$) as shown in Equation 4.5.

$$\phi_{\alpha-2}[n] = \sum_{i=1:n-1} \phi_{\alpha}[i] \tag{4.5}$$

Therefore, random walk PM noise (ϕ_2(t)) is generated by first generating white noise and then integrating. Flicker walk noise (ϕ_3(t)) is generated by integrating flicker noise. Finally random walk FM noise (ϕ_4(t)) is generated by integrating the random walk noise (or integrating white noise twice). Figure 4.3e, g, i shows the phase behaviour of random walk PM, flicker walk and random walk FM noise types respectively. Figure 4.3f, h, j shows the corresponding phase noise spectrum with decreasing power law. Just like with the flicker noise, parameters p_2, p_3 and p_4 will scale the phase that is generated from each noise type and this will move the corner frequencies. By using all 5 noise types, this is enough to simulate the phase noise profile of the oscillators used within this work for the Fourier frequencies of interest, between 1 Hz and 100 kHz (see Appendix C). More details, specifically about the different types of phase noise and a useful resource for anything involving frequency stability, see the National Institute of Standards and Technology (NIST) frequency stability report [190].

Once the signals have been combined together at the PRI level, the signal will then go through the internal processing chain. Figure 4.4 shows the steps of the internal processing with numbered probes where the simulated radar return of a single PRI containing only single radar echo will be shown.

The time delayed transmitted waveform with a delay representing the time of signal flight is shown at the receiver tile in Figure 4.5a and b in the time domain. To reduce computational load the samplesPerCycle parameter is set fairly low but this is sufficient provided that it satisfied the Nyquist sampling theorem of all frequencies involved. This should be a minimum of 3 to ensure to meet the Nyquist frequency requirement of all frequencies involved. The spectrum in

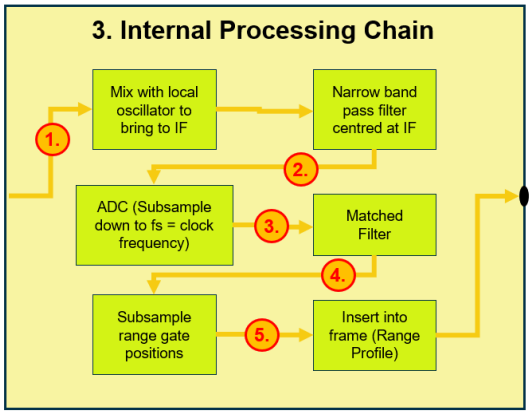

Figure 4.4: Block diagram of the internal processing chain used in the network simulations.

Figure 4.5c and d show that this signal corresponds to a single peak at the carrier frequency and a bandwidth of approximately 1 MHz as intended.

First, the combined pulsed signals at the carrier frequency are mixed together with the Local oscillator for baseband downconversion (LOBB) frequency CW signal to down-convert the radar echo information to the intermediate frequency. A narrow bandpass filter with a passband of 20 MHz, centred at the IF, is then used to filter out the sum component so that only the difference component remains from the mixer output. The pulse after it has been mixed down to IF and filtered is shown in Figure 4.6 where now it appears as a smooth waveform with a pulse envelope and the filter is shown to effectively remove the very high frequency noise.

The signals at IF are then sampled at the ADC frequency, and this is done by subsampling as the base simulation sample rate is a integer multiple of the ADC sample rate. This does not take into account clock jitter on the ADC sampling but in this situation the simplification that the transmitter is the dominating noise source is made. Jitter effects still occur due to the phase noise on the transmitter. The ADC sampling frequency is 62.5 MHz and therefore the output is undersampled and is shown near 15 MHz in Figure 4.7.

Next, the signal is matched filtered with a replica of the radar pulse at the mixed down ADC frequency to extract the desired echoes from within the noise. In this case SNR is already high so it is just further amplified as seen in Figure 4.8a. The final step before inserting into the data frame is to again subsample the data into the respective range gates to reduce data volume

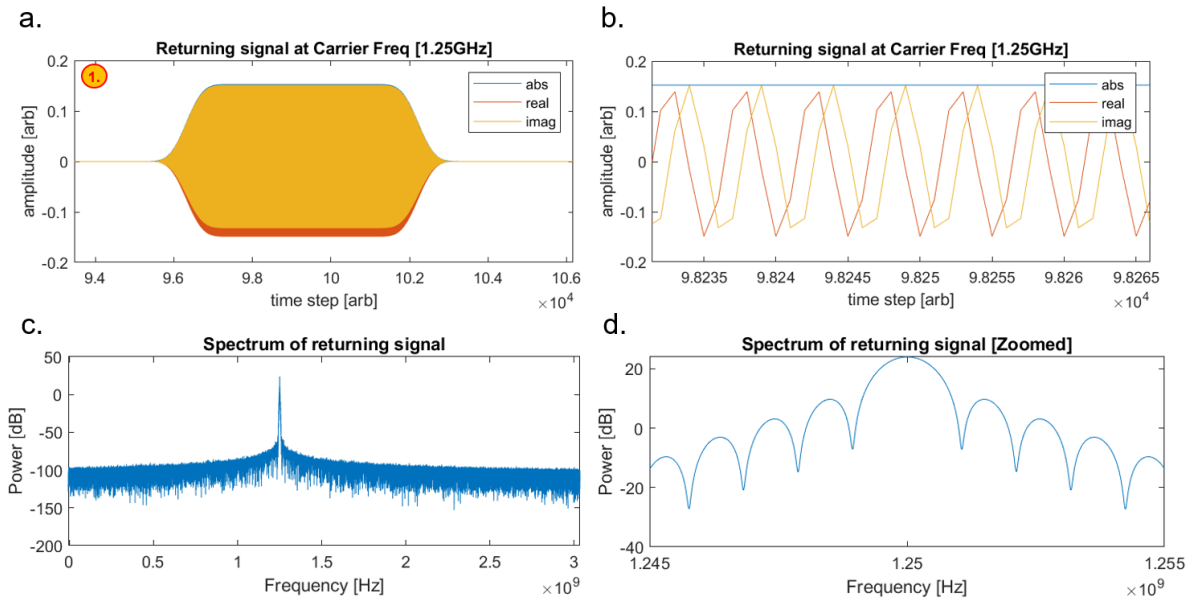

Figure 4.5: Signal return as measured at the receiver. (a) Time domain, (b) Time domain zoomed, (c) Frequency domain, (d) Frequency domain zoomed.

and the radar pulse is seen in Figure 4.8b where the peak is straddling multiple range gates and therefore can be interpolated during the digital processing stage.

At the end of each PRI, the local time for each of the radar nodes is updated taking into account each local oscillators timing offset, frequency offset and linear drifts. Also, each of the targets in the scene are updated to their new positions depending on their current positions and velocities. Parameters of the radar are also updated such as the clock frequency (f_{LO}), PRF (f_{PRF}) and the carrier frequency (f_c) as shown in (4.6) - (4.9).

$$f_{LO}(t) = f_{nominal} + f_0 + t f_1 \tag{4.6}$$

$$f_{PRF}(t) = \frac{f_{LO}(t)}{N_{cycles}} \tag{4.7}$$

$$f_c(t) = N_{PLL} f_{LO}(t) \tag{4.8}$$

$$t[p] = t[p-1] + PRI[p-1] \tag{4.9}$$

$f_{nominal}$ is the nominal clock frequency, N_{cycles} is the number of clock cycles per PRI and N_{PLL} is the PLL multiplication factor. Once the set number of PRIs is reached, the data frame is

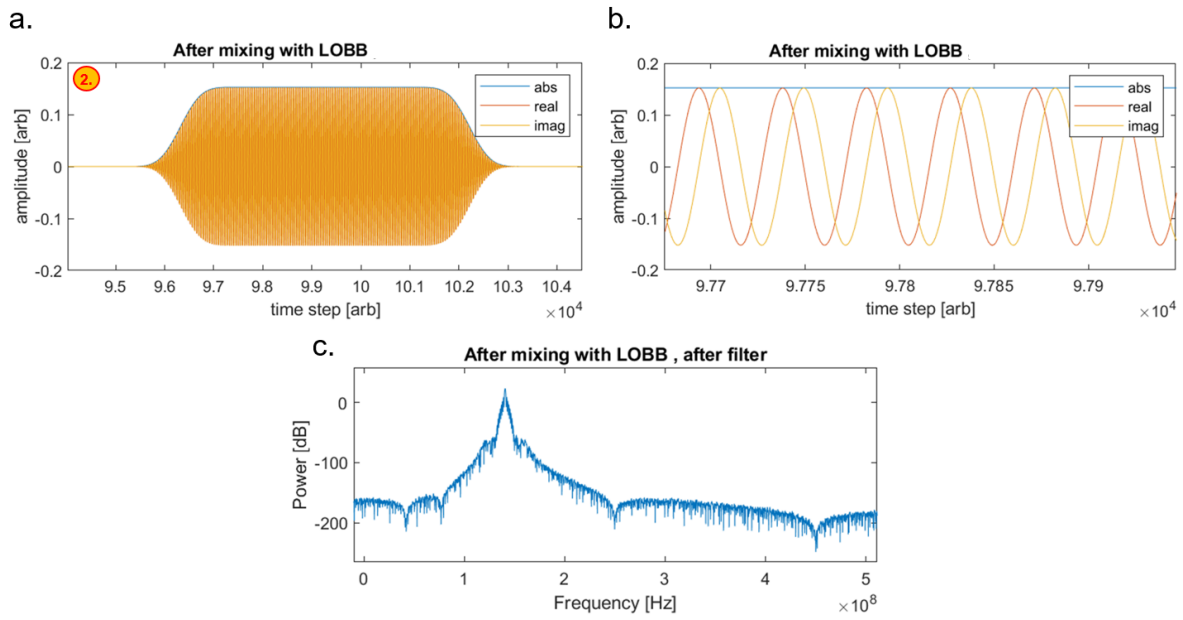

Figure 4.6: Signal after mixing to IF and filtering. (a) Time domain, (b) Time domain zoomed, (c) Frequency domain.

saved to file before starting the new frame (if applicable). The simulated data is then processed using the standard methods which we will call the internal processing chain. A window is applied across the time dimension before performing the FFT to transform to the frequency domain. The data is then beam formed in the desired direction and then a simple cell averaging constant false alarm rate detector (CA-CFAR) is applied to find the targets. The target estimation is then refined using interpolation and fine beamforming techniques.

This concludes the description of the simulation tools. Use of the staring network simulation tool is demonstrated in Appendix C for scenarios including local oscillator instability and for validation of the synchronization processing methods developed in Chapter 6.

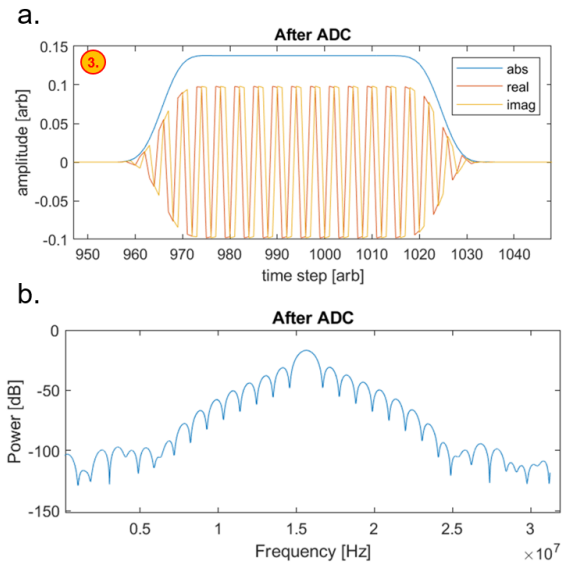

Figure 4.7: Signal after ADC subsampling (a) Time domain, (b) Frequency domain.

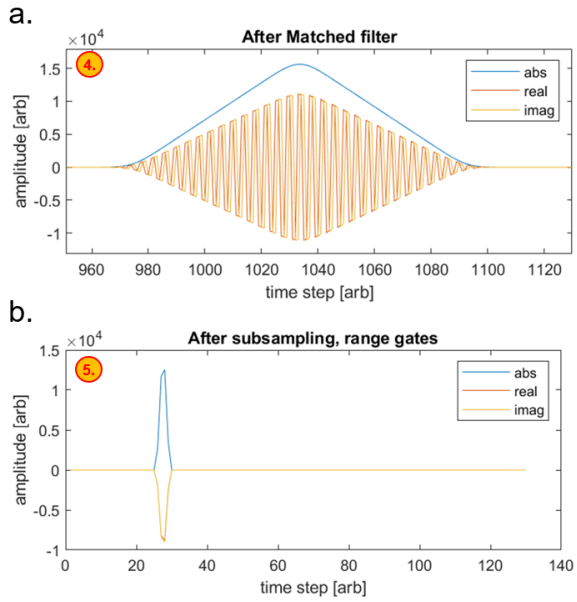

Figure 4.8: (a) Signal after matched filtering, (b) Signal after range gate subsampling.

Chapter 5

Radar Hardware and Measurement Procedure

This chapter describes the individual subsystems of the radar-oscillator interface and the radar hardware, including the transmitter and receiver. Then the experimental setup is explained for both background noise measurements and controlled drone measurements. The radar processing tools and data analysis methods are discussed, including radar sensitivity measurements, target detection, and specific figures of merit relevant to networked radar and synchronization.

5.1 The Gamekeeper Hardware Chain

As mentioned in the Chapter 4, the Gamekeeper-16U is an L-band staring radar system utilising a pulse Doppler architecture for surveillance of low altitude aircrafts. [145] An overview of the radar architecture from the collection of oscillators to the receiver radar output and digital signal processing (DSP) is sketched in Figure 5.1.

5.1.1 Oscillator Interface

The oscillator interface used for most of the measurements are shown in Figure 5.2. This enables a approach to testing radar performance with different oscillator configurations. The

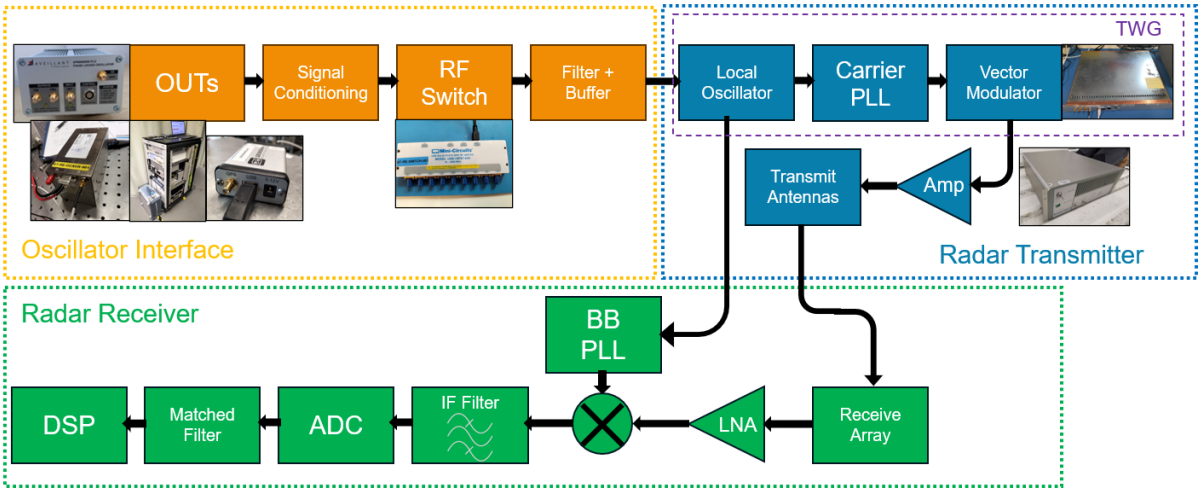

Figure 5.1: Radar schematic of the L-band staring radar. Consisting of the radar-oscillator interface, receiver RF chain and transmitter RF chain.

only exception to this are the measurements performed in Chapter 6.1, as these occurred before any modification to the radar oscillator and the measurements performed with the LNRCLOK and Thunderbolt-E GPSDOs in Chapter 7.1 due to an insufficient number of multiplier modules available during the experiment (more information is given in Chapter 7.1).

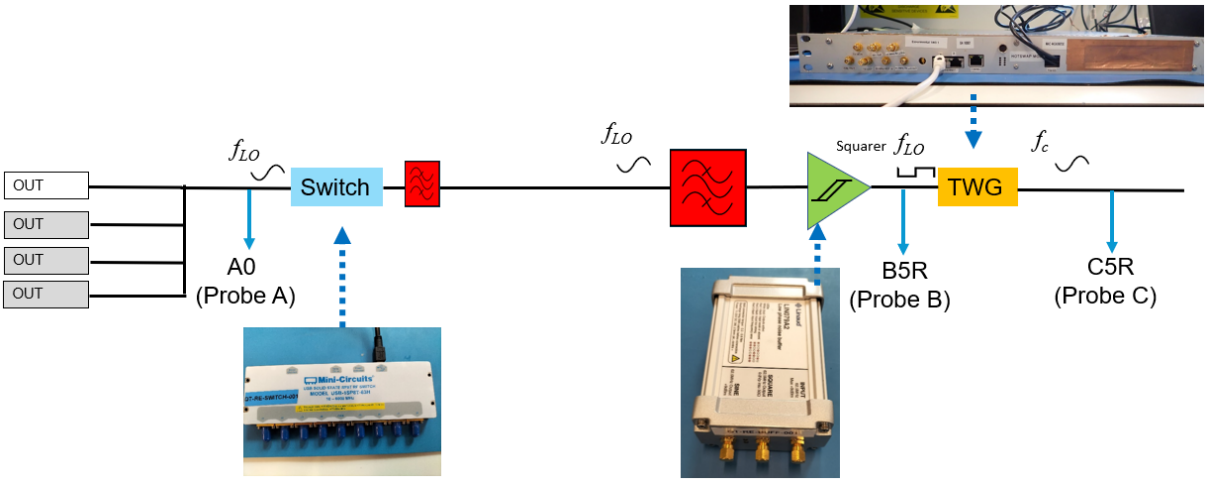

Figure 5.2: Oscillator-radar interface schematic for L-band staring radar. Consisting of OUTs, RF switch, BPF, Buffer, TWG.

The first stage of the chain is the oscillator under test (OUT), which has the functionality to switch between different signals, to feed in as the radars local oscillator. Chapter 7 characterizes various oscillators in terms of frequency stability, analyzing their distinct properties along with the advantages and disadvantages they contribute to radar systems. Various different oscillators

include OCXOs, GPSDOs and Photonic oscillators.

One challenge is that not all of the oscillators are able to output the same nominal frequency as the radar's local oscillator (LO). Therefore, the signal conditioning stage takes care of this to ensure the frequency of all the signals entering the RF switch are at f_{LO}. One example of this is the MWP, since the RF generation is at 10 GHz followed by internal frequency division to reach 1.25 GHz and then another external division to get to f_{LO}. Another example are oscillators that output only a standard 10 MHz output, these are multiplied up to the correct frequency using a bespoke frequency multiplier unit.

The RF switch provides the ability to remotely change between different OUTs during radar measurement and for monitoring and logging of the oscillator configuration. This is a mini circuits USB-1SP8T-852H [149] which is a 8 to 1 switch allowing up to 8 oscillator configurations. The switch provides a feed through to one of the 8 inputs depending on the users selection and terminates the remaining inputs. All components after the RF switch output are standard for all OUTs.

Finally, before entering the main radar transmitter chain, this is a sequence of RF components consisting of a band pass filter with a pass band containing f_{LO}. With the filter, any potential harmonics that are initially contained with the signal, are attenuated. Following this, a custom buffer unit is in place to terminate the signal unless it falls within a few hundred Hertz of the specified frequency and meets the required power level. Also, the signal is converted from a sinusoidal to a square waveform before being sent through a 5-10 m RF cable to the radar radome.

5.1.2 Radar Transmitter

The oscillator signal is input into the timing and waveform generation board (TWG) and the local oscillator is defined. A timing signal distribution unit will amplify and split the LO to other subsystems of the radar such as each of the receiver boards and part of the signal will be sent to the carrier phase locked loop (PLL). The PLL is a critical point which will be discussed at various point throughout the thesis. This is a common way to generate high frequency carrier signals

in radars as it allows for frequency flexibility and makes use of a low phase noise oscillator signal at a lower frequency. The main drawback is that there is inherent noise added via the PLL up-conversion. Regardless, this will be discussed more in Chapter 7.3 about alternative radar architecture for future radar systems. In this radar, the PLL has a fixed output frequency, with a frequency multiplier factor of approximately 20.

After the signal is multiplied, the vector modulator is used to shape the pulse waveform using a set of attenuation coefficients. The pulsed signal at f_c contains a duty cycle of approximately 1 %. The TWG board contains the local oscillator, carrier PLL and the vector modulator and is highlighted in Figure 5.3.

A high power amplifier, Microwave Amps AM84, is used to increase the power of the RF to 2 kW. The power amplification was calibrated with the pulsed TWG output within the lab using a set of attenuators and a power meter to ensure an accurate power output is transmitted. The measurement setup for this is shown in Figure 5.3 with the power amplifier shown in the bottom left.

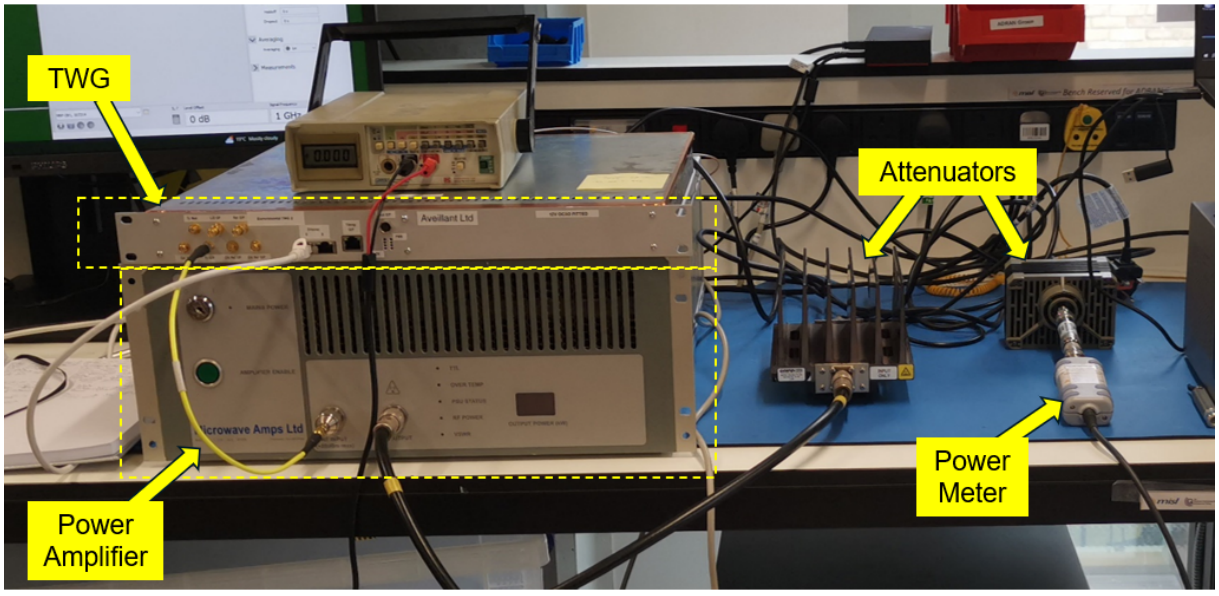

Figure 5.3: Benchtop setup of TWG and power amplifier for calibrating radar transmitter amplification.

After the pulse is amplified to the appropriate power levels it is then transmitted using an array of patch antennas in an 8x1 linear configuration. The staring radar produces a spotlight

beam, illuminating the whole FOV. There is no scanning involved for the transmitter side so from pulse to pulse, the beam profile is considered to be identical.

5.1.3 Receiver

The receiver sub chain is now described. This starts with the receive antenna which is a 2D grid of receiver elements with 16 vertically and 4 horizontally with approximately half a wavelength spacing. Each element records the echo returns from targets within the environment and using a low noise amplifier (LNA) to increase the power for subsequent stages.

Each of the 64 channels are now sent through the same sequence, next being the mixing down stage where the received pulsed are down converted to the intermediate frequency (IF). This is performed in the mixer where one arm is connected to the received signal and the other arm is connected to the LOBB PLL. The LOBB PLL takes the clock reference signal from the TWG distribution board and multiplies the frequency to $f_{LO} + f_{IF}$.

The output signal after the mixer contains the (unwanted) sum components around $2f_c + f_{IF}$ and the difference components around f_{IF}. Therefore, an IF filter is used to suppress the sum component.

Next, the analogue to digital converter (ADC) digitises the signal at a sample rate of f_{LO}. This utilizes undersampling, therefore the frequency of the radar returns are aliased and appear at a reduced frequency of f_{ADC}.

Finally, the digital signal is matched filtered via a field-programmable gate array (FPGA) using a replica of the transmitted pulse mixed down to f_{ADC} before reaching the data output and digital signal processing (DSP) stage.

5.2 Experimental Setup for Measurements

This section explains the setup for performing radar measurements. The focus of this work is on the effect of radar performance with a change in oscillator configuration. Previous sections have shown the standardised process of running the radar with a specified OUT. Further details on

each oscillator configuration will be provided in the corresponding sections, while this section focuses exclusively on the radar measurement techniques.

5.2.1 Controlled Drone Measurements

One of the main functions of a radar is to be able to detect and locate a target and one of the ways that this can be benchmarked in the radar is to perform controlled drone trials. To ensure that any difference in radar performance can be contributed to the oscillator, several factors must be controlled. Staring radar illumination provides a complex electromagnetic environment with radar scatter from various sources, therefore there is only a limited extent to which we can control all of the variables in real experiment. Regardless, what can be controlled, to some extent, is the target, location, trajectory, time of day, weather and radar parameters.

The targets used are various models of drones. The main target used for most configuration is the DJI Inspire 2 [150] and is shown in Figure 5.4a. The DJI Inspire 2 drone is large in size, weighing approximately 3.4 kg, and provides a relatively high RCS (Radar Cross Section) target, making it detectable by radar under most conditions at ranges of up to a few kilometers. Additionally, a smaller drone, the DJI Mini Mavic 3, and a larger model, the DJI Matrice, are also used in measurements, shown in Figure 5.4b, c.

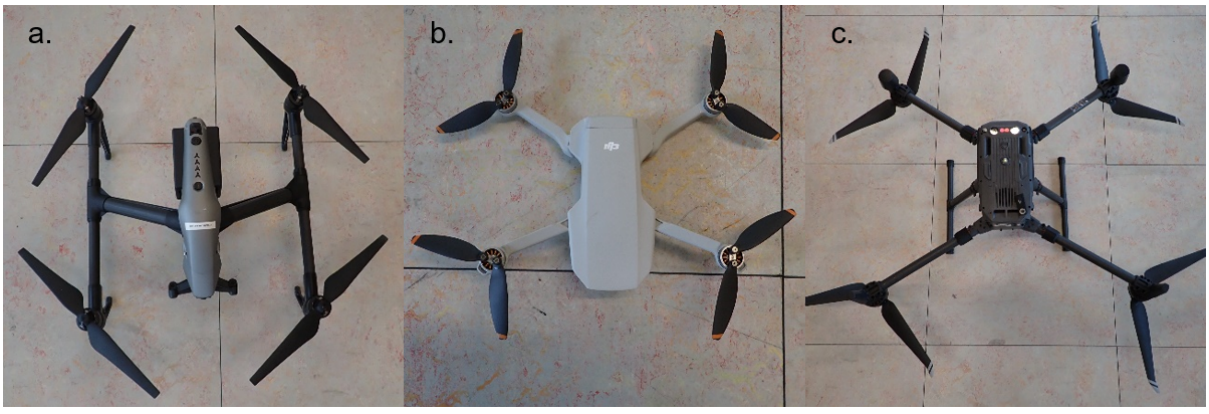

Figure 5.4: Photographs of the drones used within radar measurements. (a) DJI Inspire, (b) DJI mini mavic 3, (c) DJI Matrice.

The locations chosen are based on the feasibility to fly drones in the particular area, whether it is within the coverage area of the radars and if it is sufficiently far from any roads or buildings.

Since one of the topics of this thesis involves radar surveillance in the urban environment, it is also beneficial for there to be high clutter sources in the region. This is sometimes due to a large structure, but sometimes indirectly through high azimuthal sidelobes. For example, part of the Richmond track passes through an azimuth sidelobe of the Chamberlain hall building which is one of the largest scatterers in the FOV.

The trajectory of the drone can be controlled by setting fixed waypoints corresponding to flight scenarios and the drone can automatically follow the waypoints with a fixed speed. This is possible with the DJI Inspire and produces highly repeatable patterns. For this reason, the data analysis presented within this thesis refers to the data taken with the DJI Inspire 2. Three of the locations used within this work with their waypoints are shown in Figure 5.5. However, most the Richmond location is used for the majority of measurements due to it being more central and positioned in the overlapping region of both radars, and contains data for all oscillator configurations. To ensure consistency, the same location (Richmond) is used for the data analysis.

The time of day and the season can affect the amount of other opportune targets in the area. This is challenging to control as it severly limits when new data can be collected but generally the drone flights occur in the mornings.

The weather cannot be so precisely controlled as the temperature, precipitation, wind speeds, etc can have an effect on what the radar measures. No drone flights are performed when there is precipitation or if there are high wind speeds. Overall, this is one of the more loosely controlled factors as conditions will still vary from flight to flight, regardless of if they occur on the same day.

Other radar related parameters are also controlled. The radar position is fixed and has not been moved or rotated since their installation. The radar configs that contain information such as the waveform parameters, PRF, transmitted frequency, etc. are also standardised. A default config is used for all of the monostatic radar measurements. For the bistatic measurements, the RxBistatic config is used, this is the same apart from a fully attenuated transmit signal and an extended recording window during each PRI (130 range gates rather than 64 default).

Figure 5.5: Flight scenarios used within the radar measurements. (a) Vale, (b) Richmond, (c) Metchley Pitches, (d) Overlapping radar FOV region. Credit: Google Maps

5.2.2 Background Noise Measurements

An expected result of phase noise in a radar is that the overall noise floor is raised and therefore the smallest RCS target that is detectable will increase. One of the measurements is focused on measuring the actual noise floor and comparing this with different radar-oscillator configurations. As will be explained in later sections, noise levels are dependant on the range, angle and Doppler cell under test (CUT). Also, since the instantaneous power fluctuates, the noise level in a particular CUT is obtained by measuring the power over a longer time period. The effect of other targets in the environment can be an issue in this regard, and although, the effect of targets can be reduced by calculating the median noise, it is rarely completely removed. In other work [151] target track heatmaps with the L-band radar system were measured over different periods of the day. It was found that opportune target occupancy was relatively lower during

night-time periods (20:00 - 23:59) compared to the other times of the day. Typically, there can be multiple targets constantly in the same resolution cell during the peak periods of the day. This is demonstrated in Figure 5.6 where spectrograms are compared between a day-time period and a night-time period for the same location. Clearly, in the day-time spectrogram, the sheer number of targets present will make obtaining a measure of the noise floor very difficult, especially at close-in frequencies. However, in the night-time data for the same location, no moving targets are present within the time interval. Some specular signatures are shown at non-zero Doppler frequencies, and these are due to spurious tones in the transmitted signal and anomalies in the radar. Therefore, it is beneficial to record radar data during this night-time window to obtain a measure of the real noise floor.

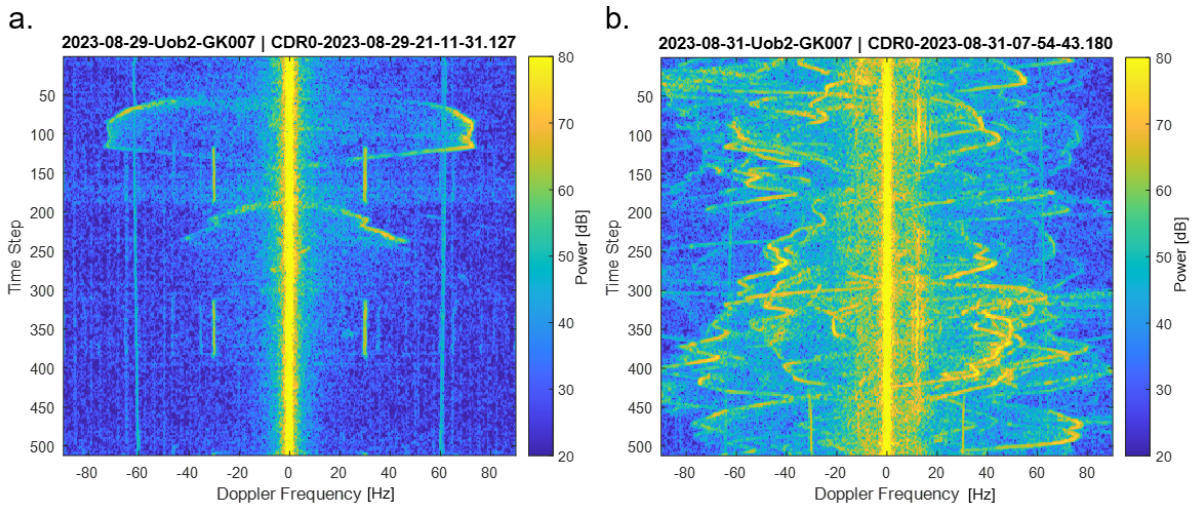

Figure 5.6: Spectrogram of data recordings from a chosen location (a) night-time data, 10pm. (b) day-time data, 9am.

The process of taking the background noise measurements consists of setting up the oscillator configuration, taking in-situ phase noise measurements and recording raw radar data for a period of 10 minutes or more to get sufficient data.

This chapter concludes the L-band staring radar measurement setup and measurement methodology. The following chapters present the results of radar network measurements using different synchronization techniques.

Chapter 6

Networked Radar: Digital Signal Processing Synchronization Techniques

Within the chapter, the focus is on the methods used to synchronize two staring radar nodes and the corresponding results from field trials. Two identical staring radar systems, described in Chapter 4.1, are placed upon two buildings on the University of Birmingham campus as shown in Figure 6.1. On the right hand side, the radar placed atop the Gisbert-Kapp building and is designated as GK000. On the left hand side, another radar node (GK007) is placed at a baseline of 180 m atop the European research institute (ERI) building.

Figure 6.1: Overview of the networked staring radar configuration in Birmingham (Google maps)

In the following sections, the effects of timing errors on a non-coherent network radar system are discussed. Then, the use of novel signal processing schemes are devised which can be used to synchronize network staring radars in an urban environment, which can overcome the instability induced from lower quality oscillators. These include range profile correlation method for range alignment, a detector for bistatic staring radar and a method for correcting sub-CPI phase errors by combining phase estimations of multiple reference sources in an urban scene.

6.1 Non-coherent radar network

This section contains data using the initial radar configuration shortly before they were moved to Birmingham in late 2020. This section consists of reused text and figures from the publication "Direct signal synchronization for staring passive bistatic radar" [11]. In this work I had created the bistatic data correction tooling and processed the results.

These are the same radar systems designated as GK000 and GK007, but they are located in Deenethorpe airfield with overlapping coverage of the rural region. Radar experiments consisted of a controlled drone flight of a DJI S900 flying in the PACMAN_S01 scenario. The radar coverage and drone checkpoints are shown in Figure 6.2. One radar (GK000) is set to be in its default radar configuration while the other (GK007) is set to receive only and acts as the bistatic receiver. These measurements had taken place prior to the implementation to the radar-oscillator interface; therefore, both radars are operating with OCXOs as their LO.

Since both LOs are not disciplined to a frequency standard or common reference and there is no external radar triggering, this is considered to be an non-coherent radar network. Although, the OCXOs have the same nominal frequency specification, the actual frequency will be offset due to external factors such a temperature variations, power supply fluctuations and ageing [152]. In terms of bistatic radar operation, this relates to an initial frequency offset and drift throughout the measurement. The effects of the incoherent network on the bistatic radar output is demonstrated by producing a range-Doppler plot at a time instance when the drone is present, shown in Figure 6.3. The peak relating to the drone is also marked in red, and its position is

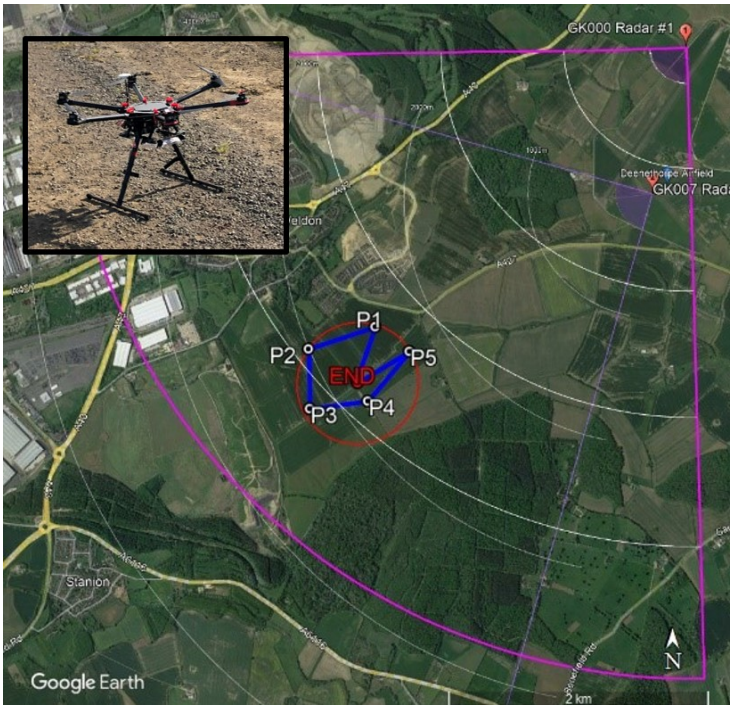

Figure 6.2: Deenethorpe experimental bistatic measurements overview showing radar coverage and PACMAN_S01 drone trajectory. Inset photo of the DJI S900 drone (Google maps).

measured in terms of the perspective of the radar and compared to its true position determined by GPS truth data.

One clear observation is there is a significant frequency offset present, evident with the clutter appearing at 280 Hz Doppler frequency offset. This is consistent with a target moving at a relative velocity of 33.6 m/s. Since the local oscillator is maintaining the radar's local time scale, the result is one radar ticking faster than the other. Ticking, in this context refers to the time progression of the local clock. Another effect is on the generation of the carrier waveform, since this is derived from the LO via PLL. The frequency errors are multiplied according to the PLL upconversion factor. On the receiver node, the echoes are retrieved and mixed down to IF and then mixed down to baseband via matched filter. In this example, the frequency errors have propagated though the radar RF chain in the receiver and resulting in a frequency offset of all signals.

Another observation is that the entire profile of the range-Doppler appears to be shifted upwards. This can also be shown via the detected position of the Drone target which is reported in Table. 6.1. One of the causes for this is the lack of triggering in the receiver node, there is an

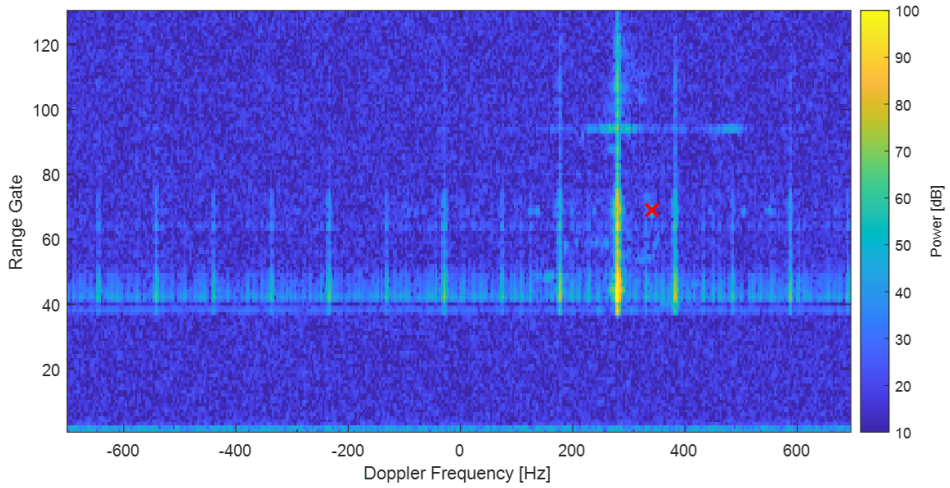

Figure 6.3: Range-Doppler plot of the non-coherent bistatic radar output.

initial time offset present causing a mismatch in the timing of the PRI between the two radars. This arbitrary timing offset causes an equivalent arbitrary error in the range as measured for all objects detected by the radar. This is detrimental to the radar, as the correct positioning of objects is crucial to its operation.

Table 6.1: Drone position as measured by the bistatic radar and the real position determined via GPS truth data.

	Bistatic radar measurement	**Bistatic truth**	**Monostatic radar measurement**	**Monostatic truth**
Range [m]	5444	2962	3417	3424
Doppler [Hz]	341	62.8	57.5	58.7

Also, since the frequency error is significant, range drift is observed over medium to long time scales. This is demonstrated in Figure 6.4, which shows as time progresses, the entire profile shifts downwards. After 284 s as seen in Figure 6.4c, the range gates consisting of the direct breakthrough signal and the near range returns are outside of the recording window and with not much useful data present.

Each of the issues described, present a challenge for accurate detections of objects within the bistatic data. This is typically addressed by providing a common local time scale or by providing each radar node with disciplined LOs. Most commonly, networked radars consisting of disciplined oscillators use GPSDOs which make use of the widely available GNSS signals [153] [154]. These techniques are more widely discussed in Chapter 7. Other methods of

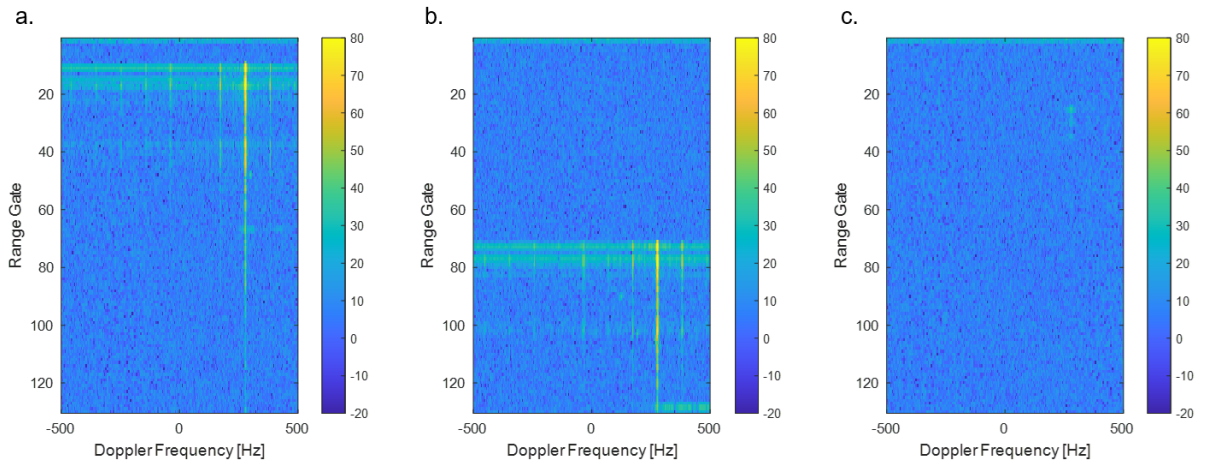

Figure 6.4: Range-Doppler plot of bistatic radar output at different times, demonstrating range drift. (a) t = 0 s, (b) t = 142 s, (c) t = 284 s.

providing synchronization are to use network time protocols and white rabbit protocols have also been implemented. [155] However, one common technique is to directly utilize the direct signal of the transmitter or an illuminator of opportunity. Direct breakthrough signals are collected using a separate reference antenna and can be used directly in the matched filter stage. Passive radar has been demonstrated using various classes of uncooperative illuminators such as DVB [156], WiFi [157], GNSS [158], 5G [159] and Starlink [160].

In this work, the timing errors are corrected for using the direct breakthrough signal of the cooperative transmitter. In this case, many factors are known already such as the waveform, carrier frequency, pulse schedule, etc. Since the radars are fixed, the locations and baselines are known. Also, due to the spotlight illuminator, there is no requirement for a separate reference channel or for beam chasing. Therefore, using the bistatic radar, synchronization can occur using the direct signal extracted from the surveillance channel, and the full coverage for the entire FOV is retained. The block diagram of the direct signal synchronization method is shown in Figure 6.5 and is published in [11].

The first stage consists of the detection of the direct signal and its corresponding range. This is accomplished by converting to the beam-Doppler domain and finding the transition between thermal noise and a powerful signal in the range dimension. Interpolation then occurs over the range gates surrounding the peak to determine the range more precisely.

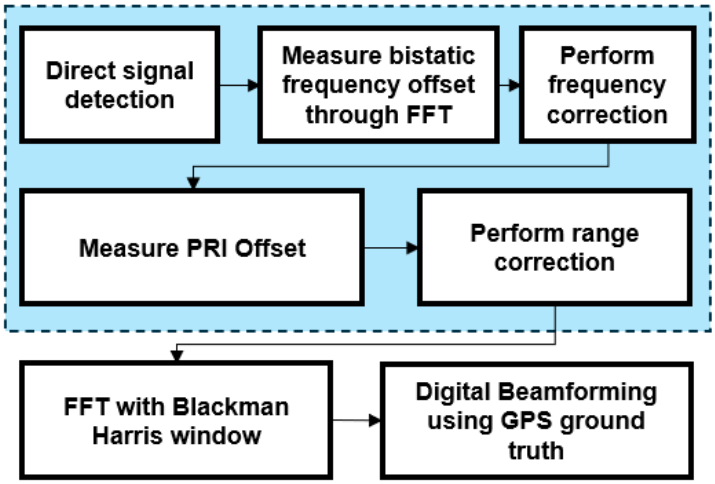

Figure 6.5: Block diagram of the direct signal synchronization method.

Clock frequency offset (f_d) can be described by Equation 6.1 where N_{PLL} is the PLL multiplication factor and f_1 and f_2 are the frequencies of the two LOs. This can be measured in the beam-Doppler domain by peak finding in the frequency dimension.

$$f_d = N_{PLL}(f_2 - f_1) \tag{6.1}$$

The value f_d [Hz] is then used to calculate the phase gradient ($\Delta\phi_1$) in Equation. 6.2, representing the phase shift required between each time step to correct for the frequency offset. An additional term containing frequency drift ($\Delta\phi_2$) is also computed with Equation. 6.3 where f_1 is the frequency drift in units [Hz/s]. Then the frequency correction is applied to the time-channel data frame (C^t) in Equation. 6.4. Within the data frame ($C^t_{h,j,k,l}$), the subscripts h, j, k and l correspond to the row element, column element, range index and time/pulse index respectively.

$$\Delta\phi_1 = \frac{-2\pi f_d}{PRF} \tag{6.2}$$

$$\Delta\phi_2 = \frac{-2\pi f_1}{(PRI)^2} \tag{6.3}$$

$$C^t_{h,j,k,l} = C^t_{h,j,k,l} e^{i(l\Delta\phi_1 + l^2\Delta\phi_2)} \tag{6.4}$$

The timing error is then estimated as a PRI offset (Δt) which requires knowledge of the

pulse scheduling. Both radars are designed to have the same pulse scheduling and therefore measurement of the PRI offset is illustrated in Figure 6.6 where the pulse is referring the direct breakthrough signal. t_i is the time interval between the PRI start and the transmit pulse. t_a is the time difference between the transmit pulse and the first range gate representing the blanking range. t_b is the measured time difference between the first range gate and the observed pulse. t_c is the computed time between the transmit pulse and the expected position of the pulse in the receiver node. PRI offset is then determined using Equation. 6.5 and is used to determine the time for the newly defined range gates using Equation. 6.6, completing the correction of the PRI offset. $t_k^{n,m}$ is the time representing the kth range gate of the nth receiver node using the mth transmitter node. t_{rg} represents the time interval between range gates. This bistatic data correction method is used on simulated data with the results shown in Appendix C.

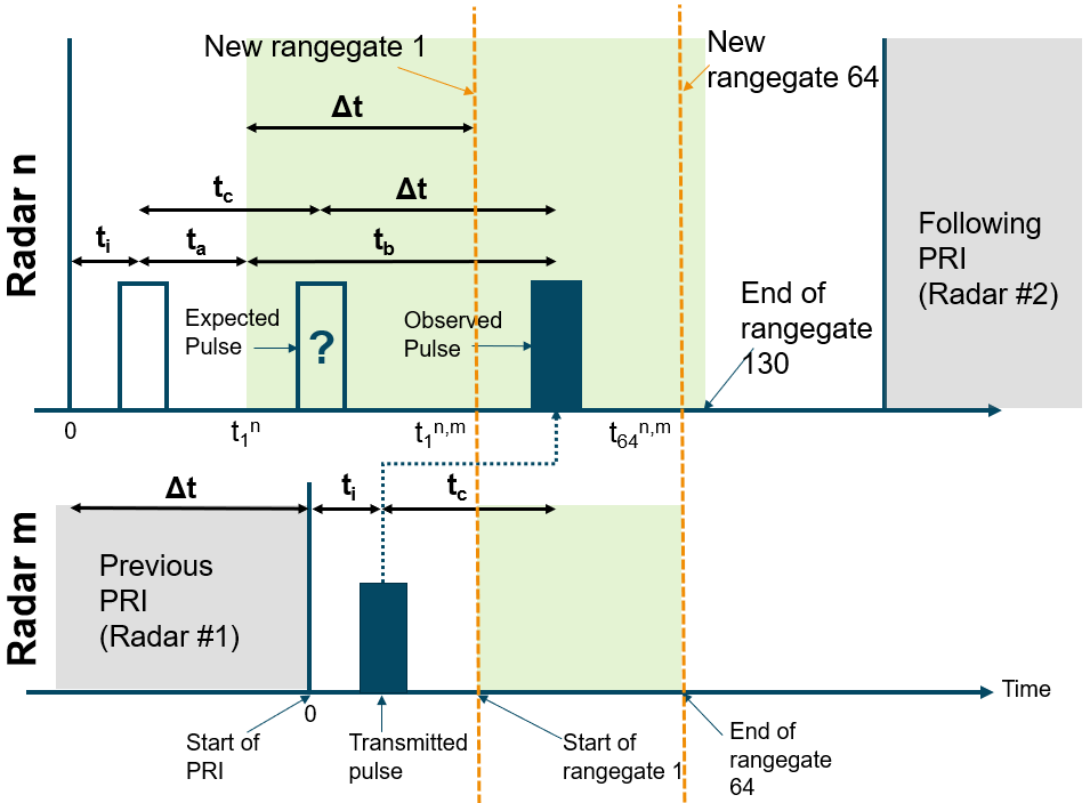

Figure 6.6: PRI offset estimation using the measured and expected time of pulse.

$$\Delta t = t_a + t_b - t_c \tag{6.5}$$

$$t_k^{n,m} = t_1^n + \Delta t + (k-1)t_{rg} \tag{6.6}$$

The direct signal synchronization method is applied to the same data frame and the range-Doppler plot is shown in Figure 6.7 with the position of the drone target marked with a red cross. The frequency offset is no longer present with the clutter appearing at 0 Hz Doppler frequency. Also, the range offset has been corrected with the direct signal now appearing closer to the start of the PRI. The position of the target is now correctly measured with a measured bistatic range of 2973 m and a Doppler frequency of 61.1 Hz.

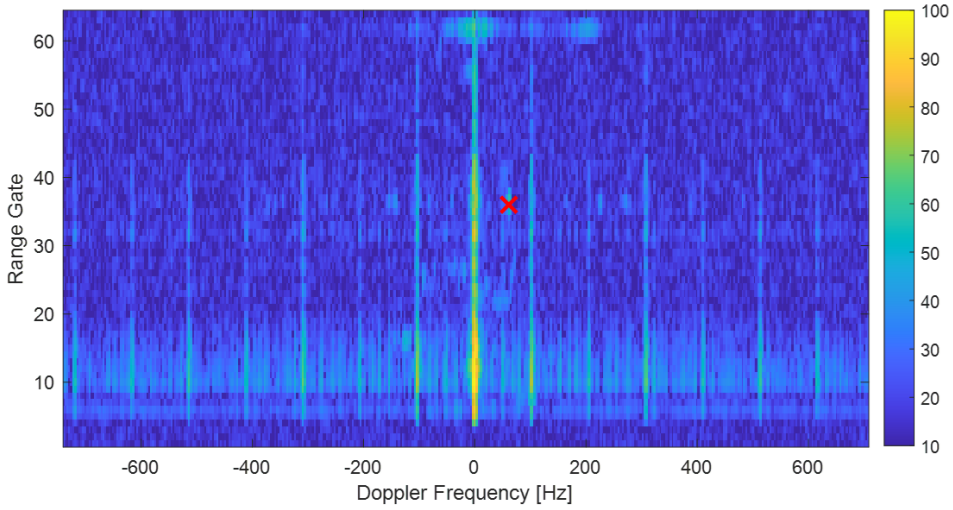

Figure 6.7: Range-Doppler plot of the bistatic radar output after applying direct signal synchronization with the position of the drone marked with a red cross.

The spectrogram for a portion of the PACMAN_S01 flight with the DJI S900 is produced in the bistatic radar after applying the direct signal synchronization for each timestep and is shown in Figure 6.8a. The clutter remains at 0 Hz throughout the flight and the main body of the target is visible throughout with high SNR. Also the micro-Doppler returns can be seen symmetrically to the fuselage. Another spectrogram for the same time interval but for the monostatic radar is shown in Figure 6.8b. The SNR visibly looks to be lower in the monostatic data with the average SNR throughout the time interval shown being. 53.2 dB and 55.4 dB respectively for the monostatic and bistatic data. However, this should not be misinterpreted in a way that suggests that this method is able to provide better performance than an equivalent monostatic radar, since there are various other factors in play. The bistatic range is lower than the corresponding

monostatic range, causing higher signal echoes and also the geometry used causes higher clutter and therefore more phase noise in the monostatic case. The increased SNR in the bistatic radar measurement demonstrates one of the several situational advantages that can be obtained using multiple radars in a network.

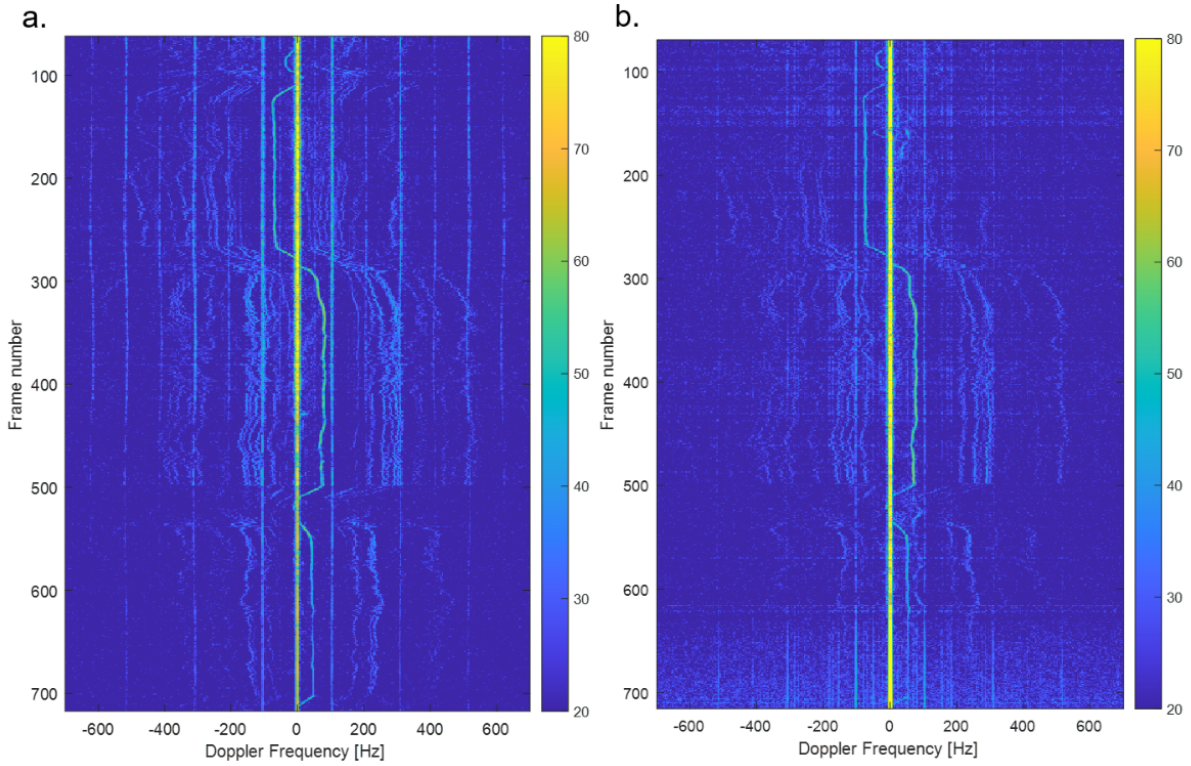

Figure 6.8: (a) Spectrogram of the DJI-S900 from the bistatic radar after direct signal synchronization, (b) equivalent spectrogram in the monostatic radar.

The direct signal synchronization is proven to be successful in correcting for the range and frequency offset present in the bistatic receiver. This has given the L-band staring radar the capability to make detections and attribute an accurate measurement of its position when using the radars as a network. Also the measurement of average SNR shows that this method can provide a comparable level of performance in the bistatic radar in this situation. However, the issue of the range drift is not resolved and is still an issue that remains at this stage. After time step 700, the target had drifted outside of the recording interval and the coverage is lost. An example is also shown in figure 6.4 where there is no direct signal to calculate the range offset. One solution is to increase the length of the recording window to be close to the entire length of the PRI, but that would result in higher requirements for data write speed and capacity beyond

what is possible with the current hardware. Another solution is to implement triggering of the receiver node and actively change the start time of the PRI, requiring knowledge of the PRI offset. This can be enabled by this method or would require a communication channel between the two nodes. Implementation of the radar triggering required alterations to the hardware which were not addressed during this work and are not discussed further but are only acknowledged as a potential solution.

Another problem is when there is no direct line of sight between the radars or if the location of the breakthrough pulse is not clear; therefore, not detectable in the same way. Yet another problem occurs where there are sub-CPI frequency fluctuations visible in the radar output as a result of oscillator instability, which can typically occur in low cost COTS oscillators. These are issues that are to be addressed with novel signal processing schemes developed and are presented in the following sections.

6.2 Novel Urban Bistatic Processing

This section consists of several novel processing schemes that are developed for L-band staring radar in an urban environment to aid with synchronization and surveillance of sUAVs. The range profile correlation method utilizes various landmarks in the environment to obtain an improved estimation of the PRI offset (Δt). A bistatic detector is developed to provide capability of detections, directly from the raw data, in the bistatic node. Also, a phase synchronization method is developed which utilizes multiple reference sources to obtain an improved estimation of the phase error between two remote radars.

6.2.1 Range Alignment via Range Profile Correlation

The upgraded bistatic correction scheme provides range profile correlation and clock drift correction in the bistatic data correction stage and is published in "Fully digital, urban networked staring radar: Simulation and experimentation" [146]. Some of the text and figures from this section are reused from this publication [146]. I was involved in the data collection along with

other members of the team. Conceptualization, developing the software and processing the results were completed by myself

The previous method is expected to struggle when there is no direct line of sight between the two radar nodes. Therefore, this method takes advantage that the spotlight transmitter beam characteristics are constant and assumes that much of the stationary returns are correlated between different times and dates. This method utilizes the newly termed, range profile reference (RPR), containing the averaged clutter power profile over an extended period. This is then used as a tool to measure Δt for future data sets.

The first stage is the generation of the RPR. This is assuming the radars are stationary, each unique combination of receiver and transmitter would require its own profile since they will each have a different perspective of the environment. It is still a question as to how long of an interval before a new RPR is needed, but it is expected that the same range profile would remain valid for more than a year. Since this will only change if there are many new developments (or demolitions) taking place in the area, dramatically changing the trends of the clutter. To generate the clutter profile, first a suitable set of data is found, this will have at least a few range gates before the direct signal available and at least 64 range gates after the direct signal (or at its expected position). Then, the range profile for multiple CPIs are generated. These are then upscaled to increase the level of precision achievable for the correlation step, defining fractional range gates. The range profiles are then aligned using a relative PRI offset before averaging them together. The fractional range gate most closely relating to the position of the direct breakthrough signal is then defined, either through the direct signal detection method described in Chapter 6.1 or via a one time manual input.

Upon reading in the bistatic data for processing, a check for a valid range profile is made, and the current range profile for the same beam is generated and upsampled in the same way as the RPR. The convolution between the range profile and the RPR is computed and an example using a range profile from a different time period used to generate the RPR is shown in Figure 6.9a. Since the RPR and range profile will have similar characteristics, a clear peak will be present and can be used to represent Δt. Then the range profile is shifted by Δt, providing the

range alignment. The combined plot of the corrected range profile and the RPR are shown in Figure 6.9b where the location of the direct breakthrough signal and large clutter sources are marked.

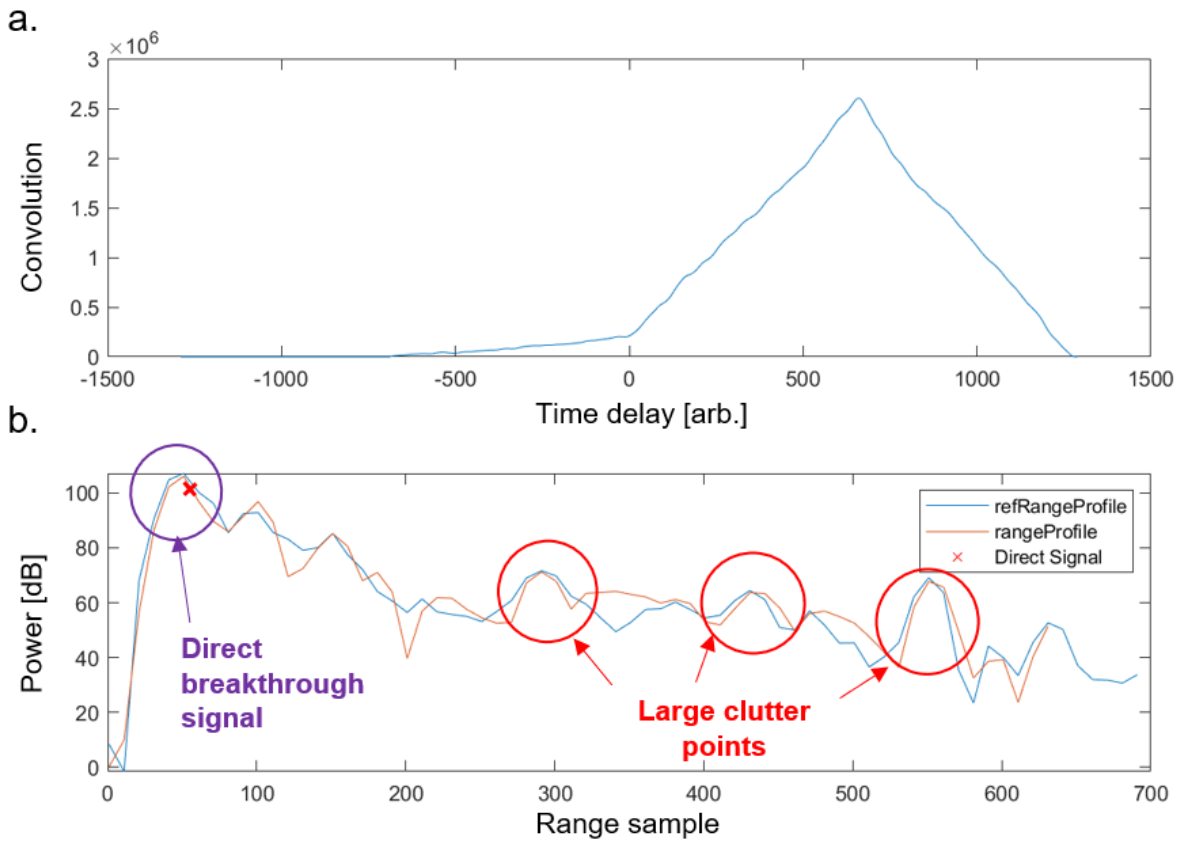

Figure 6.9: (a) Result of the convolution between range profile reference and a range profile from a different time period. (b) Combined plot of range profiles with significant landmarks marked.

It is seen that this method successfully determines and corrects for the PRI offset for this data set. Since the radar returns from large buildings produce strong returns with a lower variance as discussed in Chapter 7, each of these sources are able to aid with alignment of the range. Range profile correlation can be used when the direct signal is not available and rely on other features such as echoes from large buildings, transition from thermal noise to signal in the first range samples and the trend of higher signal powers at short ranges.

The range profile correlation method is used to correct the bistatic data after the radars were installed in Birmingham. During these initial bistatic experiments, both radars contain the default OCXO oscillators and therefore is still considered to be non-coherent. The DJI Inspire

2 is flown with the Richmond_S01R (Reverse) flight path at an altitude of 100 m. The radars were configured such that GK007 was the transmitter and GK000 acted as the passive receiver but the configuration was swapped halfway through the experiments and the same flights were repeated. The flights that are used throughout this work are shown in Table. 6.2.

Table 6.2: Drone flight used during initial bistatic experiments at Birmingham

Tx Radar	Rx Radar	Experiment Data	Target type	Flight used
GK000	GK007	2022-07-06_Uob_Trial26 M01	Inspire 2	Flight #4
GK007	GK000	2022-07-06_Uob_Trial26 M02	Inspire 2	Flight #12

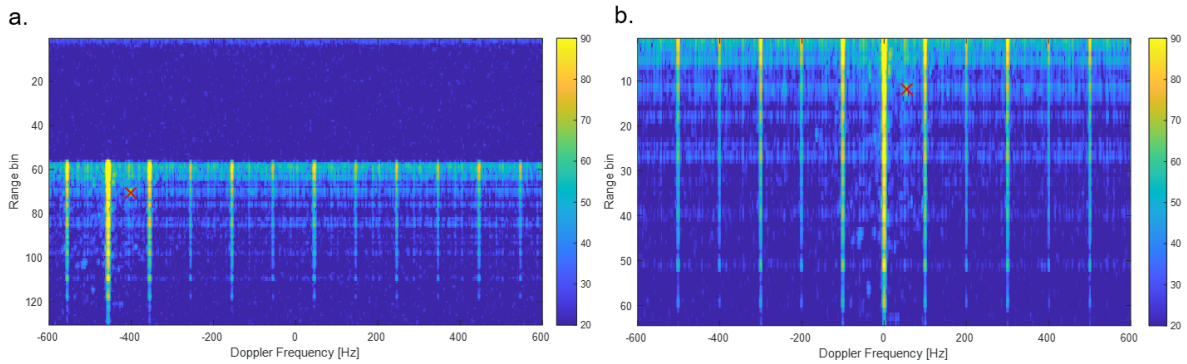

Figure 6.10: Bistatic range-Doppler plots with GK000 as the receiver node (a) before bistatic corrections, (b) after bistatic corrections.

A range-Doppler plot using GK000 as the bistatic receiver node is shown in Figure 6.10a containing the controlled drone target marked in red. The bistatic corrections are applied with the use of the range profile correlation method and the resultant range-Doppler plot is shown in 6.10b. The target is now located at the correct range gate and the expected Doppler frequency, validating the use of this processing technique. However, several vertical lines are apparent in both plots, these are termed clutter lines and are a side effect of spurious tones in the oscillator and they were very significant in this data set.

The range profile correlation method is used to generate bistatic spectrograms for Flight #4 and Flight #12 and also the equivalent monostatic spectrograms are shown in Figure 6.11 In the spectrograms, the SBM subtraction technique is used and this helps with hiding the clutter lines. The drone target is clearly visible in all radar configurations including the bistatic spectrograms where two different RPRs are used for the two different transmitter receiver pairs. As mentioned

previously, GK007 OCXO stability is superior and therefore, both body and micro-Doppler sidebands are shown more strongly in the GK007 monostatic data.

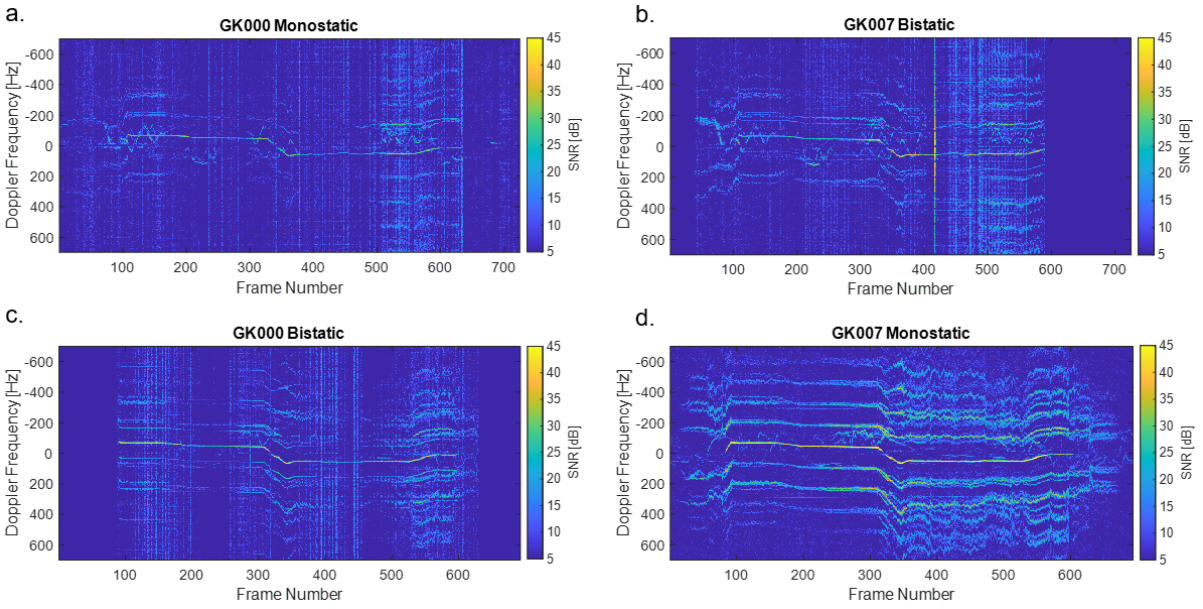

Figure 6.11: Drone spectrograms for for OCXO bistatic experiments with the DJI Inspire 2 and Richmond_S01 scenario (a) GK000 monostatic, (b) GK007 bistatic after corrections, (c) GK000 bistatic after corrections, (d) GK007 monostatic.

Table 6.3: Drone flight used during initial bistatic experiments at Birmingham

Flight Number	**Radar Configuration**	**Average SNR Scaled [dB]**	**Probability of Detection**
Flight #4	GK000 Monostatic	38.78	0.664
Flight #4	GK007 Bistatic	37.33	0.726
Flight #12	GK007 Monostatic	48.28	0.749
Flight #12	GK000 Bistatic	31.76	0.613

The average SNR is scaled to a constant range for each of the 4 spectrograms are shown in Table. 6.3. A 9-10 dB difference is seen between the GK000 and GK007 monostatic flights. There are a cascade of reasons for this including RF transmitter power and array scan losses. Although these are assumed to be small due to the similar transmit powers used between the radars and similar angles from boresight. The greatest contributor is expected to be difference in phase noise properties of the two oscillators and clutter power due to the radar geometry. The SNR values recorded from the bistatic flights are more similar to GK000, phase noise would be expected to be limited to the poorer oscillator which is observed here. There is a similar

PD for all the data sets, limited by the drone dead time at the start and end of the flight where the drone is hovering and masked by the clutter. As discussed previously, one shortfall is that the frequency offset causes significant range drift and the timing error eventually exceeds the recording length of the radar. Although the range profile correlation can potentially recover the data when the direct signal is not present, there is a point where the drone echo is missing until it loops back around into the next PRI. This can be observed in Figure 6.11b after frame 600, and 6.11c before frame 80. This challenge can be resolved by synchronizing the oscillators to a frequency standard or providing a common LO.

6.2.2 Bistatic Detector

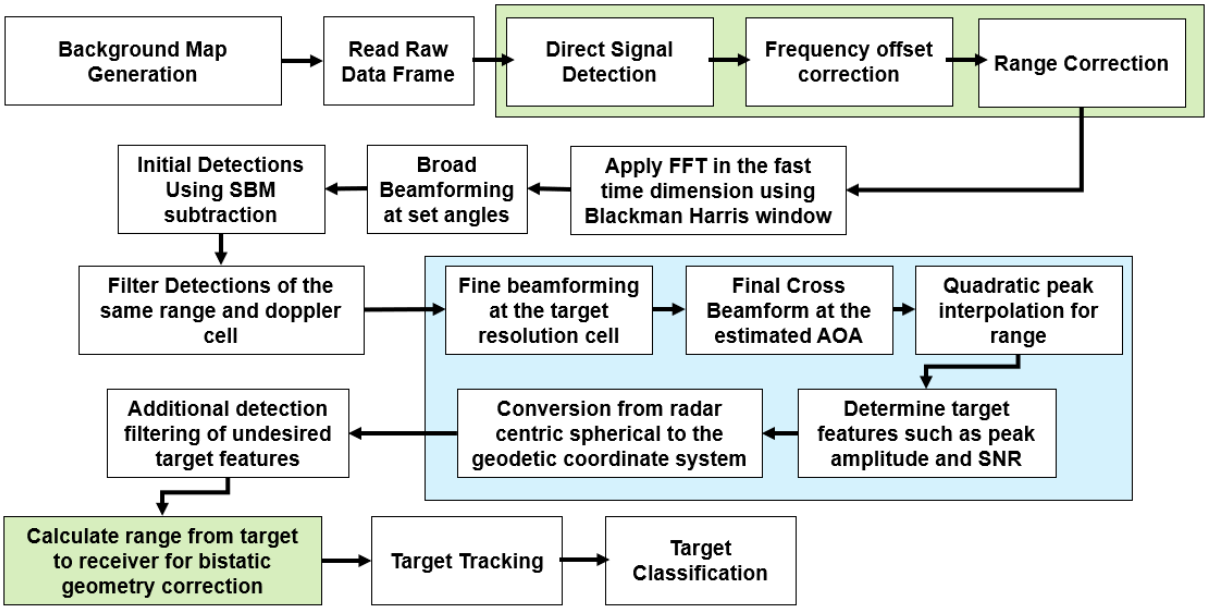

Figure 6.12: Block diagram of the bistatic detector chain [146].

Detection capability is added to the radar in the bistatic configuration. The block diagram for the detection signal processing is shown in Figure 6.12 where the green highlighted blocks are unique to the bistatic operation. Raw radar data was processed offline to generate spectal background maps (SBM) using the time criteria. Descriptions of SBMs and how they are produced from the raw radar data are described in Appendix A. Therefore, SBMs are only used if they are within 20 minutes of the selected data. Upon reading in the raw data for an entire CPI,

the bistatic data corrections are applied consisting of the range profile correlation method for estimating Δt. The first beamforming stage consisting of a course grid of beams is performed, matching with those from the SBM. The SBM is used as a cell averaging CFAR for the peak detection stage, where for each cell under test (CUT) the identical position in the SBM is used to represent the noise level and is subtracted. Subsequently, a threshold of 20 dB above the noise level is applied, peaks crossing this are marked as initial detections. Duplicate detections that are in the same range and Doppler cell, which are common when high SNR targets are detected within azimuth and elevation sidelobes, are then filtered as well as for targets with a anomalous location, such as below ground height or behind the radar. The filtered detections are then refined for range and angle. The fine beamforming stage generates a high resolution grid of beams for the cells containing detections, allowing for higher precision in angular measurement. Quadratic interpolation is performed over the range dimension, further enhancing positional measurement. Equation. 6.7 is used to convert the measured bistatic range (R_B) into the range from the receiver node (R_R).

$$R_R = \frac{R_B^2 - L^2}{2(R_B - Lcos\theta_{LR})} \tag{6.7}$$

$$R_B = R_R + R_T \tag{6.8}$$

Where L is the baseline distance and θ_{LR} is the angle between the vector connecting the baseline and the vector connecting the receiver to the target. With the position of each of the radar detections known in polar coordinate space, these can then be converted to the local Cartesian and geodetic coordinate systems.

For testing the use of the bistatic detector, Flight #4 is used as shown in Table. 6.2 using the DJI Inspire drone using the Richmond_S01R scenario. The entire map of detections from the 3 minute time interval containing the drone flight is shown in Figure 6.13 with the height above sea level (meters) indicated with the color coding and size of each point representing the SNR (dB). Various moving targets are detected, indicated by clusters of points and at varying heights.

Since, there is no implemented tracking algorithm, The detections relating to the controlled

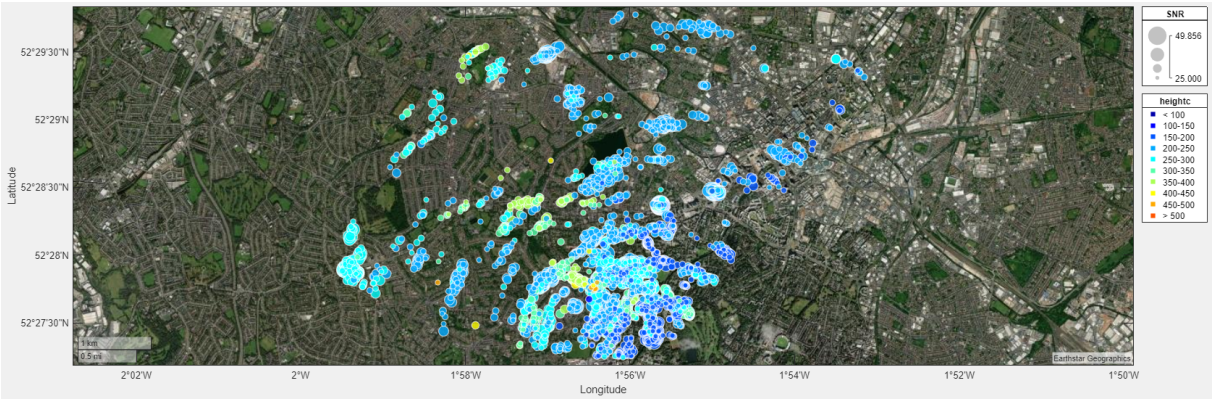

Figure 6.13: Plan view of the bistatic detection output for all detections in the FOV (Earthstar Geographics).

drone target are manually filtered for further analysis based on the expected latitude and longitude recorded from the GPS truth data. In addition, the filtered points are then smoothed using a Savitzky-Golay filter to demonstrate the type of performance that would be achievable and is shown in Figure 6.14a along with the corresponding truth data. This is repeated for the monostatic radar during the same flight and the detections and truth data are shown in Figure 6.14b. The orientation of the track appears skewed due to the different radar geometry between the monostatic and bistatic cases.

This demonstrates successful detection of the drone target throughout the flight with the bistatic radar node using the upgraded direct signal synchronisation scheme and the track matches well with the truth data in both cases. One of the main factors for the offset, in both cases is a systematic bias in the elevation and azimuth angles due to multipath reflections. The positional error of the drone in local Cartesian coordinates is shown in Figure 6.14c, d. It is observed that while the error is generally less in the monostatic case, the height of the target was more accurately measured with the bistatic radar, possibly suggesting that the effect of multipath is reduced. However, the error in the x and y position fluctuate more in the bistatic radar due to the limited synchronisation accuracy corresponding to half of a range gate (35 m).

Overall, these results demonstrate the successful implementation of the range profile correlation method and the overall bistatic detection chain. This provides the very first shown capability of synchronization and bistatic operation of these particular systems [146]. However,

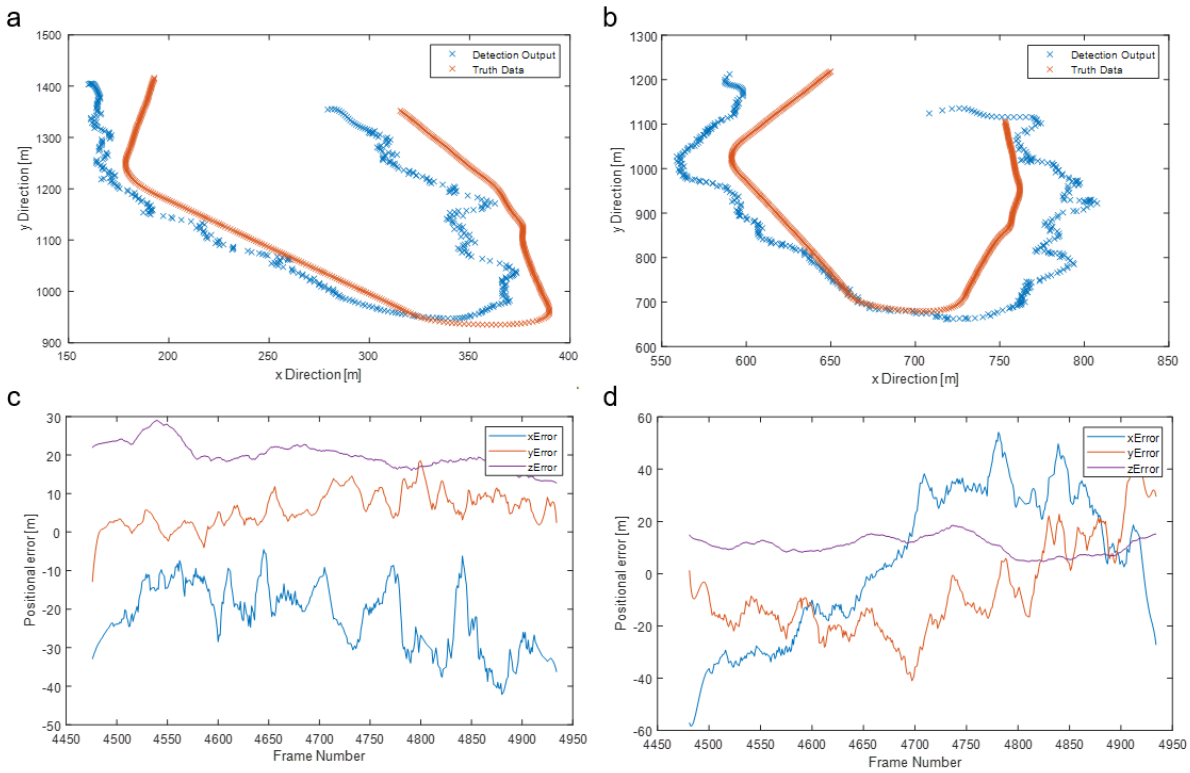

Figure 6.14: Positional accuracy measurements from a single controlled drone flight. (a) plan view detection plot for monostatic GK000, (b) plan view detection plot for bistatic GK007, (c) positional error from truth GK000, (d) positional error from truth GK007 [146].

there are still some challenges such as the range drift that can cause information to be lost and the sub-CPI phase drifts, causing coherent integration losses.

6.2.3 Phase Suppression of Bistatic Radar using Averaged Phase Estimation

The work within this section is part of a submitted paper "Phase Synchronization of Bistatic Radar by Exploiting the Urban Scene". I was involved in the data collection along with other members of the team. Conceptualization, developing the software and processing the results were completed by myself. The paper is not yet published at the time of writing and this section reuses text and figures from the paper.

To proceed with further improving the level of synchronization it is vital that the frequency offset from the large frequency offset is removed or there is a trigger implemented into the

hardware of the radar itself. While the use of oscillators are mostly the topic of the next chapter, in this section, a pair of low cost COTS oscillators are implemented. As will be seen, these are able to meet the minimum requirement for being able to remove the effects of range drift due to the disciplined aspect but the quality of the oscillator is poor in comparison to the OCXO causing considerable phase noise. Therefore, the previously mentioned sub-CPI phase drifts are more significant. The respective phase noise profiles are shown in Figure 6.15 where the Leo Bodnar GPSDO [161] is compared with the radar's default OCXOs.

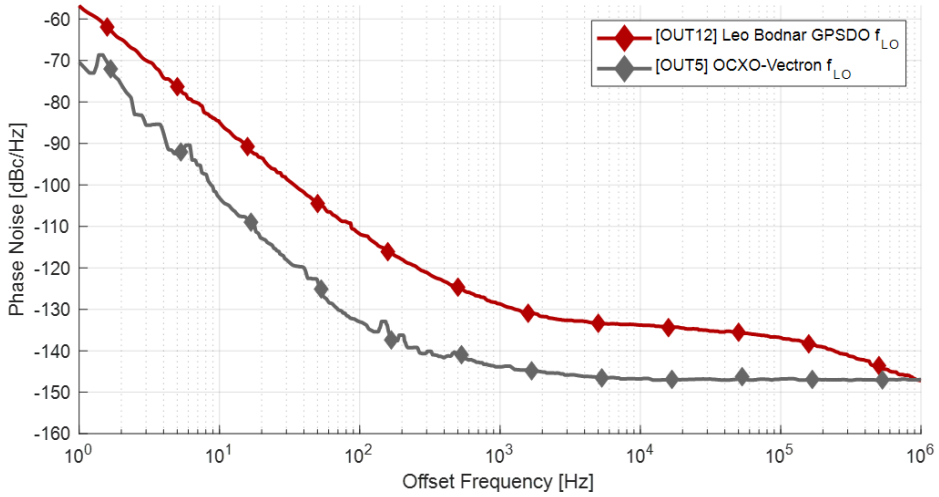

Figure 6.15: Phase noise profile for the Leo Bodnar GPSDO compared with the default OCXO.

The phase noise is significantly higher for the GPSDO, especially for the close-in frequencies such as at 100 Hz offset where the difference is approaching 25 dB. In a monostatic radar, there is a self phase noise cancellation effect. This is demonstrated in Figure 6.16 where the PSD of the radar output is measured for the Leo Bodnar monostatic case as well as when the radars are operating bistatically with a pair of Leo Bodnar GPSDOs.

In the bistatic PSD, the close-in phase noise is following the trends expected according to the phase noise of the oscillator. However, in the monostatic case there is significant suppression of phase noise resulting in an improvement of the expected radar performance. This causes an imbalance between the sensitivity of the monostatic and bistatic configurations and diminishing the advantages of networked radar. The methods described in this section aim to replicate the phase noise suppression in the bistatic radar by measuring and correcting for the phase error

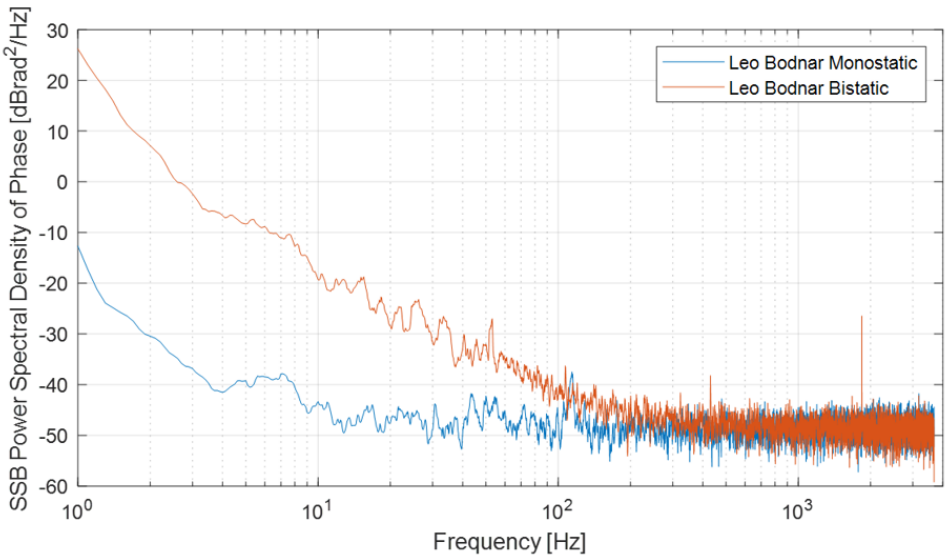

Figure 6.16: SSB Phase PSD measurement of the radars in both monostatic and bistatic configuration when using the Leo Bodnar GPSDO.

between the transmitter and receiver in digital post-processing.

A review on phase synchronization for bistatic synthetic aperture radar (BiSAR) is found in [162] consisting of the commonly used techniques to compensate phase errors. Examples of phase synchronized BiSAR systems are LuTan-1 [163] [164] [165] [166] and in TerraSAR-X [14] and in work for GNSS BiSAR [167]. For other radar types phase synchronization was achieved in a very long baseline array (VLBA) system [168], CW-MIMO [169] and FMCW MIMO [170].

Phase synchronization methods typically require either a direct line of sight, a separate reference receiver or infrastructure for a dedicated synchronization channel. In this work, the synchronization problem is addressed in the urban environment where it is not guaranteed that there is a line of sight between different nodes and there is increased dynamic range requirements due to significant clutter returns. The general idea behind the proposed method is to utilize the other reference sources in the environment (such as high rise buildings) to obtain a more accurate estimation of the phase error between the two LOs. Both radars are equipped with low cost GPSDOs and a novel phase error estimation method is applied. The proposed method, termed multiple reference phase correction (MRPC), utilizes multiple scatterers in the environment, determines which are suitable for use as a reference and then computes the average phase

accumulated over these points, for a better estimation of the phase error.

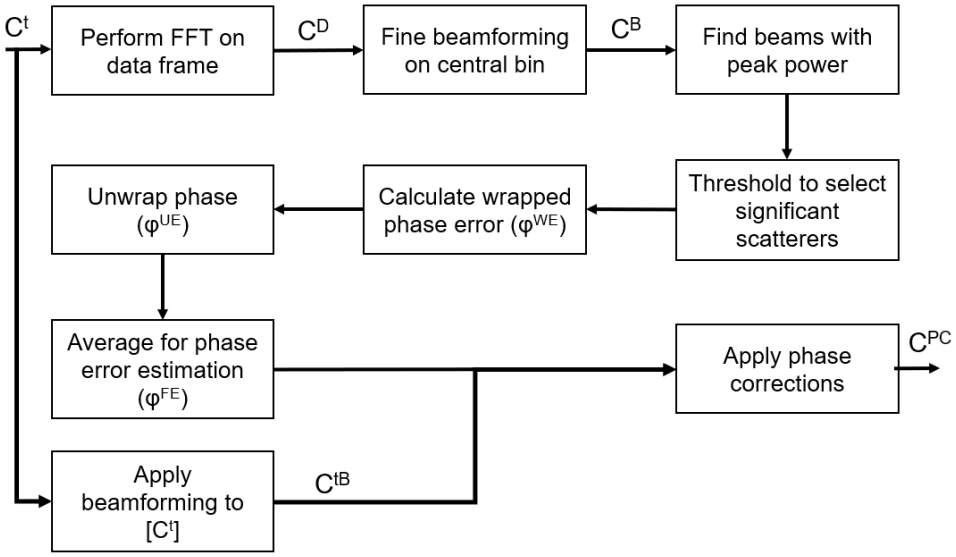

Figure 6.17: Block diagram of the MRPC scheme.

Firstly, the bistatic corrections are applied as explained in previous sections with the range profile correlation method and the frequency offset correction, if one exists [146]. The next step involves measuring the oscillator phase error. Since the two radars are using different oscillators with different random phase noise, there will be a phase difference between the two local oscillators at any given time. In a monostatic radar, there is some level of self phase noise cancellation occurring. However in the bistatic scenario, the phase error relative to the receiver will be imprinted on the transmitted signal. This can be extracted in a staring radar by recovering the phase information from the transmitted signal. The MRPC method adopts an averaged phase extraction method which utilizes the properties of the urban environment. The full block diagram is shown in Figure 6.17. In the following paragraphs, the algorithm is described and expressed in mathematical form. Variable subscripts are represented with the index of the array with the number of items in the subscript representing each dimension.

Starting with the time-channel data frame ($C^t_{h,j,k,l}$) this is transformed into the spectral domain, via FFT, using Equation. 6.9 resulting in the Doppler-channel data frame ($C^D_{h,j,k,m}$). The dimensions h, j, k, l and m represent the channel rows, channel columns, range gates, pulse number and Doppler frequency index respectively.

$$C^{D}_{h,j,k,m} = \sum_{l=1:L} C^{t}_{h,j,k,l} e^{\frac{i2\pi lm}{L}} \tag{6.9}$$

For each range gate, fine beamforming on the central clutter bin is performed to calculate the azimuth and elevation angle containing the highest clutter return and the maximum received power is stored. Equation. 6.10 - 6.12 are used to calculate the beam weights matrix ($\phi^{B}_{h,j}$) for a beam angle of $[\theta^{az}\theta^{el}]$. The variables d and λ represent the element spacing and wavelength of the transmitted signal respectively in units of meters. ϕ^{c}_{h} and ϕ^{r}_{j} are the beam weight components for the columns and rows. H and J are the total number of column and row elements present.

$$\phi^{c}_{h} = (2h - H - 1)cos(\theta^{az})\frac{-\pi d}{\lambda} \tag{6.10}$$

$$\phi^{r}_{j} = (2j - J - 1)cos(\theta^{el})\frac{-\pi d}{\lambda} \tag{6.11}$$

$$\phi^{B}_{h,j} = \phi^{r}_{j} \text{`} \phi^{c}_{h} \tag{6.12}$$

The beam weights are the applied using Equation. 6.13, resulting in the beam-Doppler data frame for all angles ($C^{B}_{\theta^{az}_{p},\theta^{el}_{q},k}$) at the central Doppler bin.

for $m = \frac{M}{2} + 1$:

$$C^{B}_{\theta^{az}_{p},\theta^{el}_{q},k} = \sum_{h=1:H} \sum_{j=1:J} \phi^{B}_{\theta^{az}_{p},\theta^{el}_{q},h,j,k,m} C^{D}_{h,j,k,m} \tag{6.13}$$

The peak power of the beams for each range index P_k are calculated in Equation. 6.14 and their respective beam numbers in Equation. 6.15.

$$P_k = max_{\theta^{az}_{p},\theta^{el}_{q}}(C^{B}_{\theta^{az}_{p},\theta^{el}_{q},k}) \tag{6.14}$$

$$P\theta^{az}_{k}, P\theta^{el}_{k} = argmax_{\theta^{az}_{p},\theta^{el}_{q}}(C^{B}_{\theta^{az}_{p},\theta^{el}_{q},k}) \tag{6.15}$$

Next the power is scaled with the bistatic range (R_k) and then a threshold (ϵ^{T}) is applied to the clutter-range profile in Equation. 6.16 with beam weights ($\phi^{B}_{h,j,k,l}$) generated according to azimuth angles ($P\theta^{az}_{k}$) and elevation angles ($P\theta^{el}_{k}$). The result is the time-beam data frame ($C^{tB}_{kT,l}$) at the range gates containing significant clutter to noise ratio (CNR) (k_T).

for $\frac{P_k}{R_k^4} > \epsilon^T$:

$$C^{tB}_{k_T,l} = \sum_{h=1:H} \sum_{j=1:J} \phi^B_{h,j,k_T,l} C^t_{h,j,k_T,l} \tag{6.16}$$

This determines the locations containing the strongest sources of stationary clutter as shown in Figure 6.18. The threshold was chosen empirically to filter out weaker reference sources. In principle, this step determines the quality of the reference source with respect to its ability to provide accurate phase information. In this work, the scaled clutter power is used to quantify this property since larger clutter returns generally relate to large structures. The range scaling is approximated with the fourth power as this has not been measured. The approximation is appropriate as this is only used to determine which clutter source to use. Otherwise, the data frame is left unscaled. The in-phase quadrature (IQ) time series data for the respective range gates are then beamformed in the direction of the maximum clutter.

For each of the range gates that were marked as crossing the threshold, the wrapped phase error ($\phi^{WE}_{k^T,l}$) is extracted using Equation. 6.17

$$\phi^{WE}_{k^T,l} = atan2(Re(C^{tB}_{k_T,l}), Im(C^{tB}_{k_T,l})) \tag{6.17}$$

The phase progression is maintained without discontinuities by performing phase unwrapping ($\phi^{UE}_{k_T,l}$). The algorithm will analyse the trend of the data and apply a shift if the phase drifts outside of the 2π region.

Then the final averaged phase error (ϕ^{FE}_l) is calculated by averaging in the range dimension using Equation. 6.18 essentially, reducing uncertainty using multiple measurement of phase.

$$\phi^{FE}_l = \frac{1}{N} \sum_{k_T=1:N} \phi^{UE}_{k_T,l} \tag{6.18}$$

It is the case that there are multiple potential sources of phase error. This estimated phase mainly contains the phase contribution from the oscillator instability and added noise from other radar hardware components. Ideally each of the extracted phase error profiles would be identical but there are some additional noise sources that are uncompensated. One such source is high frequency aliased noise which would not be common among different range gates. Also,

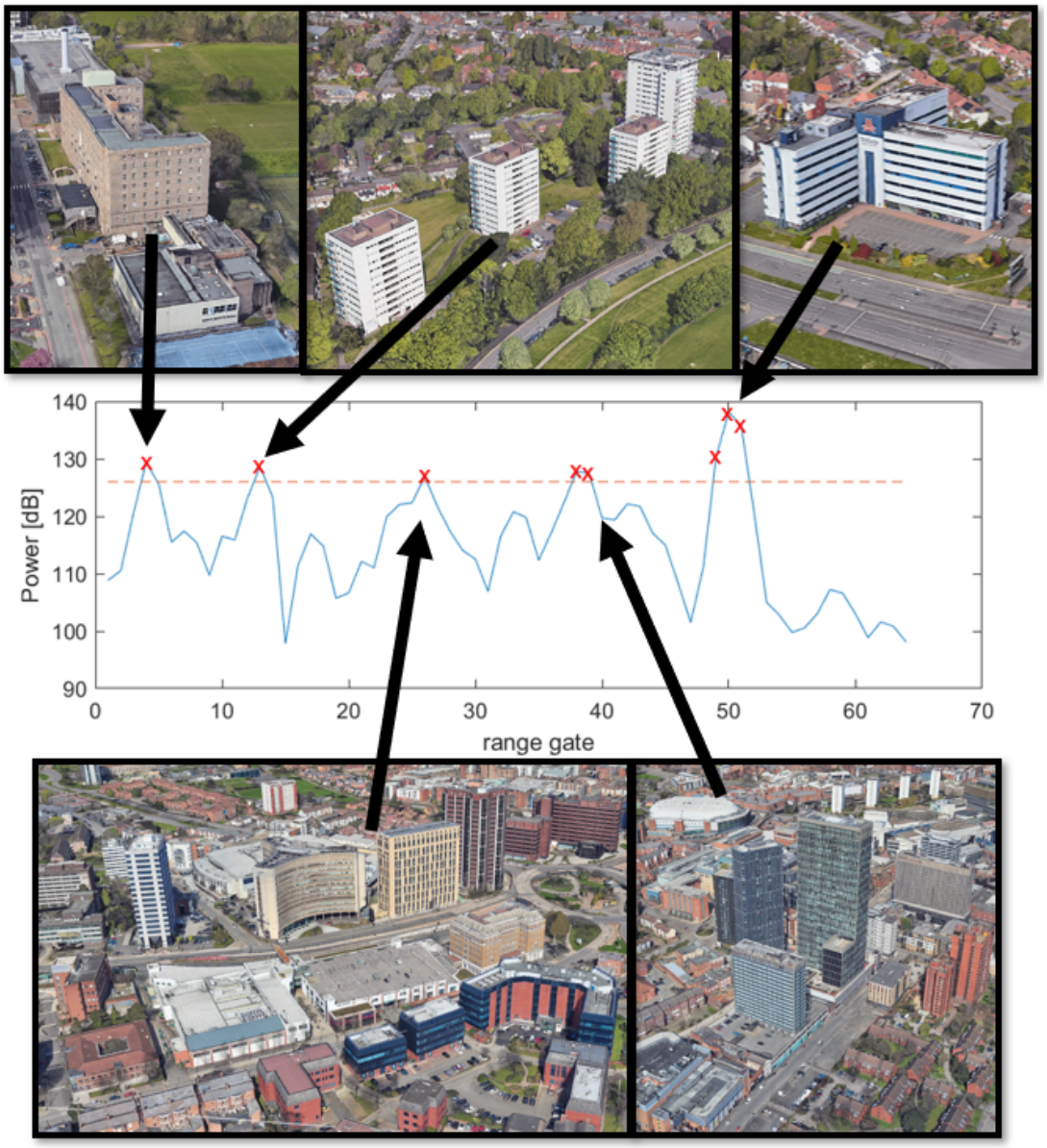

Figure 6.18: Scaled clutter power for each range gates with a threshold applied with a photo of each of the significant clutter contributions (Google maps).

other sources in the resolution cell will contribute to localised phase differences. Another is atmospheric phase fluctuations but these are not expected to be significant in this system due to the lower frequency, elevation angles and ranges involved.

Now that the phase information has been extracted, this phase shift is applied to the rest of the data frame. The data is beamformed in the desired direction (θ_a, θ_e) and then the phase shift is applied in the pulse dimension using Equation. 6.19 resulting in the beam-time, phase corrected data frame $(C^{PC}_{\theta_a,\theta_e,k,l})$.

$$C^{PC}_{\theta_a,\theta_e,k,l} = C^{tB}_{\theta_a,\theta_e,k,l} e^{-i\phi_l^{FE}} \tag{6.19}$$

The phase corrected data frame now contains significantly reduced sub-CPI phase drifts and fluctuations and can be used in subsequent processing for detections or generating spectrograms. This MRPC method is used on simulated data and the results are shown in Appendix C. The results are shown when using the MRPC method on data from Leo Bodnar GPSDO radar experiments. The two data sets used within this work are the night-time measurements from 2023-10-10_Uob_Trial43 M01 and the controlled drone measurements from 2023-10-12_Uob_Trial44 M01. In both of these experiments, GK007 operated as the transmitter and GK000 as the bistatic receiver node. Both radars contained the same model oscillator, the Leo Bodnar GPSDO to apply the frequency synchronization.

The crucial requirement for this synchronization scheme to function is that the phase error between the radars is successfully extracted. This is achieved using the methods described previously, by extracting the IQ time series data from the direct signal as well as three dominant clutter sources in the field of view. All 4 sets of phase data were extracted using the same sequence of data frames but a different beam is formed corresponding to a different reference source, and is shown in Figure 6.19a. If this method is successfully extracting the phase error between the nodes, the resultant phase accumulation from each of the sources should be correlated. It is shown that there is no observed change in the phase accumulation from the measurement of the three clutter sources. Whereas, there is some divergence observed in the phase measured in the direct signal. Several factors are involved concerning the ability to accurately extract the phase error from a clutter source, the main factor being the power of the clutter compared to the noise level of that from other targets in the region. Also, it is seen that from sample to sample the phase difference is minimal, enabling smooth phase unwrapping.

Also, from stationary manmade structures in an urban environment, the variance of the clutter power is expected to be low as shown in previous work [9]. In the case of the direct breakthrough signal, there are also multipath effects involved. Due to the positioning and the orientation of the radars, the direct signal appears in a sidelobe which could amplify this effect.

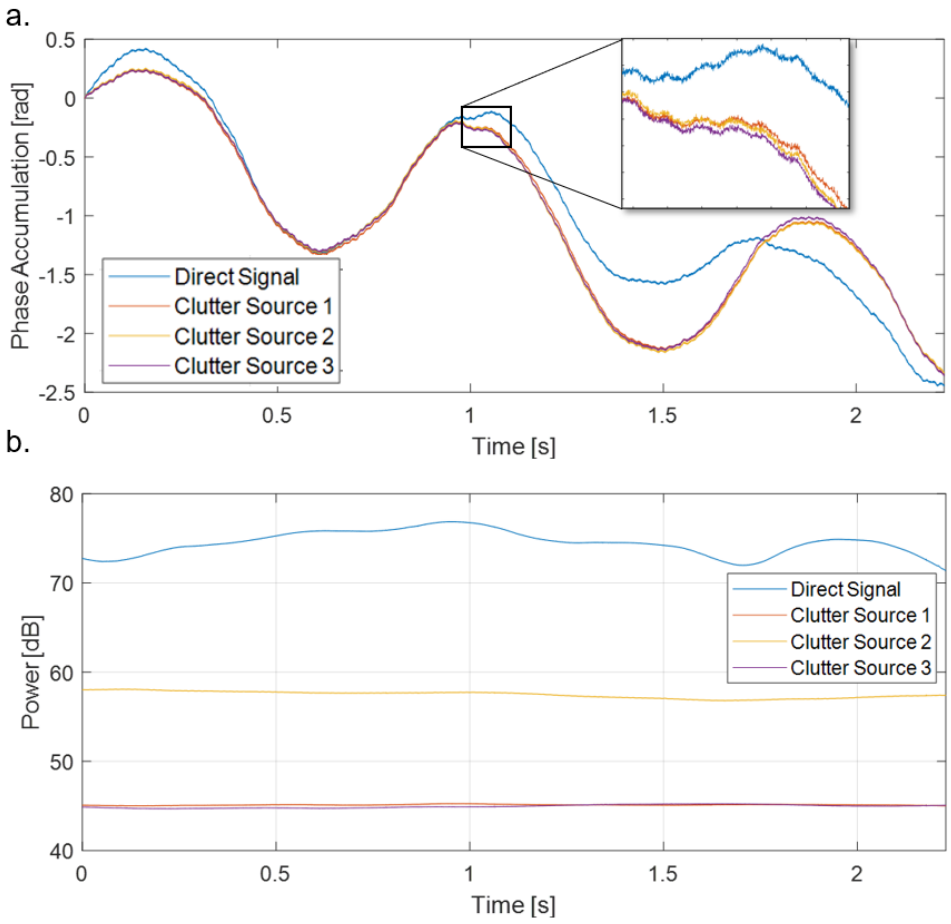

Figure 6.19: (a) Extracted phase error measured from multiple clutter sources and the direct breakthrough signal. (inset: zoomed in segment), (b) Pulse to pulse power measured in the resolution cell of multiple clutter sources and the direct signal.

The power variation of the three clutter sources as well as of the direct breakthrough signal is measured for each pulse over an interval of 2.2 s and compared in Figure 6.19b. Although the direct signal power is over an order of magnitude higher, the variation of the received power is significantly higher compared to that of the clutter sources. Overall this shows that in this system, it is more effective to use the clutter sources as a means of phase estimation rather than the direct breakthrough sources due to the high levels of multipath.

This would not also be a more robust method in this case because of the number of clutter sources to choose from; but also, allows for even better estimation of the phase by averaging together the unwrapped phase from multiple clutter sources measured simultaneously. The approach used here to observe the effect of averaging multiple clutter sources is to measure the SSB phase PSD for various cases. Both before and after applying the phase corrections to the

rest of the data frame and also when using a single source for phase estimation compared to averaging multiple sources and the results are shown in Figure 6.20 & 6.21 respectively.

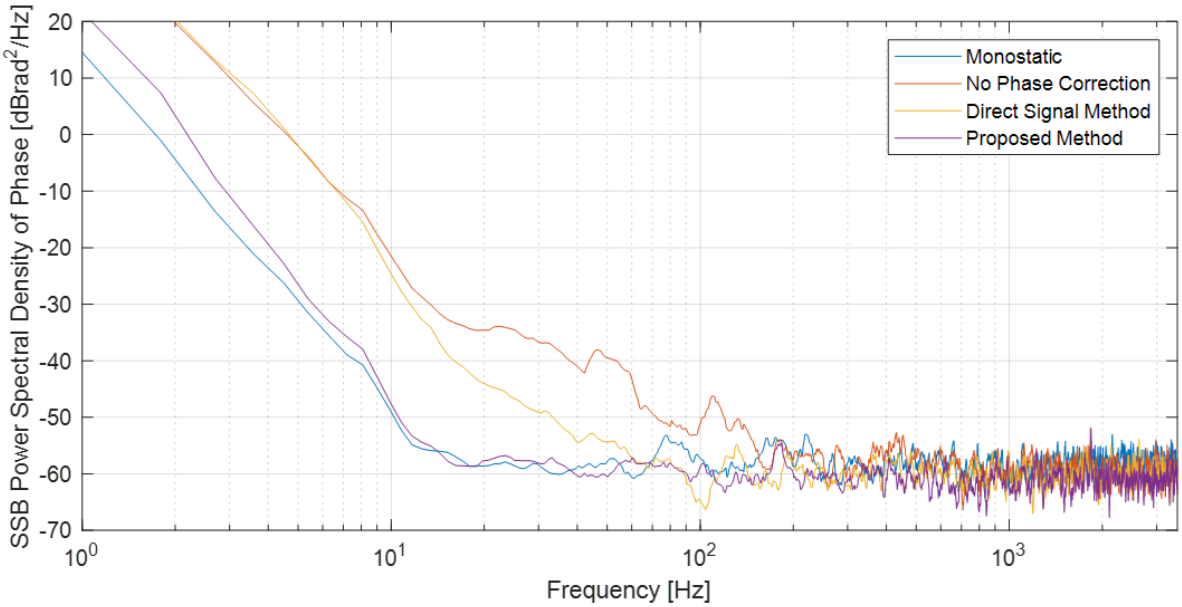

Figure 6.20: Compared SSB phase PSD calculated from the unwrapped phase for the monostatic case, bistatic case before applying phase corrections, using the direct signal method and using the MRPC method.

This method of estimating phase can be more robust for environments with a number of large clutter sources. Also, it can allow for a even better estimation of the phase by averaging together the unwrapped phase from multiple clutter sources measured simultaneously. The approach used here to observe the effect of averaging multiple clutter sources is to measure the SSB phase PSD for various cases. In Figure 6.20 the SSB Phase PSD is compared before adding any phase corrections, using only the direct signal for phase estimation and then using the MRPC method.

The SSB phase PSD is calculated using the methods shown in Appendix A. The results show the effect of the self phase cancellation effect in the monostatic radar where the lower frequency phase fluctuations are common on both the transmitter and receiver resulting in a suppression of the phase noise. By attempting to replicate this effect using the direct signal method it is shown that the phase noise is reduced but this is not able to reach the same as the monostatic case. However, the MRPC method is successfully able to bring down the phase PSD to the monostatic level resulting in a successful cancellation of the phase noise below 200 Hz. Noise beyond this

consists of mostly aliased noise which remains uncompensated.

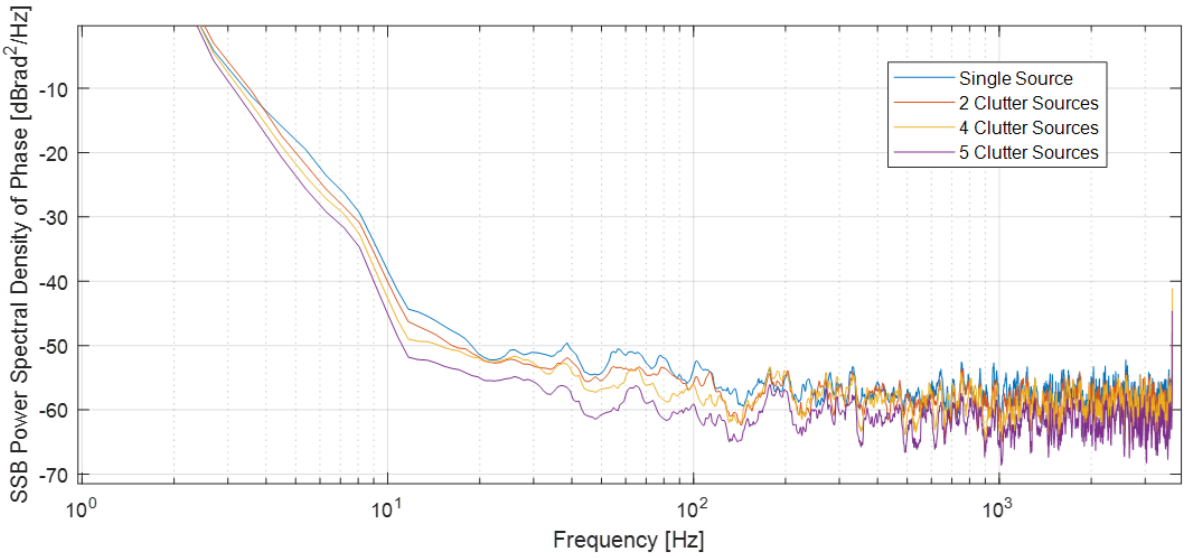

Figure 6.21: Compared the SSB phase PSD when using a single clutter source for phase estimation to using multiple clutter sources.

Figure 6.21 shows that the level of noise suppression can be increased by using multiple clutter sources in the phase estimation stage. Firstly, only a single reference clutter source is used. Similar to the direct signal method but a high CNR building is used. Then the SSB phase PSD is computed when averaging together the phase extracted from increasing numbers of reference targets. This can be useful when operating in an environment with many clutter sources as the estimation of the phase can be improved by averaging out errors from uncorrelated noise. A drawback of using the direct signal method, or a strong clutter echo, is the effect of other targets in the same resolution cell as this will be imprinted onto the phase. Therefore, cancelling this phase will also remove the target from the data. In addition, if a moving targets phase contribution is also included in the phase error estimation, this will print into the other cells and will result in additional false targets. These negative effects originating from a target in the same cell can also be reduced by using multiple clutter sources to average the phase since phase error due to oscillator instability is common between different cells whereas phase error due to moving targets remains uncorrelated.

Next, phase error is observed over longer periods and then converted into respective time and range error. Timing error accumulated over a 140 s period is shown in Figure 6.22. Without

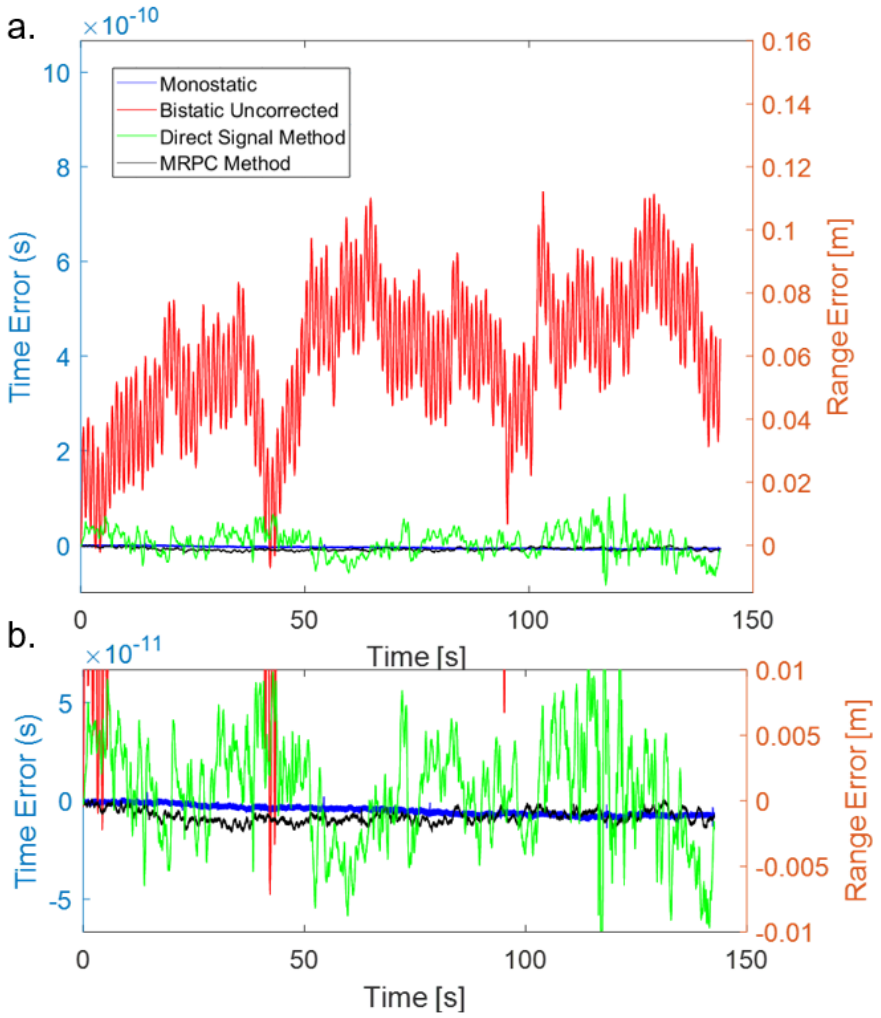

Figure 6.22: (a) Time error and range error due to accumulated phase error before phase synchronization, using the direct signal to correct the phase and the MRPC method. (b) Zoomed in version.

applying phase corrections to the bistatic data, the Leo Bodnar starts to gradually attain time error with a random walk like behaviour. On shorter time scales there are oscillations which are a characteristic of this oscillator which result in faster accumulation of positive and negative time error. Using the direct signal in the phase estimation reduces the timing error by an order of magnitude while using the proposed method reduces this even further. As seen in Table. 6.4, the phase synchronization accuracy for the 140 s period is measured to be 338.9, 48.9 and 7.2 degrees for the no synchronization method, direct signal method and the MRPC method respectively. For the phase error of 7.2 degrees obtained using the MRPC method, this corresponds to a time error of 16 ps and a bistatic range error of only 4 mm. When comparing

with the phase error measured from the monostatic node in Figure 6.22b, the phase corrections successfully reduce the errors to a similar level.

Table 6.4: Synchronization accuracy results determined from the maximum error observed over 140s.

Synchronization Method	**Phase Error [deg]**	**Time Error [ns]**	**Bistatic Range Error [m]**
No Correction	338.9	0.750	0.226
Direct Signal	48.9	0.108	0.032
MRPC	7.20	0.016	0.004

One consequence of the lack of phase synchronization is a reduction in the coherent integration gain as target power is spread into adjacent Doppler cells due to sub CPI frequency changes in the oscillator. The CNR of a large stationary target is measured for increasing CPI lengths from 0.1 s to 60 s. The CNR of the target is shown in Figure 6.23a and the coherent integration loss is shown in Figure 6.23b. The target is a building (Trigate) located around 4 km away from each of the radar nodes (close to the edge of the radars instrumented range), and therefore should include increased loss of coherence at longer distances.

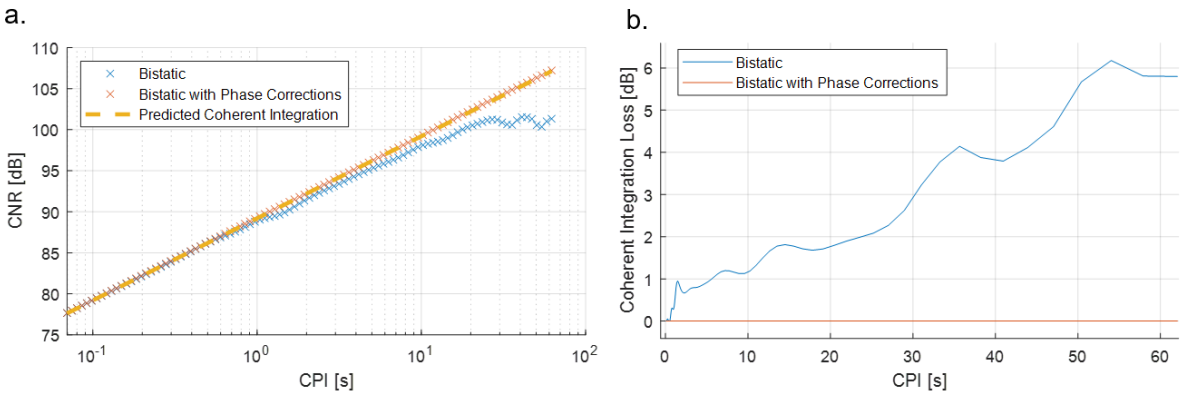

Figure 6.23: (a) CNR measured over increasing CPI lengths, (b) Coherent integration loss before and after phase corrections are applied.

When using the GPSDOs in the bistatic configuration there is a small but steadily increasing coherent integration loss which reached 6dB for a CPI of 54 s. After applying the phase synchronization method, the coherent integration curve does not deviate from the predicted integration gain. Therefore, negligible coherent integration loss has been achieved using the proposed method, for CPIs up to 60 s, which is much higher than what is typically used in the applications targeted by this radar system.

As discussed previously, the effect of phase noise in urban environments is a major concern for radar systems when it comes to detection of low RCS, low altitude or slow moving targets as the target signature can be masked by the raised noise floor due to high clutter power and oscillator phase noise. The next set of analysis involves focusing on a particular clutter source (the same cell used to inspect the coherent integration loss) where the phase noise is known to be far greater than the thermal noise floor. Consecutive spectral data sets of 2 s CPI are averaged over a duration of 2.5 mins. This suppresses other targets that may be in the scene and exposes the actual noise floor whether it has hit the thermal noise floor or is phase noise limited. The background noise floor in the selected region is shown in Figure 6.24a for the monostatic radar, bistatic before corrections and the bistatic radar after corrections. The absolute power of the clutter in the selected region is different in the monostatic and bistatic case due to the geometry, therefore, the power relative to clutter for the positive frequencies is shown in Figure 6.24.

A similar trend is shown as to what is seen in the phase PSD data where the noise floor is raised in the bistatic data set due to the lack of self phase cancellation in the bistatic radar. Using the phase synchronization method, the phase noise is reduced to the same level as the monostatic result in the frequency region of interest between 10 Hz and 90 Hz. This demonstrates a real and significant reduction of the noise floor of the bistatic radar and an increase in the overall sensitivity of the radar in urban environments. At 10 Hz offset frequency the noise floor is reduced by 20 dB allowing for detection of targets with significantly lower RCS. In addition, the significant spur shown at 50 Hz is a characteristic of the oscillator and has been suppressed by approximately 35 dB since this is a common feature imprinted into the entire data.

Both the bistatic pre-corrections and post-corrections data are shown using the same data set while the monostatic data is taken from a time period approximately 50 mins later where GK000 is operating as a monostatic radar with the same oscillator configuration. The spectrograms of the Trigate building throughout the data set used to generate the background spectrum are shown in Figure 6.25. The noise suppression and removal of the spur are seen in Figure 6.25b. However, the spurs at 30Hz and 60 Hz still remain. This is believed to be an anomalous effect from the radar system that is not fully understood but since it is not a consistent feature in the

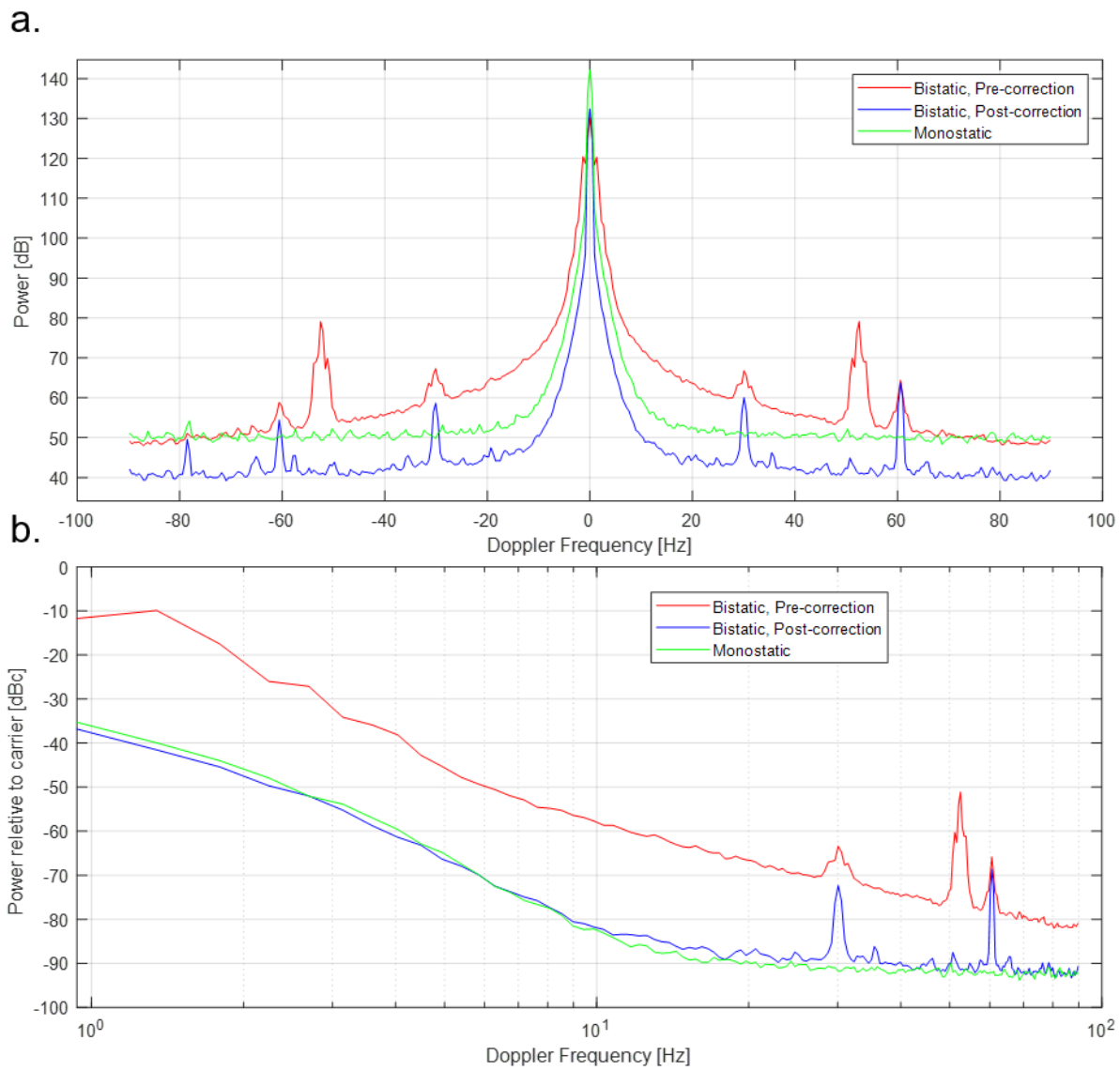

Figure 6.24: (a) Background noise level comparison at a selected high clutter region for Doppler frequencies between -90 and 90 Hz. (b) Background noise power relative to carrier.

data set, this suggests why it would remain after phase corrections are applied.

This section now examines the effect of noise suppression on target detection. Part of the radar measurements involved controlled drone flights where the DJI Inspire 2 was flown through pre-determined waypoints while the radars recorded in a bistatic configuration. This section examines the target spectrograms. Also, improvement in the detection performance using the proposed phase synchronization scheme in comparison with standard processing is analysed.

A single CPI containing the drone target is processed into a range-Doppler plot via beam-forming and FFT. The resultant range-Doppler plots for the original data and the phase corrected

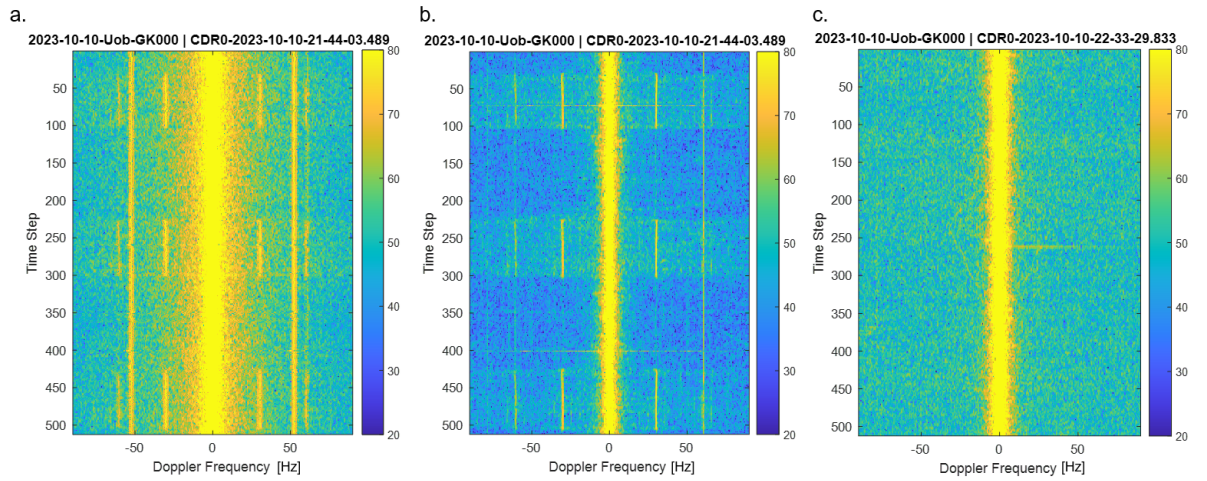

Figure 6.25: Spectrograms of the high clutter region (a) bistatic before corrections, (b) bistatic after using MRPC, (c) monostatic.

data are shown in Figure 6.26. In each plot, the drone appears in range gate 13 at a Doppler frequency of 58 Hz. After frequency correction, the clutter is now focused into the central Doppler bin and therefore improving sub-clutter visibility. The same effect can be seen in some of the moving targets. The time interval was chosen so that the drone target had a constant velocity throughout the entire CPI as is seen in the drones GPS truth logs.

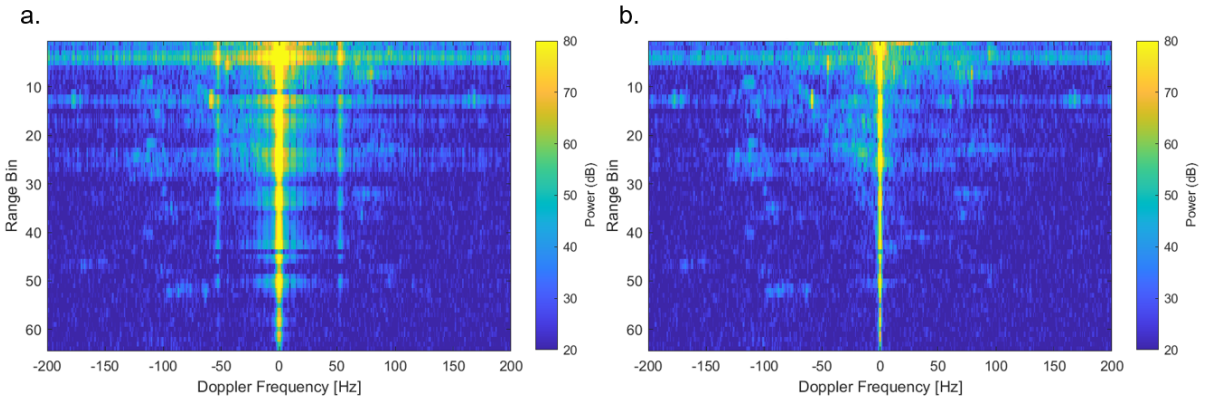

Figure 6.26: Range-Doppler plot of a 2 s CPI containing the drone target moving at a constant velocity. (a) without phase corrections, (b) with phase corrections applied.

Only one out of the eight flights is shown here for a more detailed comparison. The spectrograms of the drone target flying at an altitude of 80 m in the clockwise variant of the Richmond scenario is shown in Figure 6.27, with a reduced CPI length of 0.5 s.

Since the drone has a relatively high RCS, it is already very prominent in the original bistatic

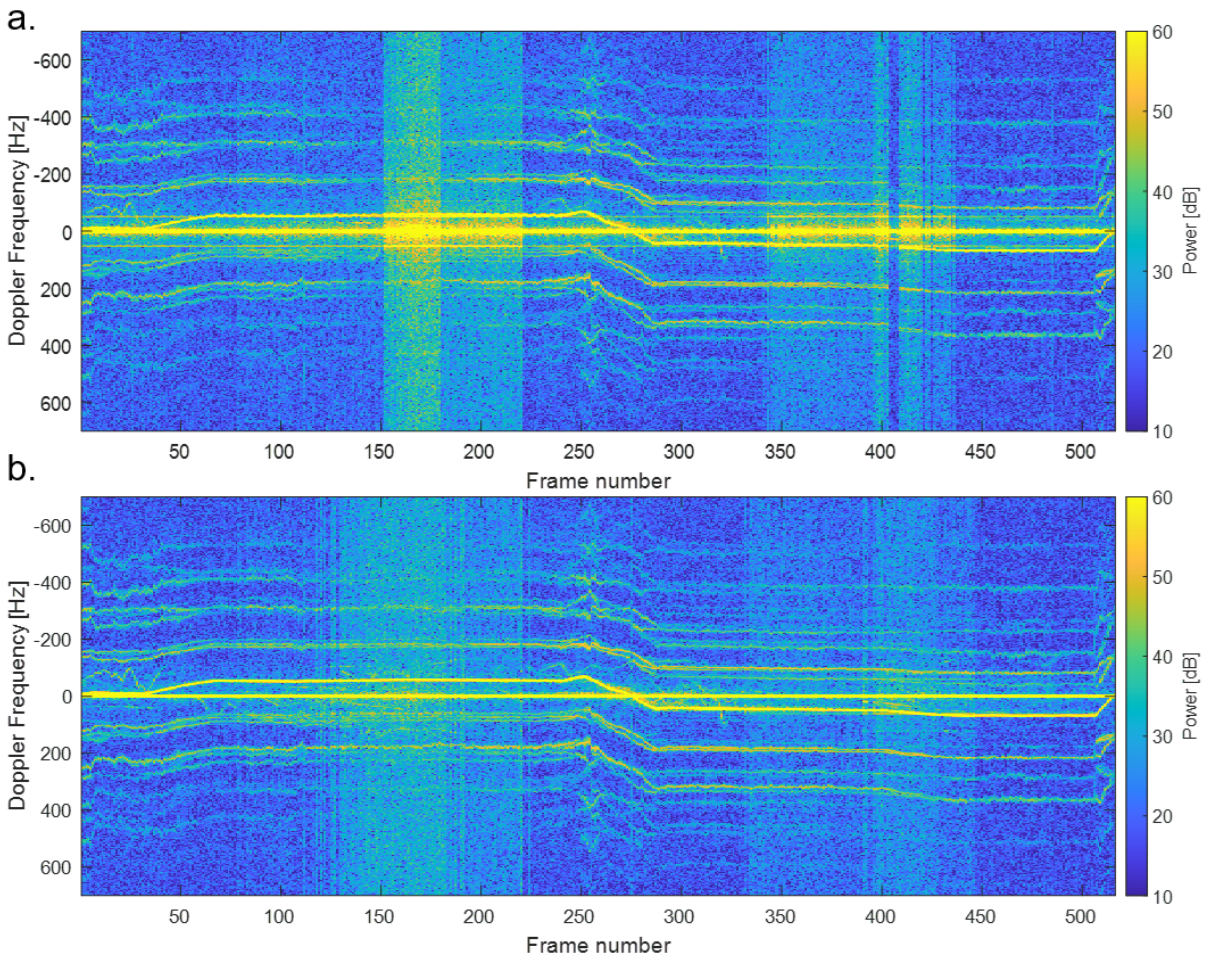

Figure 6.27: Target Spectrogram of DJI Inspire 2 for an entire flight through using Richmond scenario. (a) without phase corrections, (b) with phase corrections applied.

spectrogram but there are particular segments in the flight where the drone enters a cell with high clutter power. In these regions, the clutter appears to spread out into adjacent Doppler bins and raises the noise floor even in the far out frequencies. The effective SNR is then reduced at these stages of the flight, potentially resulting in missed detections and breaking up of the track. It is shown that after the MRPC method is applied, there is a significant reduction in the close in phase noise resulting in a more well resolved spectrogram. Another observation is that the drone micro-Doppler is also better defined in those regions which benefits the classification of drones. The spur at 50 Hz is also seen to be removed. In Figure 6.28a, b a zoomed in version of the spectrogram is shown along with the detections.

In Figure 6.28a the clutter is seen to be moving slightly, in the Doppler frequency dimension, from one CPI to the next in an oscillatory fashion as a consequence of the oscillatory behaviour

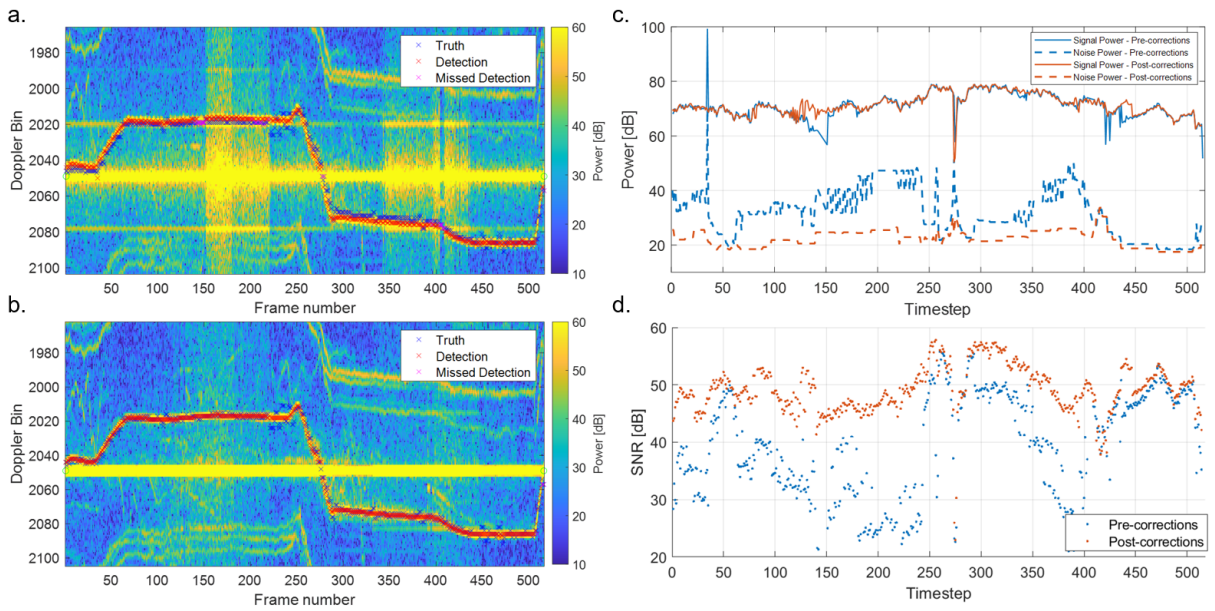

Figure 6.28: (a) Zoomed in target spectrograms with truth and detections without phase corrections, (b) with MRPC applied, (c) Signal power and noise power comparison, (d) Comparison of SNR measurement throughout the flight.

of the phase error. The MRPC method successfully stabilizes this and therefore, the velocity error is reduced and the clutter is focused into the central Doppler bin. In addition to this, the suppression of the spur as discussed previously is obvious in the spectrograms. In this flight, the velocity of the drone in the first straight, is matching that of the spur, falling into the same resolution cell and therefore, resulting in several consecutive missed detections. The spur suppression results in ensuring consistent detection throughout the entirety of the straight.

The signal and noise power throughout the drone flight are analysed in Figure 6.28c where the noise power is determined by the time averaged power in that particular range and Doppler cell over a period of 2.5 minutes. Therefore the high noise power in particular regions of the pre-correction data is due to a combination of the increased phase noise and the spurs in the signal since the noise is calculated from historical data of the same cell. The comparison of the SNR pre and post-correction is shown in Figure 6.28d. The suppression of the spur is shown to have the most significant increase in the SNR which is most notable around timestep 200-240 where SNR is increased by up to 25 dB. Since this data is taken with a relatively short CPI of 0.5 s, not much coherent integration loss (due to radar network phase incoherence) is expected. This is consistent as the signal power is mostly unchanged. However, at timesteps

130-150 the noise power change is due to the missed detections in the pre-corrected data, caused by an insufficient SNR. Therefore a different range-Doppler-angle cell is chosen during these timesteps in the pre-corrected data, so the difference in signal power here can be ignored. There are a few periods where the reduction of the phase instability resulted in a significant increase in SNR and only after applying phase corrections is the target clearly separated from the stationary clutter. One is at timesteps 290-330 where the drone velocity is not matching the spur but the noise in this region is successfully suppressed resulting in up to 8 dB increase in measured SNR. The greatest improvement however is observed for targets with very slow range rate as is shown in timesteps 0-35 where the target trajectory is almost perpendicular resulting in low Doppler frequency. Here the suppression of the noise is much greater resulting in over 10 dB increase in SNR.

Table 6.5: Comparison of the average SNR throughout each flight before and after applying the phase corrections. F - Forward, R- Reverse

Flight Description	**Pre-correction Avg scaled SNR [dB]**	**Post-correction Avg scaled SNR [dB]**	**SNR Gain [dB]**
GK000, 100m, F	45.19	48.62	3.43
GK000, 100m, R	43.47	47.32	3.85
GK000, 80m, F	43.64	47.19	3.55
GK000, 80m, R	42.40	46.25	3.85
GK007, 100m, F	42.03	45.70	3.67
GK007, 100m, R	39.65	46.16	6.51
GK007, 80m, F	41.71	46.81	5.10
GK007, 80m, R	38.93	45.60	6.67
Average of flights	**42.54**	**46.81**	**4.77**

While the detailed plots are shown for this one particular flight, the quantitative results for all 8 flights combined are shown in Table II where GK000 or GK007 indicates the node used as the bistatic receiver and reverse indicates that the drone flew through the waypoints in reverse order. Each of the flights uses the same CFAR parameters for consistency. For all 8 flights, an improvement in the SNR is observed between 3 dB and 7 dB and when taking the average of all flights the average SNR scaled to a constant range is 42.54 dB prior to phase corrections and 46.81 dB after corrections. Overall the results prove the effectiveness of cheap COTS oscillators

used in unison with the proposed phase synchronization methods for a drastic performance enhancement in networked radar systems.

This work shows that it is possible to synchronize staring radar networks using post-processing and presents a novel method that is able to reach a level of phase noise suppression matching what is achieved in the monostatic radar. Over a period of 140 s a phase synchronization accuracy within 0.02 degrees has been achieved which is on the same order of magnitude as measured from the monostatic radar. In cluttered urban environments the phase noise at 10 Hz offset has been demonstrated to be suppressed by 20 dB and the method has been used for detecting a real target with observed enhancement of the SNR on a consistent basis. Overall this method is proven to be a simple and low cost solution to achieving high levels of synchronization for radar networks operating in the urban environment when paired with cheap low cost GPSDOs. Future work can involve utilizing the full advantage of network systems where data fusion concepts can realise the full potential of coherent multistatic network systems.

6.3 Discussion

The MRPC method completes the framework for a fully synchronized networked radar utilizing the urban environment, the concept is seen in Figure 6.29. Time synchronization is achieved using the range profile correlation method to align the range dimension using landmarks in the line of sight (LOS). The frequency synchronization is achieved using a disciplined oscillator to minimize the frequency offset and therefore the range drift.

These methods exploit the feature of multiple scatterers within the urban scene for measurement of the PRI offset and for correcting phase errors on a pulse by pulse basis. Various benefits can be seen with these methods, including that there is no requirement for a separate reference channel or synchronization protocol. Also, a direct line of sight between the transmitter and receiver in principle is not required if there are other features in the environment that can be used as a replacement. In addition, with the use of cheap COTS oscillators with significant phase noise, full phase coherence for maximum coherent integration gain of the bistatic radar is

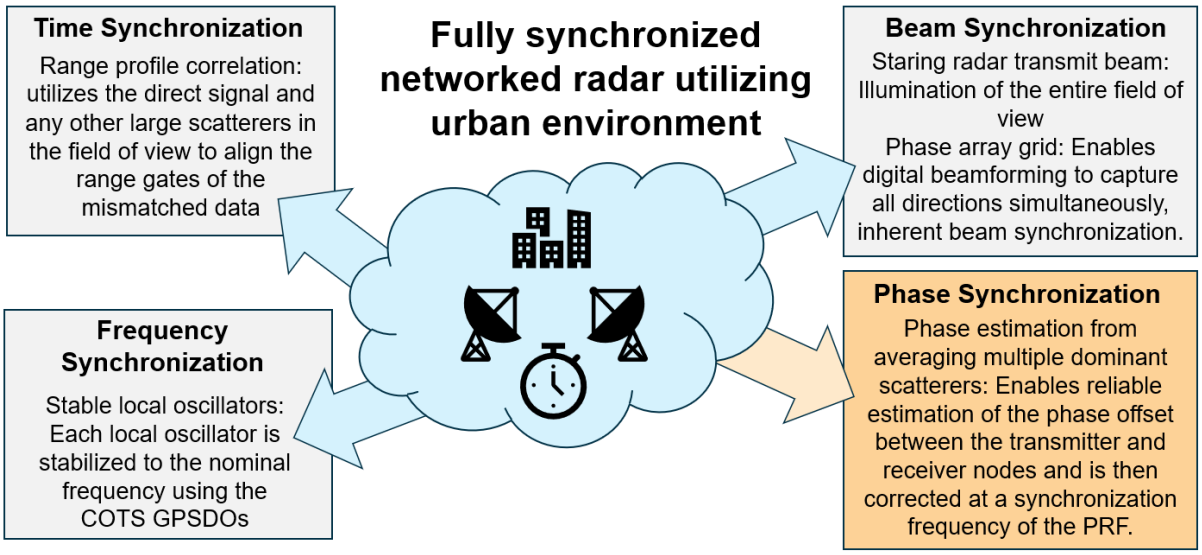

Figure 6.29: Concept for synchronization of a networked radar in an urban environment.

achieved up to a 60 s CPI.

There are some limitations however, as this is dependant on the urban scene. In more rural environments or at sea, application of this method may be limited. For the range profile correlation, significant landmarks in the data are used to align the data. If there are no substantial clutter sources then it would continue to function as it can rely on other effects such as the transition between thermal noise and the breakthrough signal. For a different transmitter - receiver combination, a new RPR is required and this includes if the position of the radars change. Therefore, the method assumes static radar systems and would not function optimally if either of the radar nodes are moving. This is due to the change in the geometry and a new RPR would need to be generated. The phase correction method is also reliant on multiple reference sources, more sources is expected to result in better suppression of phase noise. A few other limitations include that high frequency noise remains unsuppressed due to the synchronization interval being fundamentally limited to the PRF, since it is a digital signal processing technique. Also, it is assumed that each of the reference sources are pure, if there is a strong moving target present in the same cell, this will be imprinted onto the phase error estimation. The use of multiple sources can aid in averaging out the external effects such as these, but can be a problem when there are very few reference sources and they are corrupted by targets in the region. This

would result in additional frequencies being imprinted onto the entire data set; therefore, for a full implementation, precautions need to be put in place to prevent this.

With this in mind, to improve the radar performance further and push through some of the current limitations such as potential lack of reference targets or the synchronization interval limitation, the only way to proceed is to improve the oscillators used in radar systems. The implementation of higher quality, spectrally pure and stable oscillators are discussed in the next chapter along with radar experiments.

Chapter 7

Networked Radar: Synchronization Using Ultra Stable Oscillators

This chapter describes the work undertaken throughout the duration of this thesis, considering disciplined or stable oscillators for the synchronization of the L-Band staring radar network at the University of Birmingham. The first section details the experiments with different GPSDOs, which was performed in collaboration with researchers at University College London (UCL) [30], who have developed the RadSync unit and was delivered to Birmingham for testing on the radar network. The second section describes the work on using state of the art photonic oscillators for radar synchronization and represents the current progress on the development of the QER project. The use of a novel method utilizing microwave photonic and common mode cavity distribution is described and characterized within the radar network. Finally, a reflection on the current status, what is learned from this work and how it can be used to develop future radar and sensor networks is discussed.

Since this chapter is focused on the use of stable oscillators, measurements of oscillator instability are presented throughout. Additional details about each of the frequency instability measurements and how they are performed are detailed in Appendix B. In addition, measurements of the radar system using ultra-stable oscillators in the monostatic configuration are presented in Appendix D.

7.1 GNSS Disciplined Radar Systems

This section consists of work from the unpublished paper, currently in preparation at the moment of writing, "Synchronization Performance of L-Band Staring Radar with Different GPSDOs". This was a collaborative work with the radar sensing group at UCL where my role is in the data collection, processing and analysis, using software developed in Chapter 6. The development of the RadSync is the work of the UCL researchers and is detailed further in [30] [154]. This section contains text and figures that are reused from the paper.

The aims of this work presented in this section are to successfully synchronize the L-band staring radar network with the use of GPSDOs and to evaluate radar performance. The use of different qualities of oscillator are also examined, where lower phase noise can be combined with the GNSS reference.

Typical methods of synchronization include direct RF link synchronization schemes [171], the use of the direct breakthrough signal [11] and white rabbit protocol [13]. However, more common is the use of the existing global positioning systems (GPS) infrastructure by replacing the radar local oscillator (LO) with GPSDOs. Other works in the literature have experimented with this method as a means of radar network synchronization [30] [29] [172].

A GPSDO combines the short-term stability from high-quality oscillators, such as those of low-phase noise oven-controlled oscillators (OCXOs), with the long-term stability of the GPS. In general, OCXOs (among other oscillators) experience phase fluctuations and frequency drifts due to environmental change and ageing processes [173]. To maintain accurate timing over long periods, a frequency reference is required. For GPSDOs, this is provided by caesium clocks based within the existing GPS infrastructure. A receiver is used to collect signals transmitted from multiple satellites within the line of sight (LOS) to obtain common timing reference. Then a control loop is able to compare the frequency error between the GPS signal and LO and steer the frequency, enhancing the long-term stability in line with GPS.

This work, looks into which characteristics of GPSDOs are important to the performance of a bistatic radar. Performance is measured in terms of synchronization accuracy and its ability to perform drone surveillance in an urban environment.

7.1.1 Oscillator-Radar Interface for GPSDO experiments

One of the GPSDOs utilized within this work is the Leo Bodnar GPSDO [161], which is a low-cost commercial off-the-shelf (COTS) oscillator. The device, shown in Figure 7.1a, consists of a temperature-controlled crystal oscillator (TCXO) and synthesizer for generating a wide range of frequency outputs and a GPS receiver input to enable the frequency lock.

The RadSync [30] [154], shown in Figure 7.1b, contains the Thunderbolt-E [174] and LNRCLOK [175] oscillators, which are shown in Figure 7.1c and Figure 7.1d respectively. The Thunderbolt-E consists of an internal OCXO while the LNRCLOK consists of an internal Rubidium based oscillator. Both of the internal oscillators have frequency tunability, such that they can be steered to the reference GPS signal. The steering and monitoring is performed within the RadSync, with more details shown in [30] [154]. Development of the RadSync was performed entirely by the UCL researchers. At the moment of writing, the approximate price per unit of the oscillators is £200, £1,000 and £7,500 for the Leo Bodnar, Thunderbolt-E and the LNRCLOK respectively.

Figure 7.1: Photographs of the GPSDOs and timing equipment. (a) Leo Bodnar GPSDO, (b) RadSync, (c) Trimble Thunderbolt-E, (d) LNRCLOK.

One of each of the oscillator types is installed into each radar cabin for use within the radar measurements. For this work the UCL RadSync system was installed at the University of Birmingham radar testbed for three weeks. This section explains the radar-oscillator interface as illustrated in the schematic in Figure 7.2.

An RF switch is included to allow for the selection of the LO input remotely. Since the output frequency of the LNRCLOK and Thunderbolt-E are at 10 MHz, they are required to undergo an upconversion to f_{LO}. This is achieved by a bespoke multiplier unit. Within the radome, the signal is then conditioned into a square pulse before undergoing a second multiplication stage to f_c via the timing and waveform generation unit (TWG).

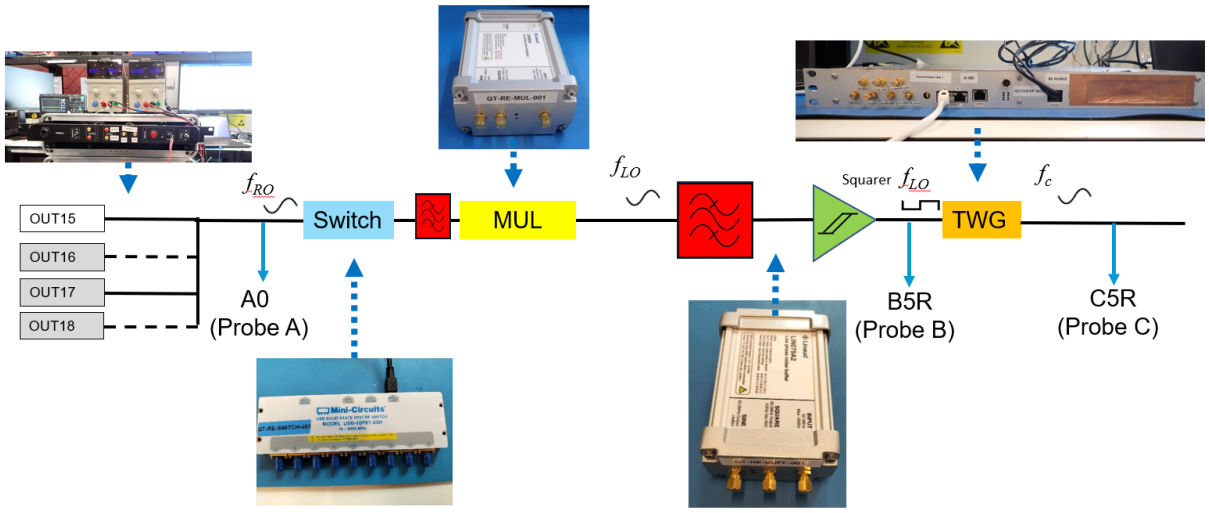

Figure 7.2: Schematic diagram of the oscillator to radar interface.

7.1.2 Oscillator Measurements

Timekeeping is crucial for the operation of the radar network and is fundamentally provided by the LO. However, different oscillators may exhibit frequency fluctuations and drifts, causing them to "tick" at different rates. Consequently, they will display different times at any given moment. Each type of oscillator is measured in the lab for its PN, using a Rohde & Schwarz FSPN [176].

The phase noise profile is measured at different stages of the RF chain, starting from the oscillator standard 10 MHz output frequency as seen in Figure 7.3a. The exception is with

the Leo Bodnar as it can directly output at f_{LO}, but it is included here for consistency. The Leo Bodnar has significantly more, low-frequency phase noise than the other oscillators with the LNRCLOK measuring more than 35 dB lower phase noise at 10 Hz offset frequency. The Thunderbolt-E performs poorest of all the oscillators at the higher offset frequencies beyond 1 kHz offset frequency and the LNRCLOK outperforms all other oscillators at all measured frequency offsets.

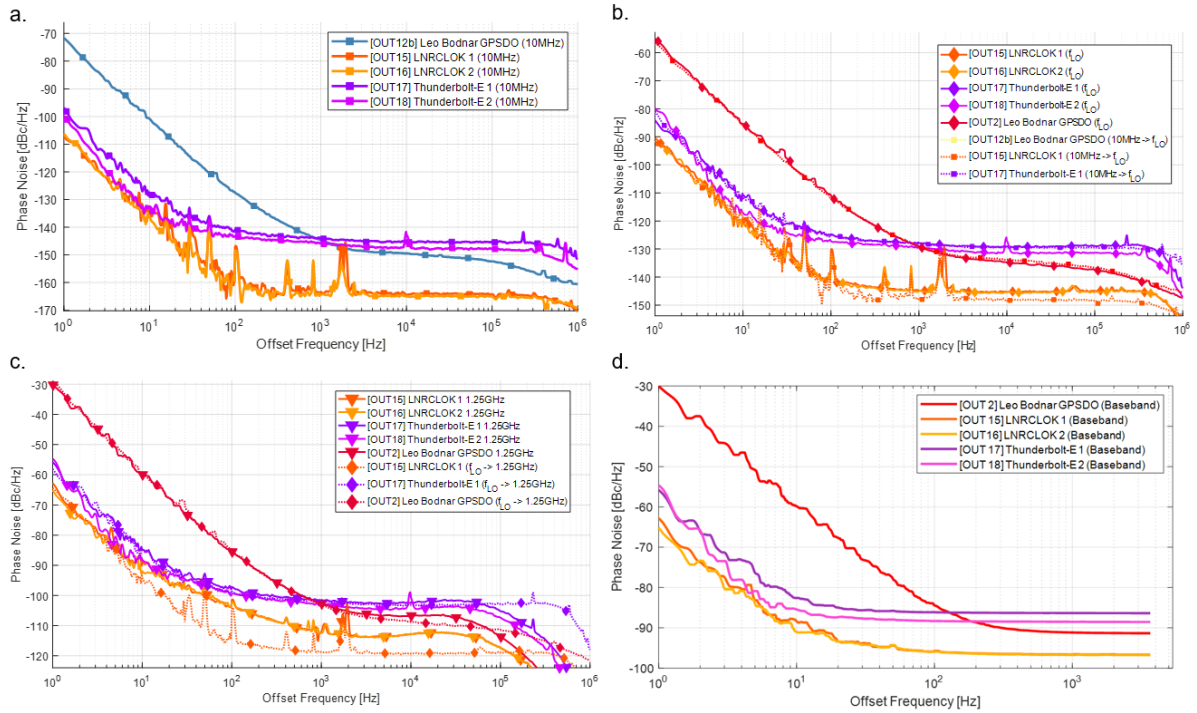

Figure 7.3: Phase noise measurements of the oscillators used within the radar experiments. (a) Oscillator outputs – 10MHz, (b) After first frequency upconversion – f_{LO} (dotted line – predicted phase noise), (c) After second frequency upconversion – 1.25GHz (dotted line – predicted phase noise), (d) Calculation of expected phase noise after PRF aliasing.

There is an upconversion stage to f_{LO} via a bespoke multiplier unit, and the phase noise is measured again in Figure 7.3b. The trends mentioned previously are maintained, but there is inherent phase noise added via the frequency upconversion. This inherent phase noise from upconversion is due to the increased sensitivity to phase fluctuations at higher frequencies for the same amount of time error. The expected additive phase noise is shown in Equation 7.1 [25], where f_1 and f_2 are the frequencies before and after upconversion respectively. However, the LNRCLOK gains an additional 4 dB of additive noise due to the multiplier unit.

$$\mathcal{L}_{additive} = 20log_{10}\frac{f_2}{f_1} \tag{7.1}$$

A second upconversion stage occurs to f_c via a phase-locked loop (PLL) and the measured phase noise is seen in Figure 7.3c. At least a 25 dB increase in phase noise is observed due to the increase in frequency. Also, the PLL synthesizer noise is contributing at the high frequencies, further raising the noise floor of the LNRCLOK, adding up to 15 dB of additive noise. This additive noise is contributed by both the buffer amplifier unit and the TWG PLL upconversion.

The pulse repetition frequency (PRF) of the radar sets a limit on the Nyquist limit and high-frequency noise will contribute at the higher frequencies. The computed folded-over phase noise due to aliasing from the 7.3 kHz PRF is shown in Figure 7.3d. Despite this, huge reductions in phase noise are achievable at lower frequencies, less than 100 Hz although effects are reduced at higher frequencies.

7.1.3 Experimental Setup

The L-band staring radars are configured in a bistatic configuration where one radar acts as a monostatic node and the other as a receive-only node, in the same way as in the experiments in Chapter 6. The radar data used within this work is exclusively from the receiver node of the bistatic system, where the contribution from both LOs is considered. The bistatic data is processed using the bistatic data corrections and range profile correlation methods discussed in Chapter 6.2.1 [146]. However, the phase correction processing is not used, such that the network is reliant on the disciplined oscillator network for maintaining synchronization. The bistatic data corrections are applied to estimate the initial timing error present between the nodes such that it can be corrected for throughout.

At any time, each radar contains the same type of GPSDO. At the end of a measurement, the radars are switched off, and the oscillator configuration for both radars is changed by reconfiguring an RF switch routed to the LO distributor before resuming the radar's operation. Each measurement consists of multiple controlled drone flights using the DJI Inspire, shown in

Figure 7.4a. The drone is configured to follow a set of pre-determined waypoints for a repeatable flight profile. The waypoints and track for the flight pattern used within the measurements are shown in Figure 7.4b.

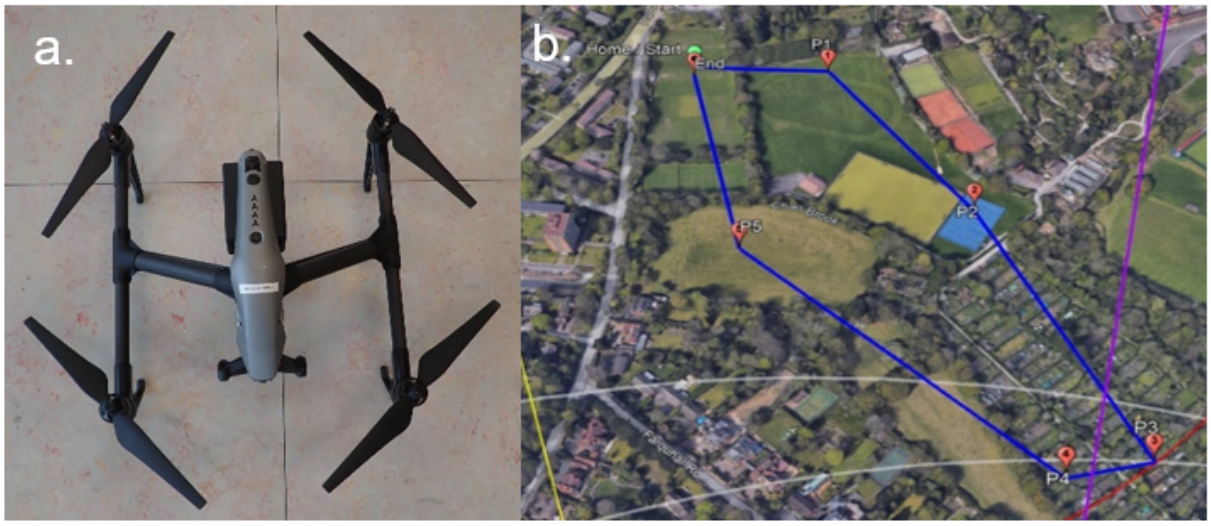

Figure 7.4: (a) DJI Inspire 3, target type used for controlled drone flights. (b) Flight path used for the experiments (Google maps).

7.1.4 Results

Time Error

The phase/time error is measured by extracting the unwrapped phase profile from a high SNR stationary target. The radars are operating at the same frequency and therefore, the direct signal ideally appears at zero Doppler frequency. Phase error is measured as a deviation of the LO in the remote node from that in the local node.

The short-term phase accumulated from the different LO configurations is shown in Figure 7.5a, where there is a visible difference between the behaviour of the LOs. The Leo Bodnar LOs exhibit oscillatory behaviour on the order of a second, suggesting the frequency is oscillating around the setpoint. Whereas LNRCLOK exhibits less frequent corrections of its frequency resulting in a smooth phase profile throughout a typical coherent processing interval (CPI). For the Thunderbolt-E, each of the frequency changes due to the steering mechanism of the GPSDO are seen.

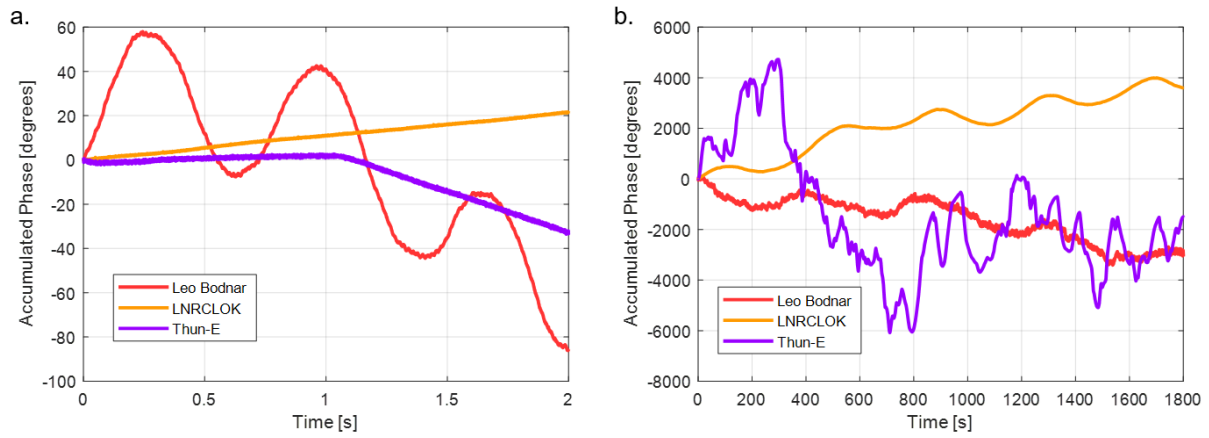

Figure 7.5: Phase error measured via bistatic direct breakthrough signal for different oscillator configurations. (a) Sub-CPI phase errors, (b) Long term phase errors.

Since it is important to retain time synchronization over longer periods of time, if there is no external synchronization mechanism, then it is reliant on retaining minimal phase error between the LOs. The long-term phase accumulation over 30 minutes is shown in Figure 7.5b. Since all are GPSDOs, relying on the same reference, each drifts by the same order of magnitude. The maximum phase error accumulated during the 30-minute interval is 3400, 4000 and 6100 degrees respectively for the Leo Bodnar, LNRCLOK and Thun-E. This corresponds to a timing error of 7.6, 8.8 and 13.5 ns respectively. For perspective, a timing error of 10 ns results in a bistatic range error of 3 m. Although this is sufficient for this radar system, it is not the case for high resolution radar networks depending on high precision target location.

SSB Phase PSD

Using the unwrapped phase data, the single sideband (SSB) Phase power spectral density (PSD) is calculated for each LO configuration and shown in Figure 7.6. Within a monostatic radar, self-phase noise cancellation can occur, but here, no suppression of phase noise is evident since both radars contain independent GPSDOs. There are resemblances between the phase PSD and the phase noise estimated after aliasing (Figure 7.3d), indicating this can be a reliable method for estimating radar phase noise in pulsed radar systems.

Background Noise Measurement

The background noise level of the radar ideally represents the thermal noise limit of the receiver. However, oscillator phase noise results in a lifted noise floor, potentially reducing

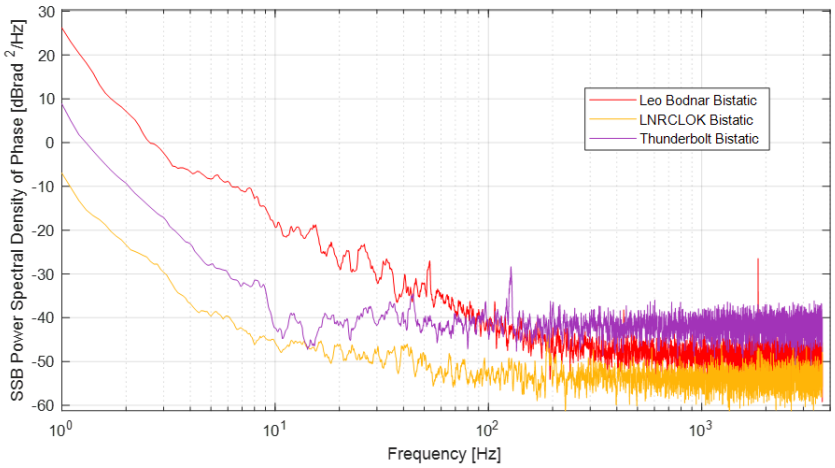

Figure 7.6: Comparison of SSD Phase PSD for each oscillator configuration.

the sensitivity of the radar. The extent to which the noise floor is raised depends on several factors, including LO phase noise, additive noise in the system, and environmental properties such as stationary clutter power. This is more pronounced in the urban environment where large structures produce significant clutter returns. In this section, the background noise floor is compared between the different LO configurations in the same selected high clutter region.

The background noise level is calculated as the average power in each frequency bin within a 3-minute period. This enables a reduction in the fluctuation of the noise as well as averaging down of moving targets that may influence the result. The computed background noise floor for each LO is seen in Figure 7.7. The measurements were taken from the location of a single dominant static clutter which was a multistory building located beyond 3 km.

For this measurement, a CPI of 2 s is used to improve the Doppler resolution and to observe phase noise effects at low Doppler frequencies. For the reference target used, the ratio between the signal power and the thermal noise floor is measured to be 103 dB on average with a variation of less than 1.5 dB between different GPSDOs. Therefore, the radar is phase noise limited for all measured Fourier frequencies in this resolution cell. As expected, the background level is much higher in the Leo Bodnar configuration, showing a 16.8 dB and 25.9 dB increase in noise over the Thunderbolt-E and LNRCLOK respectively at 10 Hz frequency offset. The noise floor of the LNRCLOK is the lowest throughout with almost 10 dB lower noise than the Thunderbolt-E at all frequencies, because of the higher quality oscillator. Spurious tones are seen in the oscillators

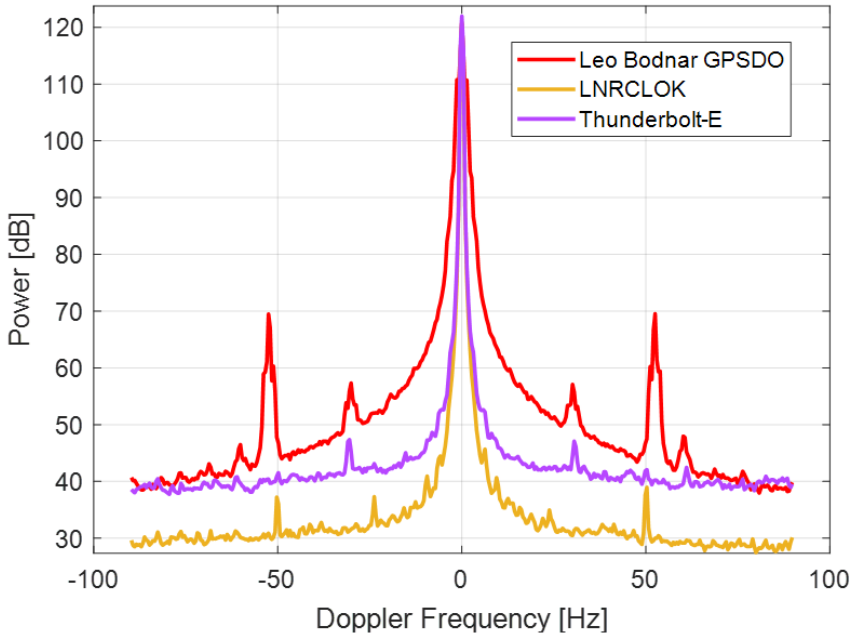

Figure 7.7: Background noise measurement comparison using the Trigate building resolution cell.

but are more prominent in the Leo Bodnar at frequencies of 30 Hz and with a power level as high as -50 dBc at 52 Hz.

Target Measurements

This section focuses on the controlled drone measurement and the impact of oscillator stability on detectability. One flight is selected for each of the LO configurations where all the flight properties (altitude, flight path, velocity) remain unchanged. A spectrogram is generated for each flight, for a CPI of 2 s, and these are seen in Figure 7.8.

The first spectrogram, in Figure 7.8 shows the Leo Bodnar LO configuration. When the flight is entering high clutter regions, in this case, there is a strong return at zero Doppler frequency due to a large building. The clutter is seen to spread out significantly and raise the noise around the target. This is most significant in frame numbers 140-200. At the start of the flight, when drone velocity is relatively low, the target is almost masked within the broadened clutter. The 52 Hz spurious tone is visible throughout the flight, harming detectability for targets moving at the same velocity. Unfortunately, the drone target occasionally moves within this cell for a sustained time.

For the Thunderbolt-E flight seen in Figure 7.8b, clutter spread is not as significant and

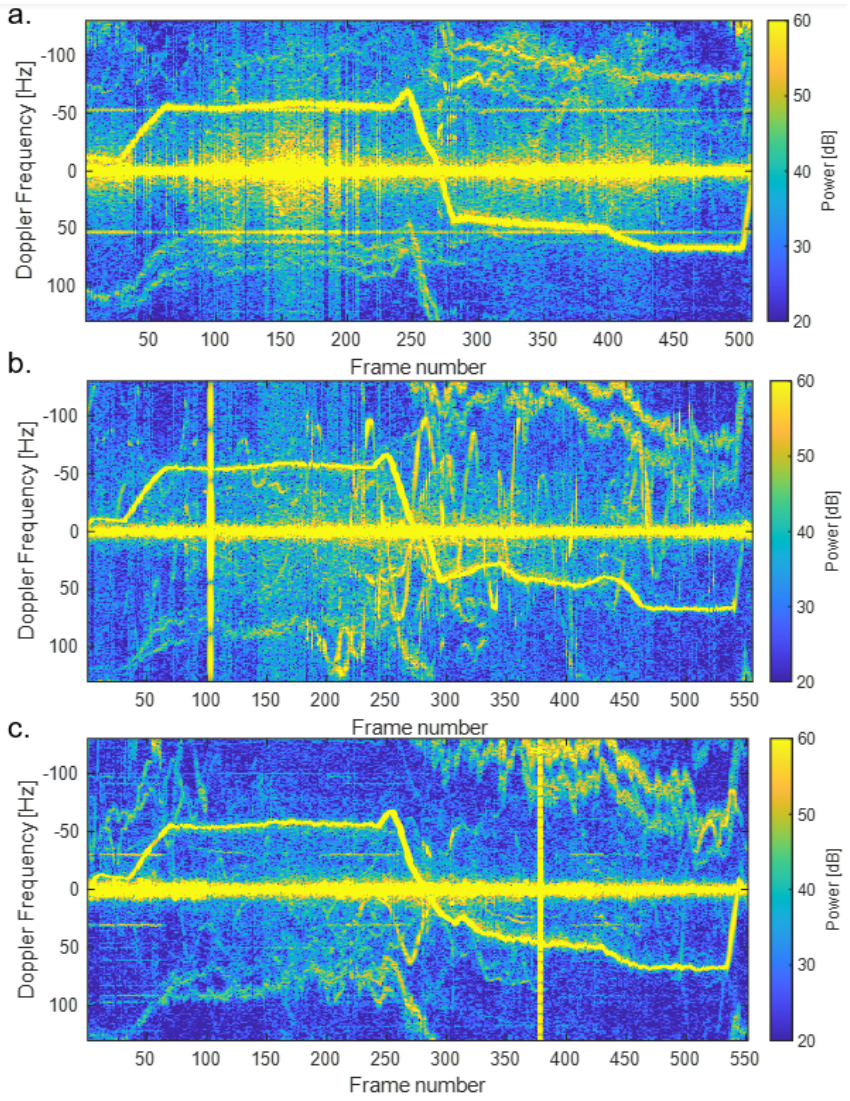

Figure 7.8: Target spectrograms for the Inspire DJI for different oscillator configurations. (a) Leo Bodnar GPSDO, (b) Thunderbolt-E, (c) LNRCLOK.

although there is still a raised noise floor in the strong clutter regions, the effect at low Doppler frequency offsets is much reduced.

However, phase noise effects are barely observed in the LNRCLOK spectrogram in Figure 7.8c, with the target being more clearly distinguishable.

Vertical lines are visible in the data at frame 100 and frame 380 in the Thunderbolt-E and LNRCLOK data respectively and this is due to an artefact in the radar and not considered as part of the analysis.

The signal-to-noise ratio (SNR) is measured using a shorter CPI of 0.5s. The target power is

measured as the power value from the maximum range-beam-Doppler cell after detection and the noise power is the average value from the same cell over the previous 3-minute interval as defined by the SBM in Chapter 5.3.4. This approach enables phase noise effects to be accounted for in the measurement while minimizing the influence of other targets on the noise measurement. The SNR measured throughout the flights is shown in Figure 7.9, with the high clutter regions highlighted.

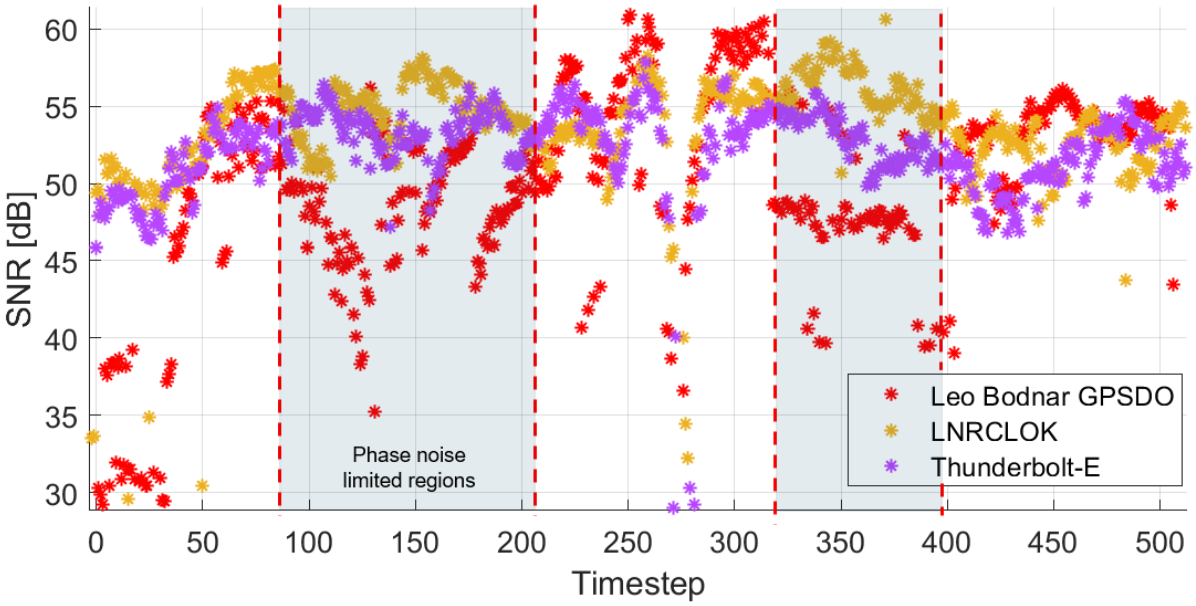

Figure 7.9: SNR measurement of the Inspire DIJ throughout the flight for each oscillator configuration.

Near the start of the flight, where velocity is low, there are up to 20 dB differences in the SNR of the drone. In the phase noise-limited regions there is also a separation of SNR values with LNRCLOK being the highest, followed by Thunderbolt-E and then by Leo Bodnar. For other regions, SNR is mostly independent of LO in thermal noise-limited regions as the coherent integration loss due to sub-CPI phase fluctuations is not significant.

7.1.5 Conclusion

Different types of GPSDOs were compared and although they all have the same reference, the oscillator is of varying quality and the steering mechanisms are different. The primary observations in this study focused on the short-term stability and phase noise of the internal oscillator.

This has been found to have a significant effect for slow moving targets with improvements in SNR of up to 20 dB when using a different LO configuration. The long-term stability effects are measured via timing error and a similar level of timing error is seen in each of the different GPSDOs. Long term stability may be able to be improved to come extent. But the choice of GPSDO design is mostly determined by the internal oscillator. The phase noise here is limited by the upconversion from 10 MHz to 62.5 MHz. To achieve optimum performance the consideration of the oscillator that provides the lowest phase noise at the radars operating frequency should be employed.

7.2 Fully Synchronized Staring Radar Network with Microwave Photonics

This section is made up of work from the unpublished paper, currently in preparation at the moment of writing "Precision Synchronization of Networked Radar using an Optical Clock Laser." I was involved in the conceptualization, experimental setup and the data collection. My role in the development of the HARPO was advisory. Also, I completed the data processing and analysis. This section contains text and figures that are reused from the paper.

Microwave photonics oscillators can provide substantial benefits to radar systems due to their superior phase noise properties. In this section, ultra-stable microwaves generated from high finesse F-P cavities and using the optical frequency division method, are used to synchronize an L-band staring radar network. The F-P cavity is undisciplined but this is overcome with the use of a common mode MWP configuration and is the first of its kind to be demonstrated in a real radar system. Fibre phase noise stabilization is utilised for dissemination of the light to remote radar nodes without degrading the stability of the oscillator. Synchronization accuracy of 14 ps is achieved over the period of an hour while relying solely on the oscillator and the fibre link. The radar noise floor and coherent processing performance are shown to be improved compared to a standard GPSDO and what can be achieved using alternative methods. The bistatic MWP common mode configuration was successfully used to detect drone targets in

an urban environment and demonstrating higher SNR and PD that the standard GPSDO and reaching the radars limit in terms of sensitivity and short term synchronization accuracy. This method provides a means for high-performance synchronization of ground-based, stationary networked radar systems.

Common methods of synchronization include using the direct breakthrough signal as a trigger point, but this fails when the direct signal is obstructed [11]. Global positioning system (GPS) disciplined oscillator (GPSDO) pulse per second (PPS) generation is also used, but is prone to global navigation satellite system (GNSS) denial or spoofing [154] [177].

Limitations involved with RF synchronization schemes can be overcome by moving the optical domain. This provides benefits such as higher precision, low attenuation for long-distance communication links and immunity to electro-magnetic field (EMF) interference. Common optical-based approaches include white rabbit protocol [13], electronic stabilization (ELSTAB) [178] and in-fibre two-way time and frequency transfer (TWTFT) [179] achieving stability levels of 10^{-12}, 10^{-13} and 10^{-17} respectively, in terms of short term stability. Although, TWTFT is currently limited to distances in the order of 10 km.

The technique in this section leverages various recent technologies such as Fabry-Perot (F-P) cavity-stabilized lasers, PN stabilized fibre links and optical frequency combs, providing the potential to synchronize systems to below 10^{-18} level over longer distances. Also, this method is able to provide lower phase noise than RF based oscillators, which would not be the case for the other optical synchronization schemes as they are only for providing timing synchronization.

F-P cavities provide the capability to stabilize lasers to a high degree. Two mirrors are fixed in place by a substrate such that light resonates within the cavity at particular frequencies corresponding to integer wavelengths. The high vacuum interior, vibration isolation, highly reflecting mirrors, low thermal expansion coefficient substrates and other environmental controls provide the current record of short-term stability for oscillators. Such examples are the 48.5 cm ultra-low expansion (ULE) glass cavity by the National Physical Laboratory (NPL) [71], and the cryogenic silicon cavity by Physikalisch-Technische Bundesanstalt (PTB) [79], both providing sub 10^{-16} fractional frequency stability. The remaining issue is that independent cavities may

have different resonant frequency modes and undergo different environmental perturbations, especially if they are located remotely. This results in frequency offsets and uncorrelated noise. To overcome this, a common-mode scheme is devised which provides a common optical reference to multiple radar nodes.

The current widespread optical fibre infrastructure provides a possibility to send light over long distances with low attenuation of 0.2 dB/km at 1550 nm [85]. However, effects of PN are induced due to path length fluctuations caused by thermal expansion, thermo optic effect and pressure perturbations [87]. A method was devised in [84], for active cancellation of PN in fibre links. This method has been proven to provide optical frequency dissemination to accuracies on the 19th decimal place and beyond, over distances of the order of 1000 km [95].

With the use of F-P cavities and stabilized fibre links, coherent optical sources at remote locations becomes possible. For the use in a radar system, the challenge of converting between the optical and microwave domain is overcome with the development of optical frequency combs [103] and microwave photonics generation [128]. The lowest PN microwave signals have been demonstrated using the optical frequency division (OFD) method [127] [132], where a mode-locked laser is locked to an F-P cavity stabilized laser. The coherent modes within the comb spectrum can then be detected on a photodiode and the rejection of common noise between adjacent modes along with the huge division factor obtained from transferring from optical to microwave domain, results in ultra-low PN signals. The OFD method is found to produce microwaves that are phase coherent with the source up to zeptosecond levels in laboratory conditions [131].

This technique allows for high spectral purity oscillators, beyond what is achievable with RF synthesizers as well as record levels of synchronization. In this section, we use all of these techniques to generate a common time scale between radar nodes with 10 picosecond level synchronization. This demonstrates the use of this method of local oscillator generation in a radar network for the first time.

The use of photonics in radar is an area developing much interest [128] [139] since the first demonstration of a fully photonic-based radar system [140]. So far, photonic based radars have

not been focused on the area of ultra-low phase noise but rather some of the other benefits to using optical signals. One such example within the same system [141], demonstrates a photonics based transceiver operating on both the S and X bands, transmitting pulses sequentially. The radar utilizes a mode locked laser, with modes located at the two bands to ensure both are coherent to each other, allowing for more effective fusion of the data. The use of phase noise stabilized links has also been explored in [28] for dissemination of an H-maser reference to radar nodes in different cities.

7.2.1 Fibre Phase Noise Stabilization

The technique of using phase noise stabilized fibre links for dissemination of optical references was introduced in chapter 3.4. Perturbations in the path length of the light travelling through the fibre cause additional phase noise contributions. It is a requirement for the QER project to be able to distribute light from one node of the network to another, whether it is a cavity stabilized laser or a clock signal. Within the entire scope of the optical clock and radar network, there may be multiple areas where phase noise stabilized links are needed and they may have different requirements, such as fibre length, operating wavelength, required frequency stability, etc. In this section the development of an in house fibre phase noise stabilization system is presented.

The phase noise cancellation system developed within this chapter is purposed for sending ultra stable lasers from one lab to another within the Alkaline research labs in the University of Birmingham. Also, it will act as a prototype for use in the various other phase noise stabilization systems needed in the project. In terms of the frequency stability requirements, the additive noise of the link must be lower than the instability of the laser source that is intended to be disseminated. The setup will differ from the generic block diagram previously shown in figure 3.8. For example, the length of this link is on the order of 100 m and therefore, optical amplification should not be required. Also, wavelength specific PM optical fibres were installed between the labs with FC-APC connectors. Therefore, back reflections at intermediate interfaces are minimised and the second AOM at the user end is also not expected to be required. With strontium clocks in mind, the clock laser and second stage cooling lasers are at wavelengths of

698 nm and 689 nm respectively and therefore, are the operating wavelengths of the system. The local and remote nodes are made out of free space optical components as they are cheaper to obtain at the wavelengths involved, compared to fibre coupled components.

For the description of the system, the phase noise stabilization will be split into 3 parts, the local optical branch, PLL electronics and remote optical board. The local optical branch along with PLL electronics are located on the input side, from where the ultra stable laser is transmitted from. The remote optical board is setup on a small, transportable optical breadboard such that it can be placed close to the user or near the local branch for testing purposes. For testing of the setup, 689 nm light was used from a F-P cavity stabilized laser system.

Local Optical Branch

The schematic diagram for the local optical branch and fibre link, as well as a photograph of the respective components are shown in Figure 7.10.

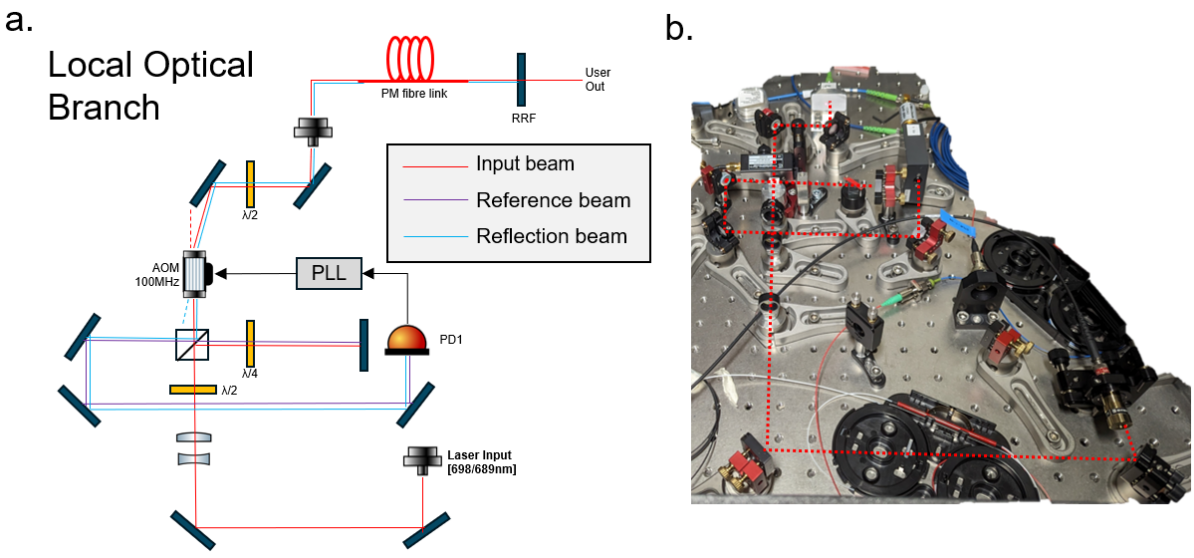

Figure 7.10: Local optical branch of the phase noise stabilization setup. (a) Schematic diagram, (b) Photograph of the setup. PLL - Phase locked loop, PD - Photodetector, AOM - Acoustic optical modulator, RRF - Retro-reflector fibre.

Firstly the fibre coupler / collimator sends the 689nm light into the setup. The half wave plate ($\lambda/2$) and the polarization beam splitter (PBS) is used to split the light based on its polarization into both legs of the interferometer. The shorter leg is reflected from the PBS, reflected from the mirror and double passed through the quarter wave plate ($\lambda/4$), such that it is transmitted

back through the PBS and aligned onto PD1. The longer leg of the interferometer, with a higher fraction of the optical power is sent into the acoustic optical modulator (AOM) which is optimised for producing the first order with a 100 MHz frequency shift. The frequency shifted light is then coupled into the PM fibre link and after propagating through the fibre a part of the light is reflected back through the same path while the remaining light is sent to the user. The back reflected light is passed backwards through the same fibre towards the local optical branch. It is then double passed through the quarter wave plate and the AOM such that the light with a 200 MHz frequency shift can be reflected by the PBS and aligned onto PD1. The 200 MHz frequency shift on the reflection beam allows the beat note to be obtained on PD1 between the two merged beams. The beatnote is crucial for the phase noise stabilization to function as it contains the information about the phase noise added via the fibre link.

PLL Electronics

The next stage is the PLL electronics where the schematic diagram and photographs are shown in Figure 7.11. The purpose is to extract the phase information from the 200 MHz beatnote and generate the correction signal to the actuator, which is the AOM.

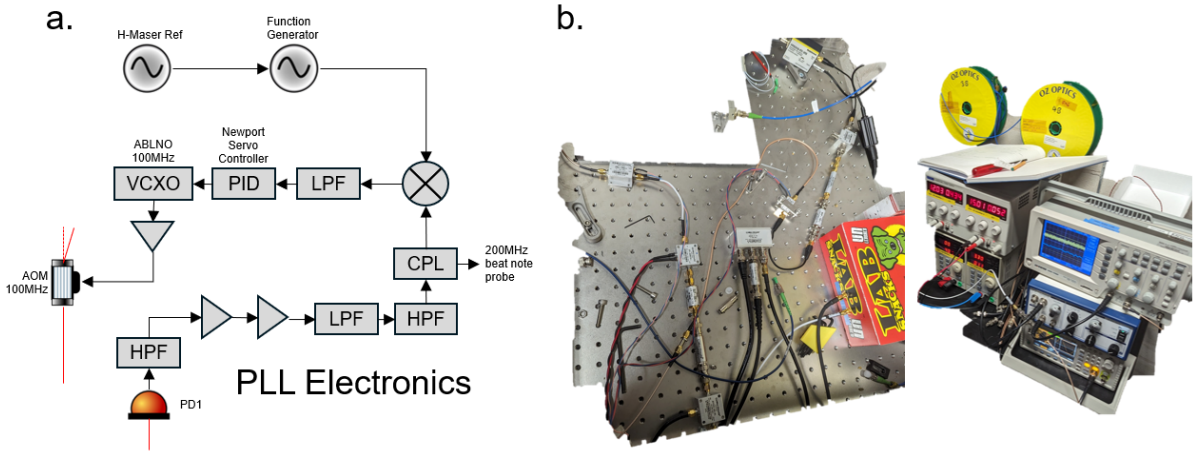

Figure 7.11: PLL electronics portion of the phase noise stabilization setup. (a) Schematic diagram, (b) Photograph of the setup. HPF - High pass filter, LPF - Low pass filter, VCXO - Voltage controlled crystal oscillator, CPL - RF Coupler.

The 200 MHz beatnote output from PD1 is of low power and must be conditioned. Therefore a series of high pass and low pass filters with 200 MHz in the passband as well as two RF amplifiers are required to bring the signal level above -10 dBm and attenuating the out of band

noise. An RF coupler is then used to monitor the beatnote on a spectrum analyser. The fibre noise component is extracted by mixing the beatnote with a 200 MHz reference signal. This is provided by a function generator which is referenced to a H-maser. The different frequency is filtered out using a low pass filter with a cut off frequency of 1 MHz resulting in an error signal. The error signal is input into a Newport LB1005 servo controller which acts as a P-I circuit. The PI parameters were optimized for phase noise suppression and are shown in table 7.1 The AOM input is steered using an ABLNO voltage controlled crystal oscillator (VCXO) with a central frequency of 100 MHz and tuning range of approximately 5 kHz. The 100 MHz VCXO output is then amplified and used to drive the AOM.

Parameter	Value
PI Corner	10 kHz
LFGL	Off
Overall Gain	650
LF Gain	20 dB
Output limits	-3.3 - +3.3 V

Table 7.1: Parameter values for the phase noise stabilization P-I controller.

Remote Optical Board

Finally the optical components on the remote end are introduced. The design choice is a small, transportable optical breadboard, such that it can be bolted onto an optical table as close to the user as possible to ensure rigid and stable operation. This enables the vibration isolation of the optical components as well as minimizing noise due to out of loop fibre on the user side. The schematic diagram for the entire phase noise stabilization setup, including the remote optical board, is shown in Figure 7.12. Alternatively, the remote optical board can be replaced with a retro-reflecting fibre but this was not available at the time for the desired wavelength.

The remote optical board consists of a simple configuration for reflecting part of the light back into the input fibre. This is achieved using a quarter wave plate and PBS such that part of the light is reflected from the PBS and the user signal is transmitted.

To measure the performance of the fibre phase noise stabilization, the beatnotes are compared for both in-loop and out of loop cases. The 200 MHz output from PD1 is shown in Figure 7.13. There is a visible reduction of the noise when the feedback loop is switched on with up to 20 dB

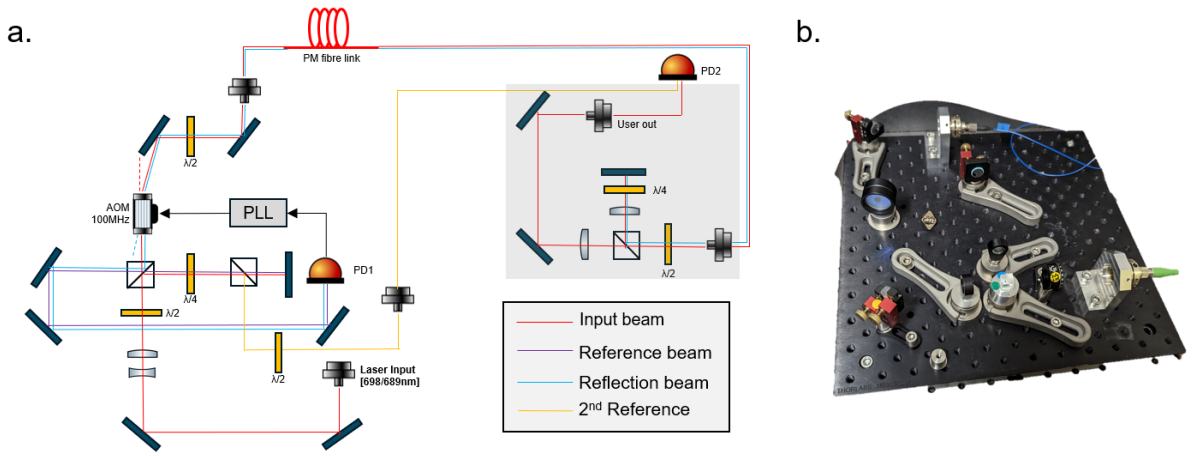

Figure 7.12: Remote optical board used for the link stability measurement. (a) Full schematic diagram, (b) Photograph of the remote board.

suppression of the noise.

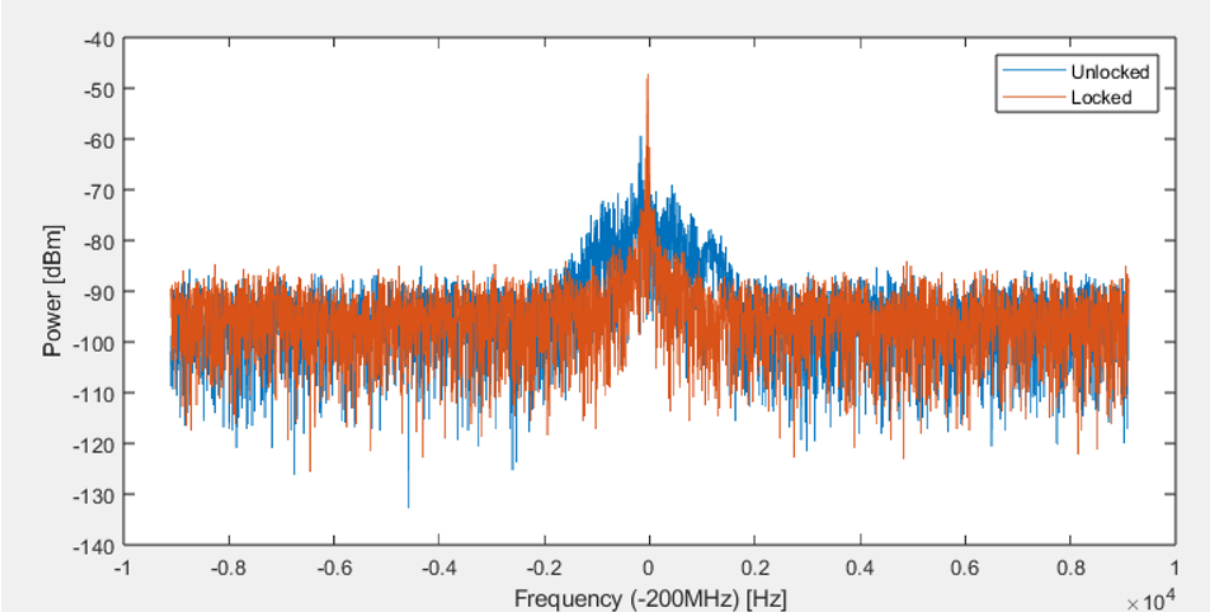

Figure 7.13: Spectrum of PD1 output with and without the stabilization loop enabled.

This work demonstrates the setup for an active phase noise stabilized fibre link. This prototype can be used for sending the clock laser from the High Spec Lab (HSL) (where most of the F-P cavities are located) to the clock lab, in which the strontium clock is being developed. The free space optical configuration allows for a high level of control. However, for the radar to radar link, it would not be practical to build the system on an optical bench and therefore a fibre based version is used. A optical configuration, but with fibre coupled components is

made by Jithin Kannanthara and Gwynfor Donlan for the wavelengths of 1397 nm and 1542 nm to be used within the quantum enabled radar project and is termed HARPO. The 1542 nm HARPO is used within the following work using the MWP common mode configuration for radar synchronization.

7.2.2 Radar Experiential Configuration

This section consists of the configuration of the MWP oscillators and how they are implemented into the staring radar network.

An RF switch containing multiple inputs corresponding to the various oscillators is inserted in the RF interface. Followed by signal conditioning steps to ensure the signal is consistent with the local oscillator specifications. The oscillators considered are GPSDOs, oven controlled crystal oscillators (OCXO) and MWP oscillators (MWPO). The conventional oscillators used are all commercial off-the-shelf (COTS) while the photonic oscillator configuration is described.

The MWPO is made up of 3 main parts, the F-P optical cavity, frequency comb stability transfer and the photonic-microwave generation, all of which are illustrated in Figure 7.17.

The laser diode (LD) at an operating wavelength of 1542 nm is locked to a cubic F-P optical cavity [75] using a 5 cm ULE spacer and a reported benchmark stability of 5 x 10^{-15} [138]. This acts as the master oscillator for the radar network and the intention is to distribute to both radar systems and down-convert to f_{LO} with minimal additive noise. The cavity is located within the transmitter radar cabin and is routed to the OFC using a short polarization maintaining (PM) optical fibre.

A photograph of the F-P Cavity system within the UMS is shown in Figure 7.14a. The cavity along with the PDH optics are contained within the thermal isolation enclosure and is placed upon a vibration isolation platform to counteract radar cabin movements. The reflection signal after enabling the PDH locking loop is shown on a spectrum analyser in Figure 7.14b. This has been optimized for a maximum locking bandwidth of 1 MHz and the PID parameters are shown in table 7.2. For free running operation there is an identical system within the receiver node cabin with similar locking bandwidth and parameters.

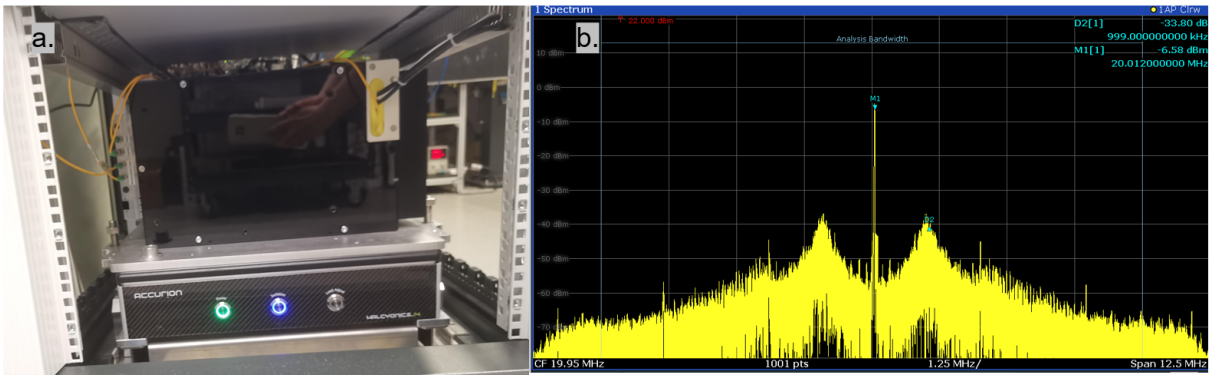

Figure 7.14: (a) Photograph of the ORS atop the vibrational stabilization platform. (b) Reflection signal spectrum when the PDH lock is enabled.

Parameter	Value
Slow integrator gain	45 dB
Slow integrator corner frequency	16 kHz
Fast integrator gain	15 dB
Fast integrator corner frequency	150 kHz
Differential corner frequency	250 kHz
Proportional gain	800
Overall gain	0.7 V

Table 7.2: Parameter values for the PID loop for the PDH lock.

The OFC used within the experiment is a MENLO Smartcomb and is used for the stability transfer from the optical to the microwave domain. The carrier envelope offset (CEO) is stabilized via f-2f self-referencing while the repetition rate is stabilized to 125 MHz via the F-P cavity.

The beatnote for the CEO frequency lock and the optical CW-Comb beatnote are both shown in Figure 7.15 when both locks are enabled in blue and red respectively. To ensure accuracy in the locking frequencies at both nodes, a 10 MHz Leo Bodnar GPSDO is used as the external frequency reference and is distributed to the both electronics modules for the CEO and Repetition rate locks. The CEO frequency is locked to the 10 MHz reference. For the repetition rate lock, the CW laser acts as an anchor point, such that the beatnote between the CW laser and the nearest mode of the OFC are locked to a defined frequency. In this case, the locking point for the CW beatnote is approximately 38 MHz. This frequency is tuned such that the repetition rate is measured to be exactly 125 MHz.

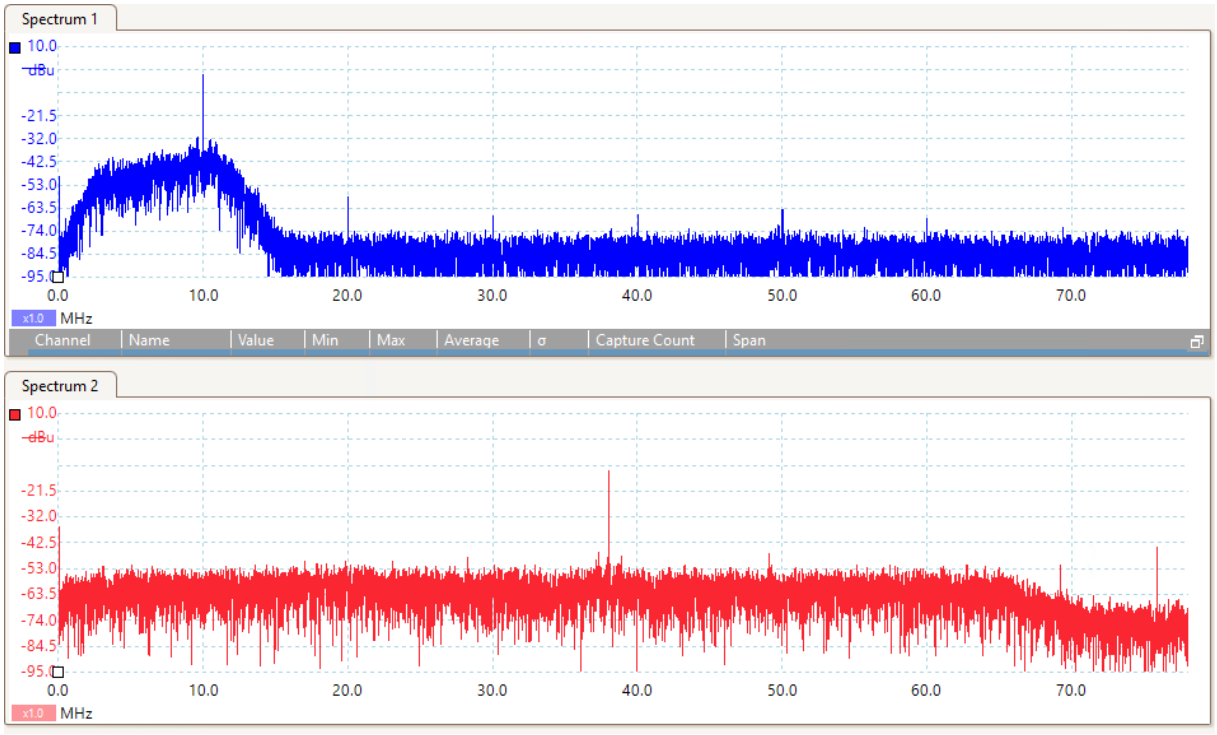

Figure 7.15: Spectrum of PD outputs for the CEO stabilization (blue, top side) and the repetition rate stabilized to the ORS (red, bottom side).

Since the F-P cavity has a slow linear frequency drift, this can cause the resulting repetition rate to also have a slow repetition rate drift when it is locked to the CW source. To counter the effect of the cavity drift, the direction and drift rate of the ORS are measured, and for this system is measured to be approximately 37 mHz/s. The locking frequency for the CW beat is also de-drifted at the same rate to minimize offsets in the repetition rate over longer time periods. For the free running configuration, the drift rate of the ORS for the other radar is also measured and is actively de-drifted within the repetition rate lock. The drift rate for OFC-2 is measured to be 23 mHz/s. The parameters for locking the OFC are pre optimized by MENLO Systems for use with the 1542 nm ORS and are shown in table 7.3.

Repetition rate multiplication is performed using a 4-stage Mach-Zender interferometer (MZM) as described in [138], resulting in a 2 GHz mode spacing. The repetition rate of the comb is extracted via a PD and the 5th harmonic at 10 GHz is filtered out. This is then downconverted down to 1.25 GHz using electronic frequency dividers. All the equipment from the F-P cavity to the 1.25 GHz output is contained within the MENLO ultrastable microwave

Parameter	Value
Repetition rate integrator 1 cut off frequency	56 kHz
Repetition rate integrator 2 cut off frequency	4.6 kHz
Repetition rate differentiator cut off frequency	491 kHz
Repetition rate proportional gain	-10 dB
CEO integrator 1 cut off frequency	56 kHz
CEO integrator 2 cut off frequency	7.4 kHz
CEO proportional gain	-8 dB

Table 7.3: Parameter values for the OFC stabilization PID loops.

system (UMS). The frequency is further divided down with an external electronic frequency divider, resulting in a low PN signal at f_{LO} and is then used as an external LO for the transmitter node.

The phase noise of the signal throughout the MWP chain, starting from the optical signal to the LO is shown in Figure 7.16. The phase noise of the beatnote between the ORS and another higher stability F-P cavity is shown in Figure 7.16a. The phase noise is then significantly reduced after OFD. There are some variations between the theoretical downconverted PN and the actual phase noise of the 10 GHz microwave signal. Figure 7.16b shows there is little reduction in PN after the first downconversion stage to 1.25 GHz, however this is still better than what can be expected in RF synthesized signals at 1.25 GHz. The second downconversion, from 1.25 GHz to 62.5 MHz, performed externally to the UMS is shown in Figure 7.16c. The PN is reduced significantly by up to 20 dB but still contains additive noise from the theoretical limit.

The LO is upconverted to the f_c internally within the radar system via a PLL and the phase noise is shown in Figure 7.16d. The 1.25 GHz upconverted signal undergoes a fundamental increase in phase noise but also there is significant additive phase noise due to the PLL synthesiser. The 1.25 GHz direct signal is also compared, showing the potential phase noise improvement that could be achieved if the radar architecture would allow for directly providing a 1.25 GHz signal from an external source. The PLL upconversion in general is understood to be a bottleneck for achieving the lowest PN signals possible but modification or designing of a new radar system is not addressed within this work. This aspect is discussed in more detail in Chapter 7.4.

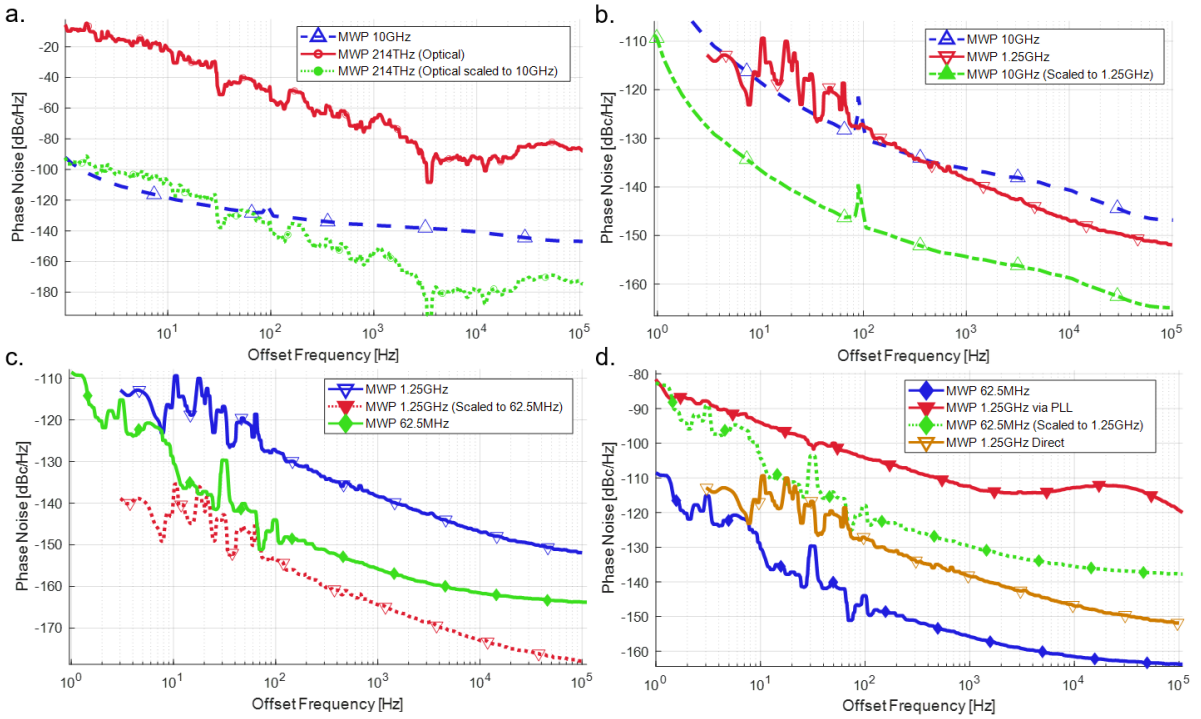

Figure 7.16: Phase noise measurements of the MWP chain. PN contributions from (a) Optical to microwave at 10 GHz, (b) 10 GHz division to 1.25 GHz, (c) 1.25 GHz division to 62.5 MHz, (d) PLL upconversion to 1.25 GHz.

For the MWP free-running bistatic radar experiments, a second identical configuration is used within the receiver radar cabin, providing the second local oscillator signal. The schematic diagram is shown in Figure 7.17. Although the signals have exceptionally low PN properties, the long-term stability and accuracy of the oscillator frequency are not sufficient for coherent network radar operation without additional frequency synchronization. The nominal frequency of lasers stabilized to independent F-P cavities are not likely to be identical, providing an initial frequency offset. Also, the effects of cavity ageing and environmental disturbances can cause slow frequency drifts in the output frequencies and fluctuations that are not correlated between the two oscillators.

However, for common-mode MWP operation, the principle is to use a single master cavity to reference both radar systems. In this way, any drifts or fluctuations are correlated, provided there is low noise dissemination of the light to the different nodes. This is obtained using an in-house active fibre PN stabilization system, termed ‘HARPO’. The HARPO consists of all fibre based components for the active cancellation of the phase fluctuations arising from the dissemination of

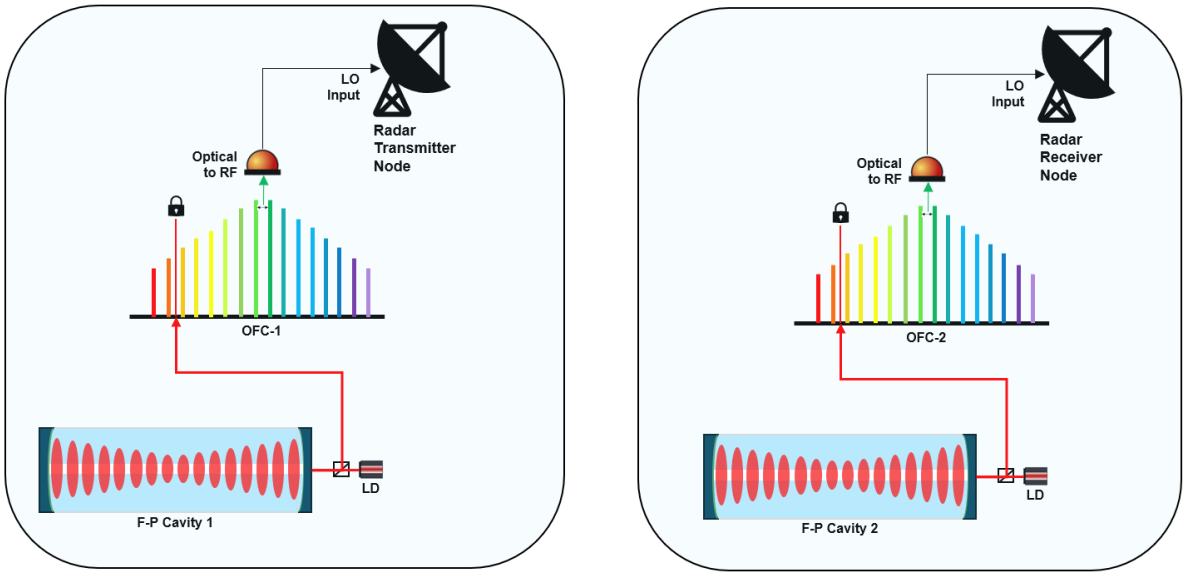

Figure 7.17: Schematic diagram for the bistatic radar using MWP free-runnung configuration. OFC - Optical frequency comb, LD - Laser diode.

the 1542 nm signal from the master cavity. The HARPO is an independent system from the one introduced in Chapter 7.3.1. The schematic diagram for the MWP common-mode configuration is shown in Figure 7.18.

The HARPO is placed at close proximity to the master cavity in the transmitter radar cabin, and the optical signal that reaches the HARPO via a short single mode fibre is stabilised with the help of an 100 MHz acoustic optical modulator (AOM), and proportional integral derivative (PID) controller in conjugation with a direct digital synthesizer (DDS) acting as a PLL. The HARPO setup contains similarities to the one mentioned in Chapter 7.3.1 , in terms of its design, but the PBS is replaced with a circulator and fibre splitters among other changes.

When using the HARPO there is the frequency shift of 100 MHz due to the AOM which must be accounted for when locking both OFCs. This scheme used to compensate for the AOM offset is shown in Figure 7.19. The variables that can be changed are the f_{CW} locking frequency, f_{CW} sign, f_{CEO} sign, and mode number. It was found that repetition rate locking performance is adequate when the locking point is between 20 MHz and 48 MHz. Another condition is that the repetition rate must be calibrated to 125 MHz for accurate RF outputs from the microwave generation. Therefore, the nearest mode must be locked at a particular position, relative to the

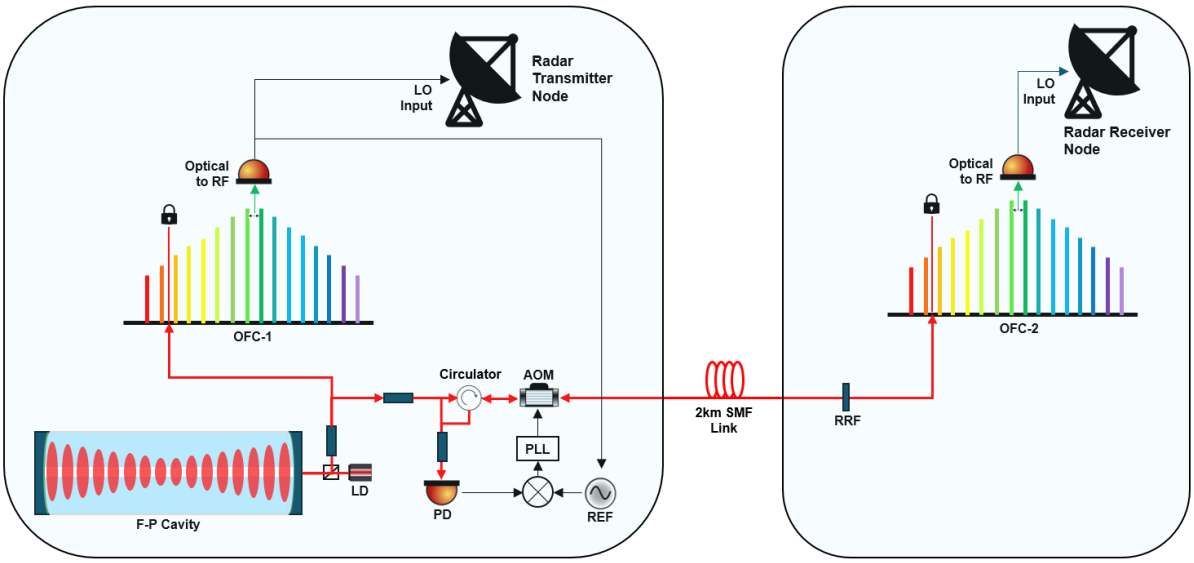

Figure 7.18: Schematic diagram for the bistatic radar using MWP common-mode configuration. OFC - Optical frequency comb, LD - Laser diode, PD - Photodetector, AOM - Acoustic optic modulator, RRF - Retro-reflector fibre.

ORS. One solution that meets both criteria is found by locking the ORS on opposite sides of the same comb mode within each of the radar cabins and using alternating CEO beat signs.

In the transmitter node, f_{CEO} is locked with negative polarity and f_{CW} is locked at -38 MHz to the nearest comb mode to obtain a repetition rate at 125 MHz. Within the receiver node, to satisfy the range of optimal locking frequencies after a 100 MHz frequency shift, f_{CEO} has its polarity reversed. In this way, the correct value for f_{CW}, to allow for coherent comb operation is satisfied by equation 7.2. Where $f_{CW-ORS1}$ and $f_{CW-ORS2}$ are the CW locking frequencies within OFC-1 and OFC-2 respectively. Therefore, f_{CW} in OFC-2 is locked at +42 MHz. Using this scheme, since the noise on both CW optical references are correlated due to the HARPO, the resultant repetition rate fluctuations should also be correlated.

$$f_{AOM} = f_{CW-ORS2} - f_{CW-ORS1} + 2|f_{CEO}| \tag{7.2}$$

As with the free running configuration, the de-drift of the repetition rate is applied to counteract the drift of the ORS. However, since the drift is now common on both nodes, the same absolute value of the de-drift frequency is used. However, due to the opposite polarity of f_{CW}, the sign of the de-drift is reversed in order to meet the criteria of equation 7.2. The locking

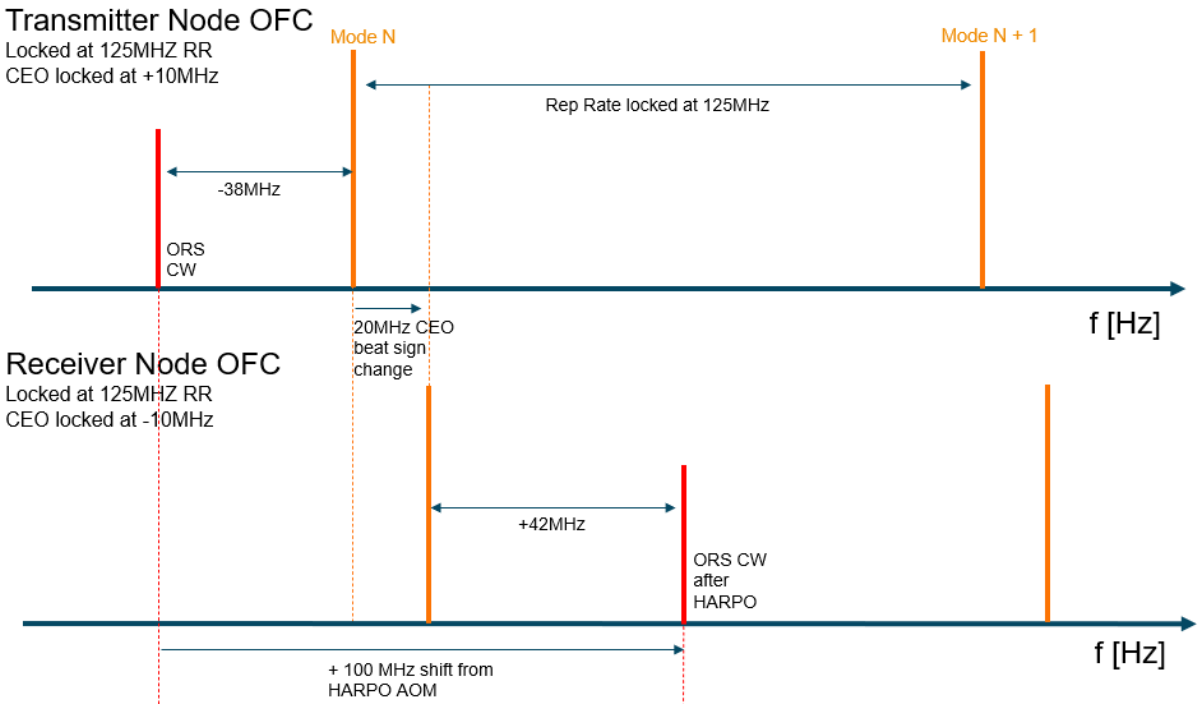

Figure 7.19: Diagram showing the OFC locking scheme for the MWP common-mode configuration.

parameters of the two OFCs for the common mode configuration is shown in table 7.4.

Parameter	Value
(OFC-1) f_{CW}	-38 MHz
(OFC-1) f_{CEO}	-10 MHz
(OFC-1) mode number n	1555199
(OFC-1) CW de-drift	+0.037 Hz/s
(OFC-2) f_{CW}	+42 MHz
(OFC-2) f_{CEO}	+10 MHz
(OFC-2) mode number n	1555199
(OFC-2) CW de-drift	-0.037 Hz/s

Table 7.4: OFC locking parameters for the MWP common-mode configuration.

The MWP common mode configuration has been described, in this section the radar interface and setup for radar measurements are introduced. The overview of the L-band staring radar infrastructure is shown in Figure 7.20. For this experiment, a dark link consisting of single-mode telecommunication fibre is installed, connecting the two radar cabins. The fibre link is routed within the campus network and the total path length spans approximately 2 km. Both radar cabins also consist of the UMS to produce photonic microwaves but during the common-mode

experiment, the F-P cavity in the receiver node is disconnected. The HARPO is installed in the transmitter node to disseminate the ultra-stable light to the receiver node via the fibre link.

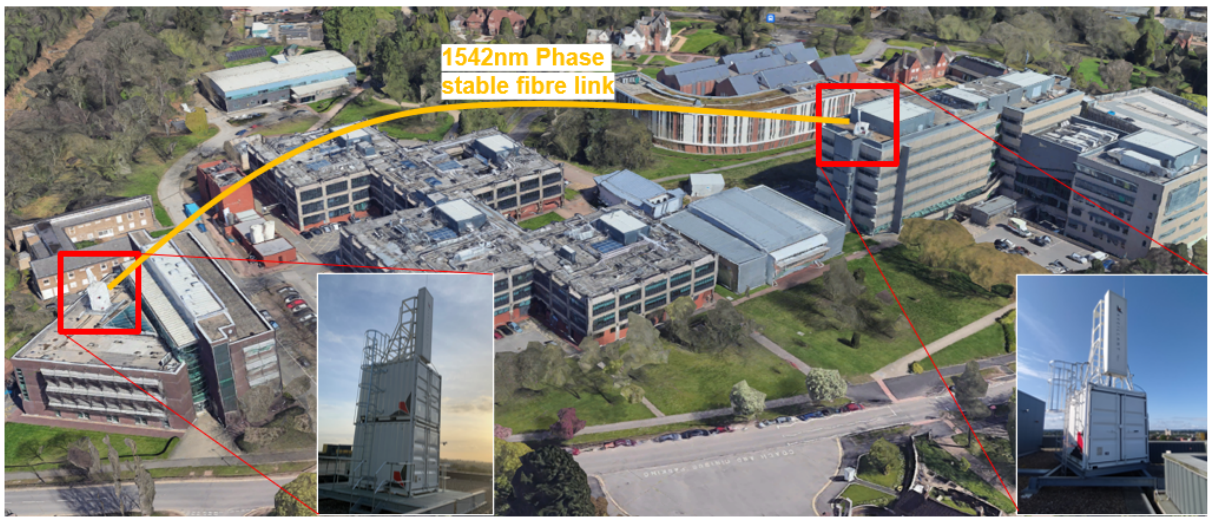

Figure 7.20: Overview of the L-band staring radar network setup for MWPO measurements and the phase noise stabilized fibre link (Google maps).

In these experiments, the same bistatic radar configuration is used, along with the same target type and scenario. Controlled drone measurements are performed with all oscillators while the background noise measurements during the night hours are performed with the MWP and GPSDO. Each of the datasets used for the respective oscillator configurations are shown in table 7.5.

The GPSDO and MWP common-mode configurations are considered to be disciplined configurations, suitable for a networked radar. Other un-disciplined configurations where there may be a frequency offset are calibrated to the nominal frequency before the trial. For the case of MWP free running, the repetition rate of each of the OFCs are manually tuned on the frequency counter to 125 MHz before starting the radar measurements using a Leo Bodnar GPSDO which is reconfigured to output at 10MHz.

Additional oscillator configurations that are considered along with the respective data sets are also listed:

Rakon OCXO - High spec OCXO at 10 MHz, upconverted to f_{LO} using the multiplier mentioned in Chapter 7.2.1. Background data measurements taken from 2024-03-06 measurements and controlled drone trials from 2024-03-11. Since this is an un-disciplined oscillator, the pre

calibration was performed in the lab by measuring the frequency against a H-Maser reference. Then, the frequency is tuned for both Rakon OCXOs such that they are as close to the nominal frequency and each other as possible before installing them in the radar. There is expected to be a small frequency offset due to the uncorrelated drift and additional warm up of the oscillators after installation.

LNRCLOK - LNRCLOK GPSDO used for comparisons. Controlled drone trial data recorded from the 2023-11-15 measurements. Measurement setup described in Chapter 7.2.

Thunderbolt-E - Thunderbolt-E GPSDO used for comparisons. Controlled drone trial data recorded from the 2023-11-15 measurements. Measurement setup described in Chapter 7.2.

PLO locked to GPS - In house version of a low phase noise OCXO locked to GPS. The Leo Bodnar GPSDO is used to reference the PLO.

Oscillator	**Background Noise Data**	**Controlled Drone Measurements Data**
Leo Bodnar GPSDO	2024-03-27	2023-10-12
LNRCLOK GPSDO	N/A	2023-11-15
Thunderbolt-E GPSDO	N/A	2023-11-15
PLO Locked to GPS	N/A	2024-03-11
Rakon OCXO	2024-03-06	2024-03-11
MWP Free Running	2024-03-06	2024-03-11
MWP Common-mode	2024-03-27	2024-05-01
MWP Common-mode (No HARPO)	N/A	2024-05-01

Table 7.5: Datasets used for the radar oscillator measurements.

7.2.3 Oscillator Frequency Stability Characterization

Within the radar system, the LO is distributed to various subsystems such as the ADC, transmitter and receiver. For generating the transmitter and receiver signals the LO is upconverted to the required frequencies using PLLs internal to the radar system.

The premise of this method relies on phase-coherent frequency comb operation and in this method, the frequency stability of the various oscillators and configurations is characterised. Frequency stability of various oscillators. The oscillators include, the low phase noise Rakon OCXO, the Leo Bodnar GPSDO, MWP free-running and MWP common-mode. These are

characterised in terms of PN, in units of dBc/Hz, which gives an idea as to the background noise levels achievable in the radar system in the presence of significant clutter [9]. Another figure of merit is the modified Allan deviation (MDEV), which characterises the long term stability and equates to the level of phase drifts that will be present between the radar nodes. Both of these measures along with the measurement setups are described in more detail within Chapter 7.1.

The PN is measured using a Rohde & Schwarz FSPN for each of the oscillators, at different stages of the radar-oscillator interface to observe the additive noise from various RF components. The measured PN at probe A is compared in Figure 7.21 for the GPSDO, OCXO and the MWPO in the free-running configuration as well as common-mode (both with and without stabilization enabled).

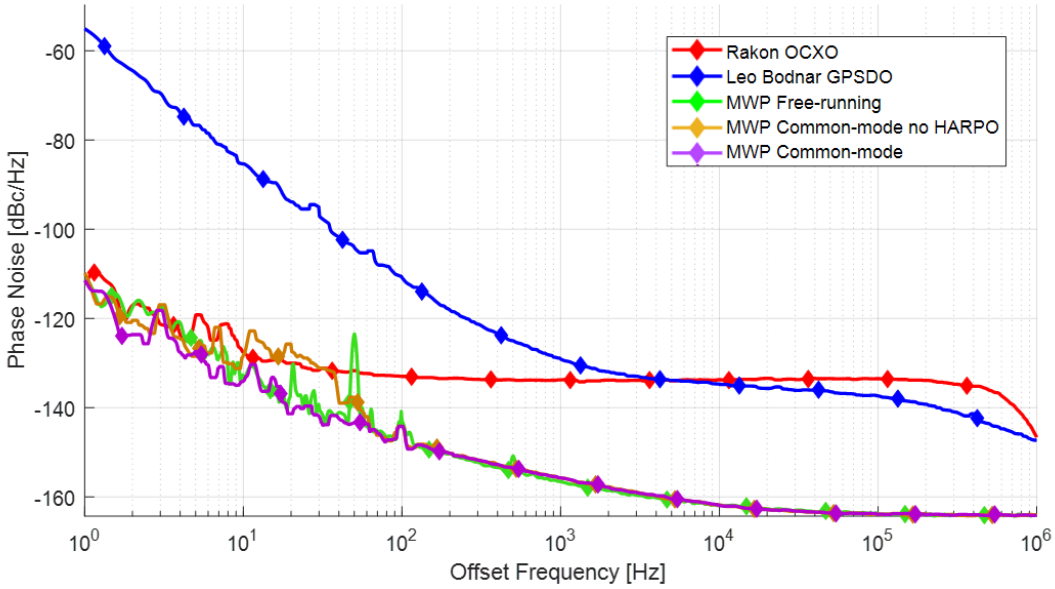

Figure 7.21: Phase noise measurements of stable oscillators at Probe A within the radar-oscillator interface. All oscillators are at f_{LO}

The MWPO can provide significantly reduced PN at the low offset frequencies, with 32 dB improvement over the OCXO at a 1 Hz offset. At the same time, the photonic oscillator's thermal noise floor is also very low, matching that of the best electronic oscillators. The out-of-loop photonic oscillator exhibits an increased PN, especially in the 10 - 50 Hz regime, where it is raised by up to 15 dB, which is the typical region corresponding to drone targets. This raised PN is suppressed after the fibre noise stabilization is applied with the PN matching that of the

system in free-running configuration. [180]

The MDEV measurements are performed using a K+K FXE (frequency counter), within the lab. The measurement consisted of a frequency ratio between two identical oscillators while both channels are referenced to a T4 science iMaser (Hydrogen maser). The MDEV measurements taken in the lab at probe A are shown in Figure 7.22

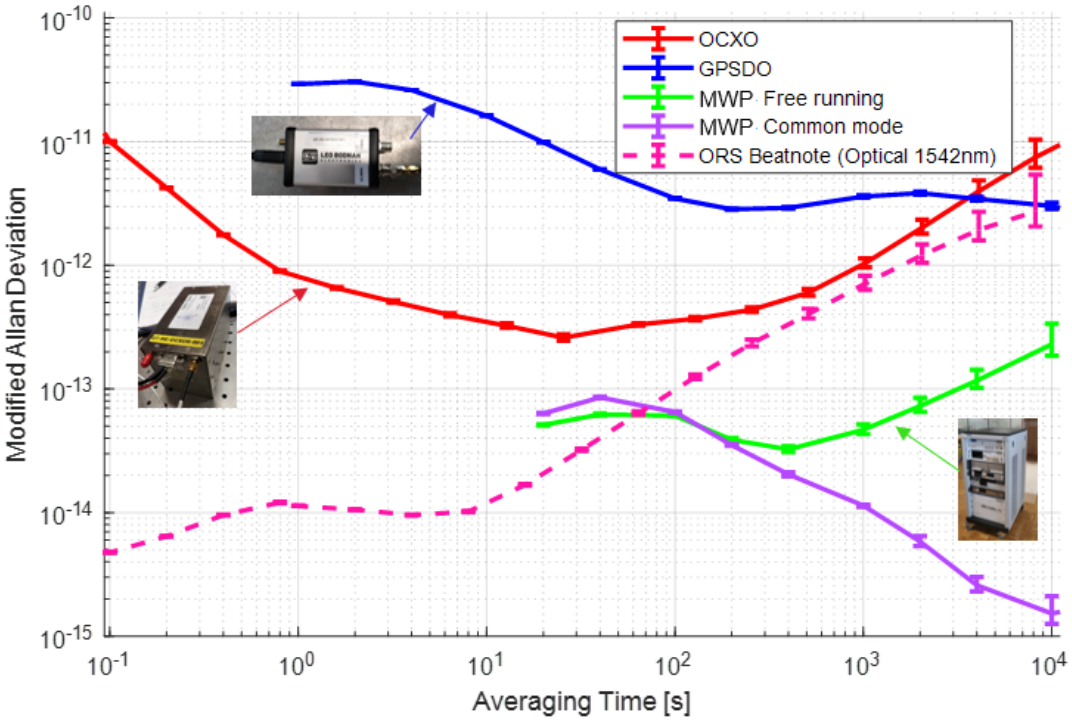

Figure 7.22: MDEV measurements of the differnet oscillator configurations used within the radar network. Measurements are performed in the lab at f_{LO}.

This shows that OCXOs are typically limited to 10^{-13} on short time scales and disciplining to the atomic reference via GPS is able to provide similar levels of stability in the longer term. Due to the orders of magnitude increase in frequency of optical signals, as well as the development of F-P cavities, oscillator frequency stabilities are pushed far beyond what is achievable with electronic oscillators. A measurement between the ORS used within this work and another with higher known stability is measured via an optical beatnote. This provides fractional frequency stability of 5 x 10^{-15} at 0.1 s averaging time which exceeds the OCXO by 3 orders of magnitude. This optical signal is used for generation of the photonic microwaves and two identical systems are compared in both a free-running and common mode configuration. For the free-running

configuration, a constant linear de-drift is applied to the comb repetition rate of the two systems to minimise the drift of the output. However, the resulting slow drift and non linear contributions are still visible beyond time scales of 1000 s. The common mode regime solves this problem, allowing for cancellation of the cavity drifts and reaching below 2 x 10^{-15} at 10000 s averaging time. The MDEV measurements of the photonic microwaves are limited below 100 s due to the noise floor of the frequency counter. This shows that the common mode photonic microwave configuration can take advantage of superior stability at all averaging times to benefit radar networks. [180]

The phase stabilized link is a crucial part of maintaining the phase coherence between the two signals. The additive noise of the fibre link is measured in 7.23. The link stability is below the level of the MWP signal, ensuring a noise-free dissemination of the signal from the transmitter cabin to the receiver cabin.

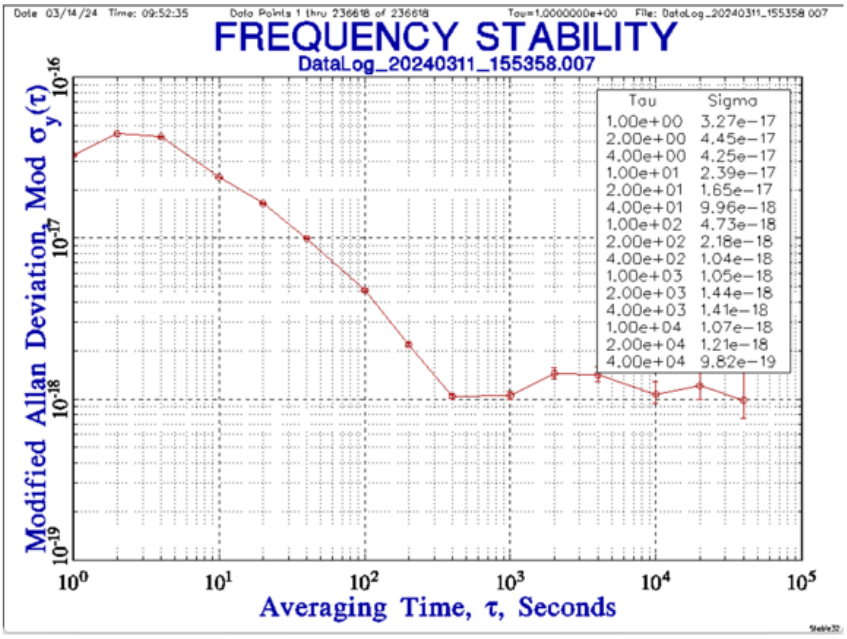

Figure 7.23: MDEV measurement of the residual link instability.

The radar-oscillator interface was described in section 5.1.1, with the default configuration being used for each of the oscillators under consideration (Figure 5.2). The measurements of the Rakon OCXO, Leo Bodnar GPSDO and the MWP at probe B of the interface are shown in Figure 7.24.

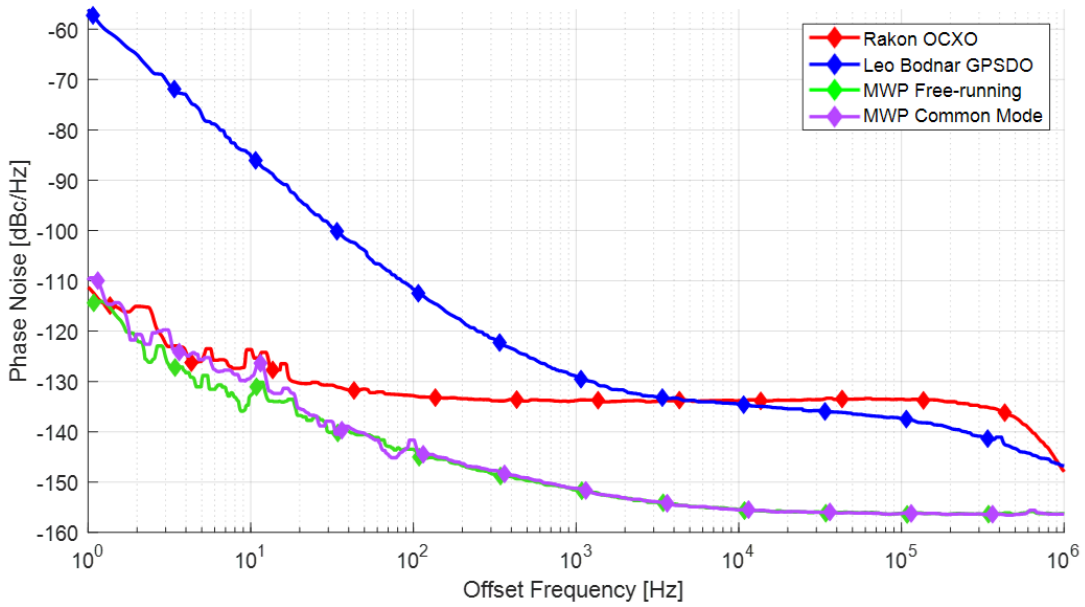

Figure 7.24: Phase noise measurements of stable oscillators at Probe B within the radar-oscillator interface. After RF switch and buffer unit f_{LO}

It is shown that the Rakon OCXO and Leo Bodnar GPSDO exhibit negligible differences between their respective probe A measurement. However, the white noise floor has been raised from -164 dBc/Hz to 156 dBc/Hz. The additive phase noise floor of the buffer amplifier is limiting the noise floor at probe B to -156 dBc/Hz. Regardless, the close in phase noise below 100Hz offset remains unchanged for the MWP oscillators.

The PN is also measured at probe C after the upconversion to f_c via the TWG board and this is shown in Figure 7.25.

The phase noise at probe C provides insights into one of the major contributions to phase noise in the radar chain. The theoretical upconversion due to equation 7.1 explains an increase in PN by 26 dB. The Leo Bodnar GPSDO follows this trend for most Fourier frequencies up to around 50 kHz. However, Rakon OCXO Phase noise is raised by 31-32 dB at the close in frequencies 1 - 100 Hz, suggesting there is further additive noise contributed by the TWG. This is even more significant for the MWP with noise increases reaching 41.6 dB at 10 kHz offset, a further 15.6 dB beyond ideal upconversion. As mentioned earlier during the measurement of the MWP chain, the TWG synthesizer is limiting PN at probe C to the level measured from the MWP oscillators.

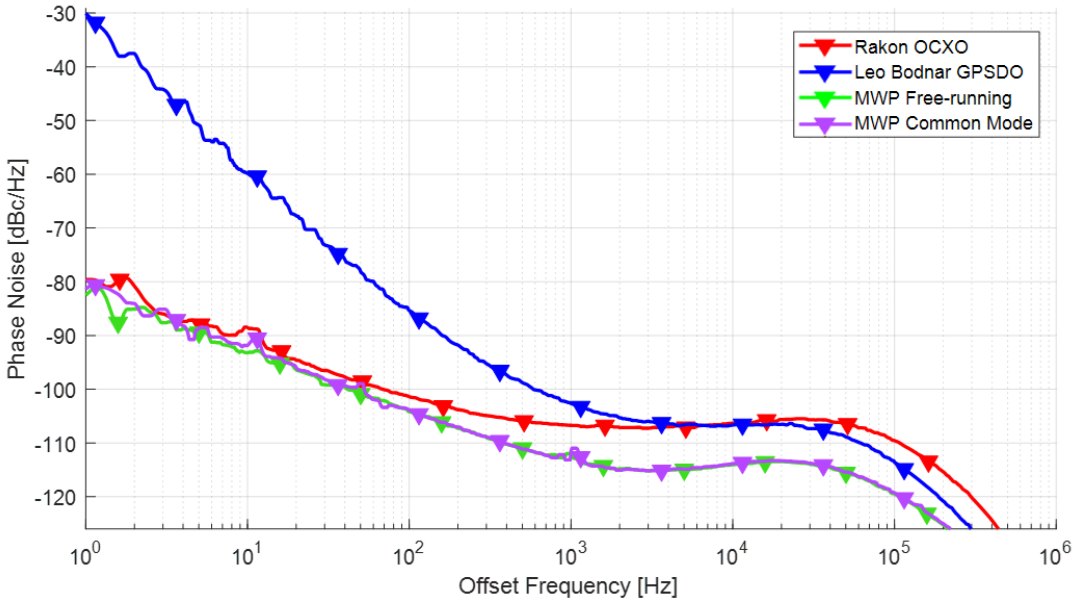

Figure 7.25: Phase noise measurements of stable oscillators at Probe C within the radar-oscillator interface. After PLL upconversion to f_c

The PRF of the radar limits the sampling frequency of the radar, causing aliasing of the phase noise. This effect is computed using the probe C measurement data for each of the oscillator and is shown in Figure 7.26.

The effect of aliasing is predicted for all oscillator configurations but is most significant for the Rakon OCXO at the frequencies of interest. At 100 Hz offset frequency there is an increase of 0.58 dB, 10.65 dB and 5.56 dB due to aliasing for the Leo Bodnar GPSDO, Rakon OCXO and MWP respectively. This demonstrates that even is the low offset frequencies are of more interest in terms of detection, it is also important to have oscillators with low phase noise at higher offset frequencies due to the aliasing contribution.

7.2.4 Radar Measurements

This section reports the results from the bistatic radar measurements with the MWP oscillator using the data from the receiver node. Firstly, measurements on static opportune reference targets will provide a benchmark for the synchronization accuracy and sensitivity of the radar system. Then, target detectability will be analysed via controlled target measurements.

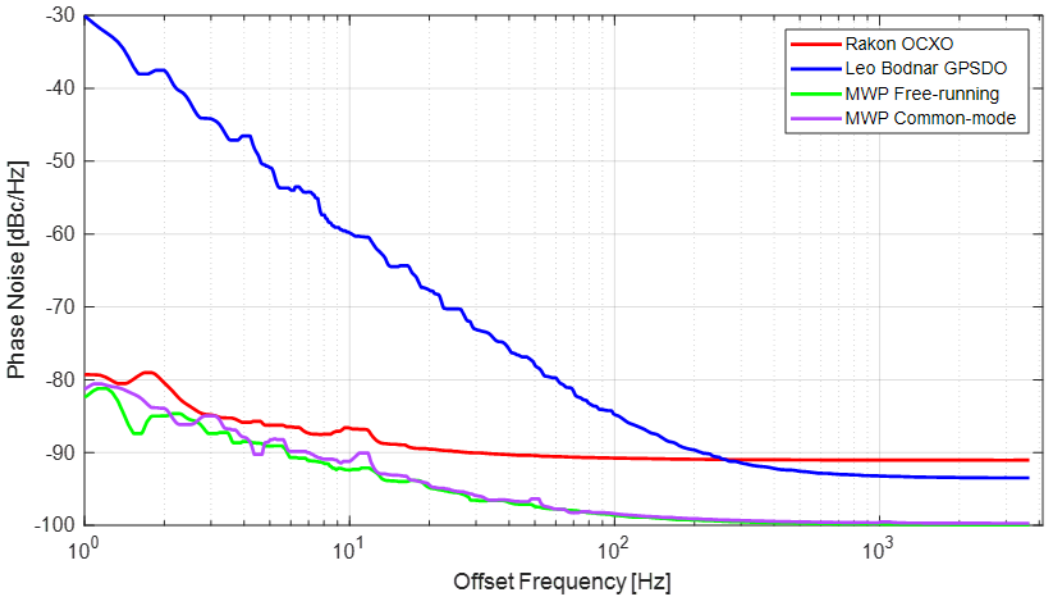

Figure 7.26: Predicted PN after aliasing at PRF.

Reference Target Measurements

Firstly, the phase error is measured via the time series data from a reference target, produced from the reflected echoes of a stationary object with high radar cross section (RCS). For the measurements within this work, a large and relatively isolated office building is used as the reference target. The bistatic unwrapped phase is calculated for a period of 600 s for each of the different oscillator configurations. The accumulated time error is computed and shown in Figure 7.27, along with the equivalent range error it implies by using the methods in Chapter 5.3.1.

The OCXO and MWP free-running configurations are both undisciplined and therefore, contain inaccuracies in the clock frequency. For the case of the Rakon OCXO, the timing drift is more severe, resulting in significant range offsets in a short period of time. An example of two range-Doppler plots are shown in Figure 7.28. After only a 600 s interval, the entire profile has drifted by 2 entire range gates, resulting in approximately 150 m range offset. The frequency offset results in a runaway of the accumulated phase as seen by the linear slope. This suggests high-frequency synchronization intervals are needed to maintain the required synchronization accuracy. From the drift rate of the time error of the two undisciplined configurations, the

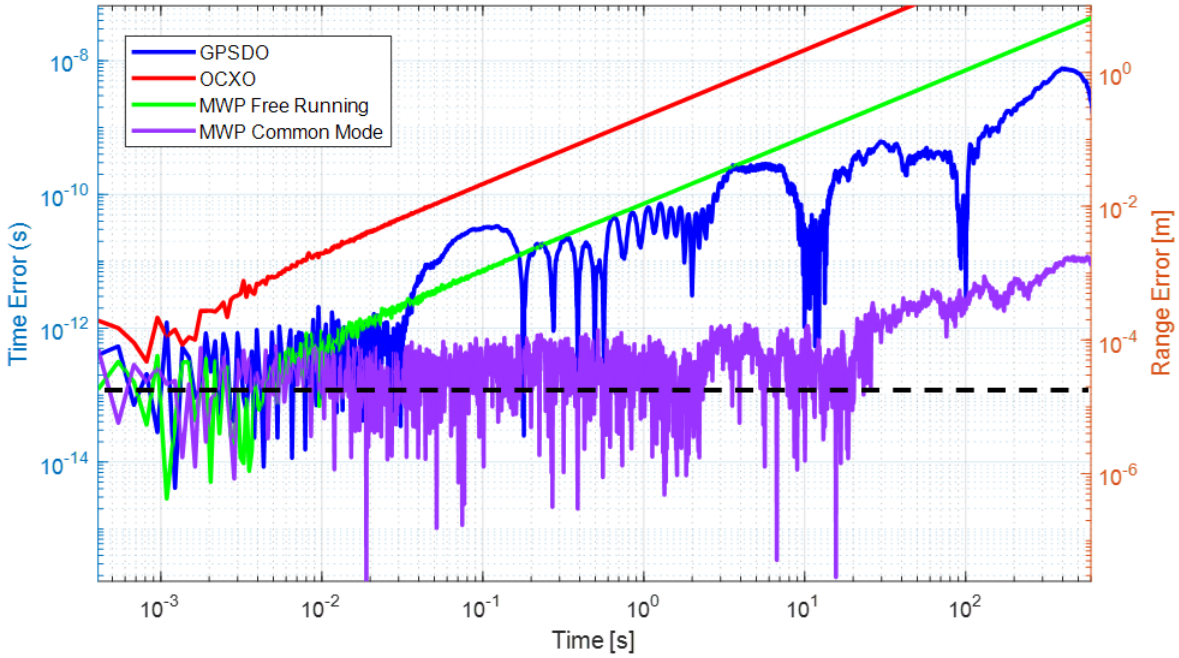

Figure 7.27: Accumulated time error and range error over a period of 700 s for each oscillator configuration.

frequency offset is calculated to to approximately 10 mHz and 2.1 Hz for the MWP free running and Rakon OCXO respectively. Now only the disciplined oscillator classes are considered, and of these, the MWP common-mode configuration has considerably less deviation between the timing of two LOs. The GPSDO reports a maximum timing error of 7.74 ns in the measurement period, relating to a range error of 1.16 m. Whereas, the MWP common mode reports a maximum timing error of only 14 ps, corresponding to a range error of only 2.1 mm. These results suggest only infrequent synchronization intervals are required.

The lack of synchronization in a radar network can have 2 main implications on target detectability. These are the coherent integration loss as well as the lack of inherent PN cancellation. Both of these aspects are analysed for the GPSDO and MWPO networked radar.

For the cases of the GPSDO and the MWP common mode, the signal power is measured for increasing coherent integration intervals (CPI). This is then compared with the theoretical limit that is obtainable to measure the coherent integration loss and is shown in Figure 7.29. Methods of computing coherent integration loss are explained in Chapter 5.3.3. All of the oscillators compared, exhibit little to no deviation from the predicted coherent integration gain except for

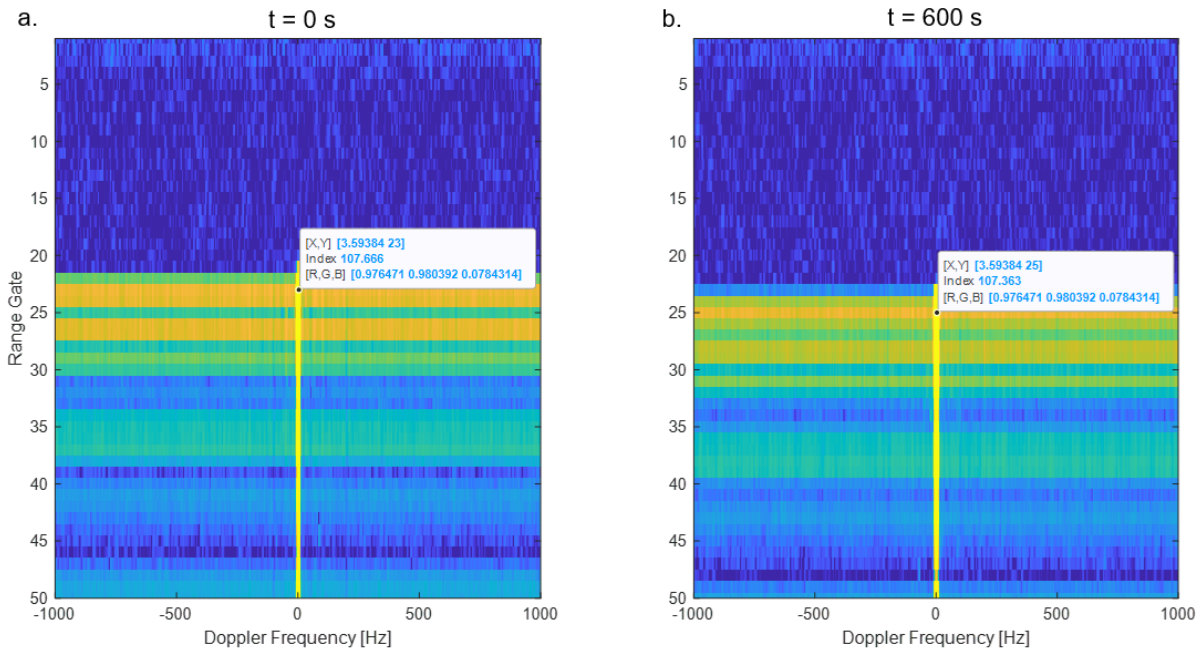

Figure 7.28: Range-Doppler plots of the bistatic Rakon OCXO configuration after a time interval of 600 s.

the Leo Bodnar GPSDO which is shown in Figure 7.29a.

The coherent integration loss is calculated as the difference between the measured SNR and the expected SNR for each of the oscillator configurations in Figure 7.29f. This shows that the bistatic L-band system meets its requirements for coherent integration gain with most of the oscillators that are compared. Especially at the typical CPIs used within this work (0.5 - 2 s), there is negligible coherent integration loss. The limit for coherent integration gain is dependant on the frequency used and the radar range resolution. Therefore, the small improvement is a limitation of the radar design, other radar systems, with a different architecture, may experience a larger improvement.

In a monostatic radar receiver, during the down conversion to the intermediate frequency, the phase is correlated between the receiver reference signal and the received echoes, causing a level of PN cancellation. For a bistatic radar, this can become more of a challenge and achieving a low PN system requires a heavier reliance in the PN of the local oscillator. To measure the effect of PN in the radar system, the background noise level is measured. During the night-time measurements, the spectral data is averaged over a period of 150 s for each Doppler cell in a

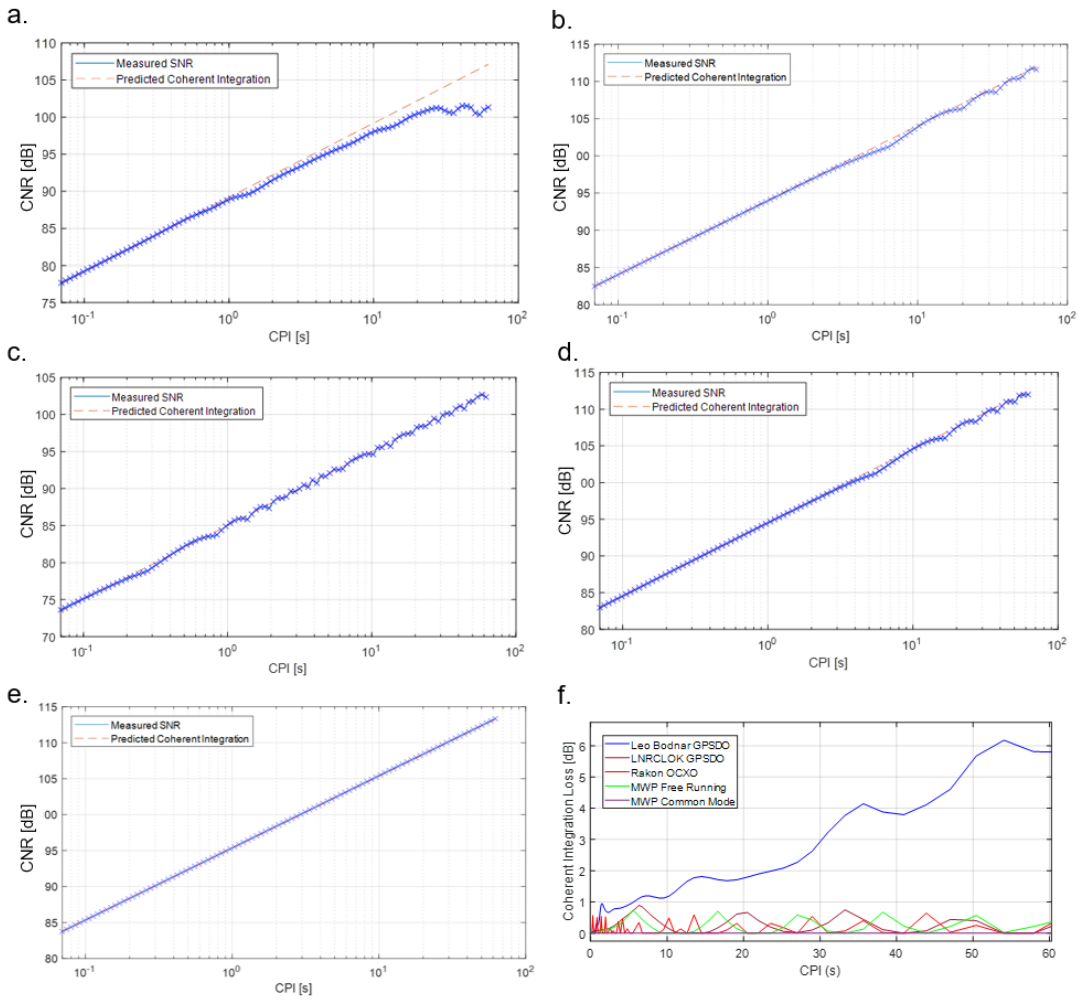

Figure 7.29: CNR as a function of CPI up to 60 s (a) Leo Bodnar GPSDO, (b) LNRCLOK GPSDO, (c) Rakon OCXO, (d) MWP free-running, (e) MWP common-mode, (f) Coherent integration loss for each oscillator configuration.

region of high clutter power. These methods are designed to remove the influence of unrelated targets in the measurement of the noise level as described in [9]. The methods for generating background noise measurements are explained in more detail in Chapter 5.3.5. Using the regions containing a large stationary target allows for a higher dynamic range, such that the PN is present and limiting the radar sensitivity.

The background spectrum, calculated using the methods described in Chapter 5.3.5, for the Leo Bodnar GPSDO, Rakon OCXO and MWP in both the free-running and common-mode configurations are shown in Figure 7.30. The background spectrum is measured at the Trigate building resolution cell where it is known that the radar is phase noise limited in the bistatic

regime. A longer CPI of 2 s is used to focus on the close in phase noise and also the improvement in frequency resolution aids with reducing the influence of opportune targets, this is shown in Figure 7.30a with the power scaled relative to the carrier in Figure 7.30b. The thermal noise floor is measured to be at 20 dB and 10.5 dB for the different CPI lengths of 2 s and 0.5 s respectively proving that this region is phase noise limited for all oscillator configurations.

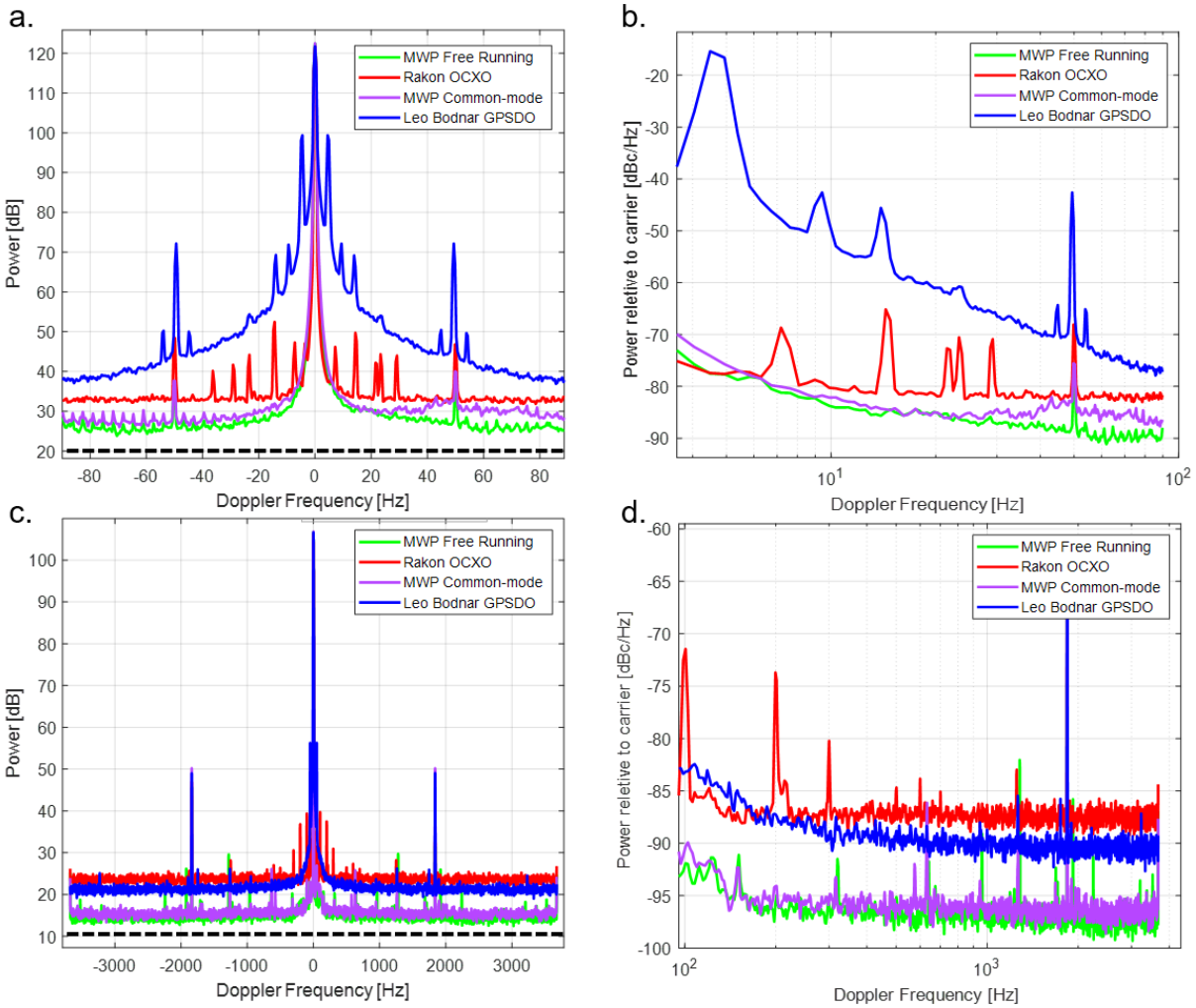

Figure 7.30: Background noise measurements of the bistatic receiver in the Trigate region. (a) Close in spectrum with CPI of 2 s, (b) Close in spectrum scaled to relative clutter power, (c) Far out spectrum with CPI of 0.5 s, (d) Far out spectrum scaled to relative clutter power.

The MWP oscillators show superior PN compared to the GPSDO with a 30 dB PN reduction at 10Hz offset, as expected from the probe C PN measurements. The Rakon OCXO is outperformed regardless of its high stability. The reason for this is due to the poor phase noise performance at higher frequencies, amplified by the fact that the nominal frequency og the

OCXO is 10MHz and has undergone more upconversions. Although the low frequency PN of the Rakon is similar to the MWP at f_{LO}, it suffers more from PRF aliasing of the PN as shown in Figure 7.26. The far out frequencies are also shown by using a shorter CPI of 0.5 s in Figure 7.30c, d. Here there is a clear separation of the MWP oscillators. However, this value of -95 dBc/Hz is not unreachable for RF based oscillators. In fact, the current MWP oscillators have reached the noise floor of the radar system due to the additive noise of various components of the radar chain, this will be discussed further in Chapter 7.4. In addition, the noise floor of each of the oscillators are higher than predicted in Figure 7.26. However, this behaviour is more of an additive noise rather than a bottleneck since all oscillators seem to exhibit a noise floor increase of around 4 dB. This is potentiality caused by the pulse modulator as there would be an attenuation of the average signal power, and therefore, reduction of SNR.

The PN reduction at a 20 Hz Doppler frequency when using the MWP oscillator over the GPSDO is shown in Figure 7.31. This plot is generated using the clutter data structure, described in Chapter 5.3.5. Most resolution cells at close range as well as areas consisting of large structures, experience a larger improvement in PN. Areas, that are thermal noise limited see no further improvement of the radar PN when improving the oscillator.

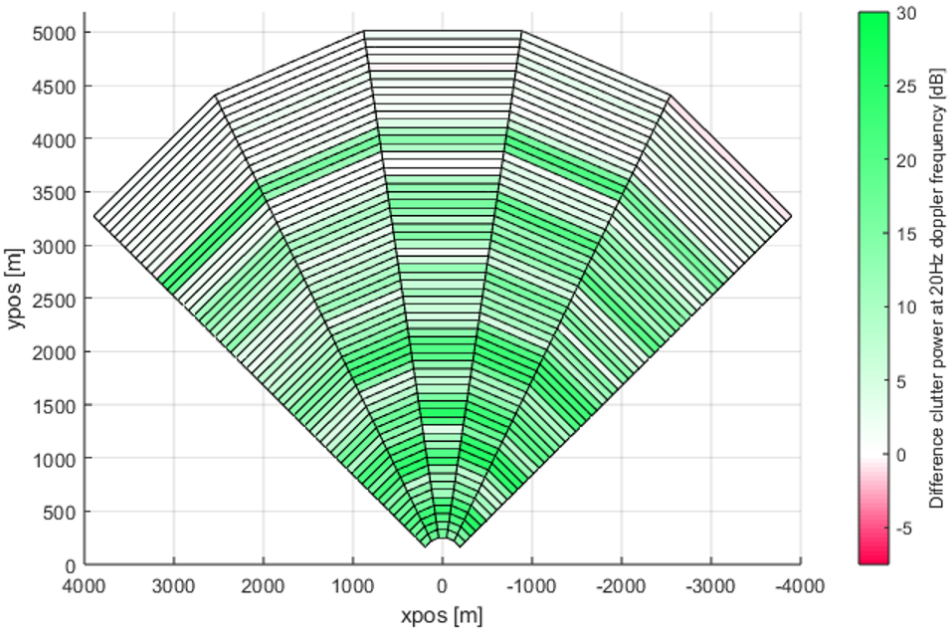

Figure 7.31: Phase noise improvement map of using MWP common-mode over a standard GPSDO throughout the FOV at a Doppler frequency of 20 Hz.

The proportion of resolution cells in the bistatic FOV that are limited by PN are computed. The decision as to whether a cell is PN limited is defined in this measurement as if the average power in that cell exceeds the thermal noise floor by a set threshold. The measurements are performed on SBM data with a 0.5 s CPI where the average level of thermal noise is measured to be 10.5 dB and a threshold for determination of a PN limited cell is set to 13.5 dB (3 dB above). This is computed for a fine grid of azimuth and elevation angles for each oscillator configuration and is shown in Figure 7.32.

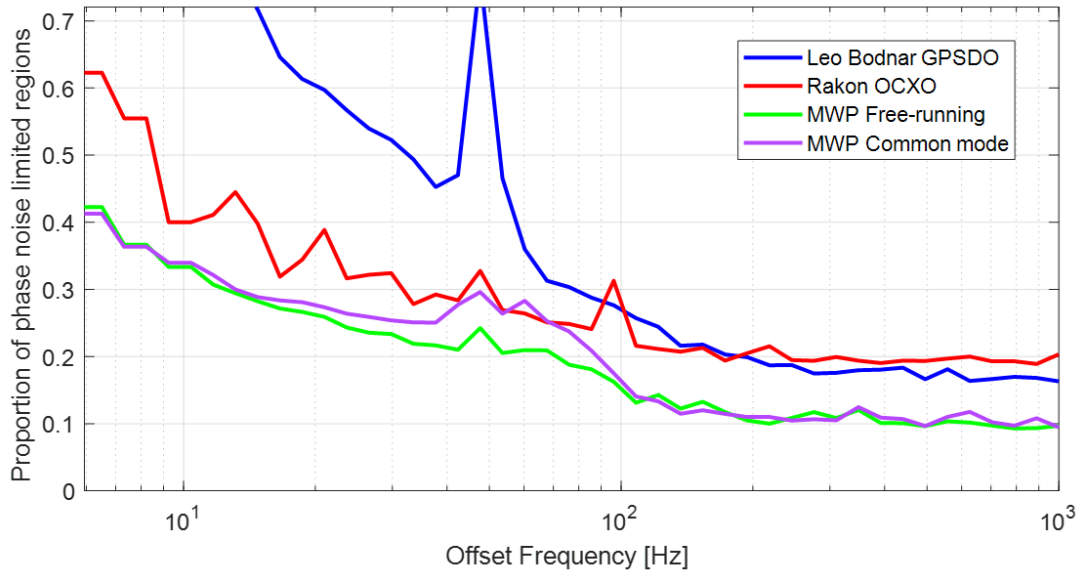

Figure 7.32: Proportion of phase noise limited regions as a function of offset frequency for different oscillator configurations.

The MWP configurations are showing a lower and consistent proportion of PN limited cells with the exception of an increased noise in the 30-90 Hz region for the common-mode configuration. There are resemblances between these results and the PN data as would be expected since at the higher offset frequencies, the Rakon OCXO tends to suffer more from phase noise limited regions.

Table 7.6 presents the quantities for proportion of PN limited resolution cells at selected Doppler frequencies of interest for detection of SUAV targets in the L-band radar. At 10 Hz, corresponding to a slow moving target, the Leo Bodnar GPSDO has 132 % more PN limited resolution cells compared to MWP common-mode. This reduces to 35 % at a Doppler frequency

Oscillator Configuration	Proportion of phase noise limited resolution cells			
	10 Hz	20 Hz	40 Hz	80 Hz
Leo Bodnar GPSDO	0.788	0.597	0.439	0.303
Rakon OCXO	0.400	0.389	0.271	0.247
MWP Free-running	0.334	0.259	0.211	0.192
MWP Common-mode	0.340	0.273	0.268	0.224

Table 7.6: Proportion of PN limited cells at 10 Hz, 20 Hz , 40 Hz and 80 Hz Doppler frequency.

of 80 Hz.

Target Detection Analysis

This section focuses on the bistatic radar's ability to make detections in the urban environment with the use of the MWP oscillators. Qualitative measurements are performed using target spectrograms using the truth GPS data and processing methods described in Chapter 5.3. The target SNR is then measured for each of the flights with the DJI Inspire and different oscillator configurations. The SNR provides a direct measure on the radars ability to detect targets as it depends on the contribution of the coherent integration gain (for changes in signal power) and the phase noise (for changes in the noise power). Since the negative impacts of phase noise are expected for slow moving targets, the SNR is measured as a function of the target velocity. Finally, the average SNR and PD for each of the drone flights are analysed with respect to the oscillator configuration. Methods of generating spectrograms and SNR analysis are described in Chapter 5.4.4.

Spectrograms are generated consisting of the resolution cell containing the drone target for each of the flights. One spectrogram from the GPSDO and MWP common mode configurations are selected and are shown in Figure 7.33. Both spectrograms are from flights using the clockwise scenario at 100 m altitude.

Since the controlled target (DJI Inspire 2) has a high RCS compared to the majority of non-stationary opportune targets and therefore is always expected to be present in the spectrogram, assuming its own relative velocity is non-zero. Within the GPSDO spectrogram in Figure 7.33a, the noise levels are higher at the close in Doppler frequencies when compared to the MWP

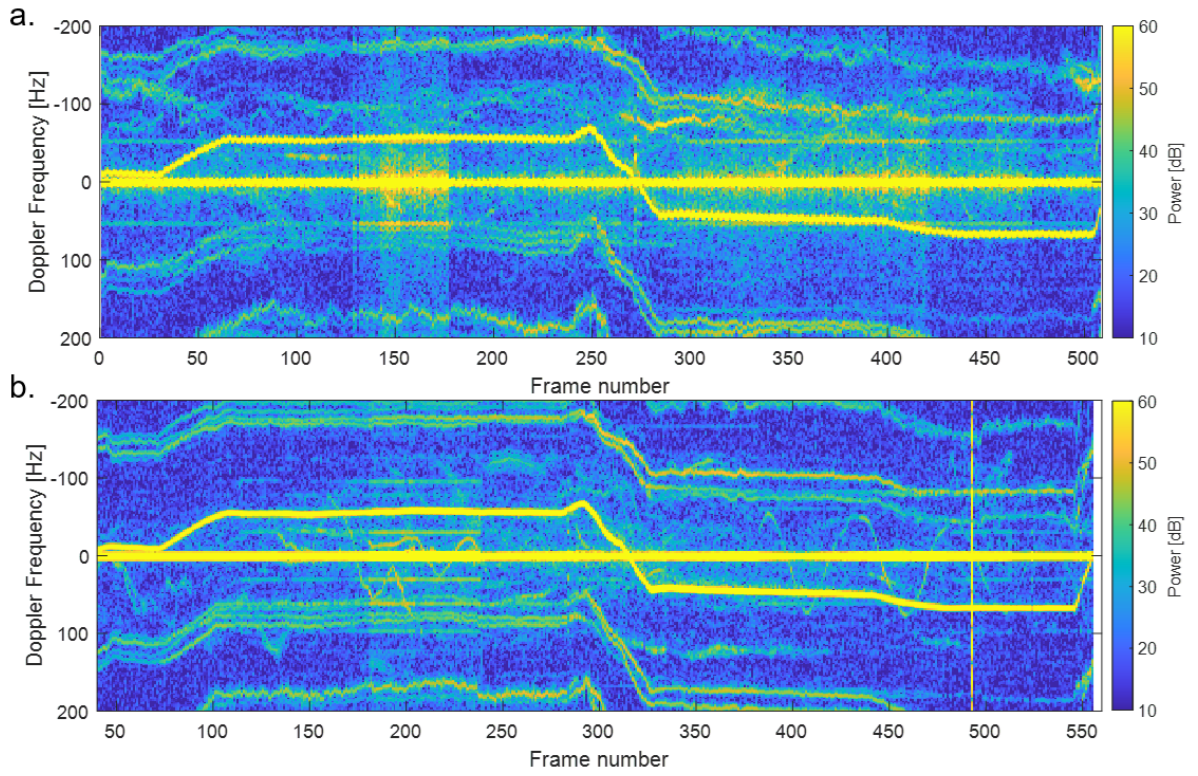

Figure 7.33: Controlled drone target spectrograms as measured in the receiver node. (a) GPSDO, (b) MWP common-mode.

common-mode spectrogram in Figure 7.33b.

Spectrograms for each of the oscillator configurations used in bistatic measurements are shown in Figure 7.34 with the detections of the drone marked in red. Similar to previous measurements, the RCS of the target is large and high SNR and probability of detection are expected. Therefore, all oscillators are able to be used to detect this target for most of the duration of the flight. The areas of difficulty are when the target is quickly accelerating/decelerating, moving at a slow velocity, near the same cell as another opportune target and when the target is within a spurious tone. Near the start of the flight, when the target is moving with a slower velocity, there are missed detections for all oscillators except the MWP oscillators and the Rakon OCXO due to their superior close in phase noise. For the PLO locked to GPSDO, the target remains undetected for that entire portion of the flight. Also, the radar will always report a missed detection when the relative velocity of the target is zero. The Leo Bodnar and PLO spectrograms contain strong spurious tones, caused by the oscillator. This is found to have a severe impact on the detections, with many missed detections occurring when the target is

near Doppler bin 2020. The strength of the clutter line (horizontal line) produced by the spur is related to the power in the zero Doppler bin, and therefore has a more significant effect on reducing the SNR in high clutter regions. Apart from oscillator spurs, there are also spurs that are independent of the oscillator configuration and are introduced by other components of the radar system. These are seen in Doppler bin 2065, within the spectrograms of the LNRCLOK, MWP common-mode and MWP common-mode without HARPO. The effect of this is also a reduction in SNR but in these cases is not severe enough for missed detections to occur.

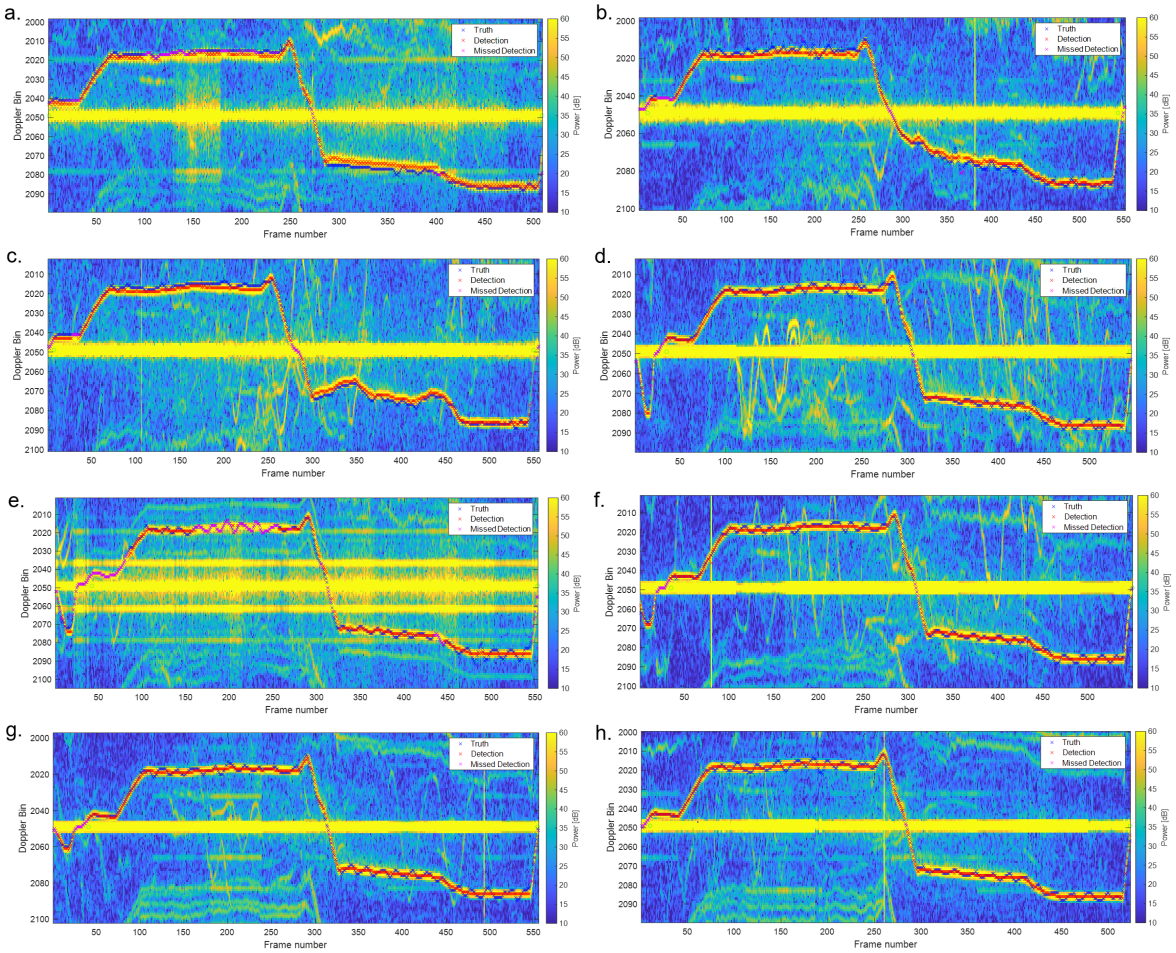

Figure 7.34: Target spectrograms for the DJI Inspire drone for different oscillator configurations. (a) Leo Bodnar GPSDO, (b) LNRCLOK GPSDO, (c) Thunderbolt-E GPSDO, (d) Rakon OCXO, (e) PLO locked to GPS, (f) MWP free-running, (g) MWP common-mode, (h) MWP common-mode without HARPO.

To quantify the detection performance, the signal-to-noise ratio (SNR) is calculated for each timestep where a detection is made. The background noise level is taken as the values from the SBM, while the signal level is the value within the peak Doppler-angle-range cell. The

detections are made using a simple cell averaging constant false alarm rate (CFAR) detector, where the signal level must exceed a fixed threshold above the background level in the same cell. An equivalent flight is compared while using the Leo Bodnar GPSDO and MWP common-mode configurations and the SNR throughout the flight is shown in Figure 7.35a.

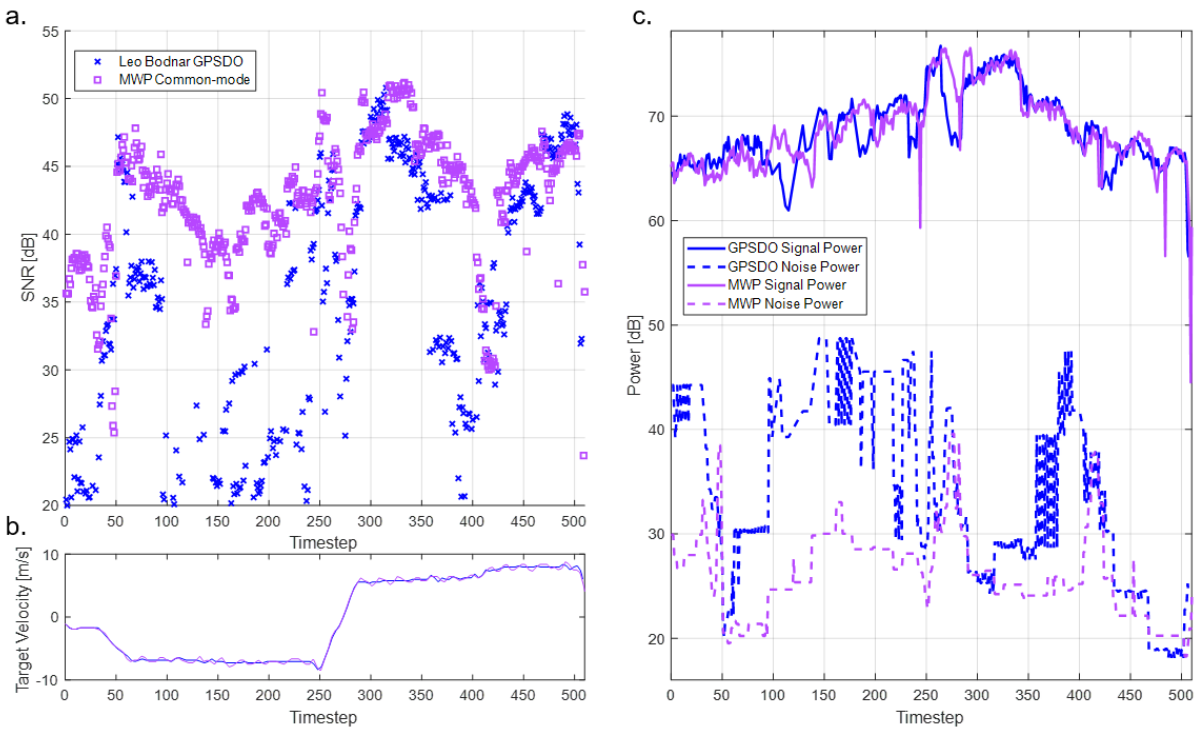

Figure 7.35: (a) SNR of the target as detected by the bistatic radar compared between GPSDO and MWP common mode oscillator configurations, (b) Relative bistatic range rate profile as measured from truth data, (c) Separated signal and noise components throughout the flight.

The SNR of the MWP common-mode is us to 18 dB higher than the GPSDO when within the slow velocity region, indicated within the relative velocity profile (Figure 7.35b) where the target is travelling at an average range rate of 1.7 m/s. Also, at portions of the flight where there is strong clutter, there is a significant decrease in SNR when using the GPSDO configuration. Around timestep 200, the SNR difference approaches 20 dB. The cause of the SNR change is examined in Figure 7.35b where the signal and noise power components are separated. There is no significant difference in the signal power due to the negligible coherent integration loss but it is mostly varying with a function of range as expected. It is rather the noise level that is the main factor in determination of the SNR where the higher phase noise of the Leo Bodnar GPSDO is

causing the overall noise level to rise when the target is in a Doppler cell close to clutter or if the overall clutter power is increased.

Since the target range varies throughout the flight, the SNR for each timestep is scaled to a constant range using the approximate R^4 scaling factor. The SNR is plotted as a function of the Doppler frequency of the target in Figure 7.36, for both the Leo Bodnar GPSDO and MWP common-mode configurations for the flights shown in the spectrograms. The data points are grouped into velocity bins before taking the average and standard deviation (STD).

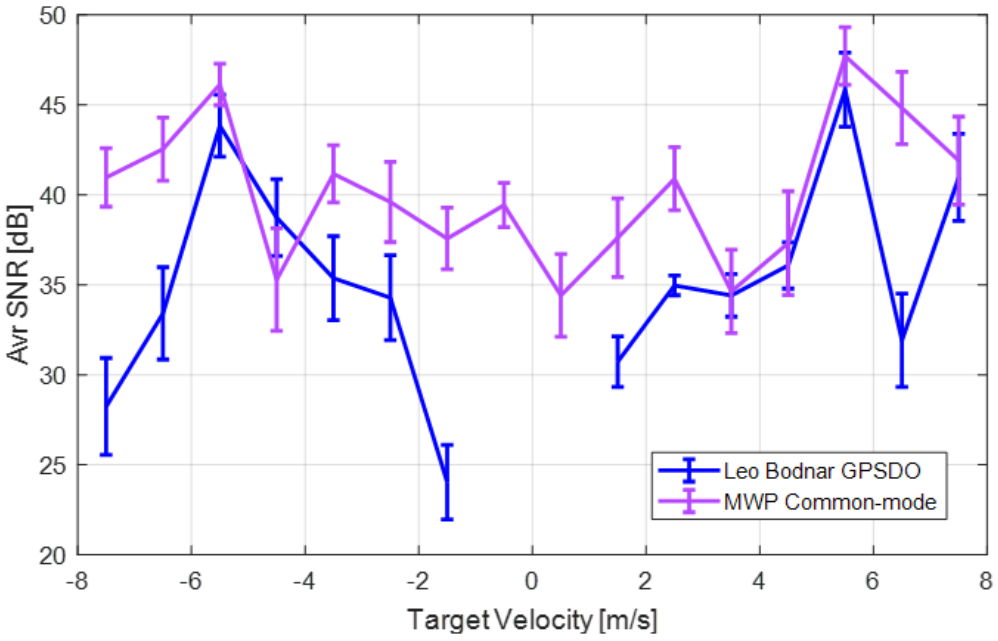

Figure 7.36: Measured average SNR as a function of the target bistatic range rate.

For the majority of target velocity ranges, the MWP common-mode configuration provides greater SNR than the GPSDO. The challenge in detection of slow moving targets is highlighted by the sharp decline in SNR, closer to 0 m/s. The improvement in SNR due to the improved oscillator quality is also evident, especially in the -1 to -2 m/s velocity range where a 14 dB improvement is measured. Also, the average SNR for the Leo Bodnar at absolute relative velocities below 1 m/s is below the detection threshold of 20 dB. Due to the superior close in phase noise of the MWP, the radar is able to detect slower moving targets that were previously undetectable using the GPSDO oscillator.

The probability of detection and the average SNR for the target with different oscillator

configurations is measured by taking into account each of the flights taken in the same location, target and oscillator. The data is taken from different dates and each oscillator configuration contains two sets of flight data. The flights are all performed using the same set of waypoints for the flight trajectory. The two flights consist of a forward and reverse flight, where the target passes through the waypoints in reverse order.

The average SNR throughout each of the respective flights with each oscillator configuration is shown in Figure 7.37. Generally, the trend is the oscillators with lower phase noise at close in offset frequencies such as the MWPOs and Rakon OCXO are producing higher SNR than the other oscillators. Also the oscillators with higher phase noise and had visible clutter broadening in the spectrogram (Leo Bodnar GPSDO and PLO locked to GPS) tend to report lower SNR. It is unexpected to see Rakon OCXO outperform the MWPOs in this regard but this could be due to the varied sample size and variability between the flights. Also, the Rakon OCXO and MWP free-running configurations are undisciplined and not suitable for use in a networked radar without external synchronization. The LNRCLOK, which also has relatively good phase noise performance is reporting similar SNR values to the most stable oscillators. The error bars represent the STD and show variability between the flights. Unfortunately, radar related spurs are occasionally present in the data, at velocities matching the drone target, this is causing large variations in the SNR. The spurs are determined to be unrelated to the oscillator and introduced by components in the radar system.

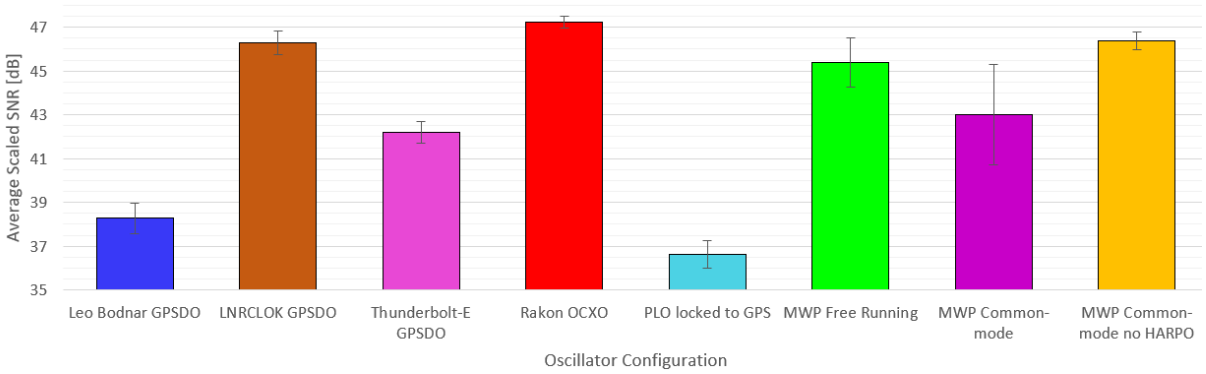

Figure 7.37: Average SNR scaled to constant range, measured from each of the different oscillator types.

The reported PD for each of the oscillators, for the same flights, are shown in Figure 7.38.

Each of the flights uses the same CFAR parameters for consistency. The highest PD is reported from the MWPOs and the Rakon OCXO, all reporting PDs over 0.98. It was mentioned during the analysis of the spectrograms, that the Leo Bodnar GPSDO and PLO reported significantly more missed detections. This results in a much lower PD throughout the flights. However, the main cause is due to the oscillator spurs rather than the phase noise.

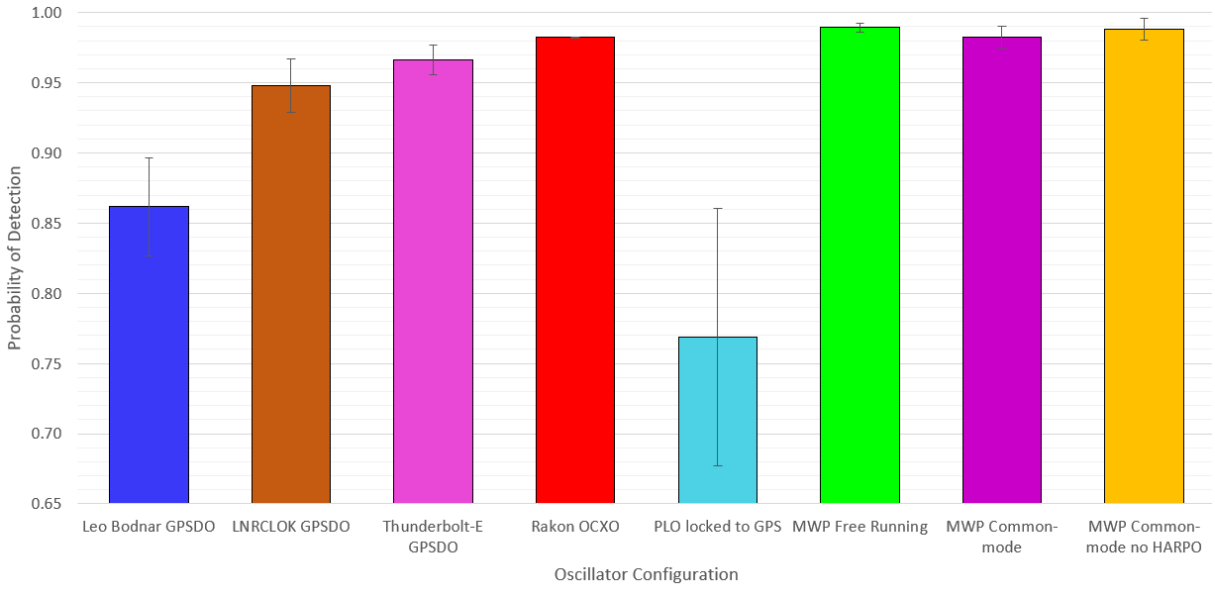

Figure 7.38: PD measured from each of the different oscillator types.

The SNR and PD show that the Leo Bodnar GPSDO and PLO locked to GPS clearly have a lower level of detection performance than the other oscillator configurations used within the experiments, for the particular flight patterns performed. However, the wider picture becomes more complex, since the level of phase noise and performance degradations are dependant on many other factors (excluding oscillator stability), especially the location and the contribution of other components in the radar system.

Within this chapter, we have demonstrated the use of ultra-stable cavities and photonic microwave generation in a radar system and compared their performance with GPSDOs. It has been shown that the timing error is reduced by more than 2 orders of magnitude using this configuration. The results infer that lower requirements for the synchronization interval would be required, no coherent integration loss up to 60 s with the L-band radar network and increased sensitivity in cluttered environments. Successful detection of a controlled drone target using the

MWP oscillator has been presented, outperforming the Leo Bodnar GPSDO at low velocities. Also, the lower phase noise oscillators are found to have better detection performance in general. However, it is difficult to quantify in terms of an SNR improvement due to the variation among the flights and small data set.

This work presents an alternative method for a disciplined network radar configuration. Future radar systems can be designed with the high stability LO in mind, the current limitation is with the high-frequency noise induced by synthesizers, PLLs and mixers within the radar RF chain, limiting to the 100 fs regime, and the background noise floor to -96 dBc/Hz. The full quantum enabled radar is believed to be able to achieve similar performance levels, without the need for a fibre link, by disciplining the oscillators to an atomic reference. Overall the methods shown using MWP common-mode are very powerful, they provide a disciplined oscillator configuration to static ground based radar systems while not relying on GNSS and also providing a significant improvement in terms of synchronization accuracy and reduced phase noise.

7.3 Future Outlook

This work on the use of common-mode MWP is as far as I am aware, the first use of this method for synchronization of network radars. There are areas for improvement to allow for even better synchronization accuracy such as better characterization of the cavity drift, changing the mechanism for the OFC repetition rate dedrift, better reference oscillators for the initial calibration. Firstly, for better cavity characterization, currently the dedrift is only applied by linearly drifting the lockpoint for the OFC repetition rate lock. The cavity is assumed in this case to be linear which is not fully accurate. It may be of use to better characterise the cavity to allow for better long term predictions of the cavity drift such has been done with other F-P cavities in the literature [181] [182] [183]. Second, the mechanism of applying the dedrift the resolution of the drift rate is limited to 1 mHz/s which is likely due to software limitations and frequency resolution limitations of the DDS. Applying the dedrift to the cavity output directly can allow for better control of the drift as well as eliminating the need for a dedrift within the frequency

combs at all nodes of the network. Although absolute frequency precision is not necessary for this method, a shift from the nominal frequency could have other adverse effects throughout the radar chain. Therefore, an initial calibration is performed before starting the radars to ensure the repetition rate of the OFC is as close to 125 MHz as possible. Currently this is done using the Leo Bodnar GPSDO but potentially a more stable oscillator could help with making this initial calibration more efficient.

These points mentioned relate to the synchronization accuracy, but improvements to the overall stability and phase noise of the oscillators are also possible in the future, beyond what is reported in this work. The maximum short term stability of the MWPO is determined by the F-P cavity. The F-P cavity used within this work has a stability of 5 x 10^{-15}, but state of the art cavities have been demonstrated to reach stabilities below 10^{-16} [73] [71]. It is expected that a better ORS would result in even better phase noise performance of the oscillator. The long term stability is also area of interest, especially for the Quantum enabled radar project. Implementation of the atomic reference is intended to compensate for the cavity drift. In a scenario where each radar is equipped with an optical atomic clock, the radar systems can operate in a 'free-running' configuration while also being in a disciplined (to the atomic transition) state, without the need for a fibre link between the nodes, an external synchronization or reliance on GNSS. This is not only relevant for L-band radar systems but any sensor network or any distributed system that requires synchronized local clocks. However, in the case of radar networks, it is crucial to verify both the system requirements and whether the radar can effectively utilize the oscillator's stability. For the L-band staring radar network, there should first be a consideration as to how to overcome current bottlenecks in the system as any further improvement in the phase noise is likely to be lost.

The major limitation of the radar system has been identified as the PLL upconversion which would be expected due to the inherent phase noise multiplication resulting from a frequency multiplication [115]. However, the phase noise inherent within the PLL from the reference synthesizer, results in additional additive noise that is above the level expected from the MWPO as discussed in Chapter 7.3.3. It is shown that the MWPO PN is bottlenecked by the upconversion

from f_{LO} to f_c and there is still room for improvement as the radar is still phase noise limited in some circumstances. For example in Figure 7.30c, the MWPO white phase noise floor is still 10 dB above the thermal limit and there can be situations where this is even higher. The ideal situation would be to remove the PLL upconversion since high frequency and low phase noise signals are possible with MWP. Future radar architectures with low phase noise requirements can be designed with this in mind since it is possible to generate different frequency signals from an OFC that are coherent with each other [131]. Within the current radar system, a theoretical phase noise improvement of the transmitted signal is shown in Figure 7.39 if a signal at f_c were given directly rather than and upconversion from f_{LO}. It is shown that after PRF aliasing there is a potential of 35 dB decrease in the phase noise floor which would ensure the radar is essentially never phase noise limited.

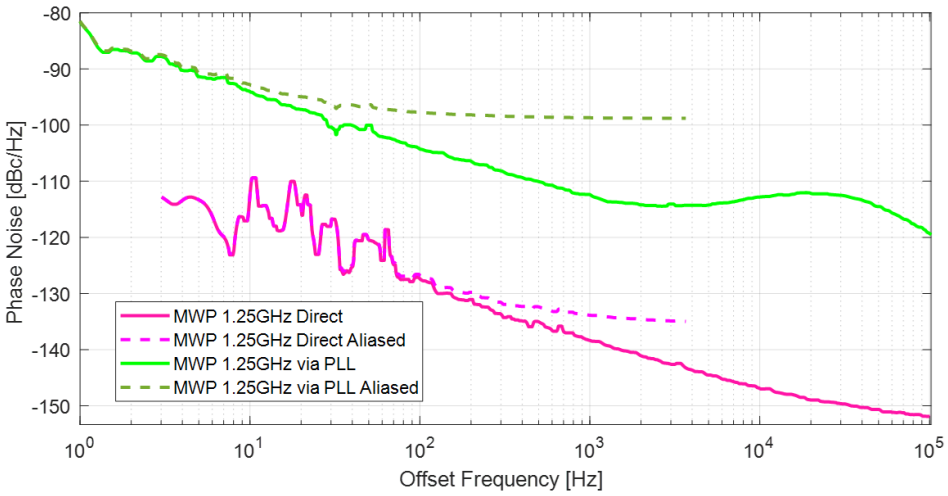

Figure 7.39: Potential phase noise if bypassing PLL.

However, this is assuming that there are no other sources of noise, which is not going to be the case. It is known that there are phase noise contributions from the buffer unit, the mixers, vector modulator and the PLL within the receiver node to mix the signal down to IF. Now that the oscillators are able to provide stability far beyond what the radar system can handle, a rethink into modern radar architecture is required for suppression of phase noise in dense urban environments. A possibility is to design a radar such that the local oscillator is in the optical domain and all the required frequencies for generating the transmitted waveform, the

receiver mixing signal and the ADC clock are all generated using MWP by careful design of the frequency comb repetition rate, and the radar frequencies involved. My opinion is that this is more likely to be achieved by moving towards photonic based radar systems where as much is performed in the optical domain as possible. It has been acknowledged that photonic based radar can potentially provide the benefit of low phase noise [128], and there are various cases of existing photonic based radars as discussed in Chapter 3.7 but to my knowledge it has not been demonstrated using OFD for this purpose. The remaining sources of potential phase noise could be the RF amplifier (which would be unavoidable for high power transmission) and vibration of the receiver array faces.

Along with the effect of phase noise within a single CPI, there is the need for highly stable and accurate oscillators for minimizing timing error in the long term. The MWP common-mode configuration has shown to perform significantly better than GPSDOs in that regard. As was observed in Figure 7.27, the high frequency noise added via the synthesizer for the upconversion, limits the noise floor at 100 fs. Therefore, it was not possible to measure the timing error contribution from the MWP common mode configuration within a typical CPI of 0.5 - 2 s. For this L-band staring radar network, it does not cause an issue since the radar would not benefit from a synchronization accuracy below 100 fs. On the other hand, this may not be the case for radar systems with high range resolution and operating at much higher bands where there are higher requirements for achieving full coherent integration gain.

This work was mostly focused on a ground based radar network, and although this is a good place to start, there are many more applications of radar networks which present additional challenges which make the common mode regime impractical. Such examples are if there is no fibre link connecting each node and they also require high synchronization accuracy. In this case an alternative solution could be to employ free space links [184]. However, this is limited by visibility. Another situation is when the nodes are on moving platforms such as a ship, a plane or even a drone. These present the challenge of reduction of SWAP. The current system used is transportable but still is too large in size for most of these applications. I imagine that this could be solved with the push towards integrated microwave photonics as discussed in Chapter 3.6.

PIC based microwave generation from an F-P cavity has been demonstrated, achieving much lower phase noise achievable from RF based synthesizers [137]. Not quite achieving the level of stability of a bulk MWP system such as the one in this work but the considerable reduction in SWAP makes this viable for use on the examples of moving platforms mentioned.

To provide the long term stability, when the use of a direct link is not possible, the only feasible solution that does not require frequent communication between the different nodes is the use of an optical atomic clock. The prospect of getting a strontium optical clock and microwave generation all within a chip, is something to look towards in the future. This would be the ultimate vision of the quantum enabled radar project and likely to be the standard for synchronization of remote networks in the future. There is still a way to go, with optical atomic clocks still being in their infancy but there are signs of progress with recent commercial atomic clocks such as the Infleqtion Tiqker [185] based on Rubidium 87 and Vector Atomic Evergreen-30 [186] based on Iodine, both reaching 10^{-15} region within a 3U form factor. Strontium optical lattice clocks are reaching 10^{-18} levels are there are a few systems that have been made transportable such as shown in Riken [67] and PTB [66], but these are not near the level of SWAP or robustness to be used on a moving sensor platform. There would need to be major technological advancements to get the physics package form factor down to this level and to reduce the power requirements of the laser systems involved.

To summarise, this work provides a useful insight into high performance radar synchronization with optical clock technologies and it will be interesting to see what the future holds, for the development of both radar systems and oscillator technology.

Chapter 8

Conclusion

This work has studied the effects of the LO on L-band staring radar systems both in simulation and experimentation. Various methods of synchronization have been proposed, demonstrated and characterised using these systems. Synchronization can be applied both via software or hardware, each with their own respective pros and cons. Overall the radar systems have been synchronized using various approaches, maximizing the coherent integration gain and minimizing the noise floor, ensuring optimal conditions for detection of S-UAV targets in the urban environment and giving insights that carry over to other radar systems and applications.

A radar model consisting of the full radar receiver chain has been developed, mimicking the hardware of the real system. Its flexibility allows for the insertion of multiple radar nodes with custom oscillator parameters and the simulation of a custom environment and range of targets. It has proven to be a high fidelity simulation of the network, successfully reproducing the level of performance from the real system when matching parameters are used. Also, it has been a useful tool in the verification of the various software synchronization approaches developed within the work.

Understanding the effect of coherency in a radar network has always been a difficulty. This work has aided in providing clarity by developing on some new and existing measures of radar synchronization performance and stability.

In a monostatic radar, the synchronization approach is simple due to the co-located transmitter

and receiver. However, the effects of phase noise on radar sensitivity have been analysed. It was determined that low frequency noise is mostly cancelled out due to the inherent phase cancellation. Instead the performance is mostly solely determined by the high frequency phase noise or the white noise floor.

Initially, the radar systems had no synchronization mechanisms in place, leading to range and frequency errors in the output. Within this work, various software based approaches are developed. Ranging from the existing direct signal synchronization and then improving on this with the novel range profile correlation method which allows for the calibration of the range measurements for static sensors without the need for a direct line of sight. The residual phase errors are then corrected using the MRPC method which is a novel approach to utilize multiple reference targets for estimating and correcting the phase error on the remote receiver. This has proven to provide improved performance over the standard method of using the direct breakthrough signal for phase estimation.

The main focus of this study is the use of optical clock on networked radar systems. Networked systems that cannot rely on the software synchronization approaches, require both stable and accurate local oscillators which is typically achieved by disciplining each of the local oscillators to a common reference. The use of different GPSDOs in the L-band staring radar network has been explored and found to provide sufficient performance in this application. The quality of the oscillator within has been determined as the main factor in determining the performance since the reduced phase noise is beneficial for detection. However, for some applications, it is importance to not have total reliance on the GNSS infrastructure since it may not always be operational whether intentional or unintentional. A method has been developed to make use of various advantages of operating in the optical domain such as ultra-stable F-P cavity oscillators and low noise and low loss fibre dissemination. This method of MWP common-mode has enabled for significant improvements over GPSDOs in terms of synchronization performance reaching synchronization accuracy of 14 ps over a period of 600 s.

The use of ultra-stable optical references enable both low phase noise LOs as well as high levels of synchronization for remote nodes. This can be even more beneficial for applications

requiring high frequency, low phase noise signals such as X-Band systems and beyond where the synchronization requirements are higher and performance gap between photonic oscillators and RF oscillators are much wider. However, to take full benefit of the oscillator phase noise, a rethink into modern radar architecture is required such that PLL upconversions are avoided and as much of the processing as possible is performed in the optical domain.

References

[1] R.J. James. A history of radar. *IEE Review*, 35:343, 1989.

[2] E. Perl. Review of airport surface movement radar technology. In *2006 IEEE Conference on Radar*, pages 692–695. IEEE.

[3] R.A. Gray and P.S. Maybeck. An integrated gps/ins/baro and radar altimeter system for aircraft precision approach landings. In *Proceedings of the IEEE 1995 National Aerospace and Electronics Conference. NAECON 1995*, pages 161–168. IEEE.

[4] Christian Waldschmidt, Juergen Hasch, and Wolfgang Menzel. Automotive radar - from first efforts to future systems. *IEEE Journal of Microwaves*, 1:135–148, 1 2021.

[5] Mark Yeary, Boon Cheong, James Kurdzo, Tian you Yu, and Robert Palmer. A brief overview of weather radar technologies and instrumentation. *IEEE Instrumentation and Measurement Magazine*, 17:10–15, 10 2014.

[6] Fabio Tosti and Lara Pajewski. *Applications of Radar Systems in Planetary Sciences: An Overview*, pages 361–371. 2015.

[7] Li Neng-Jing. Radar eccms new area: anti-stealth and anti-arm. *IEEE Transactions on Aerospace and Electronic Systems*, 31:1120–1127, 7 1995.

[8] Dusan Kocur, Jana Rovnakova, and Daniel Urdzik. Mutual shadowing effect of people tracked by the short-range uwb radar. In *2011 34th International Conference on Telecommunications and Signal Processing (TSP)*, pages 302–306. IEEE, 8 2011.

[9] Darren Griffiths, Mohammed Jahangir, Daniel White, Jithin Kannanthara, Gwynfor Donlan, Chris J. Baker, Yeshpal Singh, and Michail Antoniou. Urban clutter analysis for drone detection using l-band staring radar. In *2023 IEEE International Radar Conference (RADAR)*, pages 1–6. IEEE, 11 2023.

[10] Nicholas J. Willis. *Bistatic Radar*. 2004.

[11] D. Griffiths, M. Jahangir, J. Kannanthara, C. J. Baker, M. Antoniou, and Y. Singh. Direct signal synchronization for staring passive bistatic radar. *International Conference on Radar Systems (RADAR 2022)*, pages 220–225, 2022.

[12] Xin Quan, Ying Liu, Shihai Shao, Chuan Huang, and Youxi Tang. Impacts of phase noise on digital self-interference cancellation in full-duplex communications. *IEEE Transactions on Signal Processing*, 65:1881–1893, 4 2017.

[13] Simon Lewis and Michael Inggs. Synchronization of coherent netted radar using white rabbit compared with one-way multichannel gpsdos. *IEEE Transactions on Aerospace and Electronic Systems*, 57:1413–1422, 6 2021.

[14] Feng Hong, Robert Wang, Zhimin Zhang, Pingping Lu, and Timo Balz. Integrated time and phase synchronization strategy for a multichannel spaceborne-stationary bistatic sar system. *Remote Sensing*, 8:5–8, 2016.

[15] George W. Stimson. *Introduction to Airborne Radar*. 1998.

[16] D. Curtis Schleher. *MTI and Pulsed Doppler Radar*. Artech House, 1991.

[17] Gordon Oswald and Chris Baker. *Holographic Staring Radar*. Institution of Engineering and Technology, 12 2021.

[18] Alberto Moreira, Pau Prats-Iraola, Marwan Younis, Gerhard Krieger, Irena Hajnsek, and Konstantinos P. Papathanassiou. A tutorial on synthetic aperture radar. *IEEE Geoscience and Remote Sensing Magazine*, 1:6–43, 3 2013.

[19] Mark A. Richards, James A. Scheer, and William A. Holm. *Principles of modern radar: Basic principles*. 2010.

[20] Wulf Dieter Wirth. *Radar techniques using array antennas*. 2013.

[21] Attenuation by atmospheric gases - itu-r, 2012.

[22] Eugene F. Knott, John F. Shaeffer, and Michael T. Tuley. *Radar Cross Section*. 2004.

[23] E. J. Kelly, I. S. Reed, and W. L. Root. The detection of radar echoes in noise. i. *Journal of the Society for Industrial and Applied Mathematics*, 8:309–341, 6 1960.

[24] Bjorn Staufenbiel, Olaf Lambert, and Michael Krist. Noise figure verification and optimization of an undersampled software defined radio based radar receiver for a phased array radar system. In *2018 48th European Microwave Conference (EuMC)*, pages 894–897. IEEE, 9 2018.

[25] Enrico Rubiola. *Phase Noise and Frequency Stability in Oscillators*. Cambridge University Press, 11 2008.

[26] Gerhard Krieger and Marwan Younis. Impact of oscillator noise in bistatic and multistatic sar. *IEEE Geoscience and Remote Sensing Letters*, 3:424–428, 7 2006.

[27] Hans C. Strifors. Bistatic radar cross-sections of low-signature targets, 2004.

[28] Cecilia Clivati, Roberto Aiello, Giuseppe Bianco, Claudio Bortolotti, Paolo De Natale, Valentina Di Sarno, Pasquale Maddaloni, Giuseppe Maccaferri, Alberto Mura, Monia Negusini, Filippo Levi, Federico Perini, Roberto Ricci, Mauro Roma, Luigi Santamaria Amato, Mario Siciliani de Cumis, Matteo Stagni, Alberto Tuozzi, and Davide Calonico. Common-clock very long baseline interferometry using a coherent optical fiber link. *Optica*, 7:1031, 8 2020.

[29] J S Sandenbergh. Synchronising coherent networked radar using low-cost gps-disciplined oscillators. 2019.

[30] Piers J. Beasley, Nial Peters, Colin Horne, and Matthew A. Ritchie. Global navigation satellite systems disciplined oscillator synchronisation of multistatic radar. *IET Radar, Sonar and Navigation*, 18:23–40, 1 2024.

[31] M. Weiss. Synchronisation of bistatic radar systems. In *IEEE International IEEE International IEEE International Geoscience and Remote Sensing Symposium, 2004. IGARSS '04. Proceedings. 2004*, pages 1750–1753. IEEE.

[32] Wen-Qin Wang. Gps-based time and phase synchronization processing for distributed sar. *IEEE Transactions on Aerospace and Electronic Systems*, 45:1040–1051, 7 2009.

[33] Another step in the journey to quantum-enabled radar, 10 2022.

[34] Alexander Aeppli, Kyungtae Kim, William Warfield, Marianna S. Safronova, and Jun Ye. A clock with 8 times 10-19 systematic uncertainty. 3 2024.

[35] T.E. Parker. Environmental factors and hydrogen maser frequency stability. *IEEE Transactions on Ultrasonics, Ferroelectrics and Frequency Control*, 46:745–751, 5 1999.

[36] A Clairon, P Laurent, G Santarelli, S Ghezali, S N Lea, and M Bahoura. A cesium fountain frequency standard: Preliminary results. *IEEE TRANSACTIONS ON INSTRUMENTATION AND MEASUREMENT*, 4, 1995.

[37] Rasmus Flytkjær, Farooq Sabri, Romain Esteve, Wesley Jessie, Tom Goulding, and Patrick Mathewson. The economic impact on the uk of a disruption to gnss, 2023.

[38] Fred L Walls and Andrea Demarchi. Rf spectrum of a signal after frequency multiplication; measurement and comparison with a simple calculation, 1975.

[39] S. Levantino, L. Romano, S. Pellerano, C. Samori, and A.L. Lacaita. Phase noise in digital frequency dividers. *IEEE Journal of Solid-State Circuits*, 39:775–784, 5 2004.

[40] Markus Gellesch, Richard Barron, Jonathan M. Jones, Alok Singh, Qiushuo Sun, Kai Bongs, and Yeshpal Singh. An optical lattice clock testbed system for the iqclock project

demonstrator. In *2020 Joint Conference of the IEEE International Frequency Control Symposium and International Symposium on Applications of Ferroelectrics (IFCS-ISAF)*, pages 1–2. IEEE, 7 2020.

[41] Abhilash Jha, Alok Singh, Yogeshwar Kale, Jordan Wayland, Yuheng Huyan, Qiushuo Sun, Jonathan Jones, Markus Gellesch, Kai Bongs, and Yeshpal Singh. Towards the development of an optical lattice clock testbed setup for the iqclock project. In *2023 Conference on Lasers and Electro-Optics Europe and European Quantum Electronics Conference (CLEO/Europe-EQEC)*, pages 1–1. IEEE, 6 2023.

[42] Ums-compact ultrastable microwave generator.

[43] Anne Curtis. Tutoral - optical clocks, 2024.

[44] Fritz Riehle, Patrick Gill, Felicitas Arias, and Lennart Robertsson. The cipm list of recommended frequency standard values: Guidelines and procedures. *Metrologia*, 55:188–200, 2 2018.

[45] Patrick Gill. Timing and synchronisation with atomic clocks, 2019.

[46] L Essen and J V L Parry. Royal society of london the caesium resonator as a standard of frequency and time, 1957.

[47] Paul Horowitz. "unprecedented spectral purity", 2022.

[48] William Riley. A history of the rubidium frequency standard. *IEEE*, 2019.

[49] N. Poli, C. W. Oates, P. Gill, and G. M. Tino. Optical atomic clocks. 1 2014.

[50] T.W. Hänsch and A.L. Schawlow. Cooling of gases by laser radiation. *Optics Communications*, 13:68–69, 1 1975.

[51] William Phillips. Laser cooling and trapping of neutral atoms. *Nobel Lecture*, 1997.

[52] Jun Ye, Long Sheng Ma, and John L. Hall. Molecular iodine clock. *Physical Review Letters*, 87:270801, 12 2001.

[53] J C Bergquist, U Tanaka, R E Drullinger, W M Itano, D J Wineland, S A Diddams, L Hollberg, E A Curtis, C W Oates, and T H Udem. A mercury-ion optical clock*.

[54] T Rosenband. Frequency ratio of al+ and hg+ single-ion optical clocks; metrology at the 17th decimal place. *Science*, 2008.

[55] Hidetoshi Katori, Tetsuya Ido, and Makoto Kuwata-Gonokami. Optimal design of dipole potentials for efficient loading of sr atoms. *Journal of the Physical Society of Japan*, 68:2479–2482, 1999.

[56] Masao Takamoto, Feng Lei Hong, Ryoichi Higashi, and Hidetoshi Katori. An optical lattice clock. *Nature*, 435:321–324, 5 2005.

[57] Yogeshwar B. Kale, Alok Singh, Markus Gellesch, Jonathan M. Jones, David Morris, Matthew Aldous, Kai Bongs, and Yeshpal Singh. Field deployable atomics package for an optical lattice clock. *Quantum Science and Technology*, 7, 10 2022.

[58] Xinye Xu, Thomas H. Loftus, John L. Hall, Alan Gallagher, and Jun Ye. Cooling and trapping of atomic strontium. *Journal of the Optical Society of America B*, 20:968, 5 2003.

[59] Richard Hobson. An optical lattice clock with neutral strontium. 2016.

[60] T. L. Nicholson, S. L. Campbell, R. B. Hutson, G. E. Marti, B. J. Bloom, R. L. McNally, W. Zhang, M. D. Barrett, M. S. Safronova, G. F. Strouse, W. L. Tew, and J. Ye. Systematic evaluation of an atomic clock at 2 × 10-18 total uncertainty. *Nature Communications*, 6, 4 2015.

[61] Jie Li, Xing Yang Cui, Zhi Peng Jia, De Quan Kong, Hai Wei Yu, Xian Qing Zhu, Xiao Yong Liu, De Zhong Wang, Xiang Zhang, Xin Yun Huang, Ming Yi Zhu, Yu Meng Yang, Yi Hu, Xiang Pei Liu, Xiao Min Zhai, Peng Liu, Xiao Jiang, Ping Xu, Han Ning Dai, Yu Ao Chen, and Jian Wei Pan. A strontium lattice clock with both stability and uncertainty below 5 × 10 18. *Metrologia*, 61, 2 2024.

[62] Stephan Falke, Nathan Lemke, Christian Grebing, Burghard Lipphardt, Stefan Weyers, Vladislav Gerginov, Nils Huntemann, Christian Hagemann, Ali Al-Masoudi, Sebastian Häfner, Stefan Vogt, Uwe Sterr, and Christian Lisdat. A strontium lattice clock with 3 × 10-17 inaccuracy and its frequency. *New Journal of Physics*, 16, 2014.

[63] W. F. McGrew, X. Zhang, R. J. Fasano, S. A. Schäffer, K. Beloy, D. Nicolodi, R. C. Brown, N. Hinkley, G. Milani, M. Schioppo, T. H. Yoon, and A. D. Ludlow. Atomic clock performance enabling geodesy below the centimetre level. *Nature*, 564:87–90, 12 2018.

[64] M. Schioppo, R. C. Brown, W. F. McGrew, N. Hinkley, R. J. Fasano, K. Beloy, T. H. Yoon, G. Milani, D. Nicolodi, J. A. Sherman, N. B. Phillips, C. W. Oates, and A. D. Ludlow. Ultrastable optical clock with two cold-atom ensembles. *Nature Photonics*, 11:48–52, 1 2017.

[65] S. M. Brewer, J. S. Chen, A. M. Hankin, E. R. Clements, C. W. Chou, D. J. Wineland, D. B. Hume, and D. R. Leibrandt. Al+ 27 quantum-logic clock with a systematic uncertainty below 10-18. *Physical Review Letters*, 123, 7 2019.

[66] Stefan Vogt, Sebastian Häfner, Jacopo Grotti, Silvio Koller, Ali Al-Masoudi, Uwe Sterr, and Christian Lisdat. A transportable optical lattice clock. In *Journal of Physics: Conference Series*, volume 723. Institute of Physics Publishing, 7 2016.

[67] Noriaki Ohmae, Masao Takamoto, Yosuke Takahashi, Motohide Kokubun, Kuniya Araki, Andrew Hinton, Ichiro Ushijima, Takashi Muramatsu, Tetsuo Furumiya, Yuya Sakai, Naoji Moriya, Naohiro Kamiya, Kazuaki Fujii, Ryuya Muramatsu, Toshihiro Shiimado, and Hidetoshi Katori. Transportable strontium optical lattice clocks operated outside laboratory at the level of 10 18 uncertainty. *Advanced Quantum Technologies*, 4, 8 2021.

[68] S. Origlia, M. S. Pramod, S. Schiller, Y. Singh, K. Bongs, R. Schwarz, A. Al-Masoudi, S. Dörscher, S. Herbers, S. Häfner, U. Sterr, and Ch. Lisdat. Towards an optical clock for

space compact, high-performance optical lattice clock based on bosonic atoms. *Physical Review A*, 98:053443, 11 2018.

[69] Scott Diddams, Frank Quinlan, and Peter Rakich. Compact ultrastable lasers supporting fundamental physics in space, 2023.

[70] R. Paschotta. *Narrow-linewidth Lasers - an encyclopedia article*. RP Photonics AG, 2007.

[71] Miguel Dovale Álvarez. Optical cavities for optical atomic clocks, atom interferometry and gravitational-wave detection, 2018.

[72] M. Schioppo, J. Kronjäger, A. Silva, R. Ilieva, J. W. Paterson, C. F.A. Baynham, W. Bowden, I. R. Hill, R. Hobson, A. Vianello, M. Dovale-Álvarez, R. A. Williams, G. Marra, H. S. Margolis, A. Amy-Klein, O. Lopez, E. Cantin, H. Álvarez Martínez, R. Le Targat, P. E. Pottie, N. Quintin, T. Legero, S. Häfner, U. Sterr, R. Schwarz, S. Dörscher, C. Lisdat, S. Koke, A. Kuhl, T. Waterholter, E. Benkler, and G. Grosche. Comparing ultrastable lasers at 7 × 10 17 fractional frequency instability through a 2220 km optical fibre network. *Nature Communications*, 13, 12 2022.

[73] Jialiang Yu. Cryogenic silicon fabry-perot resonator with al 0.92 ga 0.08 as/gaas mirror coatings, 2023.

[74] Alexandre Didier, Jacques Millo, Clément Lacroûte, Morvan Ouisse, Jérôme Delporte, Vincent Giordano, Enrico Rubiola, and Yann Kersalé. Design of an ultra-compact reference ule cavity. In *Journal of Physics: Conference Series*, volume 723. Institute of Physics Publishing, 7 2016.

[75] Stephen Webster and Patrick Gill. Force-insensitive optical cavity. 8 2011.

[76] R W P Drever, J L Hall, F V Kowalski, J Hough, G M Ford, A J Munley, and H Ward. Laser phase and frequency stabilization using an optical resonator, 1983.

[77] Eric D. Black. An introduction to pound-drever-hall laser frequency stabilization. *American Journal of Physics*, 69:79–87, 1 2001.

[78] Thomas Kessler, Thomas Legero, and Uwe Sterr. Thermal noise in optical cavities revisited. *Journal of the Optical Society of America B*, 29:178, 1 2012.

[79] John M. Robinson, Eric Oelker, William R. Milner, Wei Zhang, Thomas Legero, Dan G. Matei, Fritz Riehle, Uwe Sterr, and Jun Ye. Crystalline optical cavity at 4 k with thermal-noise-limited instability and ultralow drift. *Optica*, 6:240, 2 2019.

[80] D. G. Matei, T. Legero, S. Häfner, C. Grebing, R. Weyrich, W. Zhang, L. Sonderhouse, J. M. Robinson, J. Ye, F. Riehle, and U. Sterr. 1.5 um lasers with sub 10 mhz linewidth. 2 2017.

[81] Ors ultrastable laser system.

[82] P Defraigne and C Bruyninx. Gps time and frequency transfer: State of the art, 2005.

[83] Ahmed Elmaghraby, Thomas Krawinkel, and Steffen Schon. Inventory of error sources limiting gnss-based frequency transfer. In *2022 Joint Conference of the European Frequency and Time Forum and IEEE International Frequency Control Symposium, EFTF/IFCS 2022 - Proceedings*. Institute of Electrical and Electronics Engineers Inc., 2022.

[84] Long-Sheng Ma, Peter Jungner, Jun Ye, and John L Hall. Delivering the same optical frequency at two places: accurate cancellation of phase noise introduced by an optical fiber or other time-varying path, 1994.

[85] SVG: Sassospicco Raster: Alexwind. Optical fiber transmission windows.

[86] Etienne Cantin, Mads Tonnes, Rodolphe Le Targat, Anne Amy-Klein, Olivier Lopez, and Paul Eric Pottie. An accurate and robust metrological network for coherent optical frequency dissemination. *New Journal of Physics*, 23, 5 2021.

[87] G B Hocker. Fiber-optic sensing of pressure and temperature, 1979.

[88] T R Woliński. Polarization in optical fibers, 1999.

[89] F. Guillou-Camargo, V. Ménoret, E. Cantin, O. Lopez, N. Quintin, E. Camisard, V. Salmon, J.-M. Le Merdy, G. Santarelli, A. Amy-Klein, P.-E. Pottie, B. Desruelle, and C. Chardonnet. First industrial-grade coherent fiber link for optical frequency standard dissemination. *Applied Optics*, 57:7203, 9 2018.

[90] O Terra, G Grosche, H Schnatz, T Udem, Z Lu, L Wang, W Ertmer, J Friebe, A Pape, E m Rasel, M Riedmann, and T Wub. Brillouin amplification in phase coherent transfer of optical frequencies over 480 km fiber, 2010.

[91] C Clivati, G Bolognini, D Calonico, S Faralli, F Levi, A Mura, and N Poli. Distributed raman optical amplification in phase coherent transfer of optical frequencies, 2013.

[92] Sebastian Koke, Alexander Kuhl, Thomas Waterholter, Sebastian M F Raupach, Olivier Lopez, Etienne Cantin, Nicolas Quintin, Anne Amy-Klein, Paul-Eric Pottie, and Gesine Grosche. Combining fiber brillouin amplification with a repeater laser station for fiber-based optical frequency dissemination over 1400 km. *New Journal of Physics*, 21:123017, 12 2019.

[93] P A Williams, W C Swann, and N R Newbury. High-stability transfer of an optical frequency over long fiber-optic links, 2008.

[94] N R Newbury, P A Williams, and W C Swann. Coherent transfer of an optical carrier over 251 km, 2007.

[95] Katharina Predehl. A 920 km optical fiber link for frequency metrology at the 19th decimal place, 2012.

[96] Yoshitomo Okawachi, Bok Young Kim, Michal Lipson, and Alexander L. Gaeta. Chip-scale frequency combs for data communications in computing systems. *Optica*, 10:977, 8 2023.

[97] Lukasz A. Sterczewski, Jonas Westberg, Yang Yang, David Burghoff, John Reno, Qing Hu, and Gerard Wysocki. Terahertz spectroscopy of gas mixtures with dual quantum cascade laser frequency combs. *ACS Photonics*, 7:1082–1087, 5 2020.

[98] H. Schnatz, B. Lipphardt, J. Helmcke, F. Riehle, and G. Zinner. First phase-coherent frequency measurement of visible radiation. *Physical Review Letters*, 76:18, 1 1996.

[99] H R Telle, D Meschede, and T W Hansch. Realization of a new concept for visible frequency division: phase locking of harmonic and sum frequencies, 1990.

[100] A. I. Ferguson, J. N. Eckstein, and T. W. Hänsch. A subpicosecond dye laser directly pumped by a mode-locked argon laser. *Journal of Applied Physics*, 49:5389–5391, 11 1978.

[101] M. Niering, R. Holzwarth, J. Reichert, P. Pokasov, Th. Udem, M. Weitz, T. W. Hänsch, P. Lemonde, G. Santarelli, M. Abgrall, P. Laurent, C. Salomon, and A. Clairon. Measurement of the hydrogen 1s 2s transition frequency by phase coherent comparison with a microwave cesium fountain clock. *PHYSICAL REVIEW LETTERS*, 2000.

[102] Kluwer Academic, Springer Norwell, Ma Jun Ye, and Steven T Cundiff Editors. Femtosecond optical frequency comb: Principle, operation, and applications.

[103] Andreas Trabesinger. Nobel prize 2005: Glauber, hall and hänsch. *Nature Physics*, 1:930–930, 11 2005.

[104] Scott A. Diddams, Kerry Vahala, and Thomas Udem. Optical frequency combs coherently uniting the electromagnetic spectrum. *Science*, 369, 7 2020.

[105] L C Sinclair, J.-D Deschênes, L Sonderhouse, W C Swann, I H Khader, E Baumann, N R Newbury, and I Coddington. A compact optically-coherent fiber frequency comb.

[106] Klaus Döringshoff, Franz B. Gutsch, Vladimir Schkolnik, Christian Kürbis, Markus Oswald, Benjamin Pröbster, Evgeny V. Kovalchuk, Ahmad Bawamia, Robert Smol, Thilo Schuldt, Matthias Lezius, Ronald Holzwarth, Andreas Wicht, Claus Braxmaier, Markus

Krutzik, and Achim Peters. Iodine frequency reference on a sounding rocket. *Physical Review Applied*, 11:054068, 5 2019.

[107] Wolfgang Hänsel, Heinar Hoogland, Michele Giunta, Sebastian Schmid, Tilo Steinmetz, Ralf Doubek, Peter Mayer, Sven Dobner, Carsten Cleff, Marc Fischer, and Ronald Holzwarth. All polarization-maintaining fiber laser architecture for robust femtosecond pulse generation. *Applied Physics B: Lasers and Optics*, 123, 1 2017.

[108] J. M. Dudley and J. R. Taylor, editors. *Supercontinuum Generation in Optical Fibers*. Cambridge University Press, 4 2010.

[109] Florian W. Helbing, Günter Steinmeyer, and Ursula Keller. Carrier-envelope offset phase-locking with attosecond timing jitter. *IEEE Journal on Selected Topics in Quantum Electronics*, 9:1030–1040, 7 2003.

[110] Michele Giunta, Wolfgang Hänsel, Marc Fischer, Matthias Lezius, Thomas Udem, and Ronald Holzwarth. Real-time phase tracking for wide-band optical frequency measurements at the 20th decimal place. *Nature Photonics*, 14:44–49, 1 2020.

[111] J. Zhang, Z. H. Lu, Y. H. Wang, T. Liu, A. Stejskal, Y. N. Zhao, R. Dumke, Q. H. Gong, and L. J. Wang. Exact frequency comb mode number determination in precision optical frequency measurements. *Laser Physics*, 17:1025–1028, 7 2007.

[112] E. Oelker, R. B. Hutson, C. J. Kennedy, L. Sonderhouse, T. Bothwell, A. Goban, D. Kedar, C. Sanner, J. M. Robinson, G. E. Marti, D. G. Matei, T. Legero, M. Giunta, R. Holzwarth, F. Riehle, U. Sterr, and J. Ye. Demonstration of 4.8 × 10 17 stability at 1 s for two independent optical clocks. *Nature Photonics*, 13:714–719, 10 2019.

[113] Smartcomb compact optical frequency comb, menlo systems.

[114] Alessia Pasquazi, Marco Peccianti, Luca Razzari, David J. Moss, Stéphane Coen, Miro Erkintalo, Yanne K. Chembo, Tobias Hansson, Stefan Wabnitz, Pascal Del'Haye, Xiaox-

iao Xue, Andrew M. Weiner, and Roberto Morandotti. Micro-combs: A novel generation of optical sources. *Physics Reports*, 729:1–81, 1 2018.

[115] Asad A. Abidi. *How Phase Noise Appears in Oscillators*, pages 271–290. Springer US, 1997.

[116] Axtal ocxo products.

[117] Jianping Yao. Microwave photonics. *Journal of Lightwave Technology*, 27:314–335, 2 2009.

[118] Jianping Yao. Microwave photonic systems. *Journal of Lightwave Technology*, 40:6595–6607, 10 2022.

[119] Wangzhe Li and Jianping Yao. Investigation of photonically assisted microwave frequency multiplication based on external modulation. *IEEE Transactions on Microwave Theory and Techniques*, 58:3259–3268, 11 2010.

[120] L. Goldberg, A.M. Yurek, H.F. Taylor, and J.F. Weller. 35 ghz microwave signal generation with an injection-locked laser diode. *Electronics Letters*, 21:814, 1985.

[121] K. J. WILLIAMS, R. D. ESMAN, L. GOLDBERG, J. F. WELLER, and M. DAGENAIS. Active offset phase locking of nd:yag 1319-nm nonplanar ring lasers to 34 ghz. In *Optical Fiber Communication*, page THC2. OSA, 1990.

[122] J.J. O'Reilly, P.M. Lane, R. Heidemann, and R. Hofstetter. Optical generation of very narrow linewidth millimetre wave signals. *Electronics Letters*, 28:2309–2311, 12 1992.

[123] Xiangfei Chen, Jianping Yao, and Zhichao Deng. Ultranarrow dual-transmission-band fiber bragg grating filter and its application in a dual-wavelength single-longitudinal-mode fiber ring laser. *Optics Letters*, 30:2068, 8 2005.

[124] Shilong Pan and Jianping Yao. Wideband and frequency-tunable microwave generation using an optoelectronic oscillator incorporating a fabry–perot laser diode with external optical injection. *Optics Letters*, 35:1911, 6 2010.

[125] Jianping Yao, José Capmany, and Ming Li. *Microwave Photonics*. Wiley, 4 2024.

[126] Wangzhe Li and Jianping Yao. Generation of linearly chirped microwave waveform with an increased time-bandwidth product based on a tunable optoelectronic oscillator and a recirculating phase modulation loop. *Journal of Lightwave Technology*, 32:3573–3579, 10 2014.

[127] T. M. Fortier, M. S. Kirchner, F. Quinlan, J. Taylor, J. C. Bergquist, T. Rosenband, N. Lemke, A. Ludlow, Y. Jiang, C. W. Oates, and S. A. Diddams. Generation of ultrastable microwaves via optical frequency division. *Nature Photonics*, 5:425–429, 7 2011.

[128] Shilong Pan and Yamei Zhang. Microwave photonic radars. *Journal of Lightwave Technology*, 38:5450–5484, 10 2020.

[129] A. Haboucha, W. Zhang, T. Li, M. Lours, A. N. Luiten, Y. Le Coq, and G. Santarelli. Optical-fiber pulse rate multiplier for ultralow phase-noise signal generation. *Optics Letters*, 36:3654, 9 2011.

[130] Tara M. Fortier, Franklyn Quinlan, Archita Hati, Craig Nelson, Jennifer A. Taylor, Yang Fu, Joe Campbell, and Scott A. Diddams. Photonic microwave generation with high-power photodiodes. *Optics Letters*, 38:1712, 5 2013.

[131] Xiaopeng Xie, Romain Bouchand, Daniele Nicolodi, Michele Giunta, Wolfgang Hänsel, Matthias Lezius, Abhay Joshi, Shubhashish Datta, Christophe Alexandre, Michel Lours, Pierre-Alain Tremblin, Giorgio Santarelli, Ronald Holzwarth, and Yann Le Coq. Photonic microwave signals with zeptosecond-level absolute timing noise. *Nature Photonics*, 11:44–47, 1 2017.

[132] Michele Giunta, Jialiang Yu, Maurice Lessing, Marc Fischer, Matthias Lezius, Xiaopeng Xie, Giorgio Santarelli, Yann Le Coq, and Ronald Holzwarth. Compact and ultrastable photonic microwave oscillator. *Optics Letters*, 45:1140, 3 2020.

[133] David Marpaung, Jianping Yao, and José Capmany. Integrated microwave photonics. *Nature Photonics*, 13:80–90, 2 2019.

[134] Jared Hulme, MJ Kennedy, Rui-Lin Chao, Linjun Liang, Tin Komljenovic, Jin-Wei Shi, Bogdan Szafraniec, Doug Baney, and J. E. Bowers. Fully integrated microwave frequency synthesizer on heterogeneous silicon-iii/v. *Optics Express*, 25:2422, 2 2017.

[135] Ki Youl Yang, Dong Yoon Oh, Seung Hoon Lee, Qi-Fan Yang, Xu Yi, Boqiang Shen, Heming Wang, and Kerry Vahala. Bridging ultrahigh-q devices and photonic circuits. *Nature Photonics*, 12:297–302, 5 2018.

[136] Junqiu Liu, Erwan Lucas, Arslan S. Raja, Jijun He, Johann Riemensberger, Rui Ning Wang, Maxim Karpov, Hairun Guo, Romain Bouchand, and Tobias J. Kippenberg. Photonic microwave generation in the x- and k-band using integrated soliton microcombs. *Nature Photonics*, 14:486–491, 8 2020.

[137] Igor Kudelin, William Groman, Qing-Xin Ji, Joel Guo, Megan L. Kelleher, Dahyeon Lee, Takuma Nakamura, Charles A. McLemore, Pedram Shirmohammadi, Samin Hanifi, Haotian Cheng, Naijun Jin, Lue Wu, Samuel Halladay, Yizhi Luo, Zhaowei Dai, Warren Jin, Junwu Bai, Yifan Liu, Wei Zhang, Chao Xiang, Lin Chang, Vladimir Iltchenko, Owen Miller, Andrey Matsko, Steven M. Bowers, Peter T. Rakich, Joe C. Campbell, John E. Bowers, Kerry J. Vahala, Franklyn Quinlan, and Scott A. Diddams. Photonic chip-based low-noise microwave oscillator. *Nature*, 627:534–539, 3 2024.

[138] M. Giunta, M. Bradler, M. Lessing, B. Rauf, S. Afrem, J. Reeves, M. Fischer, and R. Holzwarth. Ultrastable microwave system for quantum-enabled radar networks. In *2023 IEEE Research and Applications of Photonics in Defense Conference (RAPID)*, pages 1–2. IEEE, 9 2023.

[139] Giovanni Serafino, Filippo Scotti, Leonardo Lembo, Bilal Hussain, Claudio Porzi, Antonio Malacarne, Salvatore Maresca, Daniel Onori, Paolo Ghelfi, and Antonella Bogoni.

Toward a new generation of radar systems based on microwave photonic technologies. *Journal of Lightwave Technology*, 37:643–650, 1 2019.

[140] Paolo Ghelfi, Francesco Laghezza, Filippo Scotti, Giovanni Serafino, Amerigo Capria, Sergio Pinna, Daniel Onori, Claudio Porzi, Mirco Scaffardi, Antonio Malacarne, Valeria Vercesi, Emma Lazzeri, Fabrizio Berizzi, and Antonella Bogoni. A fully photonics-based coherent radar system. *Nature*, 507:341–345, 3 2014.

[141] Paolo Ghelfi, Francesco Laghezza, Filippo Scotti, Daniel Onori, and Antonella Bogoni. Photonics for radars operating on multiple coherent bands. *Journal of Lightwave Technology*, 34:500–507, 1 2016.

[142] L. Nguyen. Microwave photonic technique for frequency measurement of simultaneous signals. *IEEE Photonics Technology Letters*, 21:642–644, 5 2009.

[143] Weiwen Zou, Hao Zhang, Xin Long, Siteng Zhang, Yuanjun Cui, and Jianping Chen. All-optical central-frequency-programmable and bandwidth-tailorable radar. *Scientific Reports*, 6:19786, 1 2016.

[144] Ziqian Zhang, Yang Liu, Tegan Stephens, and Benjamin J. Eggleton. Photonic radar for contactless vital sign detection. *Nature Photonics*, 17:791–797, 9 2023.

[145] Thales Aveillant. Gamekeeper 16u, 2020.

[146] Darren Griffiths, Mohammed Jahangir, Jithin Kannanthara, Gwynfor Donlan, Chris J. Baker, Michail Antoniou, and Yeshpal Singh. Fully digital, urban networked staring radar: Simulation and experimentation. *IET Radar, Sonar and Navigation*, 18:657–673, 5 2024.

[147] Barnes; Stephen Jarvis Jr. J, A. Efficient numerical and analog modeling of flicker noise processes. *NBS Technical Note*, 1971.

[148] W J Riley. *Handbook of Frequency Stability Analysis*, volume 31. 1994.

[149] Mini circuits - global leader of rf and microwave components.

[150] Dji - official website.

[151] Mohammed Jahangir, Darren Griffiths, Daniel White, Gwynfor Donlan, Xiaofei Ren, Jithin Kannanthara, Yeshpal Singh, Joseph P. Wayman, Chris J. Baker, Jon P. Sadler, S. James Reynolds, and Michail Antoniou. Development of a networked photonic-enabled staring radar testbed for urban surveillance. *IET Radar, Sonar and Navigation*, 18:41–55, 1 2024.

[152] Raymond L. Filler and John R. Vig. Long term aging of oscillators. *Proceedings of the Annual Frequency Control Symposium*, pages 470–484, 1992.

[153] Sandenbergh J and Inggs M. A summary of the results achieved by the gps disciplined references of the netrad and nextrad multistatic radars. In *IEEE Radar Conference (RadarConf)*, 2019.

[154] P. J. Beasley and M. A. Ritchie. Multistatic radar synchronisation using cots gps disciplined oscillators. pages 429–434, 2023.

[155] M. R. Inggs, S. Lewis, R. Palama, M. A. Ritchie, and H. Griffiths. Report on the 2018 trials of the multistatic nextrad dual band polarimetric radar. *2019 IEEE Radar Conference, RadarConf 2019*, 2019.

[156] Stefan Brisken, Matteo Moscadelli, Viktor Seidel, and Christoph Schwark. Passive radar imaging using dvb-s2. *2017 IEEE Radar Conference, RadarConf 2017*, pages 0552–0556, 6 2017.

[157] H. Guo, K. Woodbridge, and C. J. Baker. Evaluation of wifi beacon transmissions for wireless based passive radar. *2008 IEEE Radar Conference, RADAR 2008*, pages 1–6, 2008.

[158] Debora Pastina, Fabrizio Santi, Federica Pieralice, Michail Antoniou, and Mikhail Cherniakov. Passive radar imaging of ship targets with gnss signals of opportunity. *IEEE Transactions on Geoscience and Remote Sensing*, 59:2627–2642, 2021.

[159] Piotr Samczy, Senior Member, Karol Abratkiewicz, Graduate Student Member, Marek Płotka, Tomasz P Zieli, Jacek Wszołek, Sławomir Hausman, Piotr Korbel, and Adam Ksi. 5g network-based passive radar. 60, 2022.

[160] Pedro Gomez-Del-Hoyo, Konrad Gronowski, and Piotr Samczynski. The starlink-based passive radar: preliminary study and first illuminator signal measurements. *Proceedings International Radar Symposium*, 2022-Septe:350–355, 2022.

[161] Leo bodnar precision gps reference clock.

[162] Da Liang, Heng Zhang, Kaiyu Liu, Dacheng Liu, and Robert Wang. Phase synchronization techniques for bistatic and multistatic synthetic aperture radar: Accounting for frequency offset. *IEEE Geoscience and Remote Sensing Magazine*, 10:153–167, 2022.

[163] Yonghua Cai, Junfeng Li, Qingyue Yang, Da Liang, Kaiyu Liu, Heng Zhang, Pingping Lu, and Robert Wang. First demonstration of rfi mitigation in the phase synchronization of lt-1 bistatic sar. *IEEE Transactions on Geoscience and Remote Sensing*, 61:1–19, 2023.

[164] Da Liang, Kaiyu Liu, Heng Zhang, Yunkai Deng, Dacheng Liu, Yafeng Chen, Chuang Li, Haixia Yue, and Robert Wang. A high-accuracy synchronization phase-compensation method based on kalman filter for bistatic synthetic aperture radar. *IEEE Geoscience and Remote Sensing Letters*, 17:1722–1726, 2020.

[165] Yafeng Chen, Da Liang, Haixia Yue, Dacheng Liu, Xiayi Wu, Heng Zhang, Yuanbo Jiao, Kaiyu Liu, and Robert Wang. Implementation of a phase synchronization scheme based on pulsed signal at carrier frequency for bistatic sar. *Sensors (Switzerland)*, 20:1–14, 2020.

[166] Yonghua Cai, Robert Wang, Weidong Yu, Da Liang, Kaiyu Liu, Heng Zhang, and Yafeng Chen. An advanced approach to improve synchronization phase accuracy with compressive sensing for lt-1 bistatic spaceborne sar. *Remote Sensing*, 14:1–19, 2022.

[167] Michail Antoniou and Mikhail Cherniakov. Gnss-based bistatic sar: A signal processing view. *Eurasip Journal on Advances in Signal Processing*, 2013:1–16, 2013.

[168] J. C. Merlano-Duncan, J. J. Mallorquí, and P. López-Dekker. Carrier phase synchronisation scheme for very long baseline coherent arrays. *Electronics Letters*, 48:950–951, 2012.

[169] Abudusaimi Abuduaini, Nobuyuki Shiraki, Naoki Honma, Takeshi Nakayama, and Shoichi Iizuka. Frequency error compensation of unsynchronized bistatic cw- mimo radar for multiple human-body localization. *IEEE Transactions on Biomedical Circuits and Systems*, 16:882–890, 2022.

[170] Michael Gottinger, Peter Gulden, and Martin Vossiek. Coherent signal processing for loosely coupled bistatic radar. *IEEE Transactions on Aerospace and Electronic Systems*, 57:1855–1871, 2021.

[171] Zhihua He, Feng He, Junli Chen, Haifeng Huang, Zhen Dong, and Diannong Liang. Echo-domain phase synchronization algorithm for bistatic sar in alternating bistatic/ping-pong mode. *IEEE Geoscience and Remote Sensing Letters*, 9:604–608, 2012.

[172] Julia Bauer, Carsten Andrich, Michael Dobereiner, Steffen Schieler, James Myint, Alexander Ihlow, Christian Schneider, Reiner Thoma, and Giovanni Del Galdo. Measurement campaign with synchronized distributed receivers and mobile emitter at 3.75 ghz in urban scenarios. In *2020 IEEE 91st Vehicular Technology Conference (VTC2020-Spring)*, pages 1–5. IEEE, 5 2020.

[173] Hui Zhou, Charles Nicholls, Thomas Kunz, and Howard Schwartz. Frequency accuracy and stability dependencies of crystal oscillators, 2008.

[174] Thunderbolt e gps disciplined clock.

[175] Lnrclok-1500 rubidium clock.

[176] Rohde and schwarz gmbh and co kg products - fspw.

[177] J. S. Sandenbergh and M. R. Inggs. Synchronizing network radar using all-in-view gps-disciplined oscillators. In *2017 IEEE Radar Conference, RadarConf 2017*, pages 1640–1645. Institute of Electrical and Electronics Engineers Inc., 6 2017.

[178] Przemyslaw Krehlik, Lukasz Sliwczynski, Lukasz Buczek, Jacek Kolodziej, and Marcin Lipinski. Elstab - fiber-optic time and frequency distribution technology: A general characterization and fundamental limits. *IEEE Transactions on Ultrasonics, Ferroelectrics, and Frequency Control*, 63:993–1004, 7 2016.

[179] Haoyuan Lu, Zhaolong Li, Jiaxin Wang, Hongling Meng, and Jianye Zhao. Two-way optical time and frequency transfer over a 20-km fiber link based on optical frequency combs. *IEEE Photonics Journal*, 11:1–7, 2 2019.

[180] D Griffiths, M Jahangir, G Donlan, J Kannanthara, M Antoniou, C Baker, and Y Singh. Microwave photonics in networked staring radar. In *2023 International Topical Meeting on Microwave Photonics (MWP)*, pages 1–4, 2023.

[181] Thomas Legero, Erik Benkler, Jialiang Yu, Chun Yu Ma, Sofia Herbers, Daniele Nicolodi, Mona Kempkes, and Fritz Riehle. Frequency drift of cryogenic silicon cavities. In *European Time and Frequency Forum*, 2024.

[182] Chang Jian Kwong, Michael G Hansen, Jun Sugawara, and Stephan Schiller. Characterization of the long-term dimensional stability of a nexcera block using the optical resonator technique. *Measurement Science and Technology*, 29:075011, 7 2018.

[183] Christian Hagemann, Christian Grebing, Christian Lisdat, Stephan Falke, Thomas Legero, Uwe Sterr, Fritz Riehle, Michael J. Martin, and Jun Ye. Ultrastable laser with average fractional frequency drift rate below 5 × 10 19 hz s. *Optics Letters*, 39:5102, 9 2014.

[184] Qi Shen, Jian-Yu Guan, Ji-Gang Ren, Ting Zeng, Lei Hou, Min Li, Yuan Cao, Jin-Jian Han, Meng-Zhe Lian, Yan-Wei Chen, Xin-Xin Peng, Shao-Mao Wang, Dan-Yang Zhu, Xi-Ping Shi, Zheng-Guo Wang, Ye Li, Wei-Yue Liu, Ge-Sheng Pan, Yong Wang, Zhao-Hui Li, Jin-Cai Wu, Yan-Yan Zhang, Fa-Xi Chen, Chao-Yang Lu, Sheng-Kai Liao, Juan Yin, Jian-Jun Jia, Cheng-Zhi Peng, Hai-Feng Jiang, Qiang Zhang, and Jian-Wei Pan. Free-space dissemination of time and frequency with 10-19 instability over 113 km. *Nature*, 610:661–666, 10 2022.

[185] Tiqker next-generation atomic frequency reference.

[186] Vector atomic - quantum advantage. today.

[187] Franqois Vernotte and Observatoire De Besanqon. Estimiation of the power spectral density of phase: Comparison of three methods. In *EFTF IFCS*, 1999.

[188] Enrico Rubiola and Vincent Giordano. Correlation-based phase noise measurements. *Review of Scientific Instruments*, 71:3085–3091, 8 2000.

[189] M. G. Arthur, C. M. Allred, and M. K. Cannon. A precision noise-power comparator. *IEEE Transactions on Instrumentation and Measurement*, IM-13:301–305, 12 1964.

[190] William Riley and David Howe. Handbook of frequency stability analysis, 2008.

[191] David W Allan and James A Barnes. A modified allan variance with increased oscillator characterization ability. In *Proceedings of the 35th Annual Frequency Control Symposium*, volume 5, pages 470–475, 1981.

[192] Hanne Ludvigsen, Mika Tossavainen, and Matti Kaivola. Laser linewidth measurements using self-homodyne detection with short delay. *Optics Communications*, 155:180–186, 10 1998.

[193] H. Stoehr, F. Mensing, J. Helmcke, and U. Sterr. Diode laser with 1 hz linewidth. *Optics Letters*, 31:736, 3 2006.

[194] Gianni Di Domenico, Stéphane Schilt, and Pierre Thomann. Simple approach to the relation between laser frequency noise and laser line shape. *Applied Optics*, 49:4801, 9 2010.

[195] Jérôme Poirson, Fabien Bretenaker, Marc Vallet, and Albert Le Floch. Analytical and experimental study of ringing effects in a fabry perot cavity application to the measurement of high finesses. *Journal of the Optical Society of America B*, 14:2811, 11 1997.

[196] Kwangyun Jung and Jungwon Kim. Characterization of timing jitter spectra in free-running mode locked lasers with 340 db dynamic range over 10 decades of fourier frequency. *Optics Letters*, 40:316, 2 2015.

Appendix A

Radar Processing Tools

One aspect is to set up the radars to be able to accept different oscillators and to measure radar data in an effective way. This section addresses the measurement of radar performance so that quantitative measures can be retrieved. The three main aspects that are discussed are the level of synchronization accuracy for radar networks, the radar sensitivity level in high clutter environments and the target detection capability.

For the measurement of the synchronization accuracy, the bistatic unwrapped phase error, single sideband (SSB) phase power spectral density (PSD) and the coherent integration loss are measured. The radar sensitivity is quantified using spectral background maps (SBM) and the background noise levels relative to the clutter. Finally, for determining the radars ability to detect targets, spectrogram generation and target SNR throughout the flights trajectory are analysed.

A.1 Phase Error

In a radar system, the transmitter oscillator will determine the purity of the transmitted waveform and the receiver will determine the purity of the signal used for mixing down to baseband. In an ideal situation, perfect oscillators will ensure the receiver mixing signal and the received signal from a stationary target are essentially the same. To measure the phase error, a reference source is used, such as the direct breakthrough signal or a large stationary clutter reference. In the radar output, this will appear as a DC signal as there is no Doppler offset and therefore, ideally should

have a constant phase. By using the unwrapped bistatic phase from a reference source, like those mentioned, phase errors on the transmitted waveform at f_c should be proportional to those observed in the unwrapped bistatic phase, assuming there are no phase errors in the receivers LO. In reality, both LOs have instability and therefore, the unwrapped phase error demonstrated phase error between the two nodes at f_c. Similar methods have been used to measure directly the phase error between two radar nodes. In the BiSAR LuTan-1 [166], synchronization pulses are used as a measure of the phase error and in the ARESTOR network system [30], an RF cable between two identical radar systems is used to simulate returns from a static target which can then be used for phase error measurement.

The method works best in situations where the clutter-to-noise (CNR) is higher and where there are less opportune moving targets in the vicinity. In this work, unwrapped bistatic phase is measured using the Trigate building as a reference source. This phase measurement is performed in the bistatic configuration, using the GK000 as the receiver node and GK007 as the remote transmitter. Also, for reduced target influence, the phase measurement is performed using background (night-time) trials data. In some cases there may be better results from using the direct breakthrough signal as it is usually the strongest possible return but in the Birmingham environment a lot of multipath effects are experienced which degrade the resultant phase estimation, more is discussed about this in Chapter 6.2.3. In this case, the Trigate reference source appears at a range gate of $k^{rg} = 50$, an azimuth angle of $\theta^{az} = 140$ [degrees] and an elevation angle of $\theta^{el} = 91$ [degrees].

The radar data frame in channel-time domain is defined as $C^t_{i,j,k,l}$ where i is the channel row index, j is the channel column index, k is the range gate and l is the time index or pulse number. The first step involves using digital beamforming [19] to generate the desired beam toward the Trigate building. The beam weights (ϕ^B) are calculated using Equations A.1 - A.3 where d is the element spacing in meters and λ is the wavelength in meters. The combined channel-time domain data for a single beam ($C_l^{Bsingle}$) is determined using A.4.

$$\phi_i^c = (2i - I - 1)cos(\theta^{az})\frac{-\pi d}{\lambda} \tag{A.1}$$

$$\phi_j^r = (2j - J - 1)cos(\theta^{el})\frac{-\pi d}{\lambda} \tag{A.2}$$

$$\phi_{i,j}^B = \phi_i^r \text{`} \phi_j^c \tag{A.3}$$

$$C_l^{Bsingle} = \sum_{i=1:I} \sum_{j=1:J} \phi_{i,j,l}^B C_{i,j,k,l}^t \; ; \; where \; k = k^{rg} \tag{A.4}$$

The unwrapped phase is determined from the beamformed data by using Equation A.5.

$$\phi^{WE}(l) = atan2(Re(C_l^{Bsingle}), Im(C_l^{Bsingle}) \tag{A.5}$$

The phase is then unwrapped at interfaces of ever interval of 2π and the result is the unwrapped phase error accumulation between the transmitter and receiver ϕ_l^{UE}. Since this is representing the phase error at f_c the phase can be translated to time error (t_l^{error}) as well as bistatic radar range error (R_l^{error}) using proportionality factors shown in Equations A.6 and A.7 respectively.

$$t_l^{error} = \frac{\phi_l^{UE}}{2\pi f_c} \tag{A.6}$$

$$R_l^{error} = \frac{ct_l^{error}}{2} \tag{A.7}$$

The phase error measurement, along with the time and range errors, is the key figure of merit in determining the radar's synchronization accuracy.

A.2 Single Sideband Phase Power Spectral Density

Another useful measure is the SSB phase PSD as it can give an insight into different noise sources. This method is used in [13] to show phase PSD in a bistatic radar system synchronized using white rabbit. Various methods of generating phase PSD can be used [187] but in this work the FFT method is employed.

To compute the phase PSD, the unwrapped bistatic phase error ϕ_l^{UE} is used. The phase

spectrum is then calculated using Equation A.8. First an FFT is performed to get the phase spectrum S_k^{ϕ}. Then the phase spectrum is normalized with the bin width and the measurement time, this is included in the factor F_N. This obtains units of rad/Hz and is independent of sample frequency and number of data points.

$$S_k^{\phi} = \frac{1}{F_N} \sum_{l=0:L-1} \phi_l^{UE} e^{\frac{-2\pi i k}{L}} \tag{A.8}$$

The phase power spectrum is then converted into a logarithmic scale and is taken as assumed to be symmetric, therefore the single sideband around 0 Hz is taken for comparisons.

A.3 Coherent Integration Loss

The effect of the measured synchronization level on the coherent integration of a target under long dwell is now described. Phase errors in the oscillator are one of the sources of decoherence and is one of the focus of this work. A non coherent radar network will experience an accumulation of phase errors and reduce the coherent gain possible, therefore maximum expected power of the target is not reached. The coherent integration loss as a function of phase creep is shown in [153] for a particular radar system. The coherent integration loss measures the reduction in SNR as a function of measurement time.

The method used will now be described. A target is chosen to be the subject in which the signal return power is measured after performing the FFT. Since the radar has coarse resolution, it is recommended to use a large, distinct stationary target. The RCS should remain constant throughout the measurement, so a target with low power variance should be selected. Fortunately, the Trigate building meets both of these conditions and is used as a target when computing the coherent integration gain.

For increasing amount of pulses (relating to increasing CPI), the time domain data is processed into the spectral domain and the peak power at 0Hz Doppler frequency is measured. According to the radar equation (equation 2.3), the gain in signal power is proportional to the measurement time and therefore, losses can be quantified as deviations from the expected power

at higher CPIs. Better levels of synchronization will result in a reduced coherent integration loss.

A.4 Spectral Background Maps

The spectral background maps (SBM) are used as a measure of the background level and is used in the CFAR for the detection processing. The first step is to read in the channel-time data frame $C^{t}_{i,j,k,l}$ and this is processed into beam-Doppler domain $C^{B}_{\theta_a,\theta_e,k,m,u}$ for each CPI index u. via beamforming and FFT. However, here the azimuth and elevation angles θ_a, θ_e represent an array of angles spanning the FOV. A average is performed in the slow time dimension as shown in Equation A.9, providing the SBM $C^{SBM}_{\theta_a,\theta_e,k,m}$ which provides an esitmate of the radar noise level in that interval for each range-beam-Doppler.

$$C^{SBM}_{\theta_a,\theta_e,k,m} = \frac{1}{U} \sum_{u=1:U} C^{B}_{\theta_a,\theta_e,k,m,u} \tag{A.9}$$

The full measurement length from 1:U affects the measurement in differnet ways. It cant be too short as it may start heavily accounting for targets in the resolution cell. Also, it cannot be too long as to start introducing time dependant effects. In this work, a spacing of 1.25 s is used for a total of 100 frames.

A.5 Clutter Data

While the SBMs are sufficient for detection, more information needs to be retained for the analysis of the background noise levels in the radar. As the noise level is frequency, time and location dependant, the data collection method is slightly different. With the focus on drone surveillance, the CPI is increased to approximatly 2 s to provide Doppler frequency resolution of 0.5 Hz. To reduce the data volume, only the low frequencies below 100 Hz are retained.

The clutter data structure is used to generate the background noise spectrum as shown in Figure A.1a in a known high clutter region, Trigate in this case. Due to power fluctuations in

the signal echos, the power relative to clutter is shown in A.1b. The entire field of view is taken into consideration by generating clutter maps as shown in A.1c. The clutter map aids with the identification of dark zones where the noise may be raised and cause a drop in the probability of detection in that region.

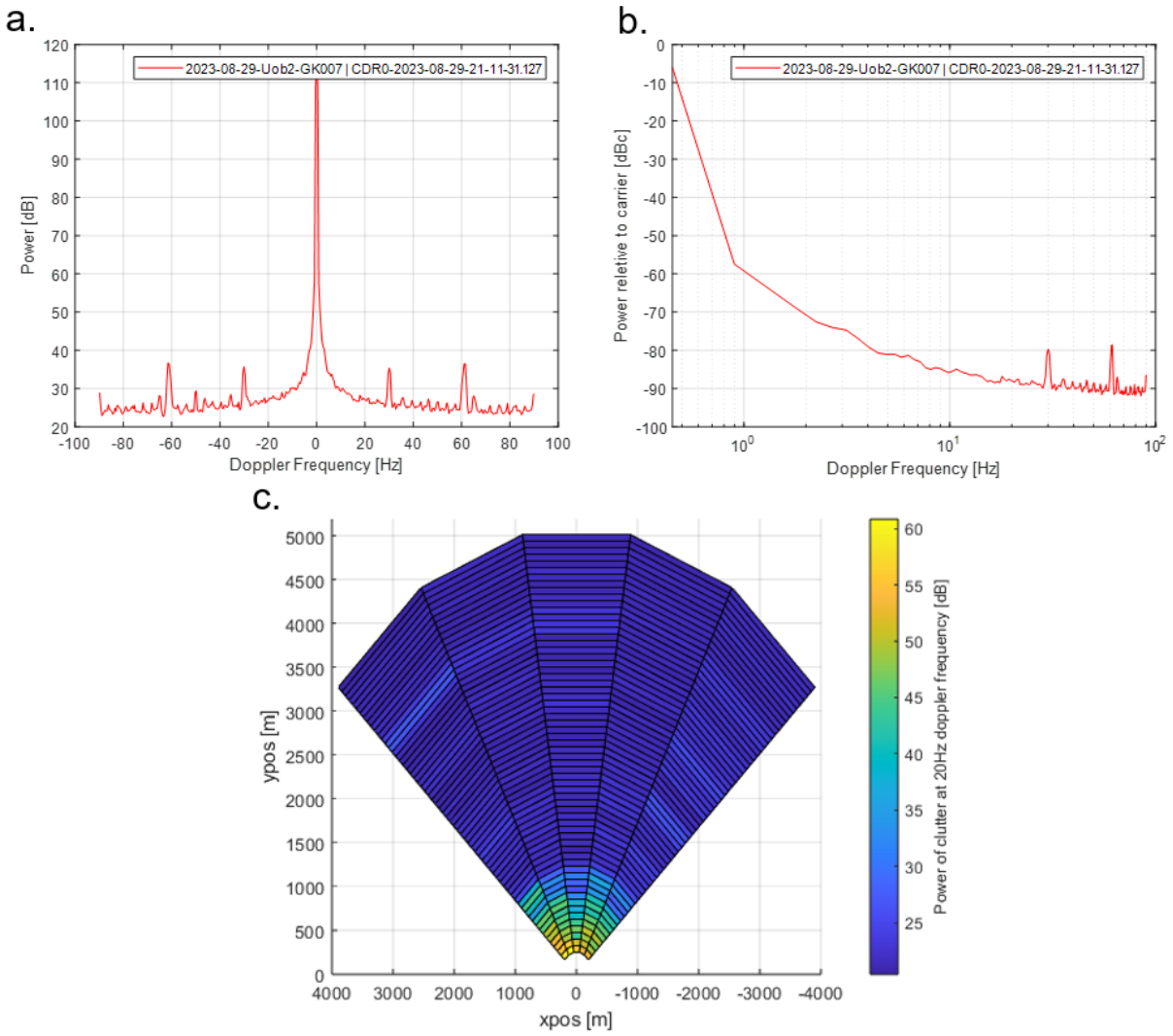

Figure A.1: (a) Averaged background spectrum at trigate location GK007, (b) Power spectrum relative to carrier, (c) Clutter map for GK007 at frequency offset of 20 Hz.

A.6 Spectrogram Generation and Signal / Noise Analysis

Previously the data gathering process was discussed but when the focus is on a specific control target the data needs to be extracted. Central to the task of radar detection is the SNR of the

target. Whilst the processing utilises instantaneous SNR, it is useful to get a handle on the target signature characteristics to obtain some subjective assessment of the quality of the target that will determine detection performance and where relevant its classification potential. Thus, for a given target an analysis of the Doppler spectrum for the duration of the target track and/or its flight can be very informative. Generating a spectrogram is performed by extracting the target Doppler from the 4-D radar data volume in range, azimuth, elevation and Doppler from the GPS truth data, taking the spectrum of the beamformed time data at that point and then concatenating these into a timeline. The SBM can then be used to subtract from the spectrogram, the result is a spectrogram representing the SNR of targets in the area. Spectrograms can potentially give plenty of useful information about a target such as its trajectory and if it has extra components. Such an example is of a Cessna 172M Skyhawk (propeller aircraft), with a spectrogram of the aircraft as it was captured while circling around Birmingham city centre. The spectrogram after SBM subtraction is shown in Fig. A.2 where the main fuselage is shown with high SNR and the micro-Doppler returns from the propellers are shown symmetrically around the fuselage.

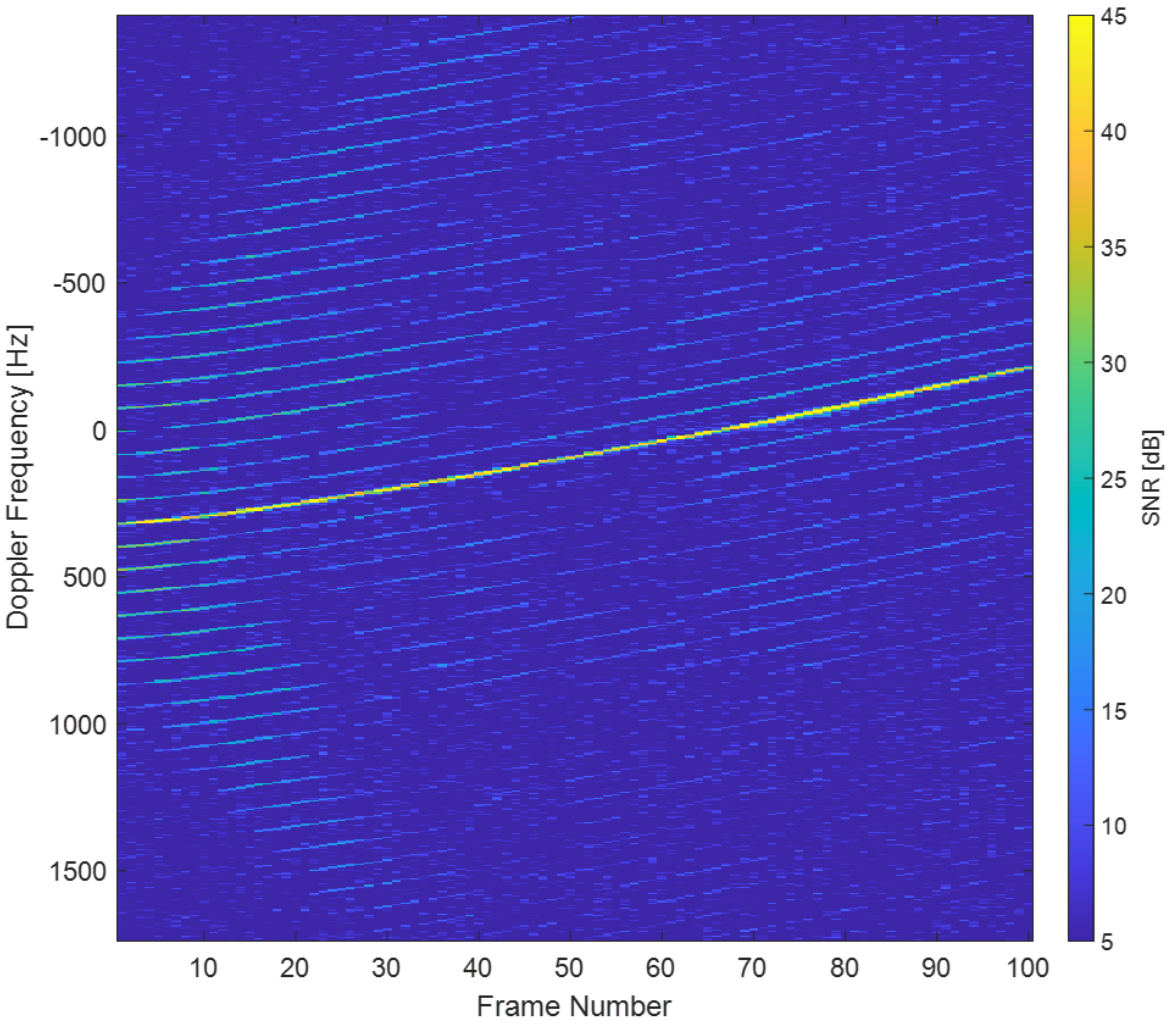

Figure A.2: SBM subtracted spectrogram of a Cessna 172M Skyhawk

Appendix B

Measurement of Oscillator Stability

Oscillators are intended to produce oscillations as a defined frequency reliably and accurately. However, all oscillators have imperfections and suffer from external perturbations which cause instability and inaccuracy. It is important to understand how the instability of an oscillator can be measured such that we can obtain insights into how it will perform in the radar. This section focused on ways that oscillator stability can be measured and then this information can be used to determine, to what extent, the oscillator stability can be correlated with radar performance. These are first characterised in the lab, such that the oscillator is running with the expected stability and also such that the properties of different oscillator types and configurations can be compared.

In the following sections, each of the main figures of merit are introduced before describing the measurement process. The focus is mostly on phase noise for short term stability and the Allan deviation (ADEV) or modified Allan Deviation (MDEV) for long term stability.

B.1 Phase Noise

Phase noise, measured in units of dBc/Hz, and is a key indicator of frequency stability, effectively characterizing various types of noise across different frequency ranges [25]. The Rohde & Schwarz FSPN is used for all the direct PN measurements as it is simple, repeatable and has a sufficiently low noise floor for most of the oscillators under test. The measurement setup is

shown in Figure B.1, simply consisting of the measurement device and the device under test (DUT).

Figure B.1: Diagram of the setup for PN measurements. DUT - Device under test.

The FSPN uses a duel-channel measurement approach [188] where there are who internal channels, both consisting of an OCXO reference and a phase detector. Typical methods using a single phase detector are limited by the stability of the reference used [189], among other limitations such as the resolution of the phase detectors and ADCs. However, the use of two channels allows for a noise floor reduction via a cross correlation algorithm. The main problem in PN measurement of ultra-stable oscillators is to resolve small phase fluctuations and this can only be achieved with comparison to a suitable reference. In a duel-channel measurement, the common noise from the DUT and the uncorrelated noise from the reference oscillators can be separated, allowing for a higher sensitivity, or in other words, the ability to resolve smaller phase fluctuations. This improved measurement sensitivity allows for reliable PN measurement of OCXOs and photonic oscillators as shown in the following sections.

The only limitation is for measurement of low phase noise, high frequency signals. For oscillators in the region of 10 GHz or higher, other methods have been devised to improve the measurement sensitivity such as in [131] where two identical low phase noise reference systems are developed and compared after mixing down to an intermediate frequency. Then in principle the methods are similar to the duel-channel measurement approach.

B.2 Allan Deviation

Another primary measure of the frequency stability is the Allan Deviation. It also allows for measurement of different noise types but is better suited for providing information on the

long term stability. The result is a fractional frequency stability which is dimensionless and independent of frequency. Therefore is sometimes preferred as it can easily give a quantitative measure and is comparable between different oscillators at different regimes (such as optical frequencies or RF) [190].

Other variants such as the modified Allan deviation (MDEV) are used [191] when there may be ambiguity in the white noise and flicker frequency noise. MDEV will be primarily used for the measurements in the thesis.

The measurement is performed using a K+K FXE frequency counter but the particular measurement setup and the post processing can differ significantly depending on the devices being measured. The measurement will be explained for 3 different cases, an RF oscillator, two optical sources of similar frequency and two optical sources of different frequency. The measurement setup for the three cases are shown in Figure B.2. Typically when measuring the frequency of an oscillator, a reference source is needed which is either of better or equal stability to the device being measured. Therefore, for the frequency counter measurements performed in this work, the frequency ratio technique is used [190].

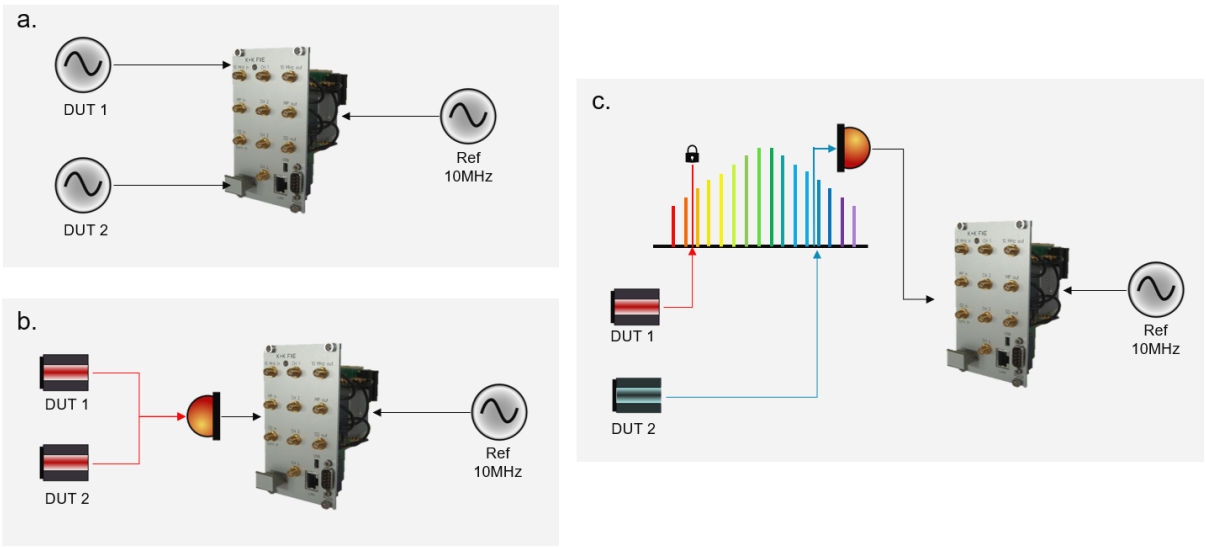

Figure B.2: Diagram of the setups used for ADEV/MDEV measurements. (a) RF oscillators, (b) Optical oscillators of similar frequency, (c) Optical oscillators of different frequencies.

Two RF Oscillators

For measurement of two RF oscillators that are within the specification of the frequency

counter (nominal frequency and power), are set up according to Figure B.2a. This consists of two devices under test (DUT) and are typically of the same model. If not then the measurement noise floor is limited by the lower quality oscillator. The frequency counter is given a frequency reference signal at 10 MHz from the H-Maser (unless specified otherwise). For most of the measurement in this work, the frequency counter is usually set to a gate time of 1 s in lambda operating mode and a measurement duration of a minimum of 12 hours. The H-Maser is the best performing 10 MHz frequency standard in the laboratory at the time of data collection. Since only one oscillator is available, the ADEV is shown from the T4 Science test report in Figure B.3.

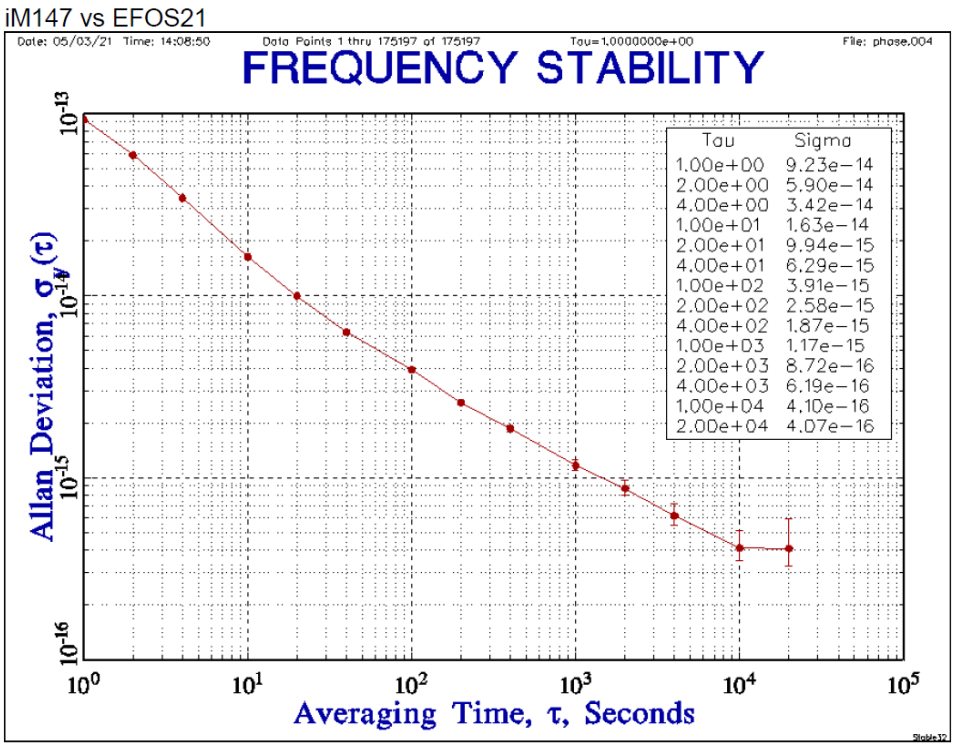

Figure B.3: ADEV measurement of the H-maser reference used, taken from the test report.

Processing of the frequency data is performed in Stable32 software. Preprocessing involves computing the frequency ratio $\frac{f_1 - f_2}{f_n}$ where f_1, f_2 and f_n are the frequency readings for channel 1, channel 2 and the nominal frequency respectively. This ensures that noise correlated noise from the reference source can be cancelled and only uncorrelated noise between the DUTs are measured. The next step involves removing the mean value from the data and then computing

the MDEV within Stable32.

Two Optical Oscillators of Similar Frequency

The method is also applicable to measurement of optical oscillators. However the frequency fluctuations are first reduced to the RF domain via a photodetector (PD) as shown in Figure B.2b. When two optical sources are coupled onto the PD, the beatnote contains the difference frequency. Therefore, similar to before, if one laser is more stable than the other, the measurement is limited by the lower quality oscillator. The RF beatnote is then measured using the frequency counter. For post-processing, the fractional frequency fluctuations are computed via $\frac{f}{fn}$, where f is the data from the counting channel (beatnote already computes the difference).

The one requirement is that the two optical sources need to be of a similar frequency, such that the difference frequency is within the bandwidth of the PD. In some cases, one of the lasers can be tuned to fit this condition. If they are F-P cavity stabilized lasers, then it may be possible by locking the laser to a different mode, separated by the free spectral range (FSR). In some occasions, additional optical components such as AOMs can be used to bridge the gap in frequency but this is limited to 100s of MHz or GHz. Also, if the frequencies are convenient, second harmonic generation or similar methods can be used.

Two Optical Oscillators of Different Frequency

If the two optical sources are in a different part of the optical spectrum (e.g 698 nm and 1542 nm), then an OFC is required to generate the beatnote. The measurement schematic diagram is shown in Figure B.2c. In this example DUT 1 is used to stabilize the repetition rate of the OFC. Each of the comb modes may then retain the stability of DUT 1. The next step involves generating a beatnote on a PD between DUT 2 and the nearest mode of the OFC. The post processing is equivalent to the method of similar frequency optical oscillators but the nominal frequency of DUT 2 should be used in the example given.

B.3 Other Measures of Oscillator Stability

A brief mention to other measures of oscillator stability are given in this subsection. These are either not commonly found in the literature or are not applicable to different regimes of oscillators but can be useful measures in particular situations.

Linewidth

The linewidth, or sometimes termed the full width half maximum (FWHM), is defined as the width of the spectral line at the point where the power is half of the maximum power. This is typically only used as a measure for optical frequencies since for highly stable RF oscillators, the linewidth can be in the region of μHz and is impractical to measure, since extremely long measurement times would be required to measure to this resolution and the oscillator will likely experience decoherence in this time..

One method is to use self-heterodyne methods such as in [192], but this method only works when the coherence time of the laser is sufficiently low. For highly stable lasers, a second, independent and equally stable source (or better) is required. The linewidth can be measured via heterodyne detection [193] or via beta separation line methods [194].

Finesse

The finesse the a measure of how narrow a resonance is in comparison to its frequency distance from neighbouring resonances. This is applicable for F-P cavities and micro-resonators among others. Typically this can be measured by studying ringing effects in a F-P cavity and is aptly named the 'ringdown measurement' for calculation of the finesse [195].

Timing Noise Density

The timing noise density (TND) is equivalent to the phase noise but is measured in units of s $\text{Hz}^{\frac{-1}{2}}$ and is independent of the carrier frequency of the oscillator. This measure may be used in circumstances where a direct measure of timing uncertainty is required such as in communication systems. The TND is computed from the phase noise profile as shown in [196] [131].

Time Deviation

Time deviation (TDEV) is equivalent to the Allan deviation and is also used for when a more

direct measure of timing uncertainty is required [190].

Appendix C

Radar Network Simulation Results

C.1 Oscillator Drift Examples

The simulation architecture has now been described, this section shows the results from various runs of the simulation. Firstly, the simulation is verified using a monostatic and bistatic scenario with an environment containing large, urban-like, clutter profiles, moving targets, phase noise and staring radar arrays. The bistatic scenario demonstrates the issues that arise in a network, when using different oscillators in each node. Then another scenario will be presented which simulated the oscillator instability of real oscillators in a GPSDO synchronized oscillator configuration. These simulations also provide the platform for benchmarking the various processing tools, relating to radar synchronization, designed in chapter 6.

The first iteration shown is the monostatic example where the transmitter and receiver are placed in the same location, to test the simulation outputs are as expected in this situation. The simulation environment used is shown in Figure C.1 where a single monostatic node is placed at the origin, 33 clutter points are positioned at increasing intervals of 150 m so that each range gate contains clutter returns but the azimuth angle and RCS of the source is adjusted for each target. In addition, 3 moving targets are placed at initial positions of [0 500 0] m, [342 940 0] m and [1690 3625 0] m respectively with RCS values of -30 dBm^{-2} and velocity of [0 10 0] ms^{-1}. For each of the clutter targets, the azimuth profile and RCS profiles are shown in Figure C.2.

Various other parameters including the phase noise parameters, phased array configuration and transmitter power are shown in C.1

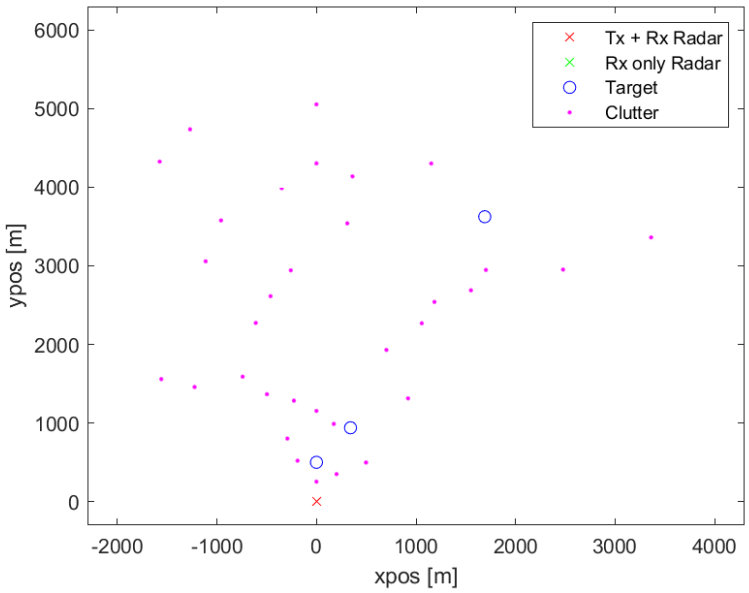

Figure C.1: Simulation environment, monostatic run.

Table C.1: Additional parameters for the monostatic and bistatic simulations.

Parameter	Monostatic Value [unit]	Bistatic Value [unit]
Number of receive element rows	16	16
Number of receive element columns	4	4
Element spacing	0.12 [m]	0.12 [m]
Number of samples per clock cycle	5	5
Transmitter power	2000 [W]	2000 [W]
Range gates	64	130
Clock frequency	62.5e6 [Hz]	62.5e6 [Hz]
Tx frequency multiplier	20	20
Linear frequency drift	0 [Hz/s]	1e-5 [Hz/s]
White phase noise	0	0
Flicker phase noise	0	0
Random walk PM	2e-5	2e-5
Flicker walk	0	0
Random walk FM	0	0
Initial Time Offset	0 [s]	13.6e-6 [s]
Initial Frequency Offset	0 [Hz]	-20 [Hz]

In total, 2048 PRIs were generated and these were processed into a range-Doppler plot as shown in Figure C.3. Standard processing techniques are used such as the FFT and beamforming,

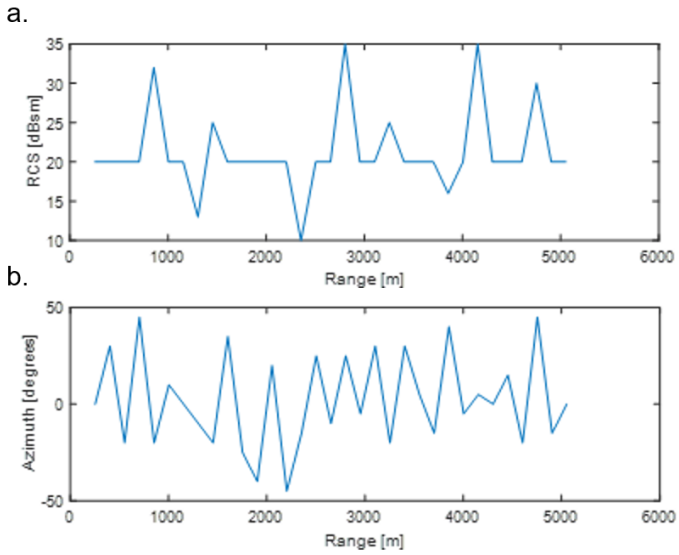

Figure C.2: Clutter profile for simulation.

in this case the beam for broadside is shown. Its seen that the 3 targets are visible on the left hand side of the clutter. The two closer targets are positioned in range gates 5 and 11 respectively at around -50 Hz Doppler frequency and possess a high SNR. Meanwhile, the third target at range gate 50 is much weaker due to the increased range and also because the target is not located in the broadside beam, so this peak represents an azimuth sidelobe of the target. If the detection processing is performed on this data set (more details on the processing in Chapter 6.2.2) then the three targets can be successfully localized with the results shown in Table C.2. Positional error of the three targets respectively are 0.7 m, 13.1 m and 74.2 m which is expected considering the resolution of the radar system. The beam profiles of the three target are shown in Figure C.4 where the mainlobe and multiple sidelobes are clear due to the high SNR and azimuth and elevation beamwidths are consistent with this radar system. The oscillator phase noise only included the random walk PM component of the phase noise as well at the receiver thermal noise but this its effect is visible in the range-Doppler plot. The raised noise floor due to oscillator noise is observed at particular range gates and this corresponds to regions where the clutter RCS was higher. This effectively means the oscillator is limiting the dynamic range as in urban environments where the clutter strength is expected to be inflated, the smallest observable target will be of higher RCS due to the raised noise floor.

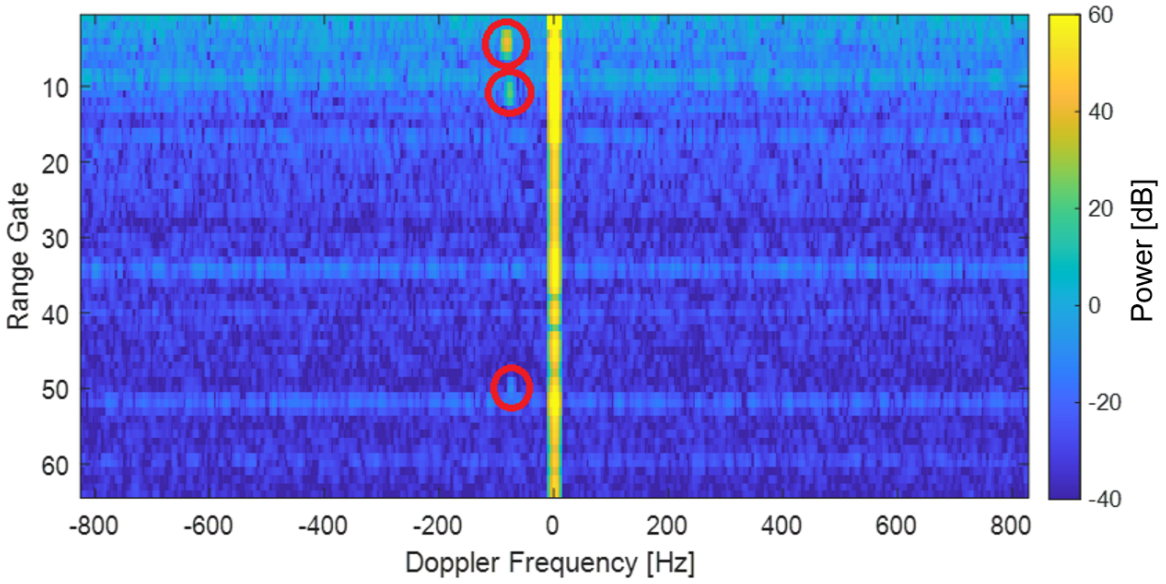

Figure C.3: Range-Doppler plot for the monostatic simulation.

Table C.2: Target detection outputs of the three targets from the monostatic simulation.

Number	**Position [m] (x, y, z)**	**Range Rate [ms^{-1}]**	**Positional Error [m]**	**SNR [dB]**
Target 1	(-0.2, 499.3, 0)	-9.9	0.7	48.5
Target 2	(355.0, 938.1, 0.2)	-9.5	13.1	46.4
Target 3	(1758.5, 3593.2, 1.3)	-9.1	74.2	42.1

The second iteration involves adding another radar node to be used as a passive bistatic receiver as well as altering the oscillator parameters to demonstrate various synchronization issues. The receiver node is placed at the origin and is set to not transmit while a separate transmitter node is placed at the position [-1000, -1000, 0] m. The targets and clutter are kept the same as in the monostatic scenario with the simulation environment of the bistatic simulation shown in Figure C.5. Other parameter changes are shown in Table C.1. To represent the lack of a synchronization link, an arbitrary time offset has been set to 13.6 μs which corresponds to a PRI offset of 10%. In addition, an initial frequency offset of -20 Hz has been applied to the transmitter node local oscillator as well as a 10 $\mu Hz/s$ linear frequency drift which can be typical values when using 2 different OCXOs. The number of range gates have been increased to 130 due to the time offset and the new geometry as the targets will now appear at a higher range gate.

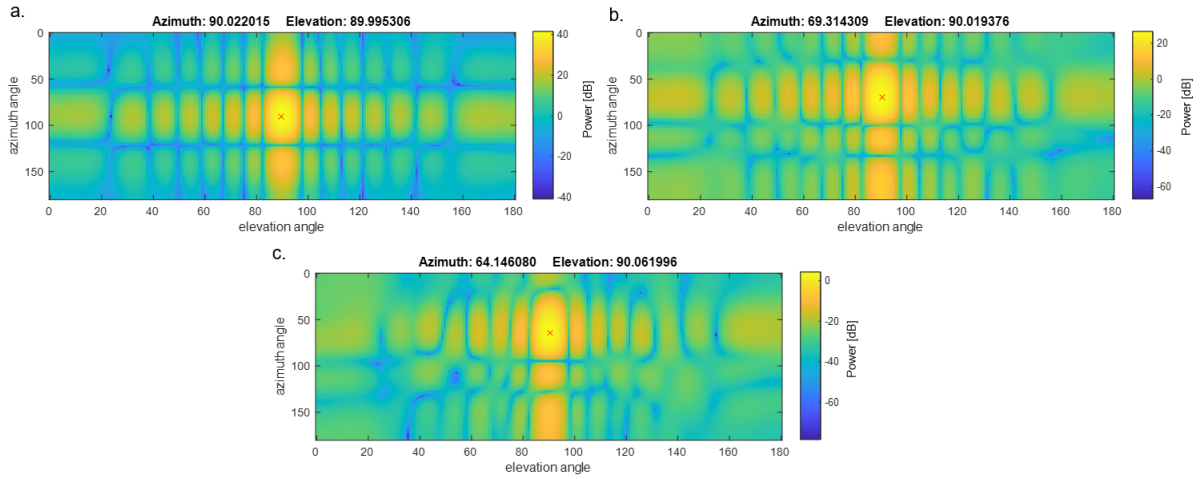

Figure C.4: Beam profiles for the 3 targets.

Table C.3: Target detection outputs of the three targets from the bistatic simulation.

Number	**Position [m] (x, y, z)**	**Range Rate [ms^{-1}]**	**Positional Error [m]**	**SNR [dB]**
Target 1	(-1.3, 506.2, 0)	-9.1	6.3	41.2
Target 2	(354.2, 939.3, 0.3)	-9.1	12.2	38.9
Target 3	(1719.0, 3613.4, -0.7)	-9.1	30.3	26.0

The range-Doppler plot generated from the bistatic simulation output is shown in Figure C.6a before any bistatic correction processing has been applied. From this there is a direct effect from the clock frequency offset, initial time offset and the bistatic geometry.

Due to the initial frequency offset and the linear drift on the transmitter, the carrier frequency of both radar nodes will not match. This is amplified due to the PLL architecture causing a 20x multiplication of the clock frequency. In this case the LO offset of -20 Hz after multiplication becomes -400 Hz. Since the receiver is configured to receive a particular frequency, the error will propagate through the RF chain even when mixing down to baseband. Therefore a stationary target would appear to be moving in the perspective of the receiver which matches the location of the clutter returns in Figure C.6a where the clutter wrongly appears to be a target moving away from the radar at 48 m/s.

Next is the timing offset caused by having a mismatch in the local time at each node, a result of the radars being switched on a different times and having two clocks running independently with their own mismatches in phase, frequency, noise, etc. Here the PRI offset of 1.36 μs is

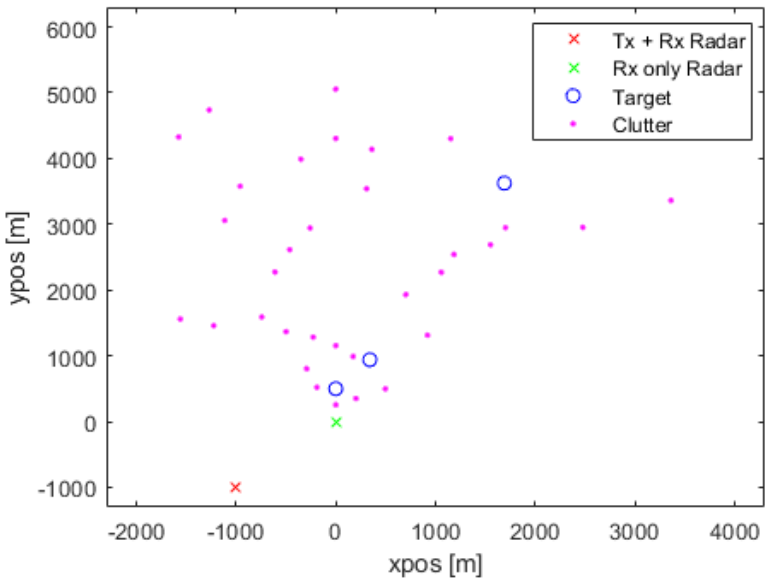

Figure C.5: Simulation environment, bistatic run.

dominant and shows as a vertical shift in the entire range-Doppler profile. The first target appears in range gate 40, representing a bistatic range of 3.24 km. As this is clearly much higher than expected, its shown that an arbitrary time offset results in an arbitrary positional error measured if there are no corrections applied.

Both of these effects can be corrected by using the bistatic data correction methods described in Chapter 6.2. After applying the corrections and generating the range-Doppler plot as seen in C.6b, the frequency offset has been removed and the target range appears more reasonable. The range gates are still not matching those shown in the monostatic simulation in C.3 due to the difference in the geometry. This can be accounted for in the bistatic detection processing as the position of both radar nodes are known. Therefore, the three targets can now be localised from the bistatic radar with the results shown in Table C.3 with positional errors of 6.3 m, 12.2 m and 30.3 m respectively demonstrating the use of the bistatic correction processing. Also to note, the SNR of the third target is significantly lower at only 26 dB which is an effect of the new geometry. As can be seen in Figure C.6b, the target is now fully in the same range bins as one of the strong clutter sources resulting in a raised noise floor due to the oscillator phase noise.

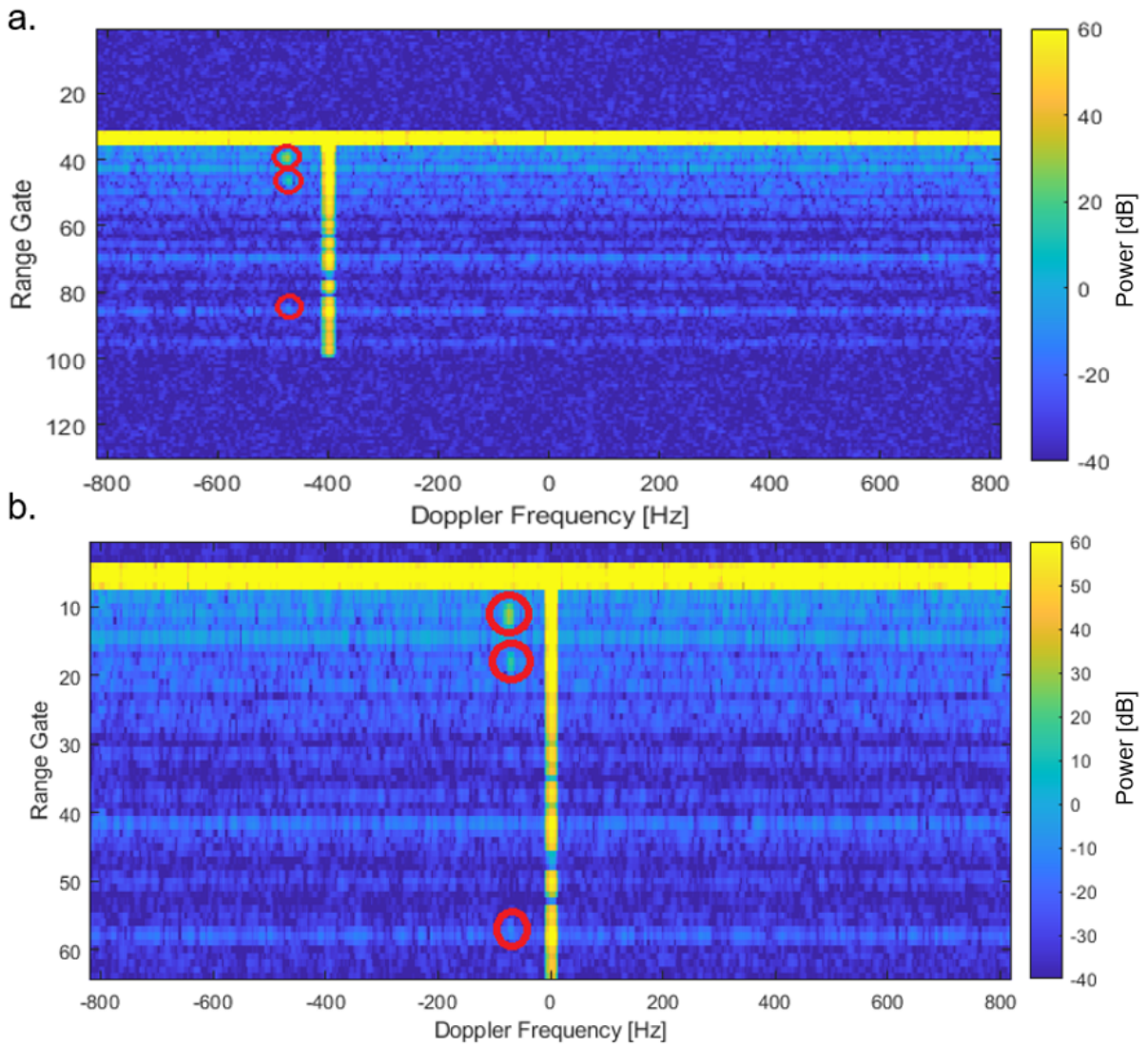

Figure C.6: Range-Doppler plot for the bistatic simulation. (a) Without bistatic corrections. (b) After applying bistatic correction processing on the time and frequency offsets.

C.2 Synchronized Radar Examples

This subsection is a part of a paper that is currently in review at the moment of writing "Phase Synchronization of Bistatic Radar by Exploiting the Urban Scene".

The next iteration of the model presents the example using synchronized local oscillators. The first example resembles a 2 node radar network synchronized using GPS disciplined oscillators (GPSDOs). The main differences, from the previous iterations, are that the initial frequency offset and drift have been removed and the focus is more on the oscillator phase noise and an effort to simulate this on the radar's carrier signal. More clutter points have been added such

that there is a clutter reference every 60m and at a randomized azimuth angle so that there can be multiple contributions per range gate. Other additional parameters used in this iteration are shown in Table C.4.

Table C.4: Additional parameters for the synchronized GPSDO radar simulation.

Parameter	**Value [unit]**
Number of receive element rows	16
Number of receive element columns	4
Element spacing	0.12 [m]
Number of samples per clock cycle	5
Transmitter power	2000 [W]
Range gates	86
Clock frequency	62.5e6 [Hz]
Tx frequency multiplier	20
Linear frequency drift	0 [Hz/s]
White phase noise	2.25e3
Flicker phase noise	1e3
Random walk PM	1.8e6
Flicker walk	6e4
Random walk FM	0
Initial Time Offset	1.36e-5 [s]
Initial Frequency Offset	0 [Hz]

The phase noise parameters have been chosen empirically such that it produces the same phase noise profile that is measured on the Leo Bodnar GPSDO [161]. More details on the phase noise measurements in the lab are presented in Chapter 7. There are several features that need to be accounted for when selecting the phase noise profile. First is the low frequency (close-in) phase noise. This can be difficult to measure for high frequency signals because of the sheer number of samples that would be required to generate a sufficient measurement time. Since the resolution bandwidth of the phase noise measurement is inversely proportional to the measurement time, at least 1 s of data is required to measure the phase noise at 1 Hz offset. When the sample frequency is 5 GHz, this would require 5e9 (5 billion) data points. To overcome this and avoid overwhelming the memory capacity of the PC, the signal is simulated at a lower frequency but the phase is scaled up accordingly (in order for the phase noise parameters p_0 - p_4 are consistent). Sampling at a lower frequency in the kHz regime allows for longer signals to be sampled with less memory requirements and the close in phase noise characteristics can

be measured.

Second is the high frequency noise which requires sampling at the actual carrier frequency. The carrier frequency is in GHz and the sampling frequency of the simulation must be at least several times this value. When white noise is applied, this is spread over all frequencies (as its definition) and this can cause problems later on down the line when radar PRF sampling causes aliasing of the noise. Since the PRF is in kHz and the noise bandwidth is in GHz, there is 10^6 factor of phase noise folding that can occur. This can be eliminated in real radar systems with the use of filters to reduce the phase noise at very far-out offset frequencies. In the simulation, a low pass filter is applied to the phase to reduce the noise bandwidth and the cut off frequency adjusted accordingly to match the measured phase noise data.

Both the close-in and far-out phase noise of the simulated carrier are shown in Figure C.7 after each of the parameters have been optimized. Also, to ensure the filter is having the intended effect on reducing the noise bandwidth, both simulated and measured phase noise profiles are calculated after PRF aliasing. There is a good match between the simulated and actual PN profiles for both the close-in and far-out regimes. Also, there is still a match after the fold over effect is applied from the PRF aliasing. Therefore, the chosen parameters are sufficient for representing the behaviour of the GPSDO for the rest of the simulation.

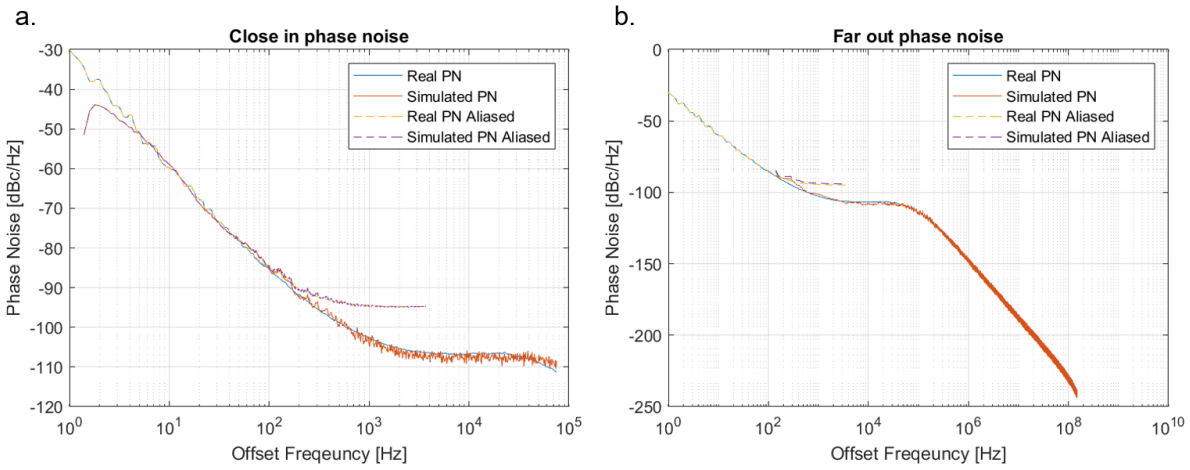

Figure C.7: Simulated GPSDO phase noise profile after parameter optimization. (a) Close-in phase noise comparison, (b) Far-out phase noise comparison.

The full simulation environment is shown in Figure C.8 with a more dense cluster of clutter

points. The clutter azimuth and RCS profiles used in the simulation inputs are shown in Figure C.9. Similar to the previous iterations, all 64 channels were used in a 16 x 4 grid configuration and a frame size of 2048 pulses were generated corresponding to a CPI of approximately 0.25 s.

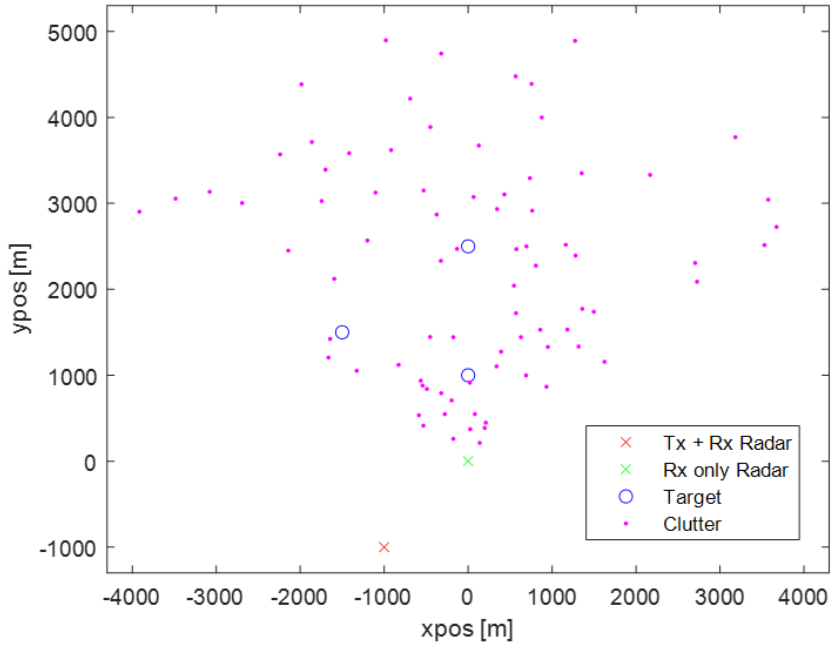

Figure C.8: Simulation environment, GPSDO synchronized radar.

The next stage involves checking to see if the phase noise profile carries through into the radar output. At this stage, the sampling frequency is limited to the radars PRF, so the theoretical effects of phase noise aliasing are also examined. Due to the shorter measurement time and the effect of the windowing, the resolution is not sufficient to measure the phase noise below 10 Hz reliably. Regardless, the phase noise at frequencies greater than 10 Hz is matching well with the expected profile after aliasing. In the 10 Hz to 100 Hz region a significant phase noise contribution from the GPSDO is successfully demonstrated in the simulated data.

Using this data set, the urban phase synchronization scheme is applied to test the effects it can have on reducing phase errors in bistatic radar scenarios. The phase estimation stage requires using multiple strong references located within the scene. Each of the range gates is scanned in azimuth and elevation to find the beams containing sufficient power to cross a set threshold. The clutter map (unscaled) is generated using the simulated output in Figure C.11a where the profile can be seen to correlate well with the input clutter positions. The scaled clutter power

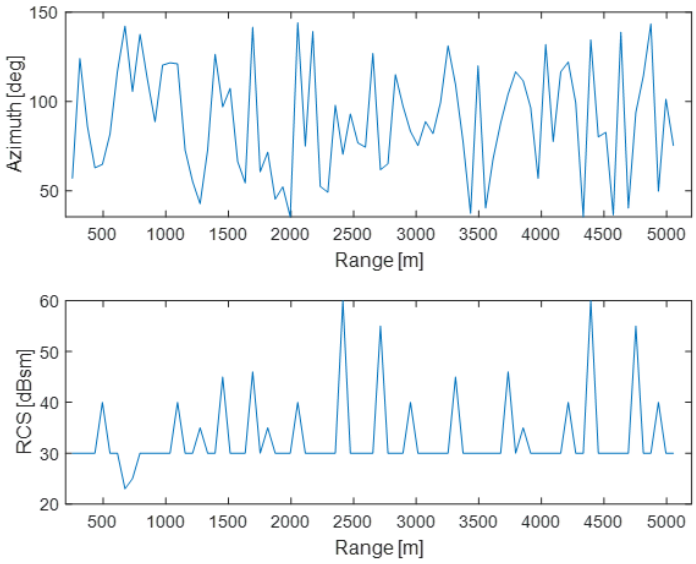

Figure C.9: Clutter profile for the synchronized radar simulation.

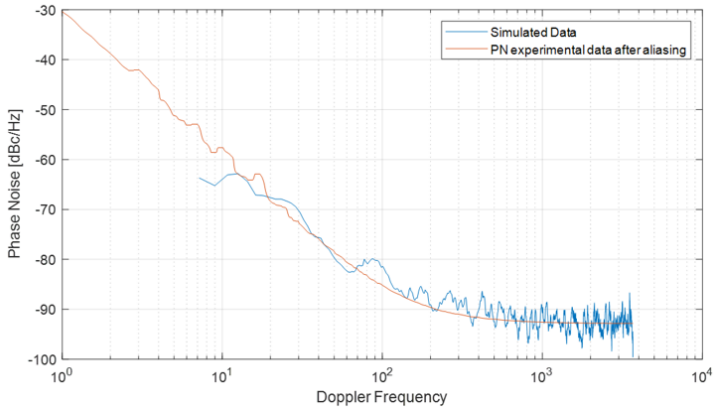

Figure C.10: Simulated GPSDO phase noise profile in the radar output.

profile is seen in Figure C.11b where there are several clutter points that have sufficient power to cross the threshold. These are the range gates containing clutter with high RCS, and are also marked on the clutter map. More will be discussed on the effects of the phase synchronization and the averaging of multiple sources in Chapter 6.2.3, but here there are 5 unique sources to used for phase estimation.

The next stage applies digital beamforming in the direction of the selected reference sources and then extracting the unwrapped phase accumulation. The unwrapped phase measured from each of the sources is shown in Figure C.12. A high correlation of the phase is seen between each of the selected sources . This is expected to be the case for the low frequency phase errors

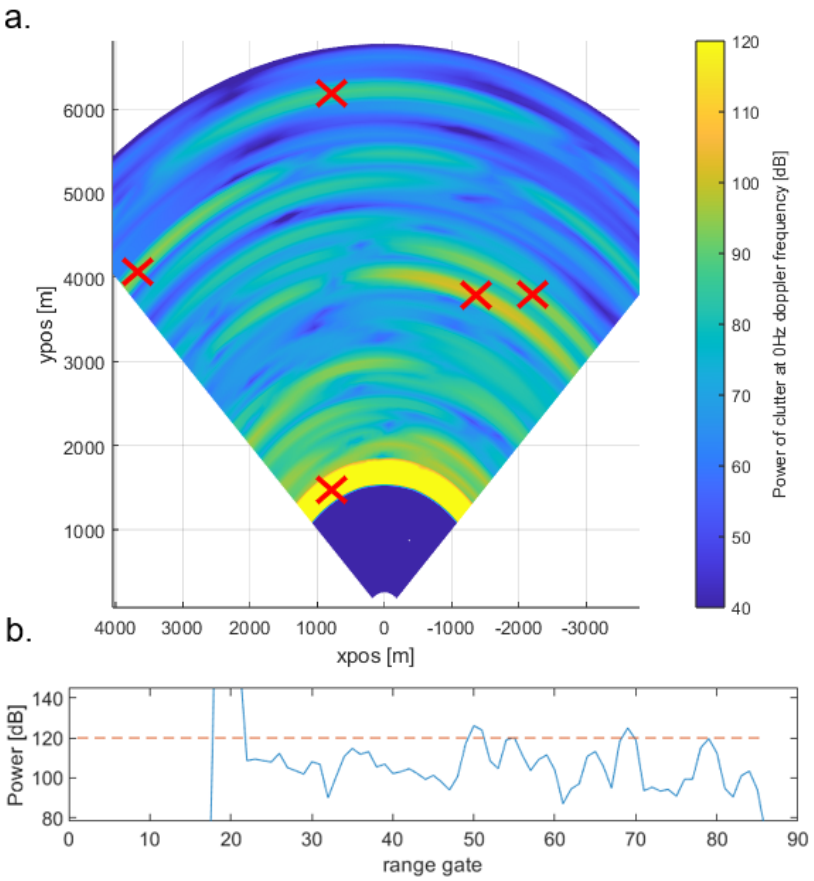

Figure C.11: (a) Unscaled clutter map at 0 Hz Doppler frequency for simulated data with significant reference sources marked. (b) Scaled clutter power profile of the simulated data with a set threshold applied.

which can be accounted for in the phase correction stage. However, upon further inspection on the very short time scales (see inset) there is some high frequency noise that is uncorrelated. This can be expected due to the PRF limitation on sampling of the radar echoes. Any behaviour of the signal at a frequency higher than the Nyquist frequency (f_{NQ}) would be ambiguous and would not be able to be accounted for in the digital domain. As discussed previously there is a significant effect due to the aliased phase noise incurred by folding over of the phase noise by a factor of 100 to 1000 so any noise contained within f_{NQ} and the noise bandwidth would appear as uncorrelated noise. The benefit of the new proposed synchronization scheme is to reduce the effect of ambiguous noise beyond f_{NQ} as the averaging process would reduce its contribution within the final phase estimation.

Once the accumulated phase error has been estimated, it can be applied to the data when

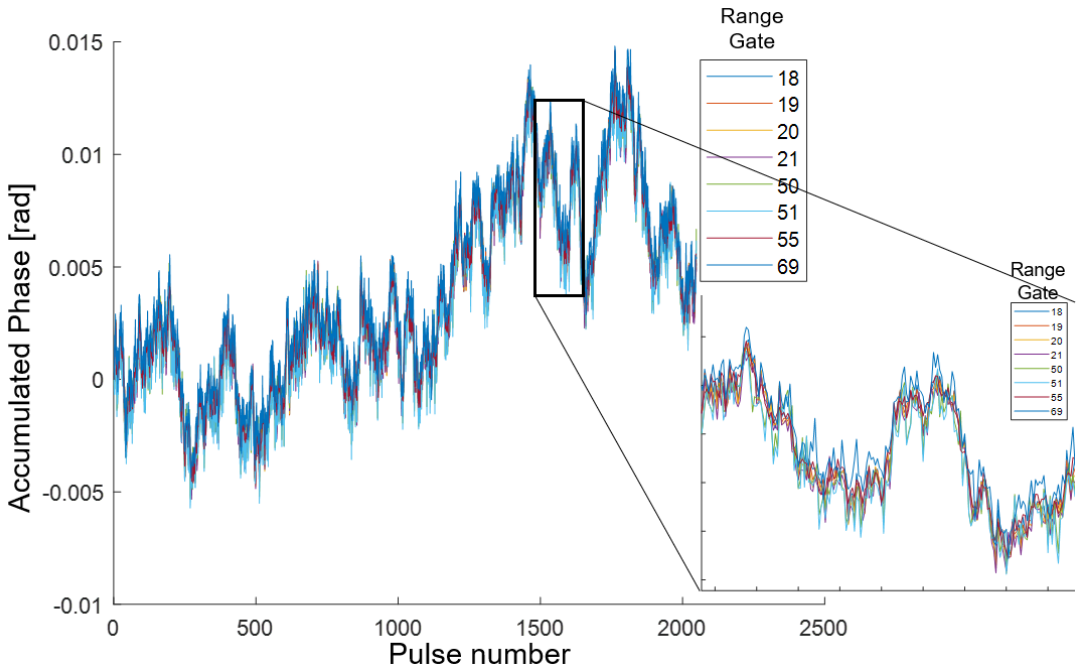

Figure C.12: Accumulated phase from several reference sources using simulated radar output data.

processing each beam. Firstly the beam is formed and then the inverse of the measured phase is applied to the time series data. Figure C.13 demonstrates the effect of the phase corrections on the overall phase error. The phase error is measured at a resolution cell consisting of strong clutter and no other moving targets. After the phase corrections are applied, the phase error is relatively constant and only containing high frequency fluctuations. Since only a stationary target is present the expected phase progression would be constant as is observed in this case.

To show that the phase synchronization is able to have a positive impact on the entire data, the range-Doppler plot comparison, before and after corrections, is shown in Figure C.14a, b. Here it can be seen that the raised clutter induced phase noise has been significantly reduced at the low offset Doppler frequencies. In this particular beam there are two targets visible. The most interesting is in range gate 31 where prior to the phase synchronization, the target is fully engulfed within the noise. The compared spectrum at this range gate is shown in C.14c where the effect of the phase correction is seen on the close-in Doppler frequencies while the high frequency noise is unable to be compensated. However, the effect of averaging out the uncorrelated noise is shown as the noise floor is not increased at the far-out frequencies. The

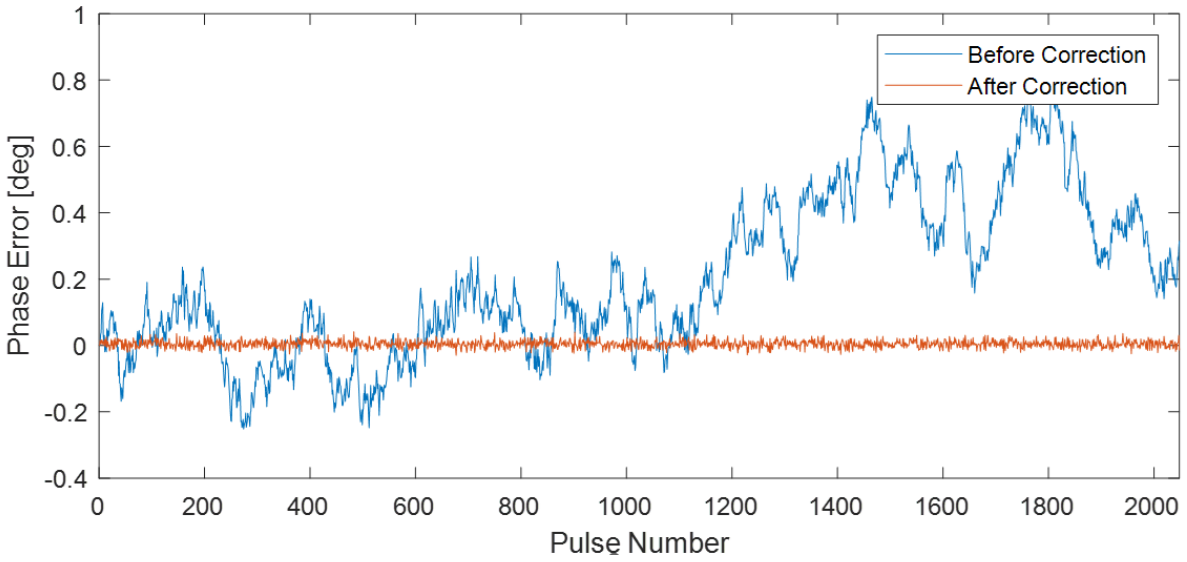

Figure C.13: Resultant phase error after applying phase synchronization.

scale is reduced in C.14d to show the effect of the phase noise suppression on the detection of the target. Clear suppression of the phase noise by approximately 20 dB around 100 Hz offset frequency allows the previously undetectable target to become unveiled as the noise is reduced.

The results show that the proposed phase synchronization method using various reference sources in the urban scene is successful in improving overall radar performance and sensitivity of targets within the simulation. In the chapter 6.2.3, this method is demonstrated on real radar measurements and the effect of phase corrections on the L-band staring radar network is quantified.

Overall, over the course of these iterations, the networked radar simulations have proven to be a useful tool in characterising the effect of time and frequency errors on a radar network. Also, the simulation framework allows for testing and verification of various signal processing techniques as was shown with the bistatic data corrections, bistatic detector and the urban phase synchronization. The simulation has been designed within this work from the ground up, with flexibility in mind, and the parameters can be adjusted to simulate the behaviour of any oscillator type to analyse its effect on radar performance. Also, the parameters of the entire radar system can be changed such as the operating frequency, array configuration and transmitted waveform, potentially opening up other use cases. In addition, due to the radars being defined and placed

as different objects, the simulation can be scaled up to more than 2 nodes, and can be configured into a multi-static network where future use of the simulations for fully synchronized multi-static networks and testing of coherent data fusion processing techniques can be applied.

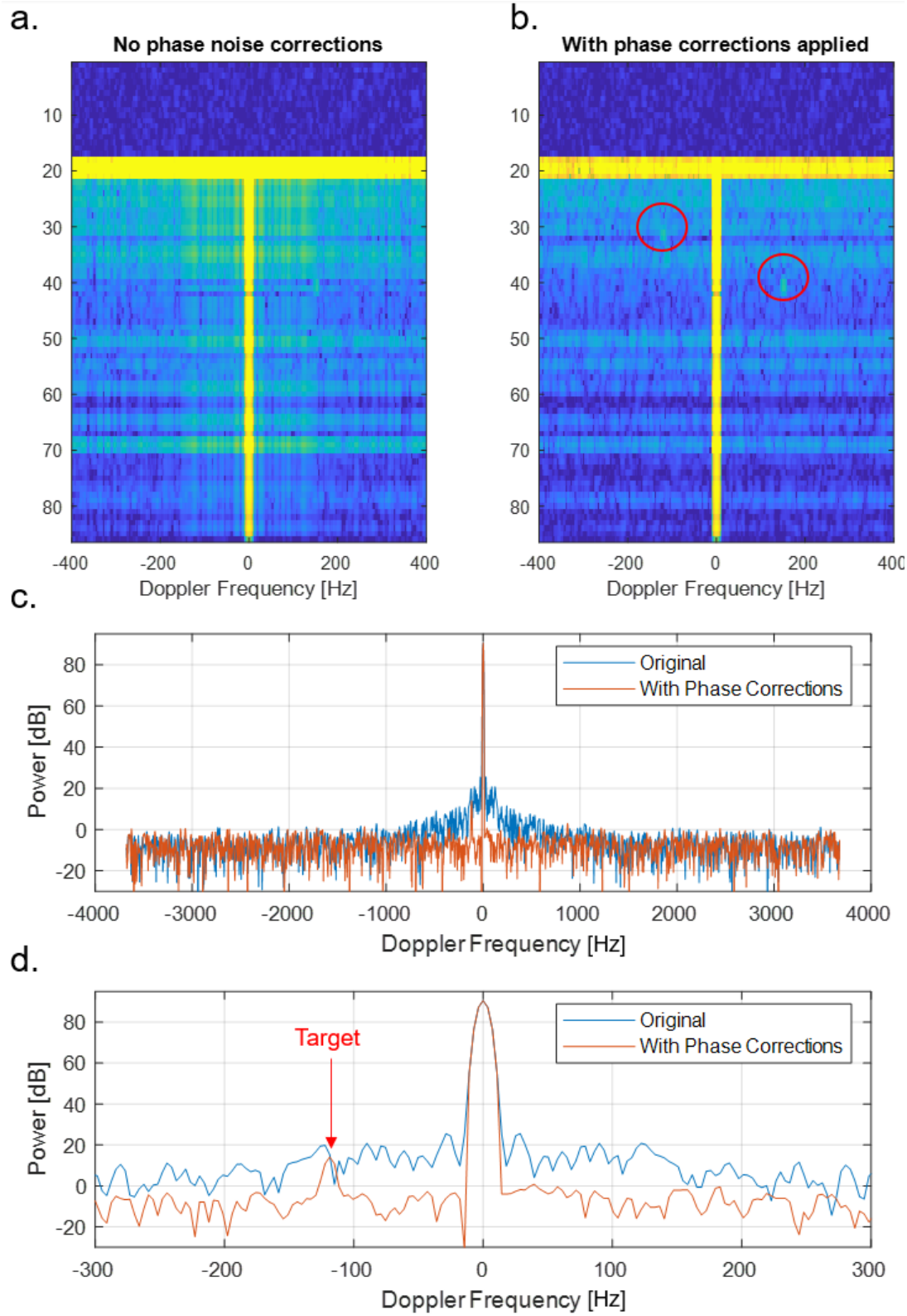

Figure C.14: Range-Doppler plot (a) before applying phase synchronization, (b) after applying phase synchronization. (c) Doppler spectrum comparison of resolution cell containing simulated target. (d) Doppler spectrum with rescaled axis.

Appendix D

Monostatic Radar Results with Low Noise Photonic Oscillator

This section describes some of the radar trials and results related to utilizing the different oscillators of varying qualities within the radar. The oscillators are characterized in section 7 regarding their frequency stability. For the case of monostatic radars, inherent phase noise cancellation is expected and therefore the long term Allan deviation measurements are not considered here, but the relevant oscillators for the monostatic radar measurements are listed in Table D.1 with corresponding phase noise values.

Table D.1: List of oscillators under test with corresponding phase noise values measured at probe B f_{LO}.

OUT	Oscillator Name	Oscillator Type	Measured PN @ 1 Hz	Measured PN @ 10 Hz	Measured PN @ 100 Hz	Measured PN @ 10 kHz
OUT7	Aveillant PLO	OCXO	-75.1	-106.1	-135.7	-155.0
OUT8	Leo Bodnar	GPSDO	-56.0	-86.1	-111.9	-133.3
OUT14	Rakon	OCXO	-106.0	-125.7	-132.8	-133.9
OUT6b	MWP	Photonic	**-113.9**	**-132.9**	**-143.4**	**-155.5**

The PLO contains an OCXO with a low white phase noise floor, producing low noise values at 10 kHz offset. The Rakon OCXO has poor performance at the high offset frequencies but has low phase noise at the close in frequencies with only -106 dBc/Hz at 1 Hz offset. The Leo Bodnar consists of an internal TCXO, resulting in comparability poor phase noise all around. The MWP

exhibits superior phase noise across all offset frequencies, despite significant degradation in phase noise improvement caused by the PLL upconversion stage from f_{LO} to f_c.

In this section the effect of the oscillator phase noise on a monostatic radar will be assessed. For measurement of the radar output phase noise and sensitivity, the night trial data will be used. For the measurement of target detection performance, the controlled drone trial data will be used. A list of the data sets used in this analysis are shown in Table D.2. Oscillator under test (OUT) sets a label to each of the oscillators used within the radar. The flight number indicates the position within the sequence of flights conducted during the trial.

Table D.2: Table of data sets used for monostatic oscillator radar assessment.

OUT	Night trial data	Drone trial data	Flight number
OUT7	2024-03-05_Uob_Trial49 M02	2024-03-13_Uob_Trial52 M02	Flight #4
OUT8	2024-03-05_Uob_Trial49 M04	2024-03-13_Uob_Trial52 M03	Flight #7
OUT14	2024-03-05_Uob_Trial49 M05	2024-03-13_Uob_Trial52 M04	Flight #10
OUT6b	2024-03-05_Uob_Trial49 M01	2024-03-13_Uob_Trial52 M01	Flight #1

D.1 Background Floor and Radar Phase Noise

Measurement of the background noise level is undertaken in optimal conditions where the target occupancy levels are at their minimum. For the data recordings listed in Table. D.2, a spectrogram of the Trigate building is generated for each 2.5 minuite interval. The spectrograms with the least moving targets present for each of the missions are chosen for the further processing. Trigate spectrograms for the MWP and PLO data sets are shown in Figure D.1. Due to the large resolution cells of the radar, it can be very difficult to get a long period of time where no targets are present whatsoever. Therefore, a few small targets are visible in Figure D.1b, but effort has been made to minimize this.

Using the data from the time intervals mentioned, the clutter data structure is generated with a CPI of 2 s and only the 200 Doppler frequency bins either side around the centre are retained. This is repeated for the 4 oscillator configurations PLO, Leo Bodnar GPSDO, Rakon OCXO and MWP.

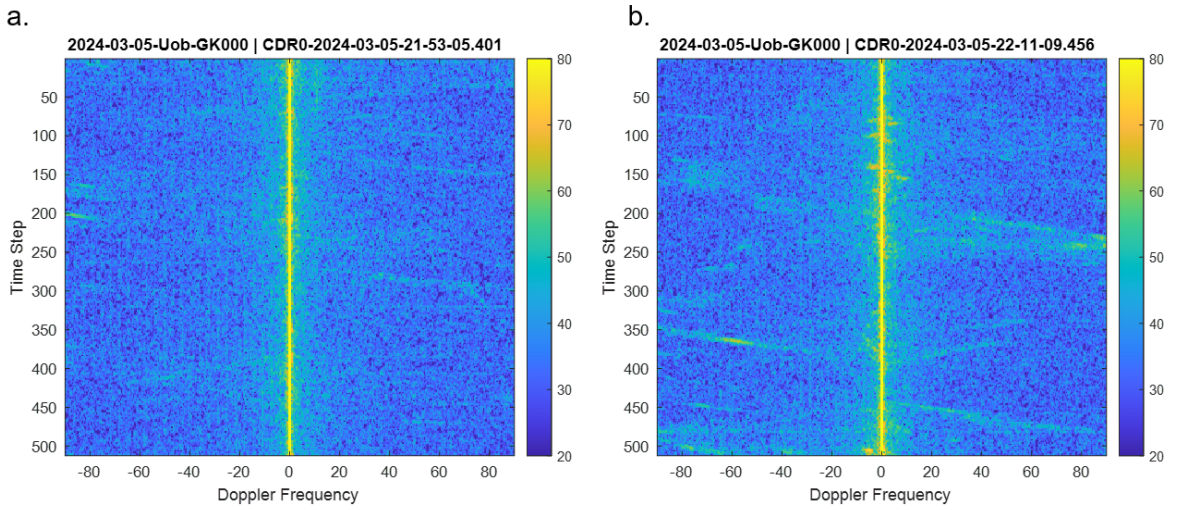

Figure D.1: Monostatic background spectrograms of the Trigate building. (a) OUT6b - MWP, (b) OUT7 - PLO. Both cases show that the target occupancy is low and the background level can be estimated with better accuracy.

The mean of the clutter data structures are taken in the slow time dimension and at the resolution cell containing Trigate. This contains the averaged sprectrum representing the noise levels in that particular region and is shown in Figure D.2a for all four oscillators. Also, since there are small changes in the overall clutter power the relative noise levels to the peak power are shown in D.2b since phase noise is expected to be proportional to the clutter power.

Below 10 Hz there are less noticeable differences in the phase noise. This can be due to non stationary clutter contributions at the low offset frequencies which will ultimately limit sub clutter visibility beyond the scope of the oscillator. Also, self phase cancellation is more effective at the lower frequencies so the phase noise is expected to be suppressed more to the radars limit [29]. In the region of 10 Hz to 100 Hz the Rakon OCXO is shown to have the highest noise level and then followed by the Leo Bodnar GPSDO. Both of these oscillators seem to be resulting in a white noise limited region beyond 10 Hz at levels of -89 dBc and -92 dBc respectively. On the other hand, the PLO and MWP noise levels are continuing to decrease as the Doppler frequency increases, approaching -99 dBc towards 100 Hz offset. Due to the TWG upconversion limit and PRF aliasing mentioned earlier, the PLO and MWP are both limited in this region and therefore, they appear to have the same noise level.

The implications of the reduced noise floor compared to the GPSDO and Rakon are the

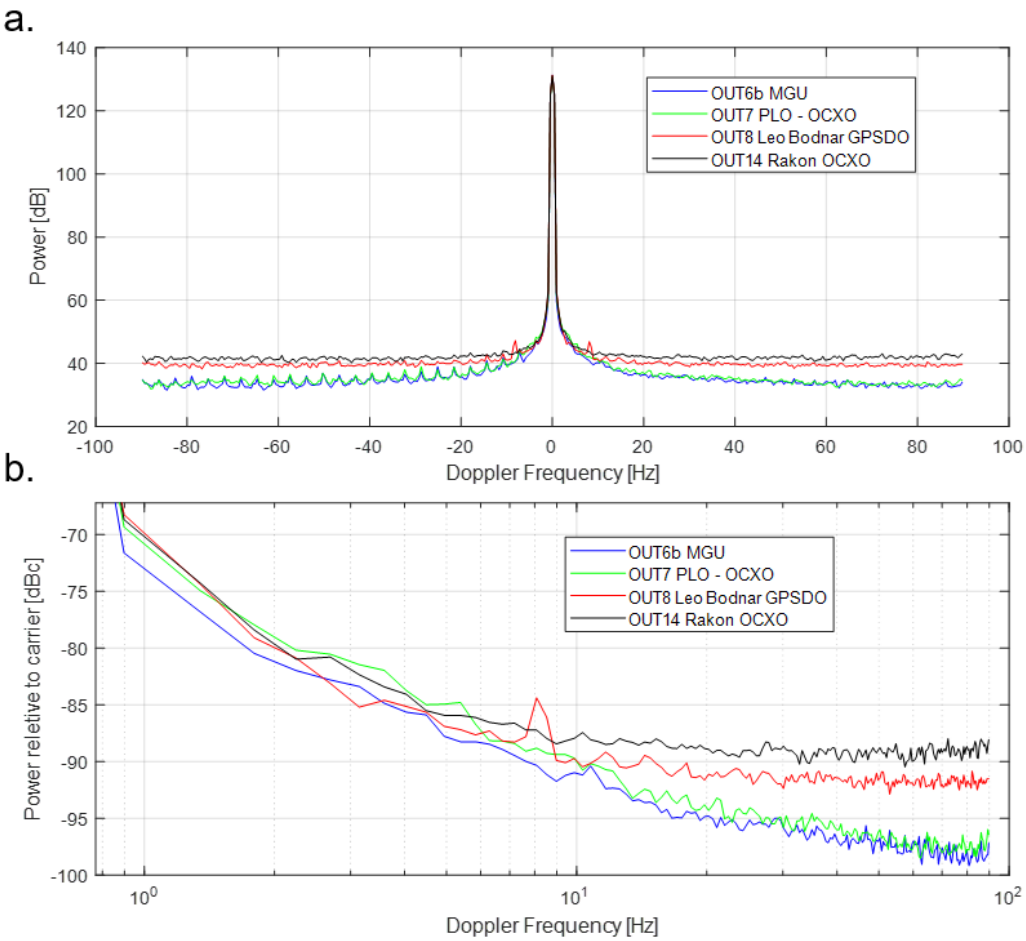

Figure D.2: (a) Monostatic background level spectrum in the Trigate region for different oscillators. (b) Background power relative to the peak clutter power.

higher dynamic range available. Smaller signals can be detected within the urban region and all targets will have have a higher SNR.

D.2 Clutter Maps

In the previous section, the focus was only on the Trigate building. However, the noise level is heavily dependant on the location under test. Clutter maps can help give a visual indication on the noise levels throughout the FOV. In Figure D.3, the clutter map at 0 Hz Doppler frequency is shown. This represents the overall clutter power and gives an indication of where a reduction in performance due to phase noise is expected. The Trigate building is one of the most noticeable regions at [2500, 3200] m as it is an isolated point where both the range from the radar and

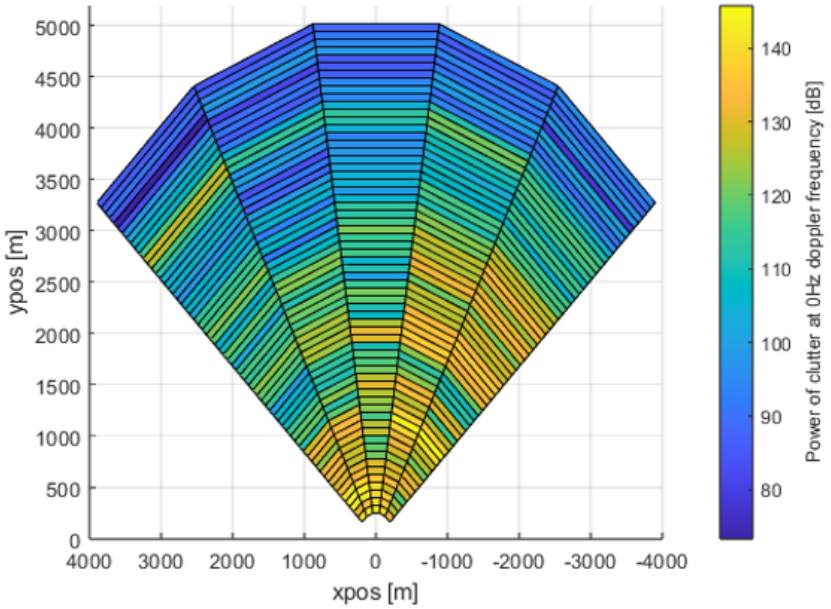

Figure D.3: Clutter map of the GK000 monostatic radar at 0 Hz.

received power levels are high. There are several other regions of interest including the bright area on the right hand side which is located closer to the city centre where more clusters of large buildings are located.

Phase noise clutter map are shown in Figure D.4 for each of the four oscillator configurations at 40 Hz Doppler frequency. As expected, the same regions tend to contain higher power. The MWP and PLO clutter maps in Figure D.4a & b respectively contain less power relative to the GPSDO and Rakon. This relates to an increase in sensitivity in all of the previously clutter limited regions. Areas in dark blue color are already thermal noise limited and are expected to remain the same regardless of whether a higher quality oscillator signal is used.

To compare the different clutter maps directly and give a quantity of improvement in the noise level, difference clutter maps (DCM) are used. Since the radar FOV is exactly the same between the different data sets, the resolution cells are expected to contain the same targets. The DCM is a direct subtraction of one clutter map from another. The DCM showing the phase noise improvement of the MWP compared to the Leo Bodnar GPSDO is shown in Figure D.5 for different Doppler frequencies.

At 10 Hz Doppler offset frequency, there is little improvement but this tends to increase

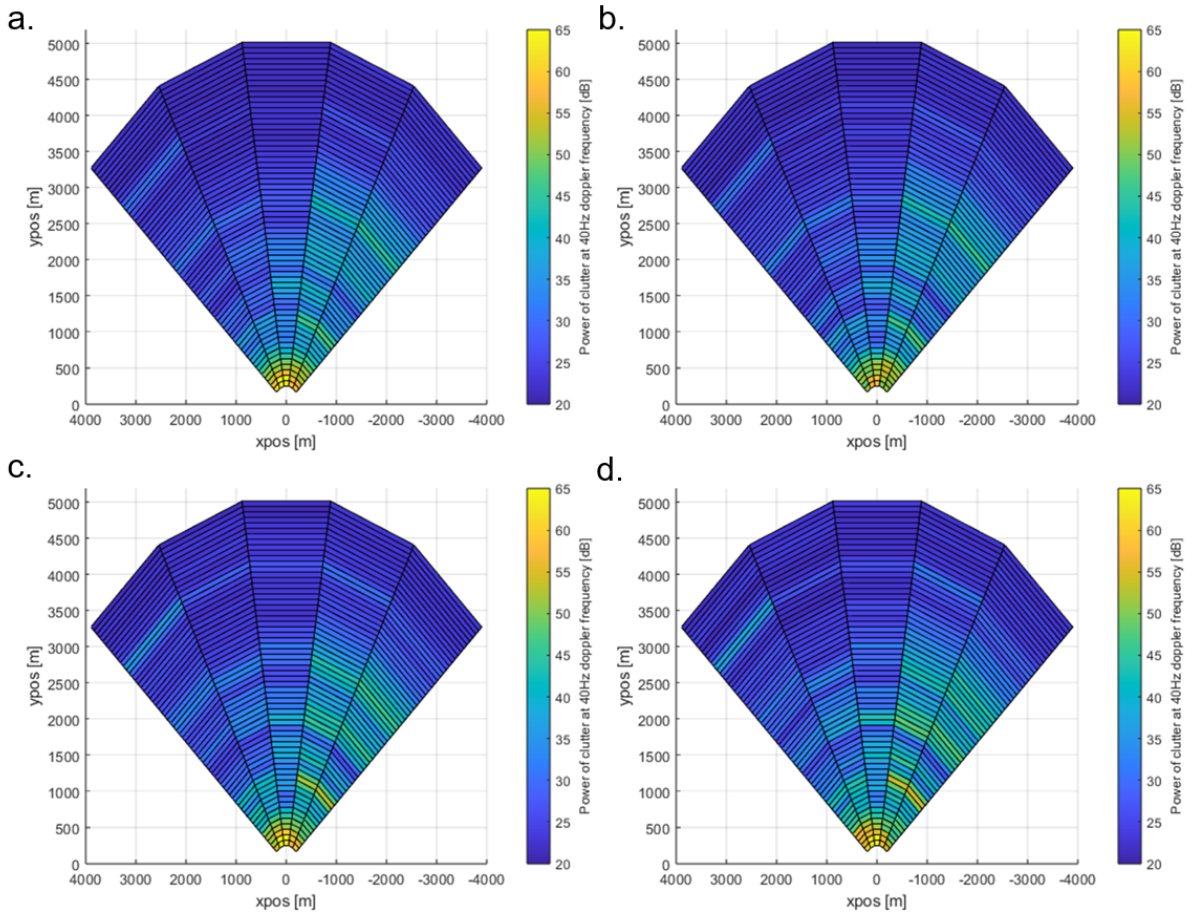

Figure D.4: Clutter maps at 40 Hz Doppler frequency, (a) MWP, (b) PLO, (c) Leo Bodnar GPSDO, (d) Rakon OCXO.

for the higher Doppler frequencies due to the continuing decrease in noise level of the MWP. At 40 Hz and 80 Hz Doppler frequency in Figure D.5 c & d, the map is dominated by green, denoting a reduction in noise levels throughout the FOV. For the Trigate region ([2500, 3200] m) in particular the phase noise improvement is 2.30 dB, 3.82 dB, 5.43 dB, 6.60 dB at 10 Hz, 20 Hz, 40 Hz and 80 Hz respectively. These figures directly represent the expected increase in SNR of a target moving at the specified velocity at each region within the FOV. Improving the oscillator will only have an impact in phase noise limited regions.

A similar figure is shown for the phase noise improvement of the MWP compared to the PLO in Figure D.6 but in this case there is no trend suggesting that one oscillator is providing better sensitivity than the other. There are several near range cells in the first 2 range bins that are shown to contain considerably lower noise for the PLO but these are localised. Since this

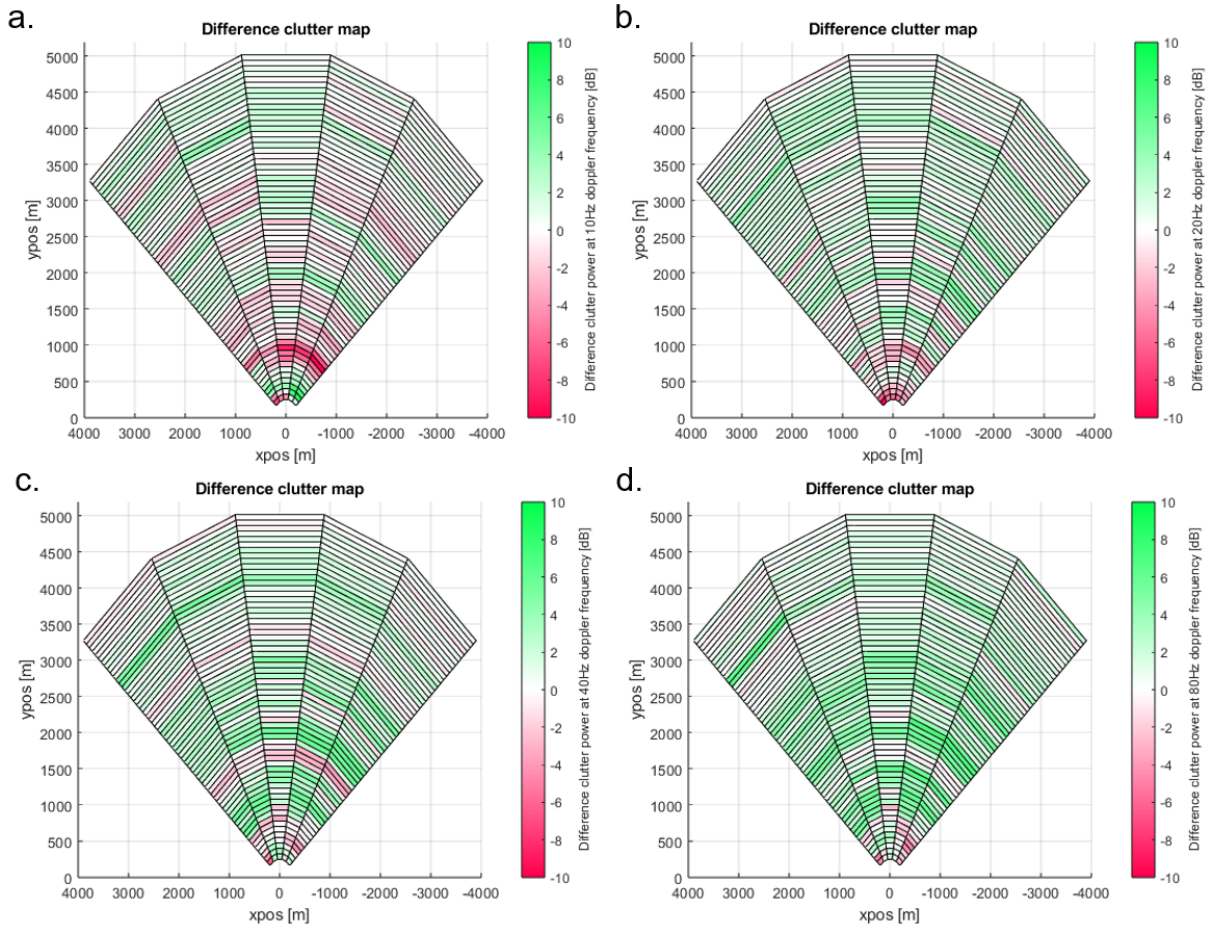

Figure D.5: Difference clutter maps showing MWP noise improvement compared with Leo Bodnar GPSDO at Doppler frequencies of: (a) 10 Hz, (b) 20 Hz, (c) 40 Hz, (d) 80 Hz

trend is not also seen within the other high clutter regions, its is unrelated to the oscillator.

D.3 SSB Phase PSD

The time series data for the Trigate returns for the monostatic GK000 radar were extracted for each of the four measurements, and the SSB phase PSD was calculated using 5 s of time series data. The phase PSD for each of the oscillators is shown in Figure D.7. Similarly to the noise spectrum, the PSD is not reliable at the low frequencies due to external effects. However, beyond 10 Hz, the same trends are shown between the different oscillators. The white noise floor was expected to be the highest in the Rakon OCXO due to the measurements in table D.1.

As will be discussed in further detail in Chapter 7, the high noise in the 100 kHz region

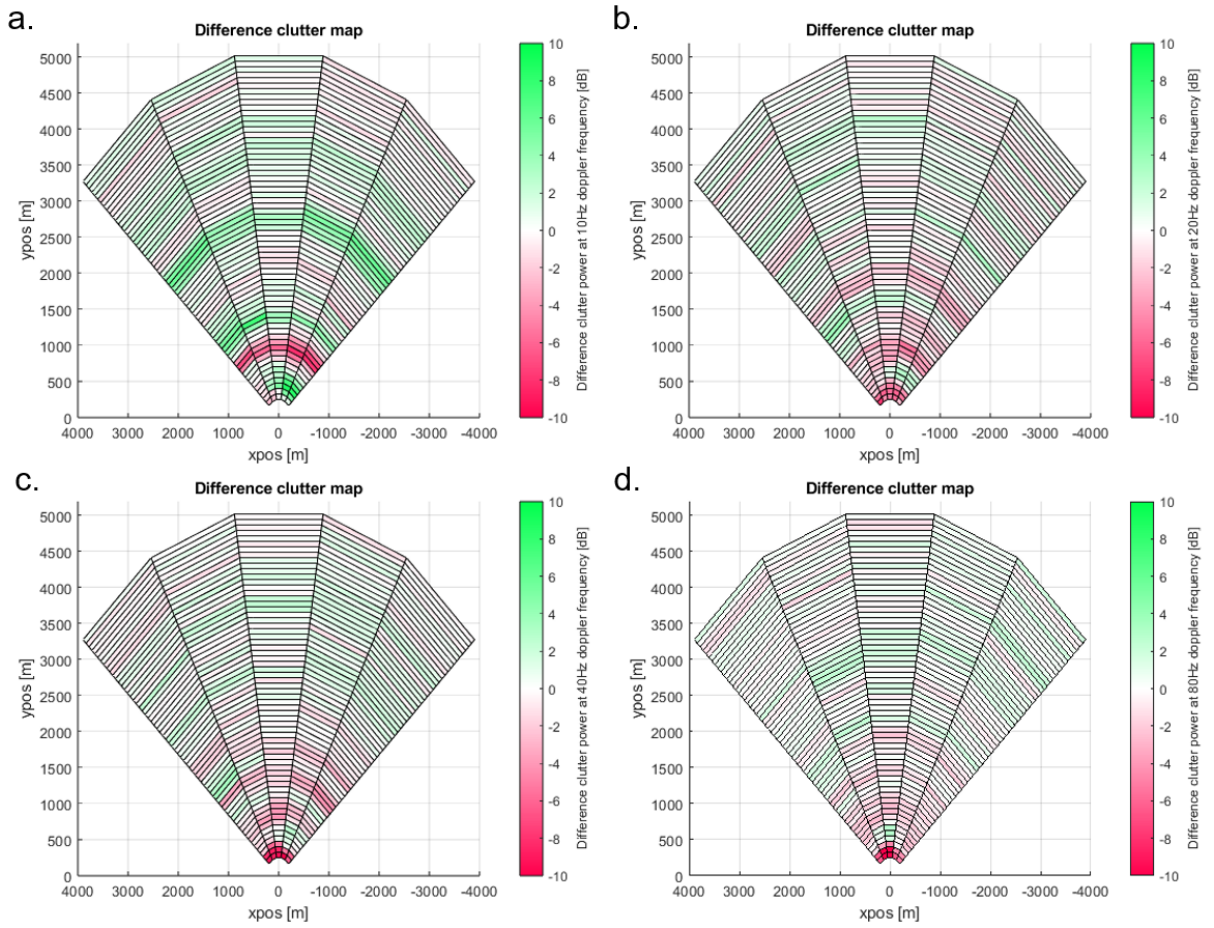

Figure D.6: Difference clutter maps showing MWP noise improvement compared with PLO at Doppler frequencies of: (a) 10 Hz, (b) 20 Hz, (c) 40 Hz, (d) 80 Hz

caused significant addition of the phase noise due to PRF aliasing and this is highlighted again in the phase PSD. Leo Bodnar GPSDO is shown to have lower phase noise than the Rakon and then followed by the MWP and PLO. The PLO and MWP have almost identical phase PSD profiles due to the additive phase noise of the TWG synthesiser, also discussed further in Chapter 7.

The coherent integration loss and timing error are not considered here since it is taken as granted in the monostatic radar configuration, so there is assumed to be no loss. Coherent integration loss will be measured in the following chapters when the radars are utilized in a network.

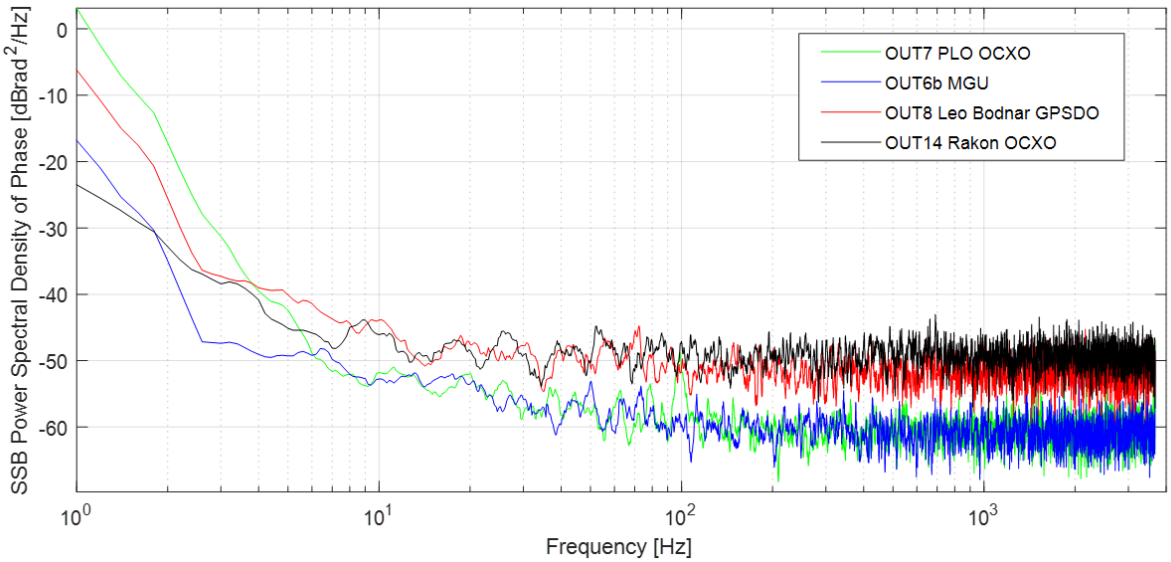

Figure D.7: SSB Phase PSD of PLO, MWP, Leo Bodnar GPSDO and Rakon OCXO.

D.4 Target Detection Analysis

Previously the radar's background noise levels were measured with different oscillators. The lower phase noise oscillators provided improvements in the expected sensitivity in the phase noise limited regions. In this section, real controlled drone measurements are analysed to determine the effect of the oscillator phase noise on the detection of SUAVs in a monostatic staring radar. The flights that are used within this section are listed in Table. D.2. These consist of flights from the 2024-03-13 radar measurements, one flight corresponding to the each of the four OUTs. To ensure the comparison is focused as much on oscillators as possible, flights are taken from the same day, the same target is used (DJI Inspire 2), with automated flight mode and other parameters such as drone set speed, altitude, processing methods are maintained constant.

The raw data is processed into spectrograms and these are shown in Figure D.8 for each of the flights. With this qualitative data, a visual indication on the detectability can be made. The signal level of the fuselage returns are high in all of the flights due to the large size of the target and the micro-Doppler returns are also visible. The main differences can be seen when the drone is passing through a phase noise limited region which for the Rakon is most of the flight from timestep 140 onwards indicated by the power of the noise floor. However, the MWP and PLO flights contain more regions where the thermal noise floor is reached, which for this

radar system is generally around 15 dB in the scale shown. There does not seem to be any clear performance difference between the PLO and the MWP in terms of noise levels. Although the main body SNR is high, the other components that are important for classifying the target type such as the micro-Doppler in this case are much lower in power. The micro-Doppler is seen clearly throughout the flight for the MWP and PLO but in the other flights they are sometimes hidden within the noise and therefore, information is lost.

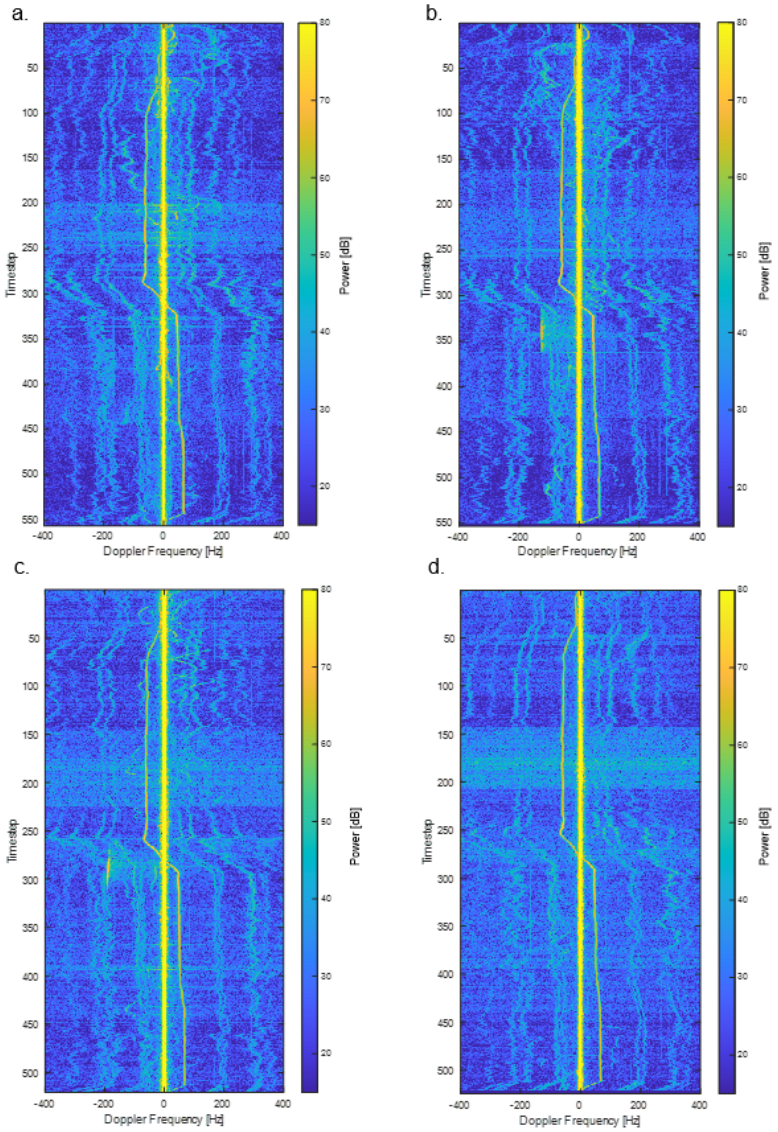

Figure D.8: Drone flight spectrograms of DJI Inspire 2 performing the Richmond_S01 100 m scenario (a) MWP, (b) PLO-OCXO, (c) Leo Bodnar GPSDO, (d) Rakon OCXO

A more direct comparison can be obtained by measuring the SNR throughout the flight and comparing directly. The signal power is determined via peak detection and the process is as

follows. Using the GPS truth data, the beam containing the predicted location of the target is generated and a scan is performed in the frequency domain to find a peak close to the predicted Doppler frequency. Fine beamforming process if used to obtain the peak power of the target and this beam is then selected for the spectrogram. For the noise power, one of the challenges as discussed previously is obtaining a true measure of the noise floor in the particular range-beam-Doppler CUT. Drone targets are generally very stable and can occupy the same cell for extended periods of time, therefore skewing the noise measurement if using the historical data method. Therefore, the method used here is to obtain a SBM from a predefined data set where the same oscillator-radar configuration is used and the target occupancy levels are low. For these measurements, SBMs from the 2024-03-05 night measurements are used to measure the noise power in the same range-beam-Doppler cell as the target.

This method of calculating the signal and noise powers to determine SNR has its own drawbacks. Time dependant noise factors are lost but this is not the focus of this analysis. The main point is, this method is able to obtain the oscillator dependant noise floor and therefore SNR. The SNR for each of the 4 flights using this method is shown in Figure.D.9a.

In Figure D.9b, the target velocity as measured from the GPS truth data is plotted and a small time delay is applied to each of the flight profiles to ensure best alignment of the data. This ensures that a focus can be given to a particular region of the flights as they are designed to be consistent. The separated signal power and noise power components are also plotted in Figure D.10.

The first region of interest is timestep 10 - 40 where the target is moving almost tangentially to the line of sight (LOS) and therefore, relative velocity is low and is competing with the clutter for detection. Phase noise is more severe at the low frequencies and at this stage the target main body is around 10 Hz Doppler frequency in each of the flights. The SNR tends to be higher per CPI for the MWP and the Rakon, corresponding to the much lower close in phase noise that they possess. These are then followed by the PLO and then finally the Leo Bodnar GPSDO with the lowest SNR. The superior phase noise of the MWP is carrying through to a lower noise level than the other conventional oscillators in this region. This is occasionally resulting in a reported

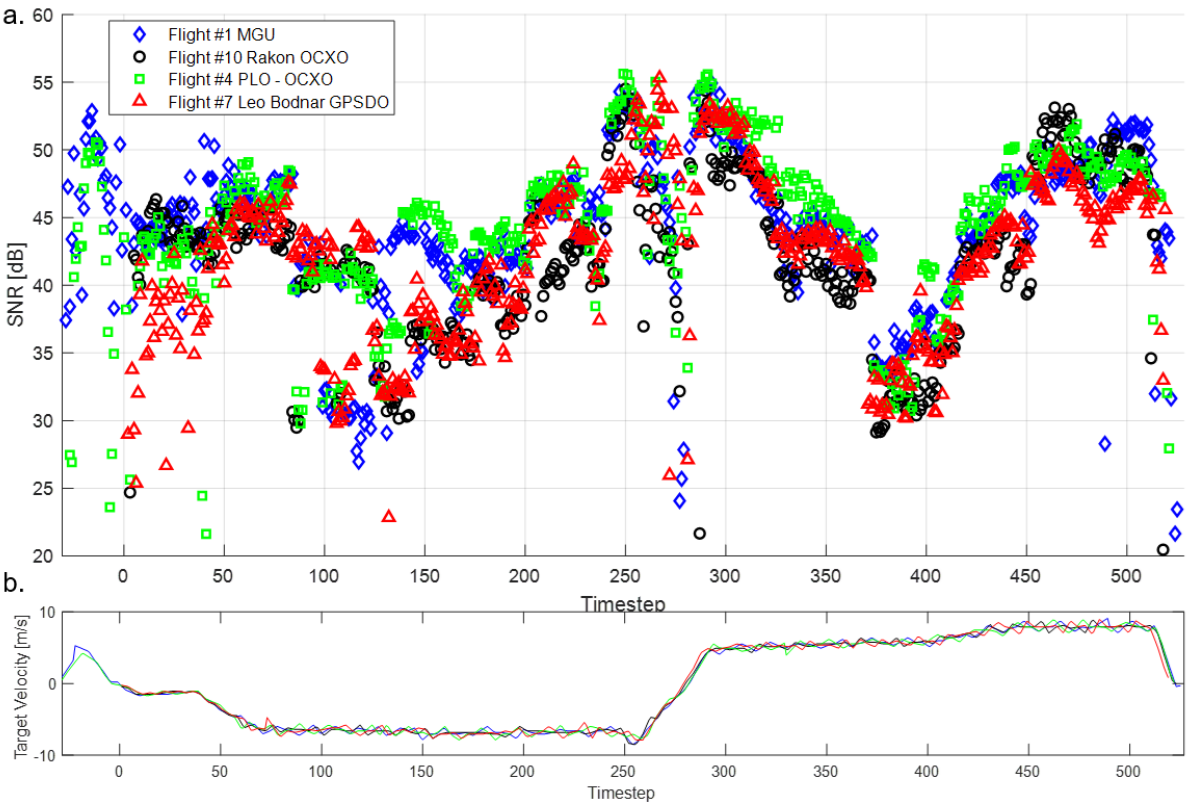

Figure D.9: (a) SNR comparison between different oscillators throughout the controlled drone flight, (b) Target velocity as measured from GPS truth data.

MWP SNR that is 10 dB higher that in the GPSDO.

The next region is timestep 140 - 200 where the clutter levels are at the highest and therefore the noise is raised accordingly.In this region, the PLO surprisingly has approximately 2 dB higher SNR than the MWP, followed by the GPSDO and the Rakon. The SNR is much lower in the GPSDO and Rakon, mostly due to the clutter induced phase noise but also there is a drop in the signal level at times, the exact reason for this is not understood.

The final region is timestep 360 - 430 is another phase noise limited region, and similar trends can be spotted here. However, between 370 - 395, the SNR is reported to be the highest in the MWP rather than the PLO.

Overall trend is that the PLO is consistently producing slightly higher SNR than the MWP during the main portions of the flight while there are particular situations where the PLO noise is higher such as for slow moving targets. There is a relatively larger degradation in performance between the other two oscillators but generally the Rakon has the lowest SNR throughout most

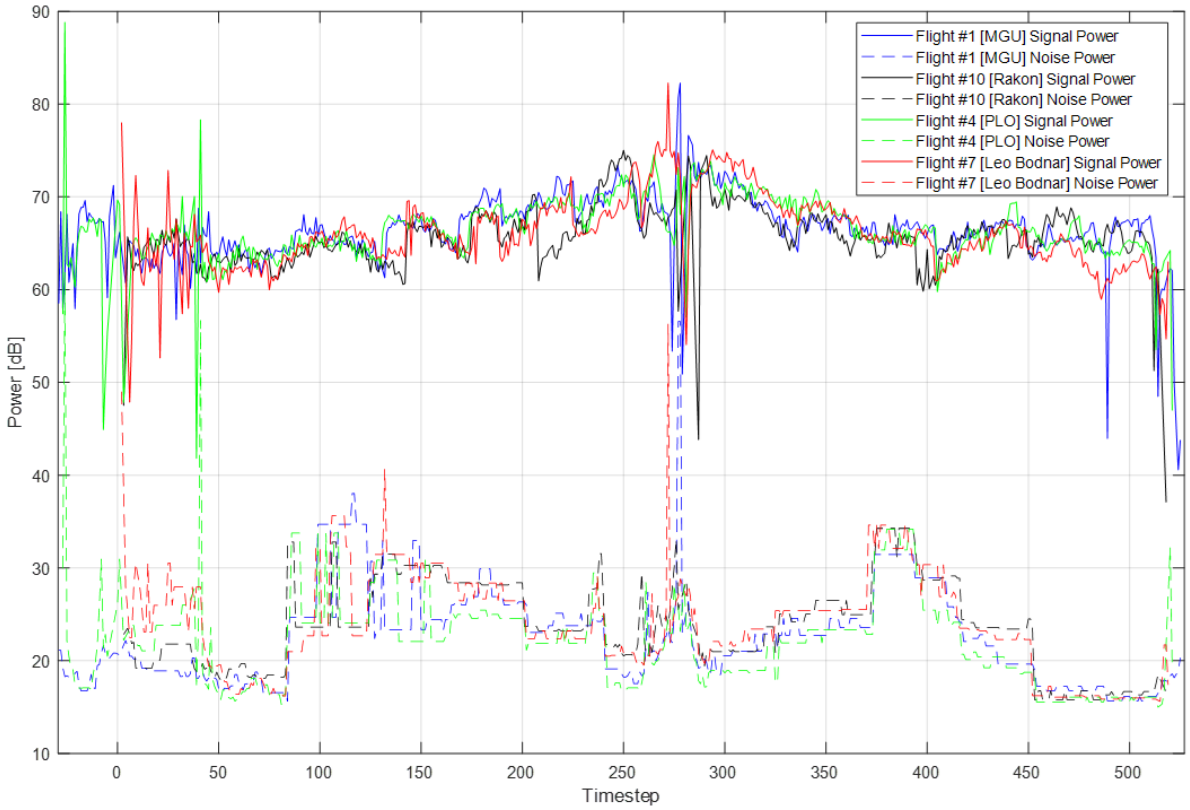

Figure D.10: Comparison of separated signal and noise components for each oscillator.

of the flight. The quantified results are shown in Table. D.3 where the average SNR throughout the flight is shown as well as the PD as measured from the SBM based CFAR with a threshold of 20 dB above the noise level.

Table D.3: Monostatic drone trial results showing average SNR and PD of the same flight parameters for each different oscillator configuration.

Oscillator Name [OUT]	**Average SNR [dB]**	**Target PD**
MWP [OUT6b]	44.03	**0.982**
PLO [OUT7]	**44.44**	0.964
Leo Bodnar GPSDO [OUT8]	42.06	0.979
Rakon OCXO [OUT14]	41.97	0.962

The results show that the higher quality oscillators are somewhat carried throughout the radar into better detection performance. The MWP/PLO obtain a lower phase noise measurement at probe C in the oscillator-radar interface and provide the radar with lower noise levels in the urban environment and higher SNR for detection. Clearly, there is still a way to go as can be seen in Figure D.10 where the noise level is still 15-20 dB above the minimum thermal limit

even for the photonic oscillator. However, these issues can only be resolved by overcoming the current bottlenecks in general modern radar architecture which is discussed more in the future outlook in Chapter 7.4.